Communications Research Centre Canada
An Agency of Industry Canada

Centre de recherches sur les communications Canada
Un organisme d'industrie Canada

Measurements of the Electromagnetic Far-Fields Produced by a Portable Transmitter (Principal Planes) Part II

By J.E. Roy

IC

LKC
TK
5102.5
.C673e
#99-001
c.2

CRC Report No. CRC-RP-99-001
November 1999

Canada

CRC

Tk
5102.5
C673e
#99-001
c.a
S-Gen

CRC LIBRARY
-12- 1 4 1999
BIBLIOTHEQUE

MEASUREMENTS OF THE ELECTROMAGNETIC FAR-FIELDS PRODUCED BY A PORTABLE TRANSMITTER (PRINCIPAL PLANES) PART II

Industry Canada
Library - Queen
AOUT AUG 2 2 2012
Industrie Canada
Bibliothèque - Queen

CRC REPORT No. CRC-RP-99-001

written by:

J.E. Roy

Communications Research Centre
3701 Carling Ave., P.O. Box 11490, Station H
Ottawa, Ontario, Canada, K2H 8S2

November 1999

© Copyright 1999: J.E. Roy

Acknowledgments

The author wishes to thank Mr. Wilfred Lauber and Mr. Jean Bertrand for supervising the creation of the drawings, for checking their accuracy and for supervising the manufacturing of the hardware, and Mr. Claude DesOrmeaux for his cooperation in acquiring the measurement data presented in this report. The author also wishes to thank Mr. Lauber and Dr. Gilbert Morin for reviewing this document. This work was supported in part by DGSE (Director General Spectrum Engineering) and FirstMark Technologies Ltd.

Table of Contents

Acknowledgments i

Table of Contents ii

List of Tables v

List of Figures vi

Chapter 1. Introduction 1

Chapter 2. Test Setup 3

2.1 Anechoic chamber setup 3

2.2 Equipment setup 14

2.3 Mechanical setup 18

2.3.1 Alignment procedure 32

2.4 Experiment setup 36

Chapter 3. Test Results 46

3.1 Plots 46

3.2 Discussion 46

Chapter 4. Sources of error **101**

4.1 Data smearing assessment 101

4.2 Repeatability assessment 114

4.2.1 Data variation due to electrical noise 114

4.2.2 Data variation due to re-positioning and re-levelling the transmitter 128

4.2.3 Data variation due to re-levelling the transmitter 135

4.2.4 Data variation due to re-positioning some absorber 140

4.2.5 Data variation due to the battery DC power level variation . . 146

4.3 Measurement error budget 147

Chapter 5. Data Comparison **151**

5.1 FDTD predicted vs 1998 measured data for the first and second tests 151

5.1.1 Generalities 151

5.1.2 FDTD simulation 152

5.1.3 Results 156

5.1.4 Discussion 171

5.2 1998 measured data vs 1997 measured data 176

5.2.1 Generalities 176

5.2.2 Results 177

5.2.3 Discussion 185

Chapter 6. Conclusion **187**

References **190**

Appendix A. Drawings **191**

Appendix B. Coordinate Transformation **216**

Appendix C. FORTRAN source code **223**

C.1 Comparison program 225

C.2 Parabolic interpolation program 244

C.3 Coordinate transformation program 249

C.4 Mapping from the measurement angle to the appropriate spherical coordinate angle 258

C.5 Power correction of the acquired data with respect to the power transfer function of the network analyzer 264

C.6 Total electric field contour level 268

Appendix D. Gain Measurement of the Receive Horn **272**

List of Tables

2.1 Mapping between measurement and spherical coordinate angular values for the first test. 20

2.2 Mapping between measurement and spherical coordinate angular values for the second and third tests. 20

2.3 Polarization mapping between measurement and spherical coordinates. 20

3.1 Description of the various runs. 47

4.1 RF Power level from the oscillator as a function of DC power supply voltage, for the oscillator working into a 50 Ω resitive load. The transmitter started from a cold state for the 16.51 V data point. . . . 148

4.2 The difference in received power level between -180° and $+180^o$ for the strongest polarization measured at these angles. 149

4.3 Summary of the measurement errors. 150

5.1 Summary of the pertinent numerical values obtained from the process of comparing the FDTD predicted and the 1998 measured data for the first test. 158

5.2 Summary of the pertinent numerical values obtained from the process of comparing the FDTD predicted data and the 1997 measured data against the 1998 measured data for the first test. 186

List of Figures

2.1 A partial view of the anechoic chamber showing the rear wall, the electromagnetic window, the positioner, the tower and a Device Under Test. 7

2.2 This photograph shows the base of the styrofoam tower cut out to position the reference horn near the centre of the azimuth table, and the absorbing material around the reference horn inside the cut out portion as well as around the base of the styrofoam tower. 8

2.3 The 91 *cm* thick absorbing cones hung from the monorail. This photograph is laid on its side. 9

2.4 The crane and its control cables padded with 23 *cm* thick absorbing cones, and the rope used for positioning the crane along the monorail. 10

2.5 The walk-on cubes piled over 2 *m* high for hiding the access door. The wall to the right of the door consists of two large hinged doors through which large equipment can be brought into the chamber with a crane riding a telescopic monorail affixed to the ceiling. These doors are covered with 23 *cm* thick absorbing cones. 11

2.6 The heavy metallic rail padded with absorbing cones of various thicknesses. This photograph is laid on its side. The large absorbing cones are shown here to lie flatly on the floor beside the rail but they were subsequently made to lean against the side of the rail. The photograph shows also the lower end of the control cable for the crane, exposed between the large cones laid on top of the rail. 12

2.7 The receive horn mounted in the large pyramidal extension in one wall of the chamber and the remotely controlled camera mounted in a corner of the chamber. This photograph is laid on its side. The receive horn was re-positioned to lie in the aperture of the pyramidal extension after this photograph was taken. 13

2.8 The schematic diagram of the equipment setup. 16

2.9 A photograph of the equipment setup. The photograph shows the receive horn positioned deep inside the pyramidal extension (i.e. near the truncated end of the extension in this photograph) but the receive horn was re-positioned to lie in the aperture of the pyramidal extension after this photograph was taken. 17

2.10 The spherical coordinate system used for the first test. 21

2.11 Schematic representation of the spherical coordinate system used for the second and third tests. The phantom head would have approximately the X axis through the nose, the Y axis through the left ear canal and the Z axis through the top of the head. The $X'Y'Z'$ coordinate system has its origin at the bottom front left corner of the styrofoam jig. 22

2.12 The vertical orientation for the first test. 23

2.13 The flat orientation for the first test. This photograph is laid on its side. 24

2.14 The edge orientation for the first test. This photograph is laid on its side. 25

2.15 The Head-up-Nose-forward orientation without the phantom head. . . 26

2.16 The Left-ear-up-Nose-forward orientation without the phantom head. 27

2.17 The Left-ear-forward-Nose-down orientation without the phantom head. 28

2.18 The Head-up-Nose-forward orientation with the phantom head. . . . 29

2.19 The Left-ear-up-Nose-forward orientation with the phantom head. . . 30

2.20 The Left-ear-forward-Nose-down orientation with the phantom head. 31

2.21 A left view of the phantom head in the dismantled styrofoam jig. . . 37

2.22 The right profile of the phantom head in the dismantled styrofoam jig. 38

2.23 A top view of the phantom head in the dismantled styrofoam jig. . . 39

2.24 A front view of the mounting of the transmitter near the phantom head in the dismantled styrofoam jig. 40

2.25 A left view of the mounting of the transmitter near the phantom head in the dismantled styrofoam jig. 41

2.26 A top view of the mounting of the transmitter near the phantom head in the dismantled styrofoam jig. 42

2.27 A diagonal view of the mounting of the transmitter near the phantom head in the dismantled styrofoam jig. 43

2.28 A rear view of the mounting of the transmitter near the phantom head in the dismantled styrofoam jig. 44

2.29 A view of the mounting of the transmitter in the dismantled styrofoam jig. 45

3.1 The horizontal polarization for the Vertical ($\theta = 90^o$) orientation in the first test. 52

3.2 The vertical polarization for the Vertical ($\theta = 90^o$) orientation in the first test. 53

3.3 The horizontal polarization for the Flat ($\phi = 0^o$) orientation in the first test. 54

3.4 The vertical polarization for the Flat ($\phi = 0^o$) orientation in the first test. 55

3.5 The horizontal polarization for the Edge ($\phi = 90^o$) orientation in the first test. 56

3.6 The vertical polarization for the Edge ($\phi = 90^o$) orientation in the first test. 57

3.7 The horizontal polarization for the Head-up-Nose-forward orientation in the second and third tests. 58

3.8 The vertical polarization for the Head-up-Nose-forward orientation in the second and third tests. 59

3.9 The horizontal polarization for the Left-ear-up-Nose-forward orientation in the second and third tests. 60

3.10 The vertical polarization for the Left-ear-up-Nose-forward orientation in the second and third tests. 61

3.11 The horizontal polarization for the Left-ear-forward-Nose-down orientation in the second and third tests. 62

3.12 The vertical polarization for the Left-ear-forward-Nose-down orientation in the second and third tests. 63

3.13 The measured power transfer function for the network analyzer. . . . 64

3.14 The horizontal polarization for the Vertical ($\theta = 90°$) orientation in the first test displayed with respect to the appropriate spherical coordinate rather than the measurement angle. Power correction with respect to both the battery discharge and the power transfer function of the network analyzer was applied for the curve in dBm unit. 65

3.15 The vertical polarization for the Vertical ($\theta = 90°$) orientation in the first test displayed with respect to the appropriate spherical coordinate rather than the measurement angle. Power correction with respect to both the battery discharge and the power transfer function of the network analyzer was applied for the curve in dBm unit. 66

3.16 The horizontal polarization for the Flat ($\phi = 0°$) orientation in the first test displayed with respect to the appropriate spherical coordinate rather than the measurement angle. Power correction with respect to both the battery discharge and the power transfer function of the network analyzer was applied for the curve in dBm unit. 67

3.17 The vertical polarization for the Flat ($\phi = 0°$) orientation in the first test displayed with respect to the appropriate spherical coordinate rather than the measurement angle. Power correction with respect to both the battery discharge and the power transfer function of the network analyzer was applied for the curve in dBm unit. 68

3.18 The horizontal polarization for the Edge ($\phi = 90°$) orientation in the first test displayed with respect to the appropriate spherical coordinate rather than the measurement angle. Power correction with respect to both the battery discharge and the power transfer function of the network analyzer was applied for the curve in dBm unit. 69

3.19 The vertical polarization for the Edge ($\phi = 90°$) orientation in the first test displayed with respect to the appropriate spherical coordinate rather than the measurement angle. Power correction with respect to both the battery discharge and the power transfer function of the network analyzer was applied for the curve in dBm unit. 70

3.20 The horizontal polarization for the Head-up-Nose-forward orientation in the second test displayed with respect to the appropriate spherical coordinate rather than the measurement angle. Power correction with respect to both the battery discharge and the power transfer function of the network analyzer was applied for the curve in dBm unit. . . . 71

3.21 The vertical polarization for the Head-up-Nose-forward orientation in the second test displayed with respect to the appropriate spherical coordinate rather than the measurement angle. Power correction with respect to both the battery discharge and the power transfer function of the network analyzer was applied for the curve in dBm unit. . . . 72

3.22 The horizontal polarization for the Left-ear-up-Nose-forward orientation in the second test displayed with respect to the appropriate spherical coordinate rather than the measurement angle. Power correction with respect to both the battery discharge and the power transfer function of the network analyzer was applied for the curve in dBm unit. . 73

3.23 The vertical polarization for the Left-ear-up-Nose-forward orientation in the second test displayed with respect to the appropriate spherical coordinate rather than the measurement angle. Power correction with respect to both the battery discharge and the power transfer function of the network analyzer was applied for the curve in dBm unit. . . . 74

3.24 The horizontal polarization for the Left-ear-forward-Nose-down orientation in the second test displayed with respect to the appropriate spherical coordinate rather than the measurement angle. Power correction with respect to both the battery discharge and the power transfer function of the network analyzer was applied for the curve in dBm unit. 75

3.25 The vertical polarization for the Left-ear-forward-Nose-down orientation in the second test displayed with respect to the appropriate spherical coordinate rather than the measurement angle. Power correction with respect to both the battery discharge and the power transfer function of the network analyzer was applied for the curve in dBm unit. . 76

3.26 The horizontal polarization for the Head-up-Nose-forward orientation in the third test displayed with respect to the appropriate spherical coordinate rather than the measurement angle. Power correction with respect to both the battery discharge and the power transfer function of the network analyzer was applied for the curve in dBm unit. . . . 77

3.27 The vertical polarization for the Head-up-Nose-forward orientation in the third test displayed with respect to the appropriate spherical coordinate rather than the measurement angle. Power correction with respect to both the battery discharge and the power transfer function of the network analyzer was applied for the curve in dBm unit. . . . 78

3.28 The horizontal polarization for the Left-ear-up-Nose-forward orientation in the third test displayed with respect to the appropriate spherical coordinate rather than the measurement angle. Power correction with respect to both the battery discharge and the power transfer function of the network analyzer was applied for the curve in dBm unit. . . . 79

3.29 The vertical polarization for the Left-ear-up-Nose-forward orientation in the third test displayed with respect to the appropriate spherical coordinate rather than the measurement angle. Power correction with respect to both the battery discharge and the power transfer function of the network analyzer was applied for the curve in dBm unit. . . . 80

3.30 The horizontal polarization for the Left-ear-forward-Nose-down orientation in the third test displayed with respect to the appropriate spherical coordinate rather than the measurement angle. Power correction with respect to both the battery discharge and the power transfer function of the network analyzer was applied for the curve in dBm unit. . 81

3.31 The vertical polarization for the Left-ear-forward-Nose-down orientation in the third test displayed with respect to the appropriate spherical coordinate rather than the measurement angle. Power correction with respect to both the battery discharge and the power transfer function of the network analyzer was applied for the curve in dBm unit. . . . 82

3.32 The horizontal and vertical polarizations for the Vertical orientation in the first test displayed in polar format with respect to the appropriate spherical coordinate and with power correction. The 0° and 90° directions correspond to the $\hat{x}$ and $\hat{y}$ directions, respectively. Horizontal polarization lies in the plane of the page. Vertical polarization is normal to the page. 83

3.33 The horizontal and vertical polarizations for the Flat orientation in the first test displayed in polar format with respect to the appropriate spherical coordinate and with power correction. The 0° and 90° directions correspond to the $\hat{z}$ and $\hat{x}$ directions, respectively. Horizontal polarization lies in the plane of the page. Vertical polarization is normal to the page. 84

3.34 The horizontal and vertical polarizations for the Edge orientation in the first test displayed in polar format with respect to the appropriate spherical coordinate and with power correction. The 0° and 90° directions correspond to the $\hat{z}$ and $\hat{y}$ directions, respectively. Horizontal polarization lies in the plane of the page. Vertical polarization is normal to the page. 85

3.35 The horizontal polarization for the Head-up-Nose-forward orientation in the second (without head) and the third (with head) tests displayed in polar format with respect to the appropriate spherical coordinate and with power correction. The 0° and 90° directions correspond to the nose and left ear directions, respectively. Horizontal polarization lies in the plane of the page. 86

3.36 The vertical polarization for the Head-up-Nose-forward orientation in the second (without head) and the third (with head) tests displayed in polar format with respect to the appropriate spherical coordinate and with power correction. The 0° and 90° directions correspond to the nose and left ear directions, respectively. Vertical polarization is normal to the page. 87

3.37 The horizontal polarization for the Left-ear-up-Nose-forward orientation in the second (without head) and the third (with head) tests displayed in polar format with respect to the appropriate spherical coordinate and with power correction. The 0° and 90° directions correspond to the top of the head and nose directions, respectively. Horizontal polarization lies in the plane of the page. 88

3.38 The vertical polarization for the Left-ear-up-Nose-forward orientation in the second (without head) and the third (with head) tests displayed in polar format with respect to the appropriate spherical coordinate and with power correction. The 0° and 90° directions correspond to the top of the head and nose directions, respectively. Vertical polarization is normal to the page. 89

3.39 The horizontal polarization for the Left-ear-forward-Nose-down orientation in the second (without head) and the third (with head) tests displayed in polar format with respect to the appropriate spherical coordinate and with power correction. The 0° and 90° directions correspond to the top of the head and left ear directions, respectively. Horizontal polarization lies in the plane of the page. 90

3.40 The vertical polarization for the Left-ear-forward-Nose-forward orientation in the second (without head) and the third (with head) tests displayed in polar format with respect to the appropriate spherical coordinate and with power correction. The 0° and 90° directions correspond to the top of the head and left ear directions, respectively. Vertical polarization is normal to the page. 91

3.41 The contour for the 1 V/m and 3 V/m levels of total electric field for the vertical orientation displayed in polar format with respect to the appropriate spherical coordinate and with power correction. The 0° and 90° directions correspond to the $\hat{x}$ and $\hat{y}$ directions, respectively. The units for distance are m. 92

3.42 The contour for the 1 V/m and 3 V/m levels of total electric field for the flat orientation displayed in polar format with respect to the appropriate spherical coordinate and with power correction. The 0° and 90° directions correspond to the $\hat{z}$ and $\hat{x}$ directions, respectively. The units for distance are m. 93

3.43 The contour for the 1 V/m and 3 V/m levels of total electric field for the edge orientation displayed in polar format with respect to the appropriate spherical coordinate and with power correction. The 0° and 90° directions correspond to the $\hat{z}$ and $\hat{y}$ directions, respectively. The units for distance are m. 94

3.44 The contour for the 1 V/m level of total electric field for the Head-up-Nose-forward orientation with and without phantom head displayed in polar format with respect to the appropriate spherical coordinate and with power correction. The 0° and 90° directions correspond to the nose and left ear directions, respectively. The units for distance are m. 95

3.45 The contour for the 3 V/m level of total electric field for the Head-up-Nose-forward orientation with and without phantom head displayed in polar format with respect to the appropriate spherical coordinate and with power correction. The 0° and 90° directions correspond to the nose and left ear directions, respectively. The units for distance are m. 96

3.46 The contour for the 1 V/m level of total electric field for the Left-ear-up-Nose-forward orientation with and without phantom head displayed in polar format with respect to the appropriate spherical coordinate and with power correction. The 0° and 90° directions correspond to the top of the head and nose directions, respectively. The units for distance are m. 97

3.47 The contour for the 3 V/m level of total electric field for the Left-ear-up-Nose-forward orientation with and without phantom head displayed in polar format with respect to the appropriate spherical coordinate and with power correction. The 0° and 90° directions correspond to the top of the head and nose directions, respectively. The units for distance are m. 98

3.48 The contour for the 1 V/m level of total electric field for the Left-ear-forward-Nose-down orientation with and without phantom head displayed in polar format with respect to the appropriate spherical coordinate and with power correction. The 0° and 90° directions correspond to the top of the head and left ear directions, respectively. The units for distance are m. 99

3.49 The contour for the 3 V/m level of total electric field for the Left-ear-forward-Nose-down orientation with and without phantom head displayed in polar format with respect to the appropriate spherical coordinate and with power correction. The 0° and 90° directions correspond to the top of the head and left ear directions, respectively. The units for distance are m. 100

4.1 Difference between a start-and-stop scan and a continuous scan. The dashed curve shows the power received in the horizontal polarization for the start-and-stop scan whereas the solid curve shows the difference in the power received in the horizontal polarization between the continuous and the start-and-stop scans for exactly the same mechanical setup. 105

4.2 The dashed curve shows the power received in the horizontal polarization for the start-and-stop scan whereas the solid curve shows the corresponding slope of the data curve. 106

4.3 Difference between a start-and-stop scan and a continuous scan. The dashed curve shows the power received in the vertical polarization for the start-and-stop scan whereas the solid curve shows the difference in the power received in the vertical polarization between the continuous and the start-and-stop scans for exactly the same mechanical setup. . 107

4.4 The dashed curve shows the power received in the vertical polarization for the start-and-stop scan whereas the solid curve shows the corresponding slope of the data curve. 108

4.5 The plot corresponds to the spread distribution of the difference curve of Figure 4.3 with respect to the slope values of Figure 4.4. The solid curve corresponds to the linear regression of the distribution. Beware that since each "x" mark can possibly correspond to more than one data point, the solid curve does not necessarily appear visually satisfactory for the result of a linear regression. 109

4.6 The dashed curve shows the slope corresponding to the data for the horizontal polarization. The solid curve shows the electrical noise level (absolute value) obtained after subtracting the data smearing effect from the difference curve for the horizontal polarization. 110

4.7 The plot shows the spread distribution of the noise amplitude of Figure 4.6 with respect to signal strength for the horizontal polarization. 111

4.8 The dashed curve shows the slope corresponding to the data for the vertical polarization. The solid curve shows the electrical noise level (absolute value) obtained after subtracting the data smearing effect from the difference curve for the vertical polarization. 112

4.9 The plot shows the spread distribution of the noise amplitude of Figure 4.8 with respect to signal strength for the vertical polarization. . 113

4.10 Repeatability test to assess the data variation due to electrical noise. The three plots correspond to the difference curves for the co-polarization with the transmitter in the three orientations of the first test. 118

4.11 Repeatability test to assess the data variation due to electrical noise. The three plots correspond to the difference curves for the cross-polarization with the transmitter in the three orientations of the first test. A different scale shown on the right of the plot was used for the flat orientation (#277-#278). 119

4.12 The top plot shows the results from two different linear regressions on the difference curve for the horizontal polarization with the transmitter in the edge orientation of the first test. The initial result with slope $m = 4.9460E - 5$ is seen to be less than fully satisfactory whereas the result with slope $m = 1.1435E - 4$ obtained from the linear regression for the vertical polarization shown in the bottom plot is seen to be more satisfactory. 120

4.13 The plot shows the spread distribution of the noise amplitude with respect to signal strength for the vertical orientation of the transmitter in the first test. 121

4.14 The plot shows the spread distribution of the noise amplitude with respect to signal strength for the edge orientation of the transmitter in the first test. 122

4.15 The plot shows the spread distribution of the noise amplitude with respect to signal strength for the flat orientation of the transmitter in the first test. 123

4.16 The plot shows the spread distribution of the noise amplitude with respect to signal strength for the horizontal polarization for the three orientations of the transmitter in the first test. 124

4.17 Repeatability test to assess the data variation due to electrical noise. The plot corresponds to the difference curve for the horizontal polarization with the Head-up-Nose-forward orientation of the second test. 125

4.18 Repeatability test to assess the data variation due to electrical noise for the horizontal polarization with the Head-up-Nose-forward orientation of the second test. The plot shows the result of applying drift correction for taking out the data variation caused by the draining of the battery. 126

4.19 The plot shows the spread distribution of the noise amplitude with respect to signal strength for the horizontal polarization of the Head-up-Nose-forward orientation in the second test. 127

4.20 Variation of the vertical polarization data due to the combination of electrical noise, changing the battery pack, re-positioning the transmitter 3 *mm* rearward and re-levelling the transmitter in the edge orientation of the first test. 129

4.21 The plot shows the spread distribution of the drift-corrected data corresponding to Figure 4.20 with respect to signal strength. 130

4.22 Variation of the horizontal polarization data due to the combination of electrical noise, changing the battery pack, re-positioning the transmitter 3 *mm* rearward and re-levelling the transmitter for the edge orientation of the first test. 131

4.23 Drift correction of Figure 4.22 to eliminate the variation caused by the drainage of the battery pack. 132

4.24 The plot shows the spread distribution of the data in Figure 4.23 with respect to signal strength. 133

4.25 Difference between two slightly shifted versions of the same radiation pattern measured with the transmitter in the edge orientation of the first test. 134

4.26 Variation of the vertical polarization data due to the combination of electrical noise, variation in the battery DC power level and a slight re-levelling of the transmitter in the edge orientation of the first test. 136

4.27 The plot shows the spread distribution of the drift-corrected data corresponding to Figure 4.26 with respect to signal strength. 137

4.28 Variation of the horizontal polarization data due to the combination of electrical noise, variation in the battery DC power level and a slight re-levelling of the transmitter for the edge orientation of the first test. 138

4.29 The plot shows the spread distribution of the drift-corrected data corresponding to Figure 4.28 with respect to signal strength. 139

4.30 Variation of the vertical polarization data due to leaning the absorbers against the side of the heavy rail and to adding absorbing material around the lower end of the control cable that was exposed through the large absorbing cones laid on top of the rail. The transmitter was in the vertical orientation of the first test. 141

4.31 The plot shows the spread distribution of the drift-corrected data corresponding to Figure 4.30 with respect to signal strength. 142

4.32 Variation of the horizontal polarization data due to leaning the absorbers against the side of the heavy rail and to adding absorbing material around the lower end of the control cable that was exposed through the large absorbing cones laid on top of the rail. The transmitter was in the vertical orientation of the first test. 143

4.33 The plot shows the spread distribution of the drift-corrected data corresponding to Figure 4.32 with respect to signal strength. 144

4.34 Difference between two slightly shifted versions of the same radiation pattern measured with the transmitter in the vertical orientation of the first test. 145

5.1 Model of the transmitter used in conjunction with the XFDTD403 software to compute the predicted data. The model shown here has the monopole antenna being 40 cells long. 154

5.2 A detail of the model for the metallic cover of the transmitter showing the presence of the two small holes modelled as two square holes with 2 cells on a side. 155

5.3 Comparison between the magnitudes of the FDTD predicted and the 1998 measured data of horizontal polarization for the vertical orientation of the first test. 159

5.4 Comparison between the magnitudes of the FDTD predicted and the 1998 measured data of vertical polarization for the vertical orientation of the first test. 160

5.5 Comparison between the magnitudes of the FDTD predicted and the 1998 measured data of horizontal polarization for the flat orientation of the first test. 161

5.6 Comparison between the magnitudes of the FDTD predicted and the 1998 measured data of vertical polarization for the flat orientation of the first test. 162

5.7 Comparison between the magnitudes of the FDTD predicted and the 1998 measured data of horizontal polarization for the edge orientation of the first test. 163

5.8 Comparison between the magnitudes of the FDTD predicted and the 1998 measured data of vertical polarization for the edge orientation of the first test. 164

5.9 Comparison between the magnitudes of the FDTD predicted and the 1998 measured data of horizontal polarization for the Head-up-Nose-forward orientation of the second test. 165

5.10 Comparison between the magnitudes of the FDTD predicted and the 1998 measured data of vertical polarization for the Head-up-Nose-Forward orientation of the second test. 166

5.11 Comparison between the magnitudes of the FDTD predicted and the 1998 measured data of horizontal polarization for the Left-ear-up-Nose-forward orientation of the second test. 167

5.12 Comparison between the magnitudes of the FDTD predicted and the 1998 measured data of vertical polarization for the Left-ear-up-Nose-forward orientation of the second test. 168

5.13 Comparison between the magnitudes of the FDTD predicted and the 1998 measured data of horizontal polarization for the Left-ear-forward-Nose-down orientation of the second test. 169

5.14 Comparison between the magnitudes of the FDTD predicted and the 1998 measured data of vertical polarization for the Left-ear-forward-Nose-down orientation of the second test. 170

5.15 Comparison between the magnitudes of the FDTD predicted and the 1998 measured data of horizontal polarization for the case corresponding to *Vert2* when minimizing the difference between the predicted and the measured data of the vertical and the horizontal polarizations. . . 174

5.16 Comparison between the magnitudes of the FDTD predicted and the 1998 measured data of vertical polarization for the case corresponding to *Vert2* when minimizing the difference between the predicted and the measured data of the vertical and the horizontal polarizations. . . 175

5.17 Comparison between the magnitudes of the FDTD predicted data, the 1997 measured data and the 1998 measured data in the horizontal polarization for the vertical orientation of the first test. 179

5.18 Comparison between the magnitudes of the FDTD predicted data, the 1997 measured data and the 1998 measured data in the vertical polarization for the vertical orientation of the first test. 180

5.19 Comparison between the magnitudes of the FDTD predicted data, the 1997 measured data and the 1998 measured data in the horizontal polarization for the flat orientation of the first test. 181

5.20 Comparison between the magnitudes of the FDTD predicted data, the 1997 measured data and the 1998 measured data in the vertical polarization for the flat orientation of the first test. 182

5.21 Comparison between the magnitudes of the FDTD predicted data, the 1997 measured data and the 1998 measured data in the horizontal polarization for the edge orientation of the first test. 183

5.22 Comparison between the magnitudes of the FDTD predicted data, the 1997 measured data and the 1998 measured data in the vertical polarization for the edge orientation of the first test. 184

B.1 Coordinate transformation between the spherical coordinates for the phantom head (XYZ) as per Figure 2.11 and those for the transmitter (UVW) in the second test. 222

D.1 The schematic diagram of the equipment setup for measuring the gain of the receive horn. 273

Chapter 1

Introduction

This document presents the procedure for, and the results from, measuring in a shielded anechoic chamber the electromagnetic far-fields produced by a battery-operated portable transmitter at 850 MHz in the vicinity of a phantom head over the three principal planes of the phantom head. The measurements took place during the summer of 1998 (July 21-27) and represent the continuation of the 1997 summer's measurements reported in the document CRC-RP-98-002 (Reference [1]), which dealt with the electromagnetic far-fields produced by the same portable transmitter in the vicinity of a box head or a sphere head over the three principal planes of the transmitter. The phantom head used herein was constituted of material simulating five tissues: skin, bone, muscle, eye and brain.

Three different tests were conducted:

1. the transmitter by itself;
2. the transmitter alone in the styrofoam jig so designed as to be capable of holding a phantom head;
3. the transmitter positioned near a phantom head in the styrofoam jig mentioned just above.

The order of the presentation in this document is as follows. Chapter Two presents in detail the test setup with respect to the shielded anechoic chamber, the electronic

equipment, the various mechanical alignments and the configuration of the device under test for each experiment. Chapter Three presents plots of the measured data in various forms: raw data without any correction, data corrected for the power droop incurred by the battery discharge, data presented in both rectangular and polar formats, with respect to the spherical coordinate of the phantom head rather than the angular position of the azimuth table, and contour levels of the far-fields in polar format. A measurement error budget is also developed based in part on the noise analysis made from the results of a few repeated measurements that were carried out for the purpose of assessing data repeatability and data smearing. Chapter Four presents the comparison between the 1998 measured results, the 1997 measured results, and predicted results computed for the transmitter in free space, by the FDTD method using Remcom's XFDTD software (version 4.03).

Chapter 2

Test Setup

This section presents the details about the anechoic chamber setup, the equipment setup, the mechanical setup and the experiment setup. The anechoic chamber setup deals with the permanent features of the chamber. The equipment setup deals with the configuration of the various pieces of electronic equipment used during the test. The mechanical setup deals with the identification of the coordinate system and of various orientations of the transmitter, and with the mounting and the alignment of the tower, the receive horn and the Device Under Test (D.U.T.). The experiment setup deals with some specifics like the battery pack, the data averaging, the table scanning speed, the brain fluid. The terminology "test setup" is used herein to refer to the ensemble of all these individual setups.

2.1 Anechoic chamber setup

The measurements took place in the $6.1m \times 6.7m \times 6.1m$ David Florida Laboratory (DFL) anechoic chamber. This chamber is a shielded room that has its four walls and the ceiling covered permanently with absorbing cones (45 cm thick on the wall facing the receive horn, 23 cm thick on the ceiling and on the three other walls). One side wall has a 5.5 m × 5.5 m electromagnetic window made of 30 cm thick white styrofoam panels dove-tailed together without the use of adhesives. A metallic rolling door can be lowered to protect the styrofoam window against high wind loads from

the outside. This sliding door was fully raised for all tests mentioned herein, thus leaving the chamber opened, in effect, to free space through the styrofoam window. The other side wall which faces the electromagnetic window encompasses two large hinged doors through which large equipment can be brought into the chamber with a crane riding a telescopic monorail affixed to the ceiling. These doors are covered with 23 cm thick absorbing cones. There is also a regular access door in the corner of the anechoic chamber as shown in Figure 2.5.

Unfortunately, the performance of this chamber has not been systematically characterized for the frequency (850 MHz) and the configuration of interest, and thus, the size, location and quality of the quiet zone is not known. Since the efficiency of the absorbing material is not large at 850 MHz, some reflections should be expected from the metallic walls of the shielded room even though they were covered with absorbing material. The information found in Reference [2, p. 28] states that the quiet zone of the chamber is located at the centre of the chamber and has a maximum amplitude taper of 0.5 dB over an aperture with a maximum linear dimension of 79 cm at 1.5 GHz, when using the full length of the pyramidal extension of the one wall. However, only part of the pyramidal extension was used herein (see Figure 2.9) and the frequency of operation was much lower than 1.5 GHz.

At the centre of the chamber was an azimuth-over-elevation-over-azimuth positioner, Scientific Atlanta model 5524-7, (see Figure 2.1). Note, however, that the lowermost azimuth axis remained fixed for all tests mentioned herein. The positioner was also set on two lift jacks to level the upper azimuth table in the direction perpendicular to the motion of the elevation plane in order to correct for the wear on the large bearing at the base of the positioner. The floor was covered with a combination of various sizes of removable absorbing cones (122 cm thick and 91 cm thick in front of the positioner, 61 cm thick around the positioner, and 23 cm thick everywhere else).

A styrofoam tower of about 61 cm on a side was centred and anchored to the top surface of the upper azimuth table. A $0.95 - 1.15$ GHz waveguide transition acting as a reference signal pick-up horn was located directly on the upper azimuth table so that the reference horn would rotate in the azimuth plane along with the

transmitter. The reference horn was thus located about 2 m vertically down from the transmitter and pointing vertically toward the ceiling. A 30 cm wide, 46 cm high swath was cut out along the entire length of the base of the styrofoam tower in order to accomodate the presence of the waveguide transition near the centre of the azimuth table. The reference horn within the cut out portion of the styrofoam tower as well as the styrofoam tower itself were surrounded with absorbing material in order to couple mostly only the direct wave from the transmitter to the reference horn (see Figure 2.2).

In order to minimize possible scatterers in the chamber, the following steps were taken:

- one obsolete camera bracket was removed from the wall facing the receive horn;
- one obsolete heavy support bracket adjacent to the remaining camera was removed;
- the camera support was padded with 23 cm thick absorbing cones (see Figure 2.7);
- four pieces of 91 cm thick absorbing cones were hung from the metallic monorail on which rides the overhead crane near the ceiling (see Figure 2.3). These pieces were used to minimize the amplitude variations incurred in the reference signal when the azimuth table was rotated since the metallic monorail then appeared, in effect, to be swept across the radiation beam of the reference horn as the azimuth table was rotated;
- the crane was retracted as far to the side as possible and was partly padded with 23 cm thick absorbing cones (see Figure 2.4);
- the control cable and the power cable for the crane were sandwiched between two 23 cm thick absorbing cones with the cones pointing toward the vertical axis of the azimuth table (see Figure 2.4);
- walking-on absorbing cubes (see Figure 2.5) were piled over 2 m high to hide the door which was lined with flat rather than conical absorbing material;

- a heavy (though removable) rail lying on the floor along the side wall opposite to the styrofoam window was heavily padded with a variety of absorbing cones (see Figure 2.6);
- a lamp affixed to the rear wall in a corner of the chamber was removed and the associated electrical socket was covered with absorbing material;
- the gates controlling the passage of the vehicules nearby the chamber were lowered for all tests herein so that no vehicule would be parked or passing by the electromagnetic window.

Another horn, the receive horn, was positioned in the aperture of a large 1.83 $m \times$ 1.83 m pyramidal extension protruding from one wall of the chamber (see Figure 2.7). The walls of this pyramidal extension were lined with flat sheets of absorbing material (Emerson and Cuming AN-75) and the remaining area of the aperture was loaded with pieces of absorbing material so as to leave free only the aperture of the receive horn. The pieces of absorbing material, however, were positioned around the receive horn in recess with respect to the aperture of the receive horn in order to avoid disturbing the performance of the receive horn.

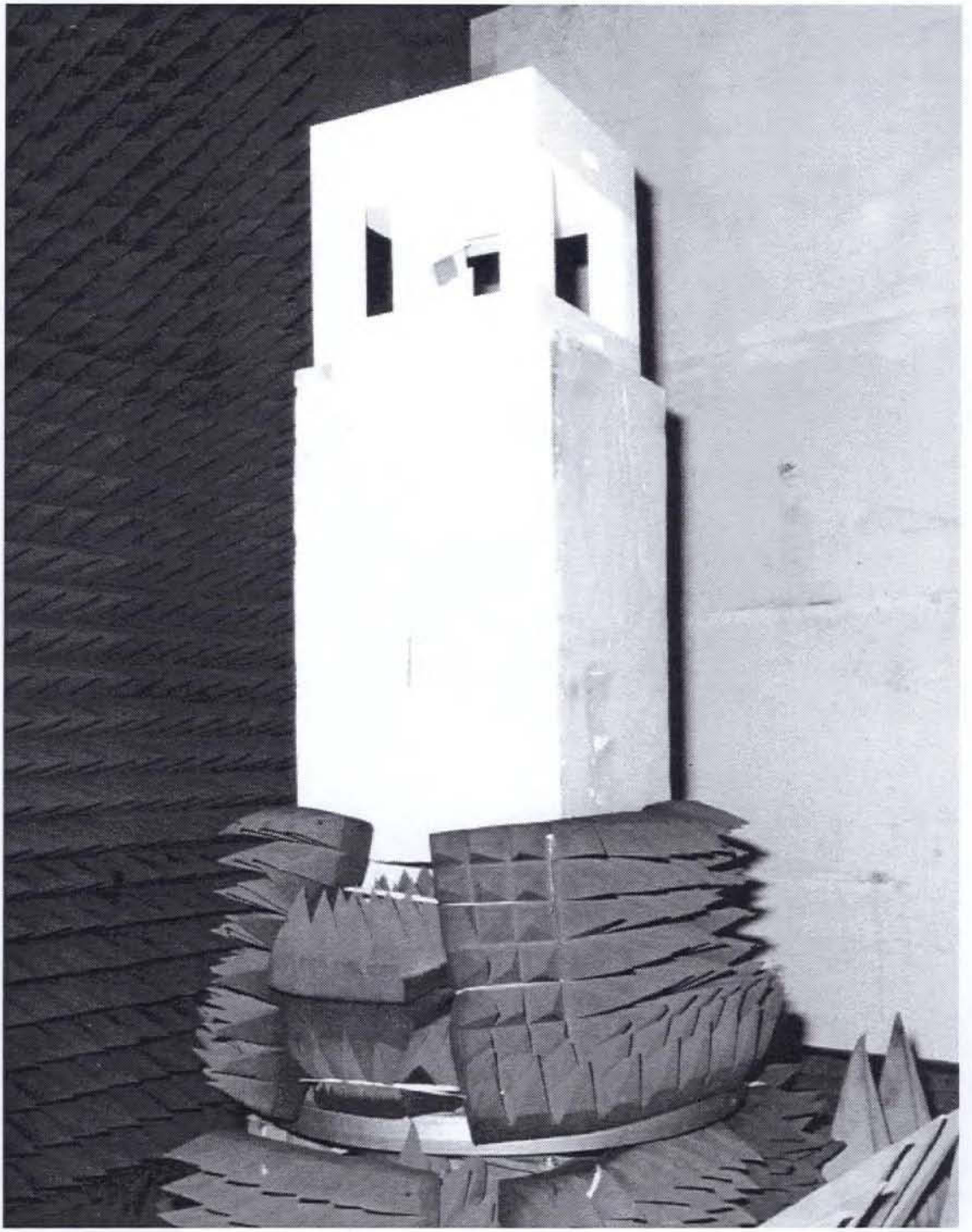

Figure 2.1: A partial view of the anechoic chamber showing the rear wall, the electromagnetic window, the positioner, the tower and a Device Under Test.

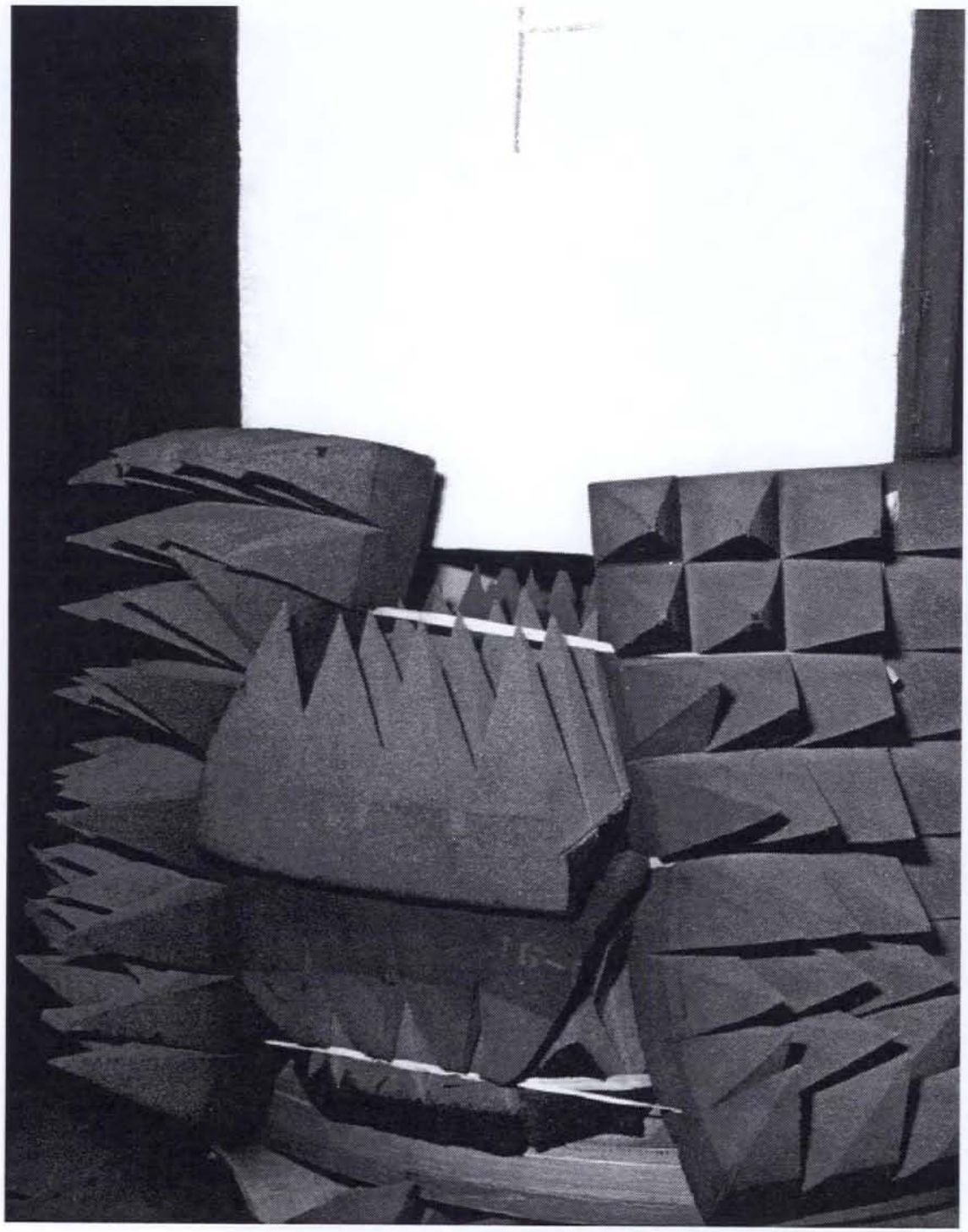

Figure 2.2: This photograph shows the base of the styrofoam tower cut out to position the reference horn near the centre of the azimuth table, and the absorbing material around the reference horn inside the cut out portion as well as around the base of the styrofoam tower.

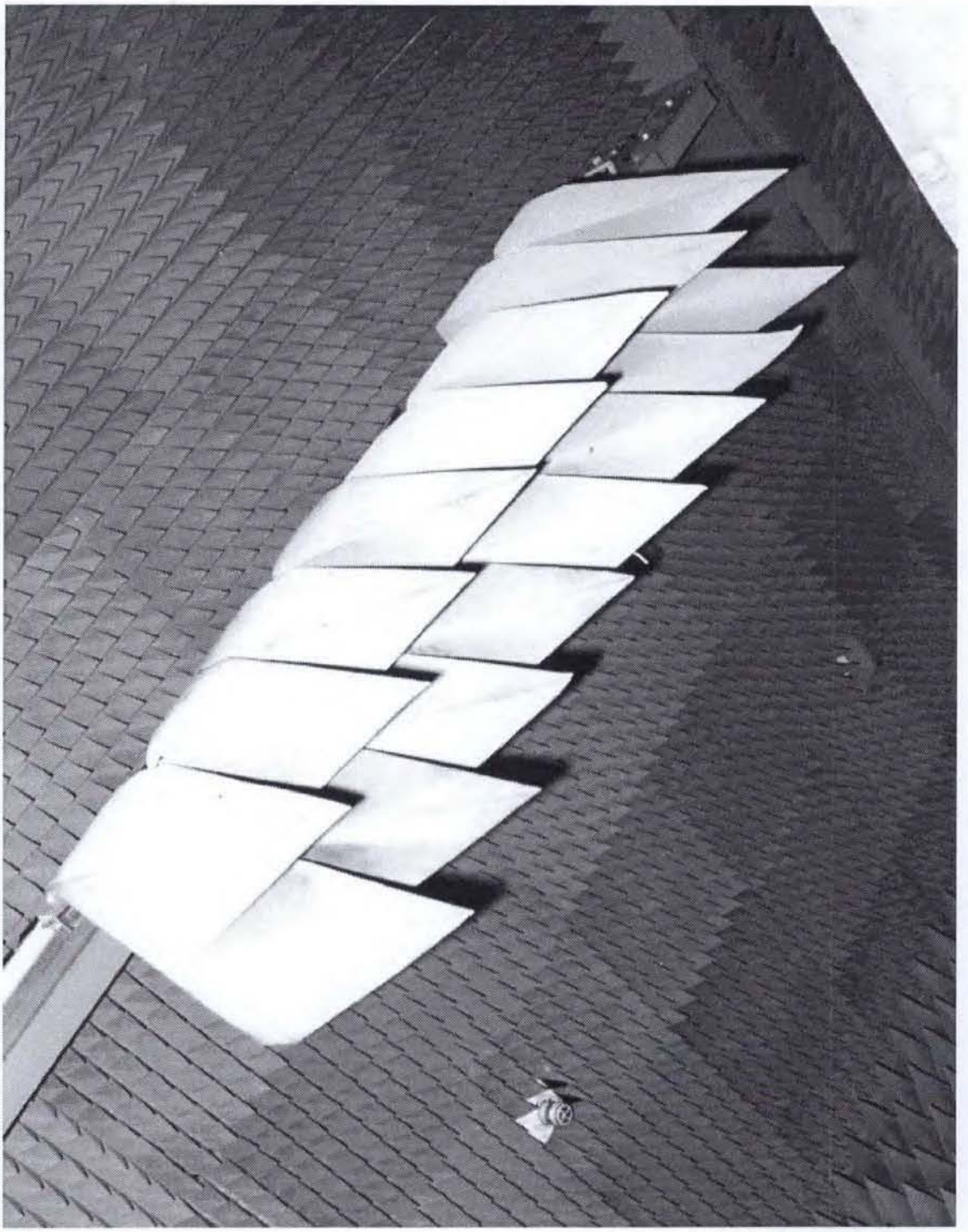

Figure 2.3: The 91 *cm* thick absorbing cones hung from the monorail. This photograph is laid on its side.

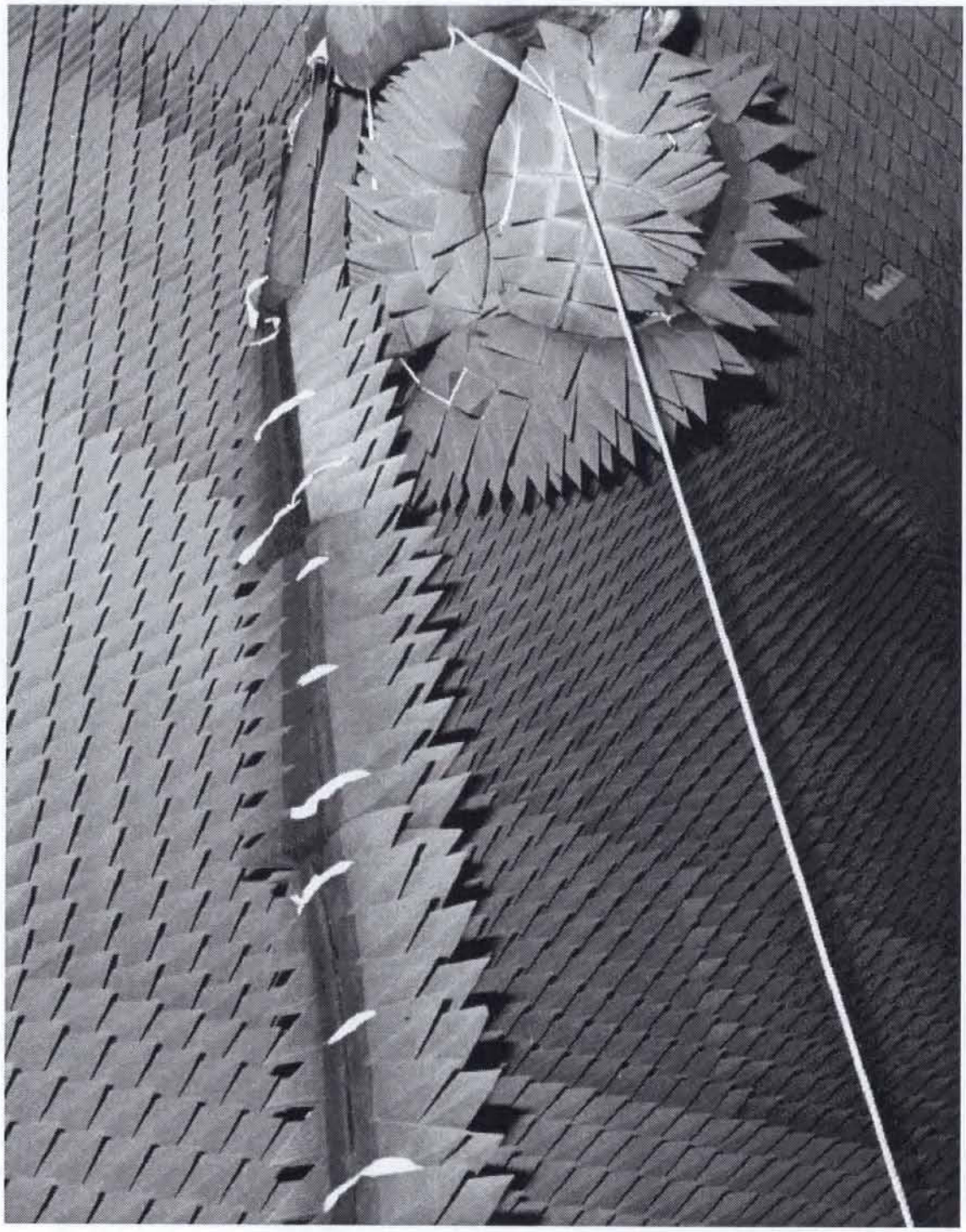

Figure 2.4: The crane and its control cables padded with 23 *cm* thick absorbing cones, and the rope used for positioning the crane along the monorail.

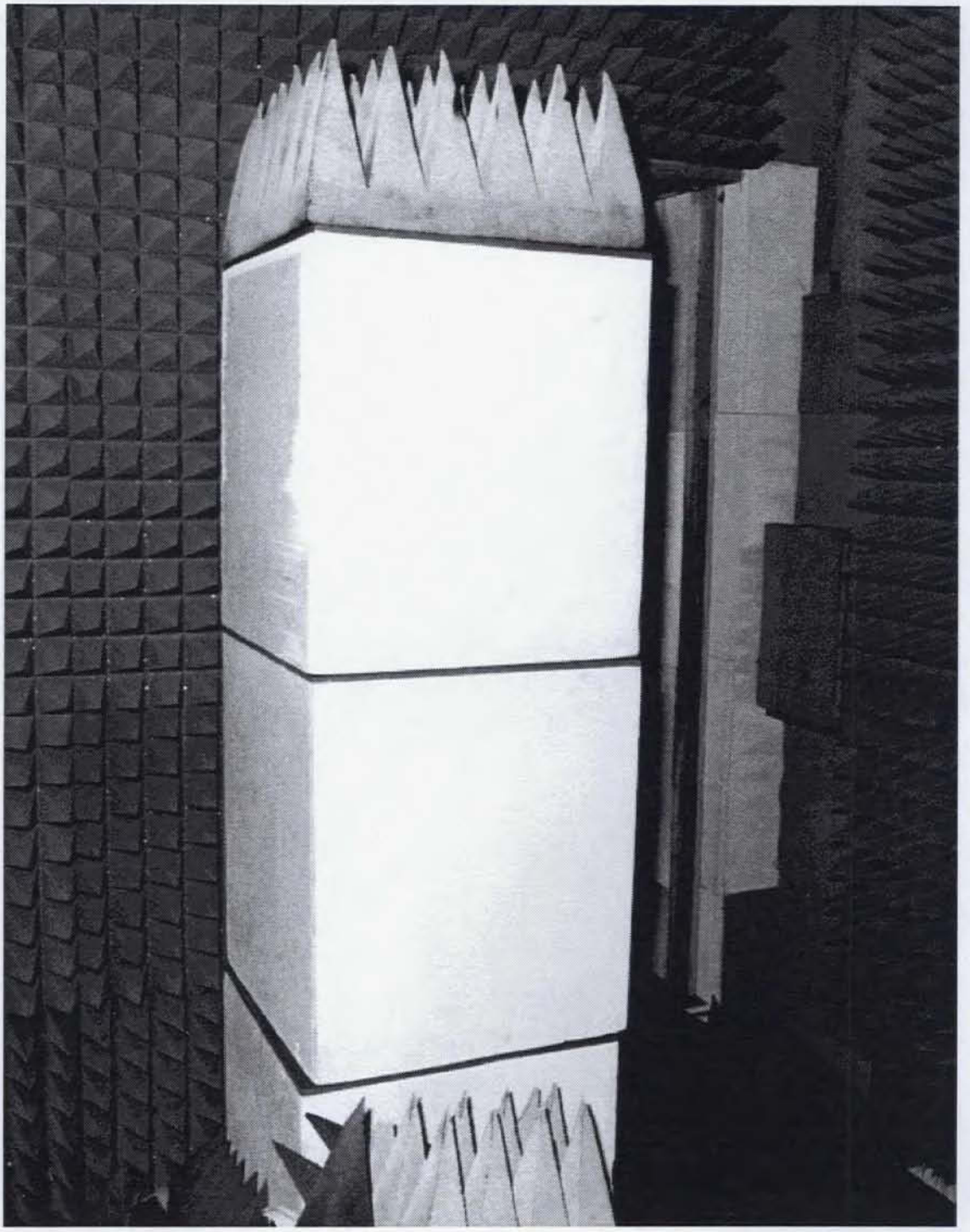

Figure 2.5: The walk-on cubes piled over 2 m high for hiding the access door. The wall to the right of the door consists of two large hinged doors through which large equipment can be brought into the chamber with a crane riding a telescopic monorail affixed to the ceiling. These doors are covered with 23 cm thick absorbing cones.

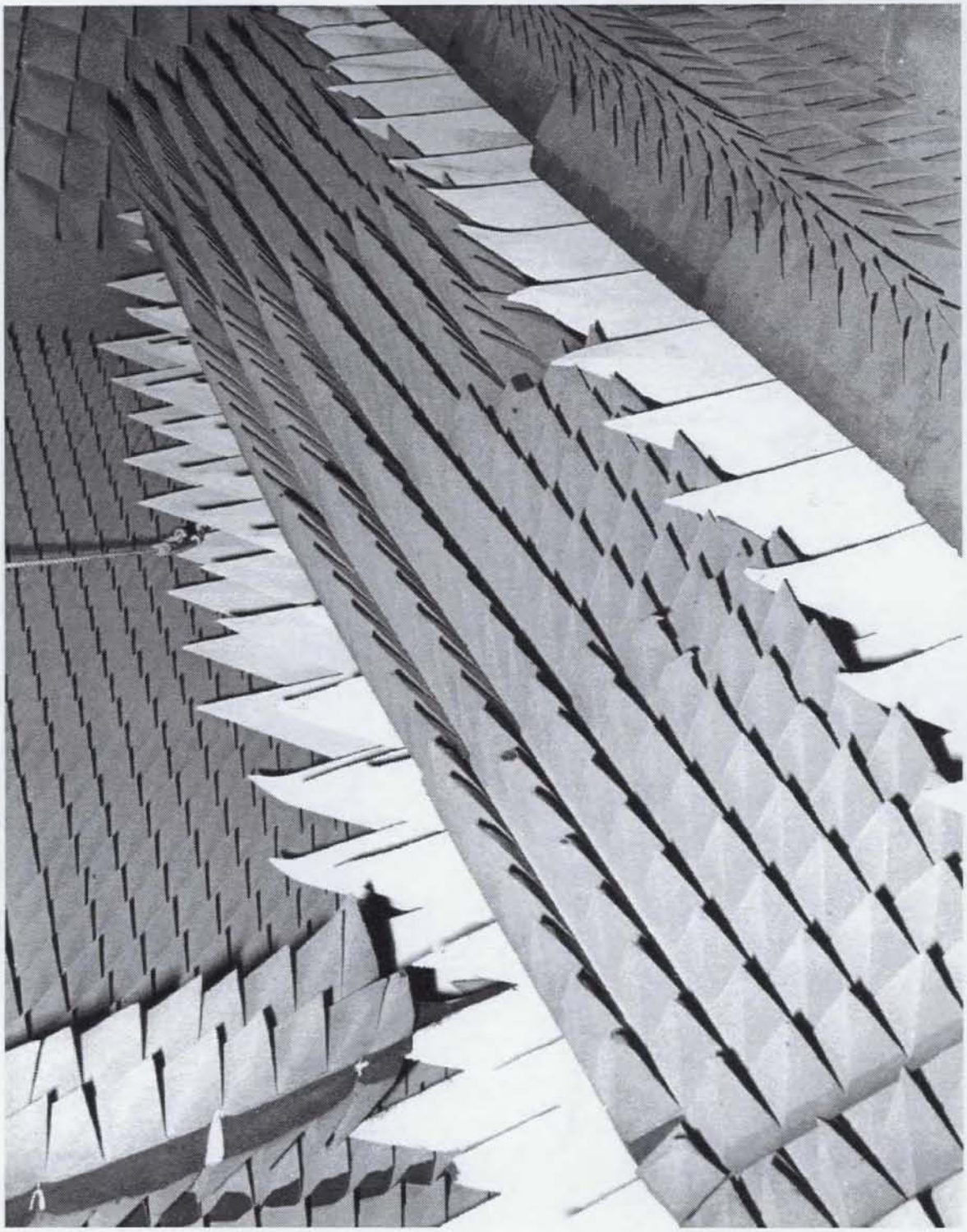

Figure 2.6: The heavy metallic rail padded with absorbing cones of various thicknesses. This photograph is laid on its side. The large absorbing cones are shown here to lie flatly on the floor beside the rail but they were subsequently made to lean against the side of the rail. The photograph shows also the lower end of the control cable for the crane, exposed between the large cones laid on top of the rail.

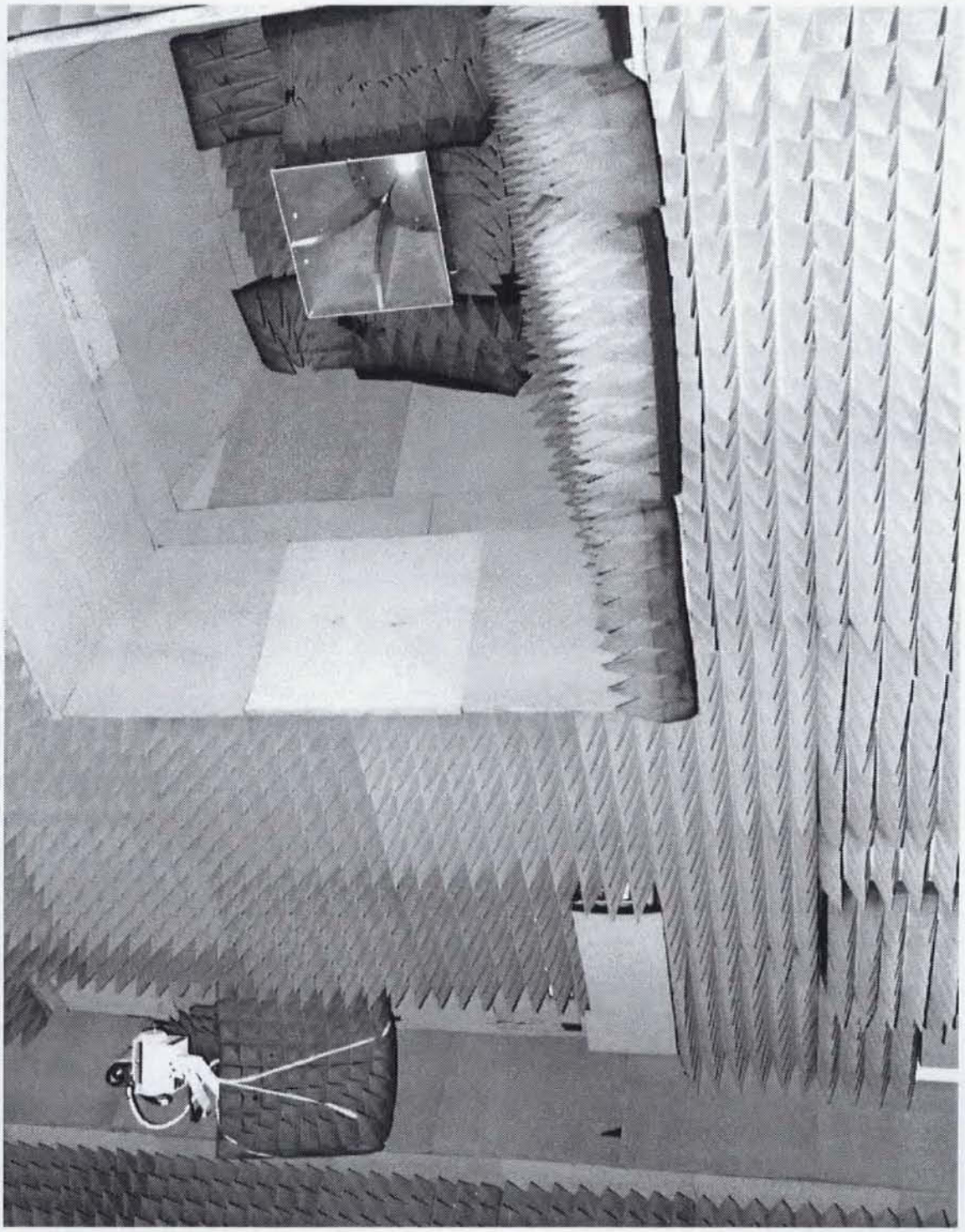

Figure 2.7: The receive horn mounted in the large pyramidal extension in one wall of the chamber and the remotely controlled camera mounted in a corner of the chamber. This photograph is laid on its side. The receive horn was re-positioned to lie in the aperture of the pyramidal extension after this photograph was taken.

2.2 Equipment setup

The setup of the equipment is shown in Figures 2.8 and 2.9.

The Device Under Test (D.U.T.) corresponded to:

1. in the first test, the transmitter held by styrofoam blocks;
2. in the second test, the transmitter in the styrofoam jig without a phantom head;
3. in the third test, the transmitter in the styrofoam jig with a phantom head.

Technical specifications for the transmitter can be found in Reference [3]. The drawings for the styrofoam blocks and the styrofoam jig can be found in Appendix A.

The receive horn was a dual polarization quad-ridged horn (Condor Systems, AS-48450) with a measured gain of 9.05 dB at 850 MHz for the vertical polarization (see Appendix A of Reference [1] reproduced here as Appendix D). Although not measured, the gain for the horizontal polarization can be assumed to be equal to that for the vertical polarization since the horn geometry had a four-fold rotational symmetry.

Since the vertically and the horizontally polarized signals were obtained from the quad-ridged horn, horizontal and vertical are designations that refer to the chamber, not the transmitter. The vertically and the horizontally polarized signals were fed to a network analyzer (HP8530A) which had a very narrow effective bandwidth from synchronous demodulation. The network analyzer was configured for no ratio since the network analyzer did not provide the RF signal to the transmitter in order to avoid the presence of any conducting cable in the vicinity of the transmitter (a previous test had shown that the presence of the conducting cable perturbed significantly the near-field of the transmitter). Both phase and amplitude were measured during each run, but the phase measurement results were not of interest and are not reported herein. A waveguide launcher acting as the reference horn was installed on the azimuth table and pointed upward in order to obtain a reference signal on which to phase-lock the

vertically and horizontally polarized signals so that the network analyzer could track the frequency drift of the oscillator in the battery-operated transmitter.

The signal from the reference horn was connected to a variable bandpass filter (K&L Microwave, 3BT-500/1000-SN C691-1) followed by a 20 dB coupler (HP778D terminated into an external 50 Ω resistive load) then a 26 dB RF amplifier (HP8447D), then optionally a 20 dB or a 6 dB attenuator, and finally the reference port of the network analyzer (HP8530A). The coupled port of the coupler was connected to a spectrum analyzer (HP8560E). Since the network analyzer operated most accurately with the power level of the phase-locking signal lying between -10 dB and -50 dB, the signal level at the reference port of the network analyzer was adjusted by selecting the appropriate attenuator value. As a result, the signal level measured at 0° azimuth angle was found to lie between about -10 dB and -22 dB for all tests herein. No filter was needed in the path of the vertically or the horizontally polarized signals because of the very narrow bandwidth of the HP8530A network analyzer. The variable bandpass filter (with a 3 dB bandwidth of 5% or less) was tuned about 850 MHz to provide maximum signal strength of the reference signal at the $a1$ port of the network analyzer. The $a2$ port of the network analyzer was terminated into a 50 Ω resistive load.

The spectrum analyzer and the 26 dB RF amplifier were passed their respective calibration date but this situation was not deemed to be critical, owing to the secondary importance of the spectrum analyzer and to the fact that the amplifier was of fixed gain without external adjustments.

The positioner was controlled by a Flam & Russel 8502 positioner programmer controller and a Flam & Russel 8601A power amplifier. Although the resolution of the numerical display on the controller was 0.001^o, the mechanical resolution of the positioner was about 0.007^o (see Reference [2, p. 2]).

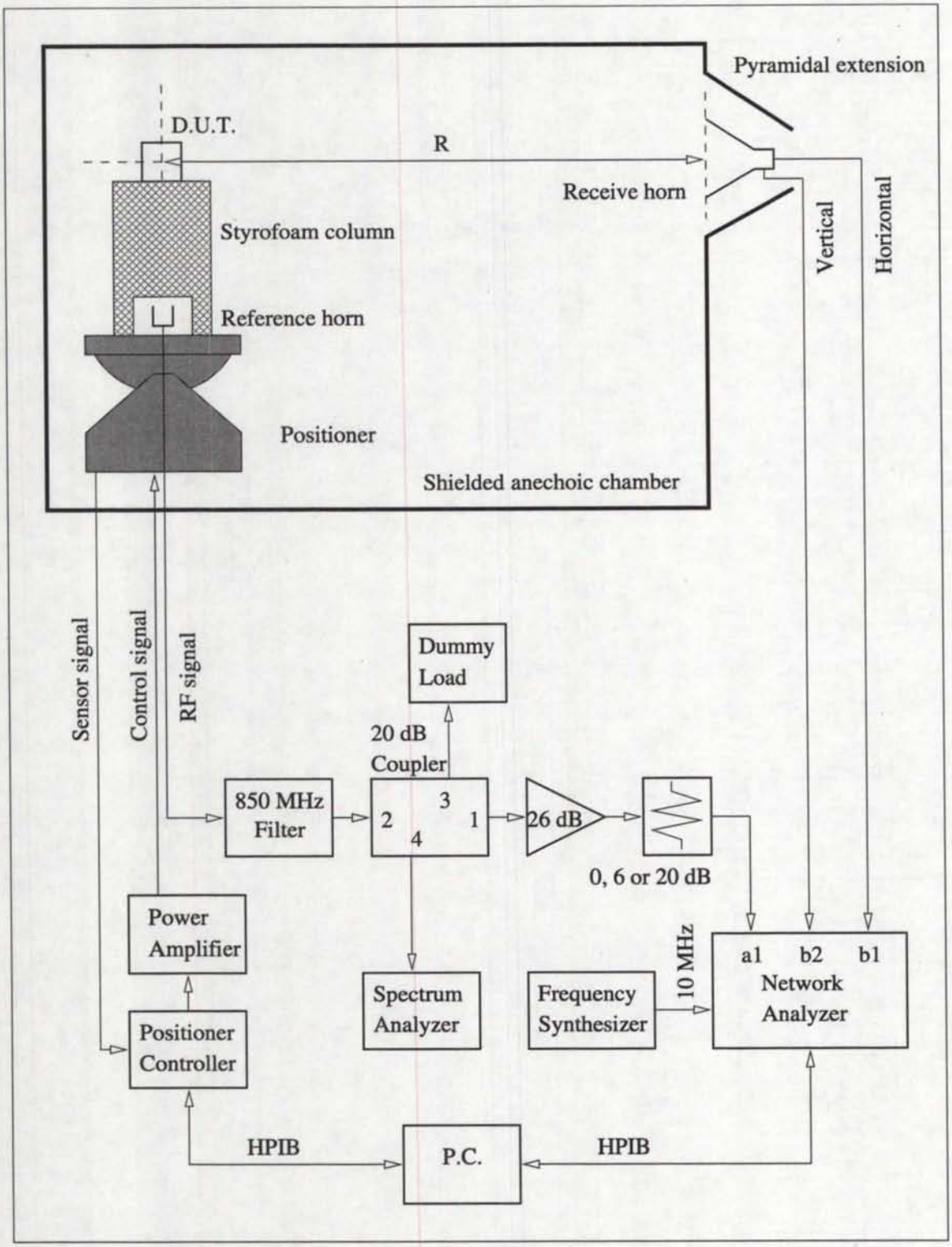

Figure 2.8: The schematic diagram of the equipment setup.

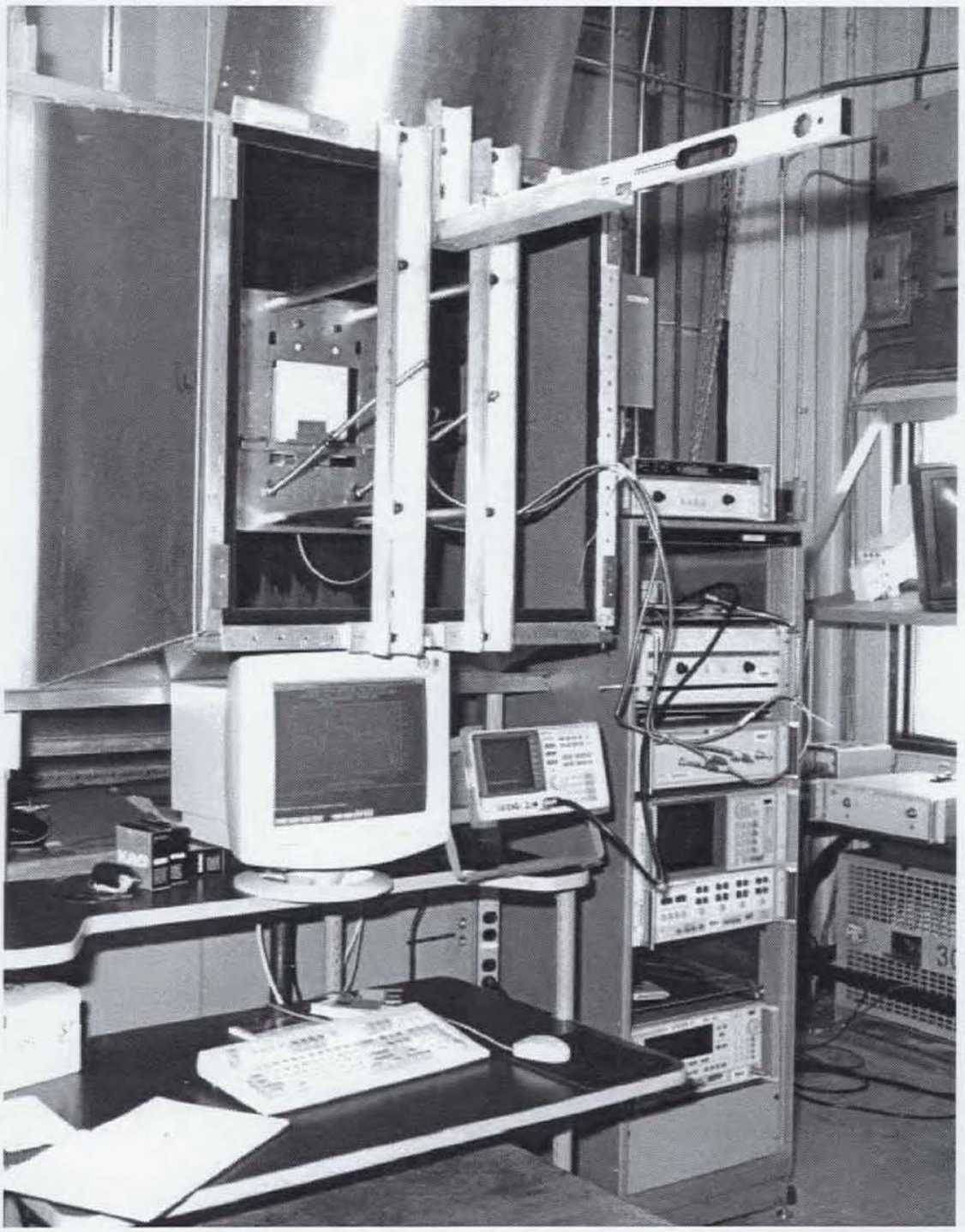

Figure 2.9: A photograph of the equipment setup. The photograph shows the receive horn positioned deep inside the pyramidal extension (i.e. near the truncated end of the extension in this photograph) but the receive horn was re-positioned to lie in the aperture of the pyramidal extension after this photograph was taken.

2.3 Mechanical setup

The far field radiation patterns in both the horizontal and the vertical (with respect to the chamber) polarizations were taken with:

1. the transmitter being in either one of three orientations for the first test:
   (a) the vertical orientation, corresponding to the $\theta = 90^o$ principal cut (see Figure 2.12);
   (b) the broad flat side orientation, corresponding to the $\phi = \{0^o, 180^o\}$ principal cut (see Figure 2.13);
   (c) the edge side orientation, corresponding to the $\phi = \{90^o, 270^o\}$ principal cut (see Figure 2.14);
2. the phantom head being in either one of three orientations for the second and third tests. The three orientations are identified by the orientation that the phantom head would assume as seen by an observer at the position of the receive horn when the azimuth table is positioned at 0°:
   (a) Head up, nose forward: the observer faces the phantom in the vertical orientation (see Figures 2.15 and 2.18);
   (b) Left ear up, nose forward: the phantom head lies on its right side, facing the observer (see Figures 2.16 and 2.19);
   (c) Left ear forward, nose down: the phantom faces downward and the observer sees the left side of the phantom head (see Figures 2.17 and 2.20).

The transmitter is positioned near the right ear of the phantom head.

The angles θ and ϕ are the angles for the spherical coordinate systems in Figures 2.10 and 2.11. These coordinate systems are used herein only to describe the angular cuts. The measurement angle was related to these spherical coordinate angles as summarized in Tables 2.1 and 2.2. The tower was operated in azimuth from -180° to $+180^o$, with 0° corresponding to the D.U.T. facing the receive horn and -90° corresponding to the D.U.T. facing the styrofoam window.

The origin of the coordinate system was shifted from the base of the monopole antenna in the first test to the centre of the styrofoam jig in the second and third tests in order for the origin to remain at the same point in space when the styrofoam jig was positioned in either one of the three orientations. In the second and third tests, the principal planes are those for the phantom head rather than those for the transmitter since the transmitter is tilted in two planes with respect to the phantom head (the transmitter lies on its narrow side, rotated 10° on a 26° inclined plane). Seen from the receive horn, the transmitter was obstructed by the phantom head in the range of measurement angle values about $+90^o$ for the Head-up-Nose-forward orientation, about 0° for the Left-ear-forward-Nose-down orientation, and about 0° for the Left-ear-up-Nose-forward orientation.

Table 2.3 presents the polarization mapping between the measurement and the spherical coordinates for the various test orientations. Horizontal and vertical polarizations refer to the polarization direction with respect to the chamber. Co-polarization, cross-polarization and mixed polarization refer to the polarization direction with respect to the orientation of the monopole antenna of the transmitter. The unit vectors $\hat{\theta}$ and $\hat{\phi}$ refer to the unit vectors for the spherical coordinate system attached to either the transmitter for the first test, or the phantom head for the second and third tests.

Table 2.1: Mapping between measurement and spherical coordinate angular values for the first test.

Orientation	Measurement Angle (^{o})	Spherical Coordinate Angle (^{o})
$\theta = 90^o$	-180 $\longrightarrow$ -90	$\phi = +270 \longrightarrow +360$
	-90 $\longrightarrow$ +180	$\phi = \ \ 0 \longrightarrow +270$
$\phi = \{0^o, 180^o\}$	-180 $\longrightarrow$ 0	$\theta = 180 \longrightarrow 0$ ... $\phi = 0^o$ cut
	0 $\longrightarrow$ +180	$\theta = 0 \longrightarrow 180$ ... $\phi = +180^o$ cut
$\phi = \{90^o, 270^o\}$	-180 $\longrightarrow$ 0	$\theta = 180 \longrightarrow 0$ ... $\phi = +90^o$ cut
	0 $\longrightarrow$ +180	$\theta = 0 \longrightarrow 180$ ... $\phi = +270^o$ cut
For easing the writing process the $\phi = \{0^o, 180^o\}$ and the $\phi = \{90^o, 270^o\}$ cuts will be referred to more simply as the $\phi = 0^o$ and the $\phi = 90^o$ cuts, respectively.		

Table 2.2: Mapping between measurement and spherical coordinate angular values for the second and third tests.

Orientation	Measurement Angle (^{o})	Spherical Coordinate Angle (^{o})
Head-up-Nose-forward	-180 $\longrightarrow$ 0	$\phi = +180 \longrightarrow +360$
	0 $\longrightarrow$ +180	$\phi = \ \ 0 \longrightarrow +180$
Left-ear-up-Nose-forward	-180 $\longrightarrow$ -90	$\theta = \ 90 \longrightarrow \ \ 0$ ... $\phi = 180^o$ cut
	-90 $\longrightarrow$ +90	$\theta = \ \ 0 \longrightarrow 180$ ... $\phi = \ \ 0^o$ cut
	+90 $\longrightarrow$ +180	$\theta = 180 \longrightarrow \ 90$ ... $\phi = 180^o$ cut
Left-ear-forward-Nose-down	-180 $\longrightarrow$ -90	$\theta = \ 90 \longrightarrow \ \ 0$ ... $\phi = 270^o$ cut
	-90 $\longrightarrow$ +90	$\theta = \ \ 0 \longrightarrow 180$ ... $\phi = \ 90^o$ cut
	+90 $\longrightarrow$ +180	$\theta = 180 \longrightarrow \ 90$ ... $\phi = 270^o$ cut

Table 2.3: Polarization mapping between measurement and spherical coordinates.

Orientation	Horizontal	Vertical
$\theta = 90^o$	$\hat{\phi}$ (cross-polarization)	$\hat{\theta}$ (co-polarization)
$\phi = \{0^o, 180^o\}$	$\hat{\theta}$ (co-polarization)	$\hat{\phi}$ (cross-polarization)
$\phi = \{90^o, 270^o\}$	$\hat{\theta}$ (co-polarization)	$\hat{\phi}$ (cross-polarization)
Head-up-Nose-forward	$\hat{\phi}$ (mixed polarization)	$\hat{\theta}$ (mixed polarization)
Left-ear-up-Nose-forward	$\hat{\theta}$ (mixed polarization)	$\hat{\phi}$ (mixed polarization)
Left-ear-forward-Nose-down	$\hat{\theta}$ (mixed polarization)	$\hat{\phi}$ (mixed polarization)

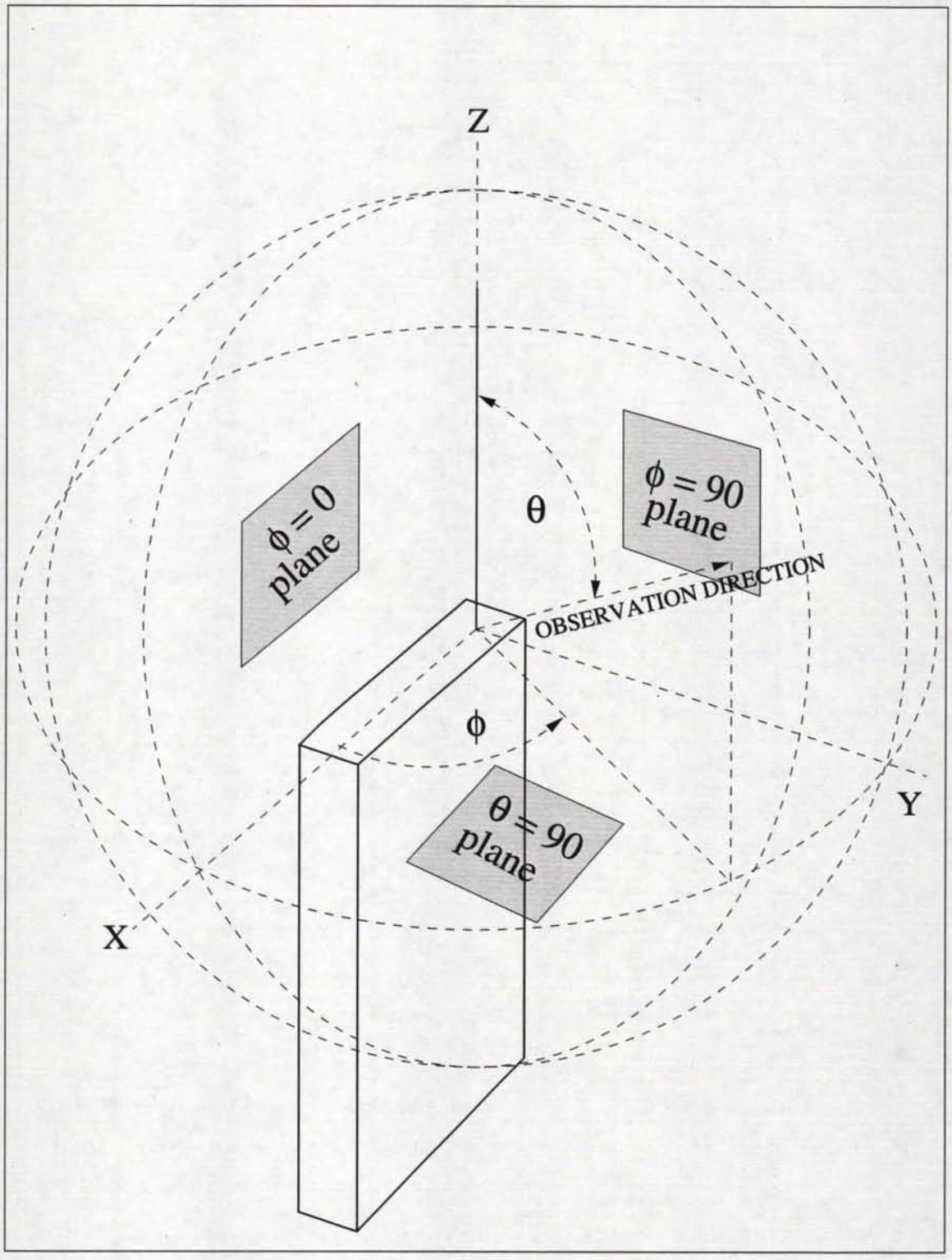

Figure 2.10: The spherical coordinate system used for the first test.

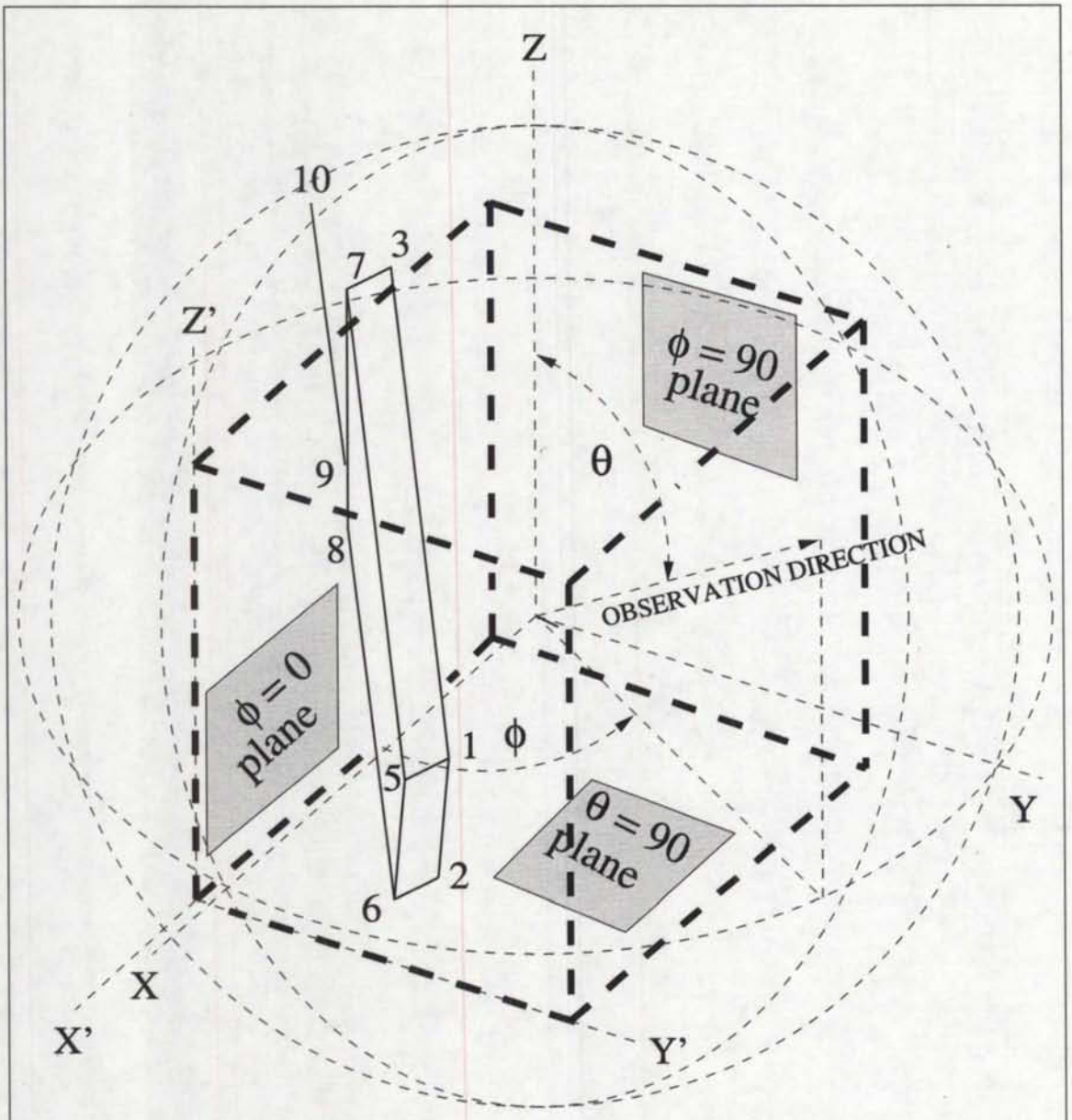

(mm)	1	2	3	4	5	6	7	8	9	10
X'	-147.0	-170.4	-295.4	-318.9	-144.2	-167.7	-292.7	-316.1	-313.9	-391.8
Y'	+226.3	+226.3	+197.1	+197.1	+209.1	+209.1	+180.0	+180.0	+188.6	+173.3
Z'	+245.1	+197.0	+317.5	+269.4	+243.8	+195.7	+316.2	+268.1	+276.5	+314.6

Figure 2.11: Schematic representation of the spherical coordinate system used for the second and third tests. The phantom head would have approximately the X axis through the nose, the Y axis through the left ear canal and the Z axis through the top of the head. The $X'Y'Z'$ coordinate system has its origin at the bottom front left corner of the styrofoam jig.

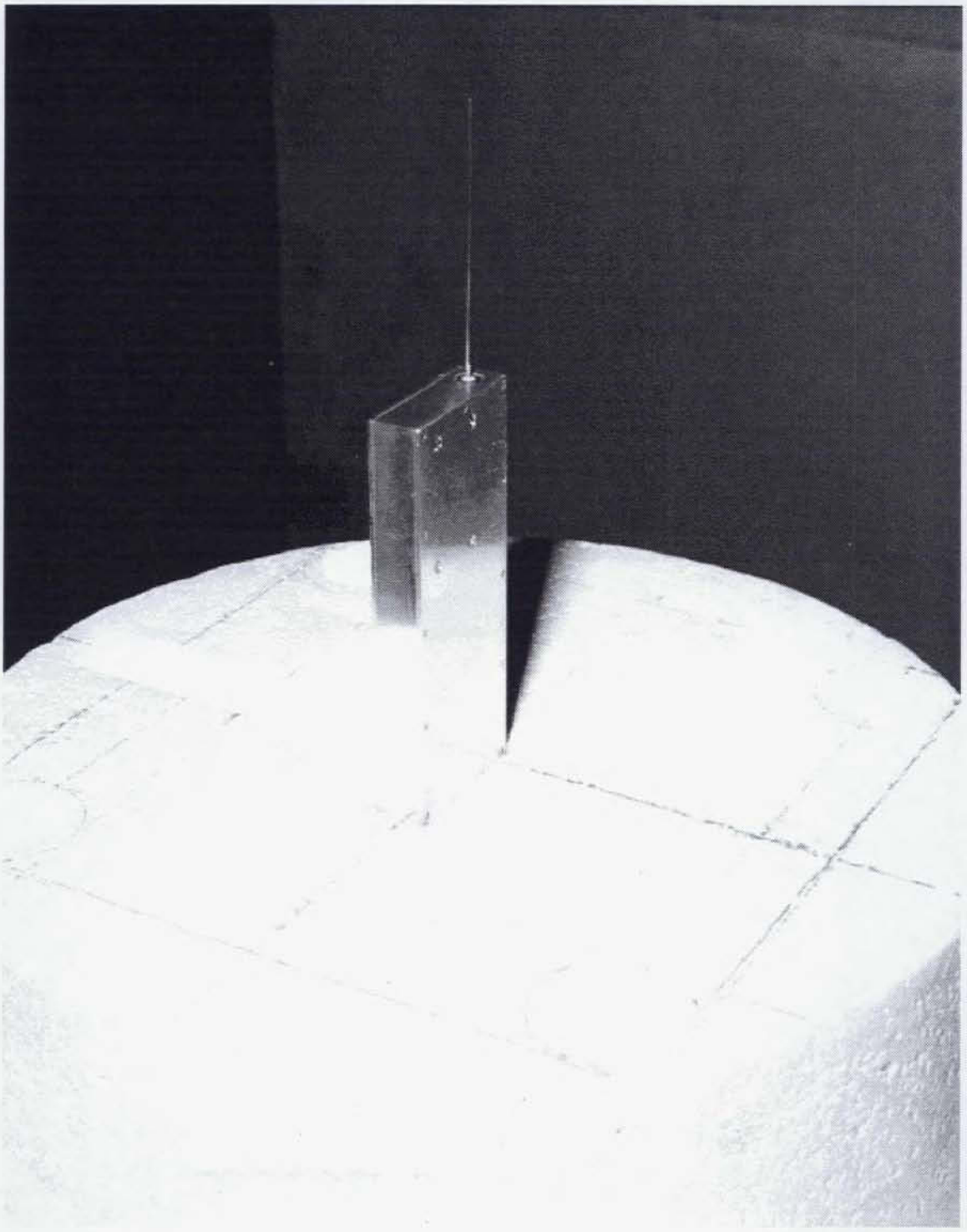

Figure 2.12: The vertical orientation for the first test.

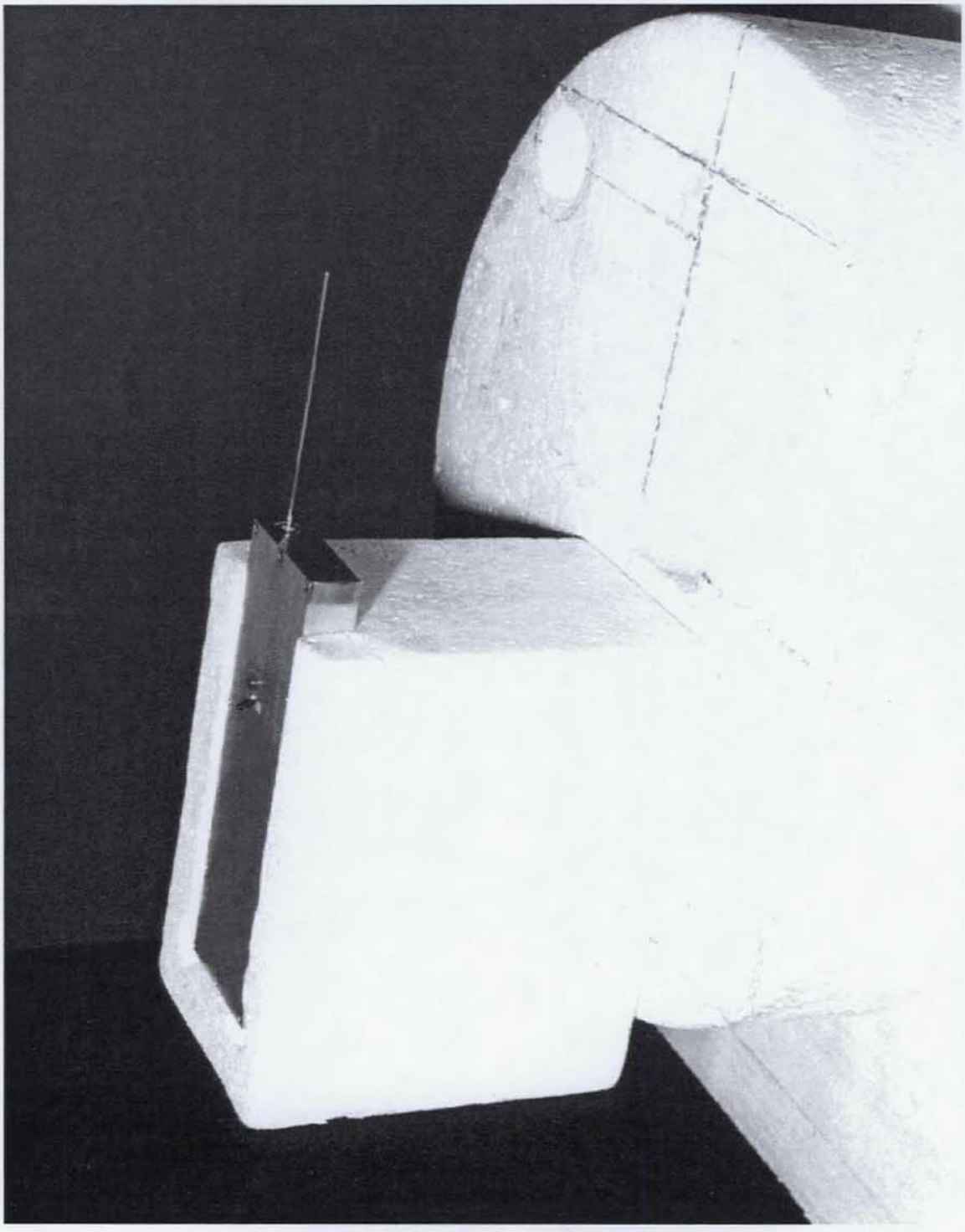

Figure 2.13: The flat orientation for the first test. This photograph is laid on its side.

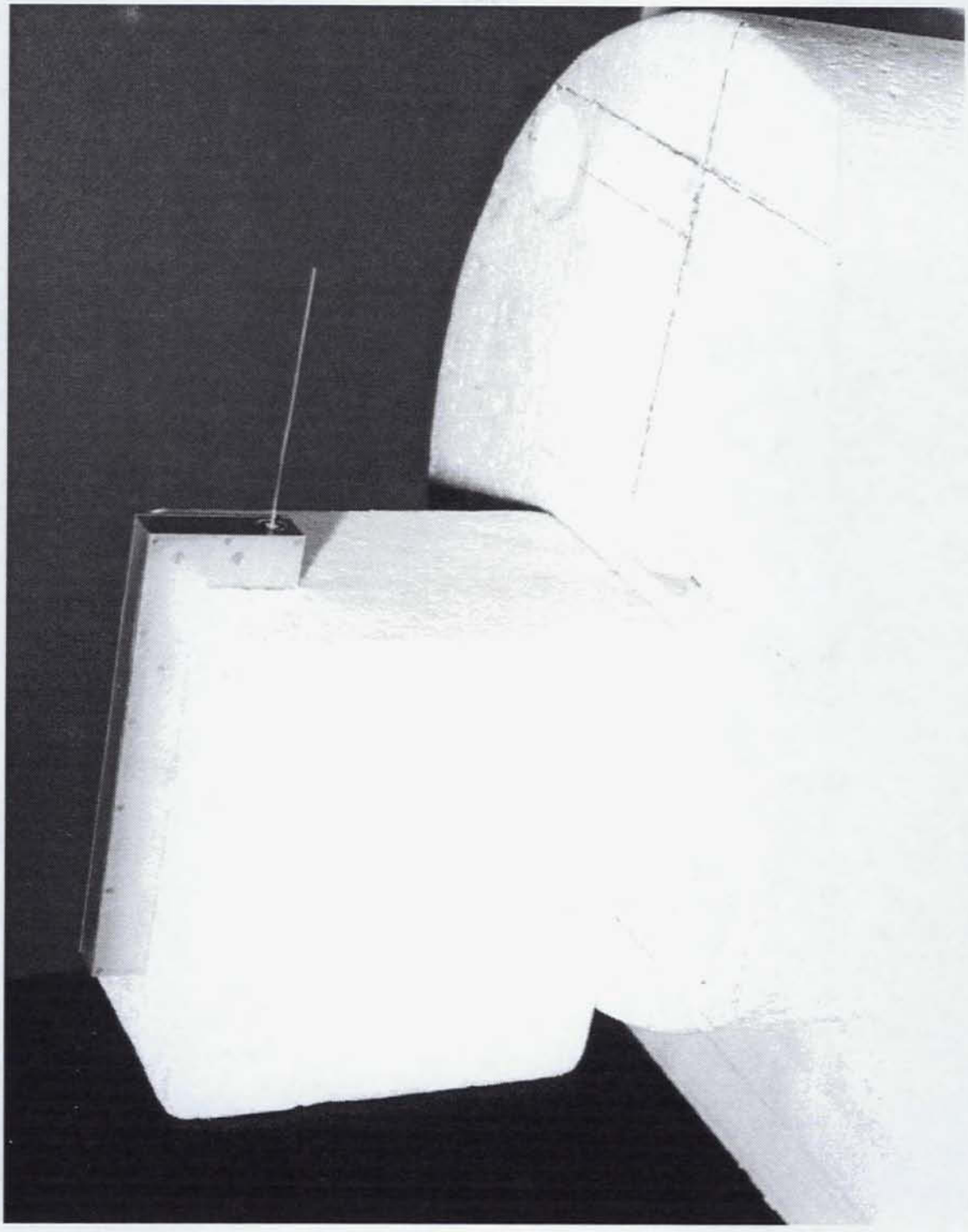

Figure 2.14: The edge orientation for the first test. This photograph is laid on its side.

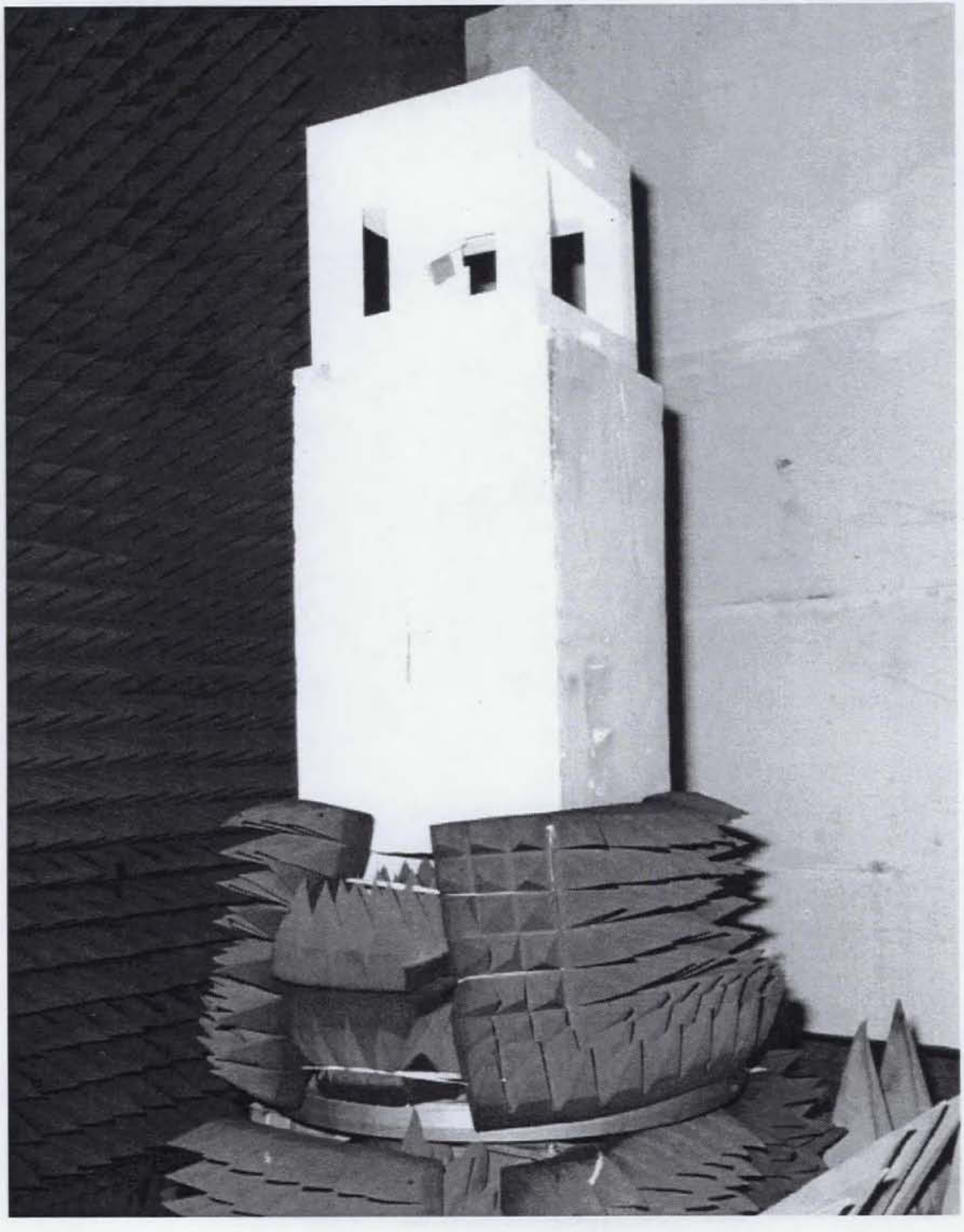

Figure 2.15: The Head-up-Nose-forward orientation without the phantom head.

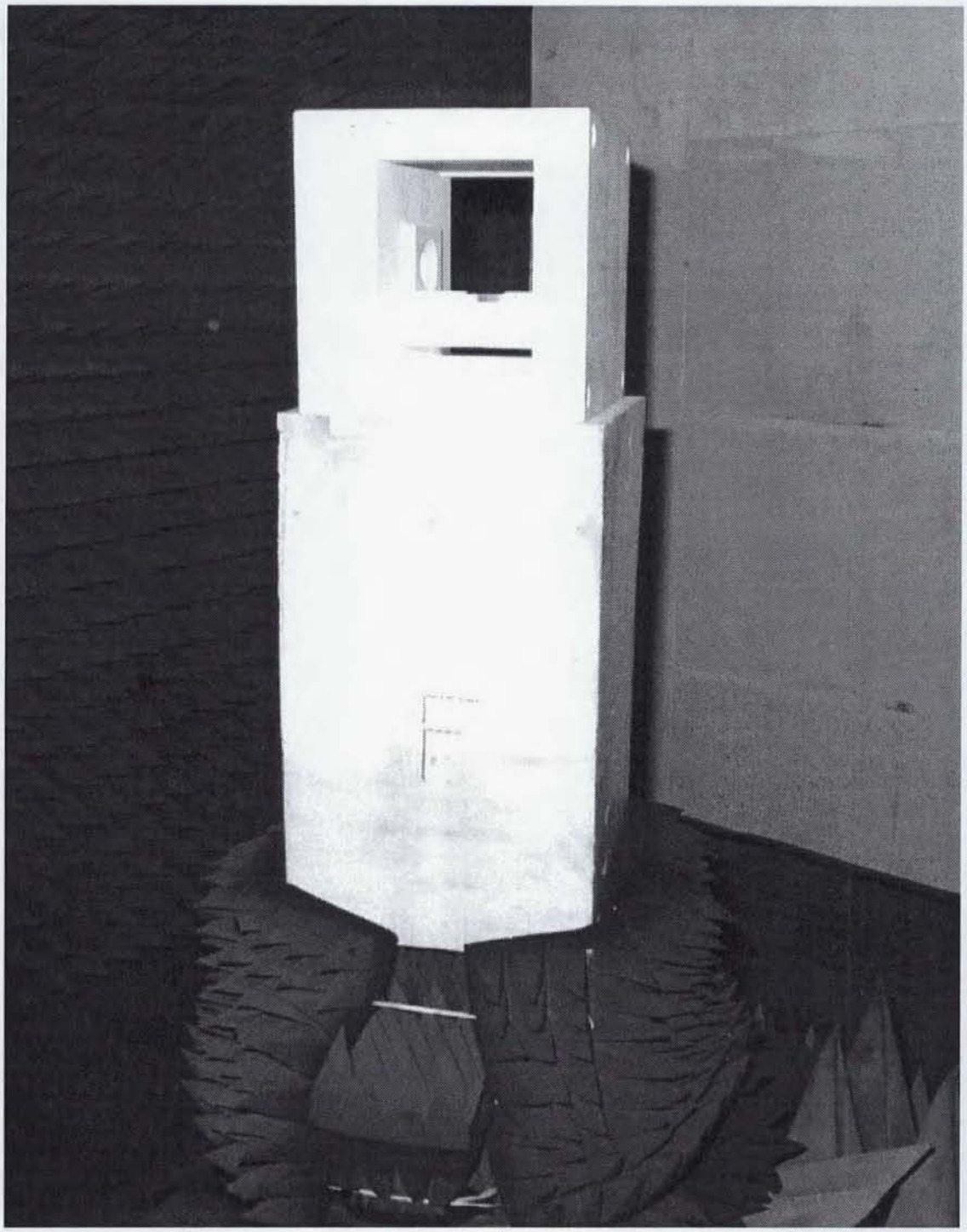

Figure 2.16: The Left-ear-up-Nose-forward orientation without the phantom head.

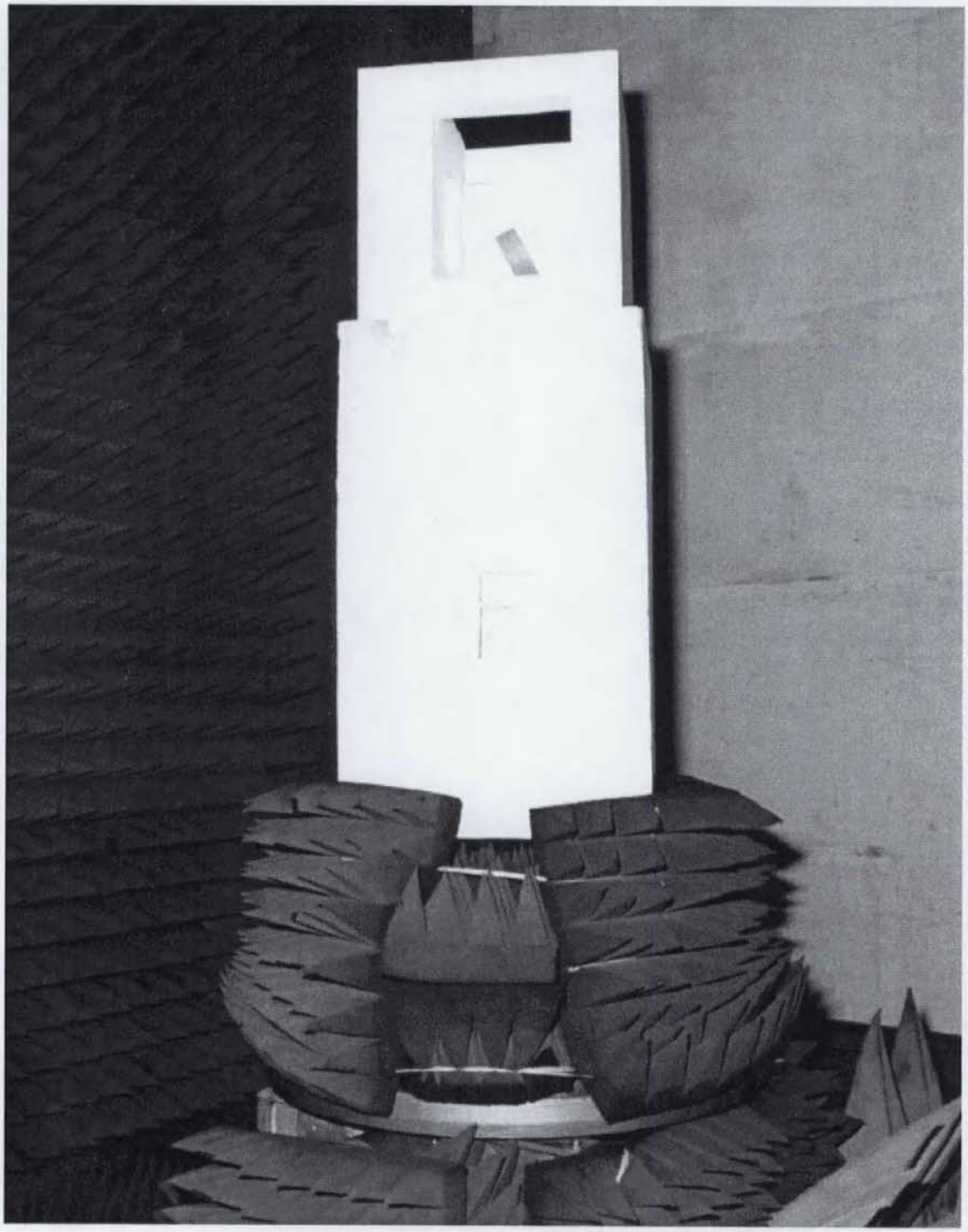

Figure 2.17: The Left-ear-forward-Nose-down orientation without the phantom head.

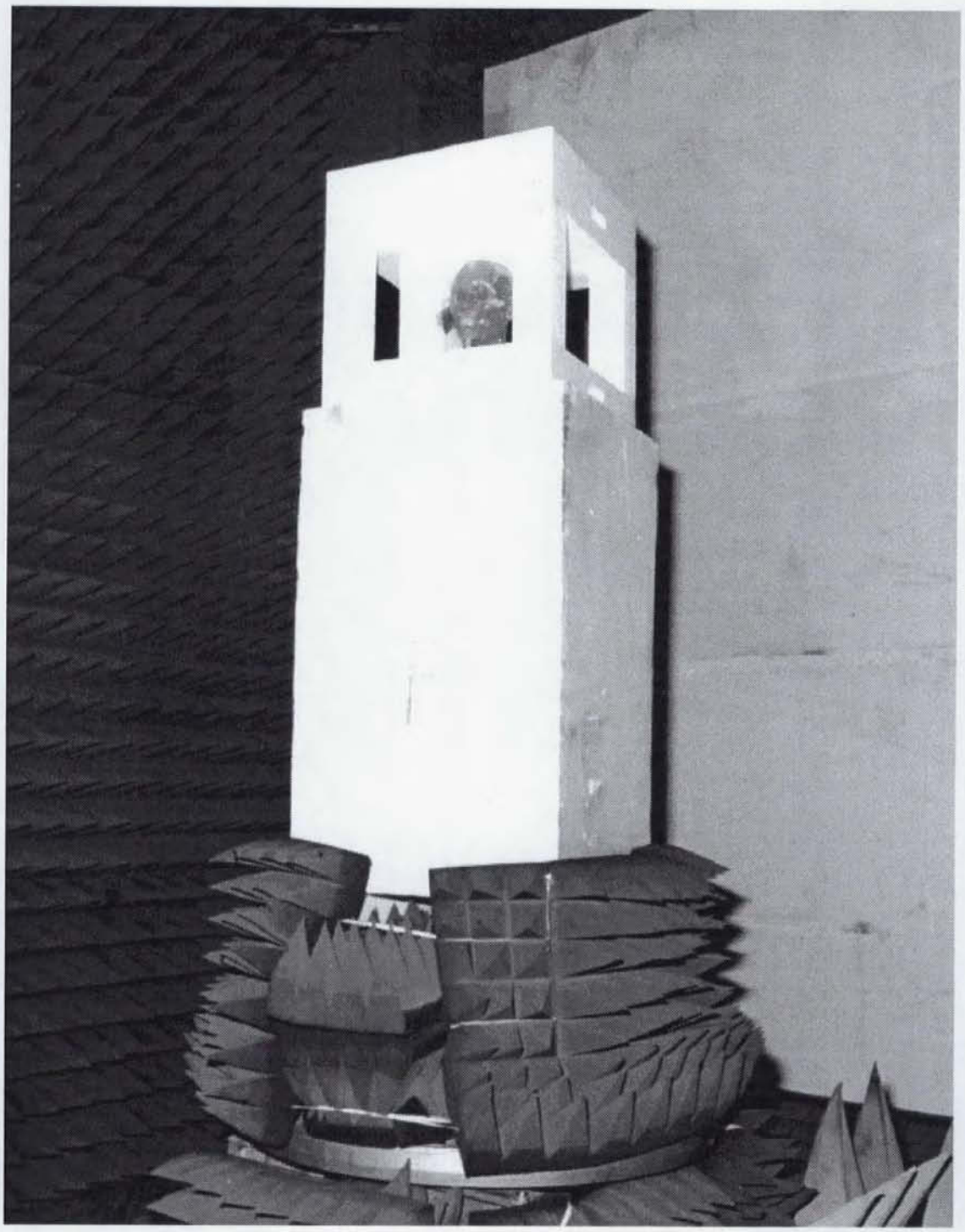

Figure 2.18: The Head-up-Nose-forward orientation with the phantom head.

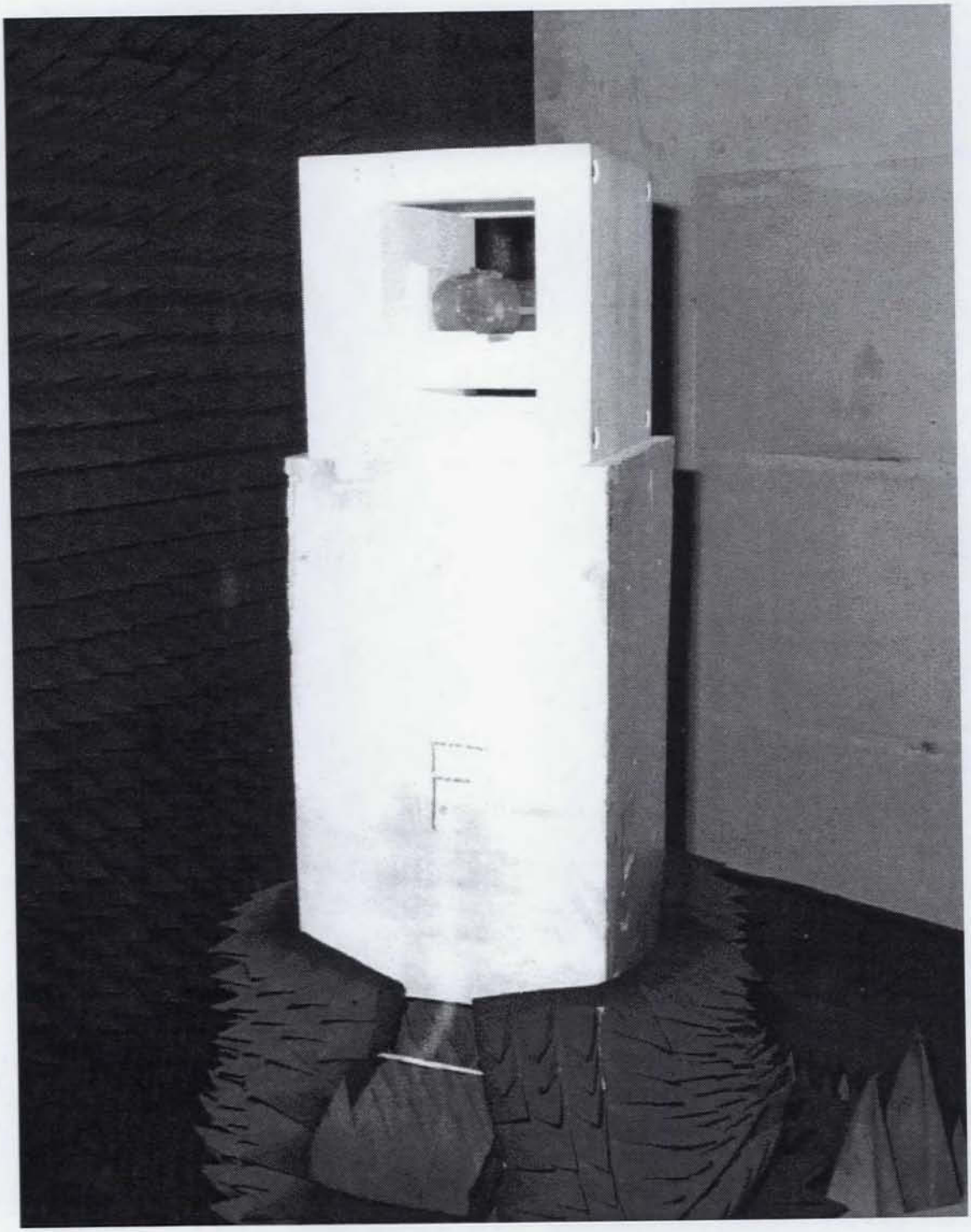

Figure 2.19: The Left-ear-up-Nose-forward orientation with the phantom head.

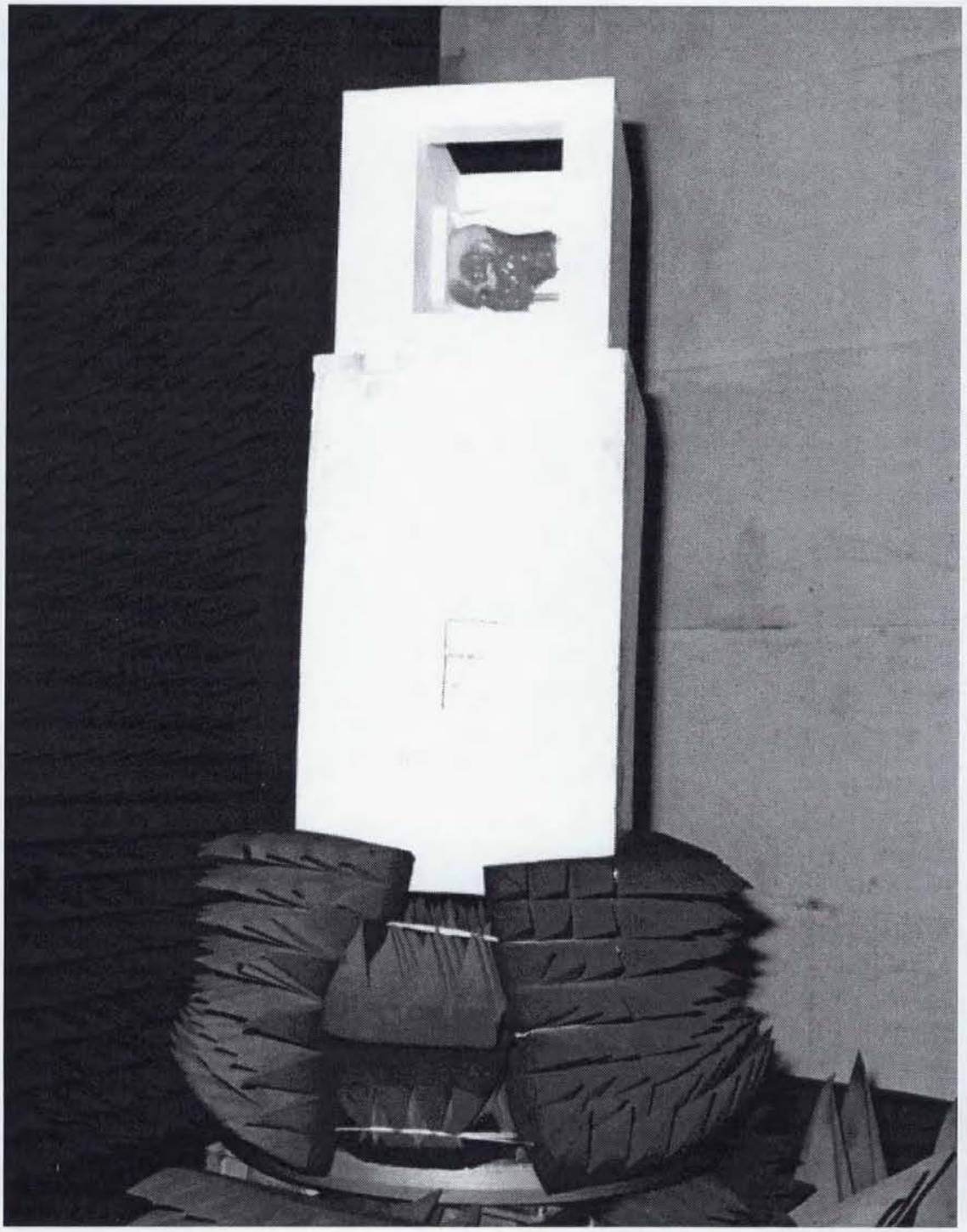

Figure 2.20: The Left-ear-forward-Nose-down orientation with the phantom head.

2.3.1 Alignment procedure

This section describes each step tak[illegible] align the receive horn, the azimuth table, the styrofoam tower and the transmitt[illegible] such that horizontal and vertical polarizations in the chamber would correspond [illegible] the co-polarization or cross-polarization of the desired far-field radiation patterns.

1. Position the receive horn in the ap[illegible]rture of the pyramidal extension and adjust the horn such that the phase centre of the receive horn was levelled with the base of the monopole in the first test or the centre of the styrofoam jig in the second and third tests, while also levelling the roll and the pitch of the horn. This step was carried out with a laser beam mounted 180.34 *cm* above the upper azimuth table, facing the receive hor[illegible] and vertically in line with the centre of rotation of the table. The length of the four horizontal mounting bars and the thickness of the shim behind the horn were adjusted until the laser beam spot traced the entire length of the forward edge of the two horizontal ridges of the quad-ridged horn as the azimuth table was rotated. The roll and pitch were also checked with a bubble level gauge placed against a horizontal and a vertical flat surfaces of the mounting bracket of the horn, respectively.

2. Adjust the yaw of the receive horn and measure the separation distance between the centre of rotation of the azimuth table and the aperture of the receive horn. This step was carried out by hanging from a high tripod a long plumb line over the centre of rotation of the azimuth table and measuring at a height of about 180.34 *cm* above the azimuth table the distance between the plumb line and each side edge of the receive horn. The measured distance was obtained with a metallic measuring tape as 3.358 *m* which corresponded to a separation distance of 3.350 *m* between the centre of rotation of the azimuth table and the aperture of the receive horn, given that the receive horn was 44.61 *cm* wide. Geometrically, these values correspond to the sides of a right angle triangle. The hypothenuse has the length 3.358 *cm*, the base has the length 3.350 *cm* and the height has the length 44.61/2 *cm*.

3. Mount and level the laser beam on a bracket affixed to the frame of the pyramidal extension behind the receive horn such that the beam shone with maximum intensity onto the plumb line hanging over the centre of the azimuth table, with the laser beam passing just over the top edge of the receive horn;

4. Mount the styrofoam tower on top of the azimuth table. This step was carried out by:

   - removing the plumb line setup used in the previous step;
   - mounting and approximately centring the styrofoam tower on top of the azimuth table;
   - levelling the base of the styrofoam jig on top of the tower by inserting thin flat metallic plates underneath the base of the styrofoam tower;
   - anchoring the tower to the table by wrapping each end of a strip of a sturdy plastic tape around two metallic bolts protruding about 3 cm vertically from the surface of the azimuth table, one bolt at each end of the strip, and running one strip along each side of the base of the tower. Hence, a total of four separate strips and eight bolts were used to anchor the tower in two horizontal perpendicular directions.

5. Align the 0° of the azimuth table. This step was carried out by hanging a plumb line over a point on the forward edge of the azimuth table and finding the angular offset required for the laser beam to shine on the plumb line when the azimuth table was rotated alternately between 0° and 180°. In the process of carrying out this step, it was discovered that the plumb line did not remain above the desired point as the table rotated by 180° (the azimuth table was not levelled in the direction perpendicular to the elevation plane, which direction is not a variable axis of the positioner). The cause was attributed to the wear of the bearing at the base of the positioner. The positioner was then set on two lift jacks to level the azimuth table before resuming the alignment process.

6. Mount the reference horn with the aperture facing the ceiling, on top of the azimuth table inside the cut out section at the base of the styrofoam tower. The reference horn within the cut out portion of the styrofoam tower as well as

the styrofoam tower itself were surrounded with absorbing material in order to couple only the direct wave from the transmitter to the reference horn.

7. Mount and align the styrofoam disk that holds the transmitter in the first test. This step was carried out by placing the plumb line on top of the styrofoam tower such that the laser beam shone on the plumb line for a complete rotation of the azimuth table. The styrofoam disk was then mounted on top of the styrofoam tower between the legs of the tripod such that the top of the antenna of the vertically mounted transmitter was underneath the plumb while the transmitter was levelled vertically in both directions with a bubble level gauge. The disk was then aligned such that the transmitter faced the receive horn for 0° azimuth angle by using the reflection of the laser beam off a small mirror mounted at the tip of the rotating axis of a small bearing mounted on top of the styrofoam tower. First, the bearing was oriented such that the beam reflected off the mirror followed the entire length of the forward edges of the two vertical ridges of the quad-ridged receive horn as the mirror was rotated on the bearing. Then, the mirror was further rotated such that the reflected beam followed the alignment lines on the styrofoam disk, then along the antenna, then down the transmitter such that the light reflected off the flat cover of the transmitter also followed the alignment line on the styrofoam disk. This process was repeated with the $+90^o$ azimuth angle to check that the alignment remained correct. The same scheme was used to align the transmitter in the flat and edge orientations of the first test.

8. Mount the styrofoam jig. After the end of the first test, the styrofoam disk was replaced with the styrofoam jig and the jig was centred and aligned on top of the styrofoam tower such that the laser beam shone on the centre lines of each one of the four faces of the styrofoam jig.

In the first test, the three orientations were held fixed by means of slots in styrofoam blocks designed to maintain the base of the monopole antenna of the transmitter at the same location in the chamber, regardless of the orientation of the transmitter. The styrofoam blocks were propped up with small styrofoam pieces as needed to have the transmitter properly levelled and aligned. For the second and third tests, the

transmitter and the phantom were locked in place by the very design of the styrofoam jig.

For the first test, the accuracy in aligning the zero azimuthal angle of the transmitter was estimated by aligning the styrofoam disk of diameter 36.1 cm with the 6 mm wide laser beam spot as the beam was made to sweep over the disk by rotating the mirror on the axis of the bearing. The corresponding angular ambiguity was Arctan(12/361) = 1.90°. Admittedly, this situation indicates that a serious misalignment was possible. Centring the styrofoam disk over the centre of the azimuth table by the process of positioning the disk such that the antenna of the transmitter in the vertical orientation laid directly below the plumb line lit by the 6 mm laser beam spot over a full rotation of the azimuth table, produced a worst case centring error of 3 mm. This estimation is based on the assumption that no error was incurred in the preceding process of positioning the laser beam onto its mounting bracket behind the receive horn such that the laser beam shone with maximum intensity on a plumb line lying directly over the centre of the azimuth table. The worst case centring error of 3 mm would produce a corresponding measurement angle error of Arctan(3/3350) = 0.05°.

For the second and third tests, the accuracy in aligning the zero azimuthal angle of the styrofoam jig was estimated by aligning the centre line on each face of the 55.88 cm wide cube styrofoam jig within the 6 mm spot width of the laser beam at a distance of $3.350 - (0.5588/2) = 3.071$ m. The corresponding angular ambiguity was Arctan(6/3071) = 0.11°. Centring the styrofoam jig over the centre of the azimuth table by the process of positioning the jig such that the centre line of each side of the jig laid within the 6 mm laser beam spot, produced a worst case centring error of 6 mm. This estimation is based again on the assumption that no error was incurred in the preceding process of positioning the laser beam onto its mounting bracket behind the receive horn such that the laser beam shone with maximum intensity on a plumb line lying directly over the centre of the azimuth table. The worst case centring error of 6 mm would produce a corresponding measurement angle error of Arctan(6/3350) = 0.10°.

2.4 Experiment setup

For every one of the three tests, a different fully charged battery pack was used in the transmitter but the same battery pack was used for all three orientations of a same test. The DC voltage of the battery pack was measured under a 100 Ω resistive load before and after each run and was found to be well within the regulation zone of the battery pack (between about 14 V and 15.5 V). A good electrical contact between the metallic front cover of the transmitter and the rest of the metallic chassis was insured after every change of the battery pack by firmly tightening every one of 14 tiny screws by hand. A warm up period of 10 minutes was allowed prior each run that followed any turning off of the transmitter so as to insure that the quartz crystal of the oscillator had reached a stable temperature inside its oven.

An averaging of 64 consecutive measurements was used for each point, one point per degree, from -180° to $+180^o$. The averaging was performed within the network analyzer, hence it is assumed that the averaging was carried out on the linear scale prior to converting the result to dB in order not to corrupt the data. The rotational speed of the azimuth table was adjusted to be $\approx 0.3^o/s$ for a continuous but slow motion such that each run lasted about 18 minutes. The scan motion ranged from about -190° to about $+190^o$ in order to insure that the scan speed was stablilized when the scan angle laid within the range of -180° to $+180^o$.

For the third test, the phantom head was filled with the brain fluid provided by the manufacturer of the phantom head (Microwave Consultants Ltd in London, UK). It was insured that both the head and the fluid reached ambiant temperature after being taken out of their refrigerated storage environment and that all air bubbles had been evacuated from the brain cavity before sealing the hole of the phantom head. The plug that seals the hole at the top of the phantom head was made by CRC in such a way as to contain no metallic constituent in order to minimize the perturbing effect of the presence of the plug on the radiation. Figures 2.21 to 2.23 show the phantom head by itself from various angles. Figures 2.24 to 2.28 show the mounting of the transmitter near the phantom head. Figure 2.29 shows the mounting of the transmitter by itself.

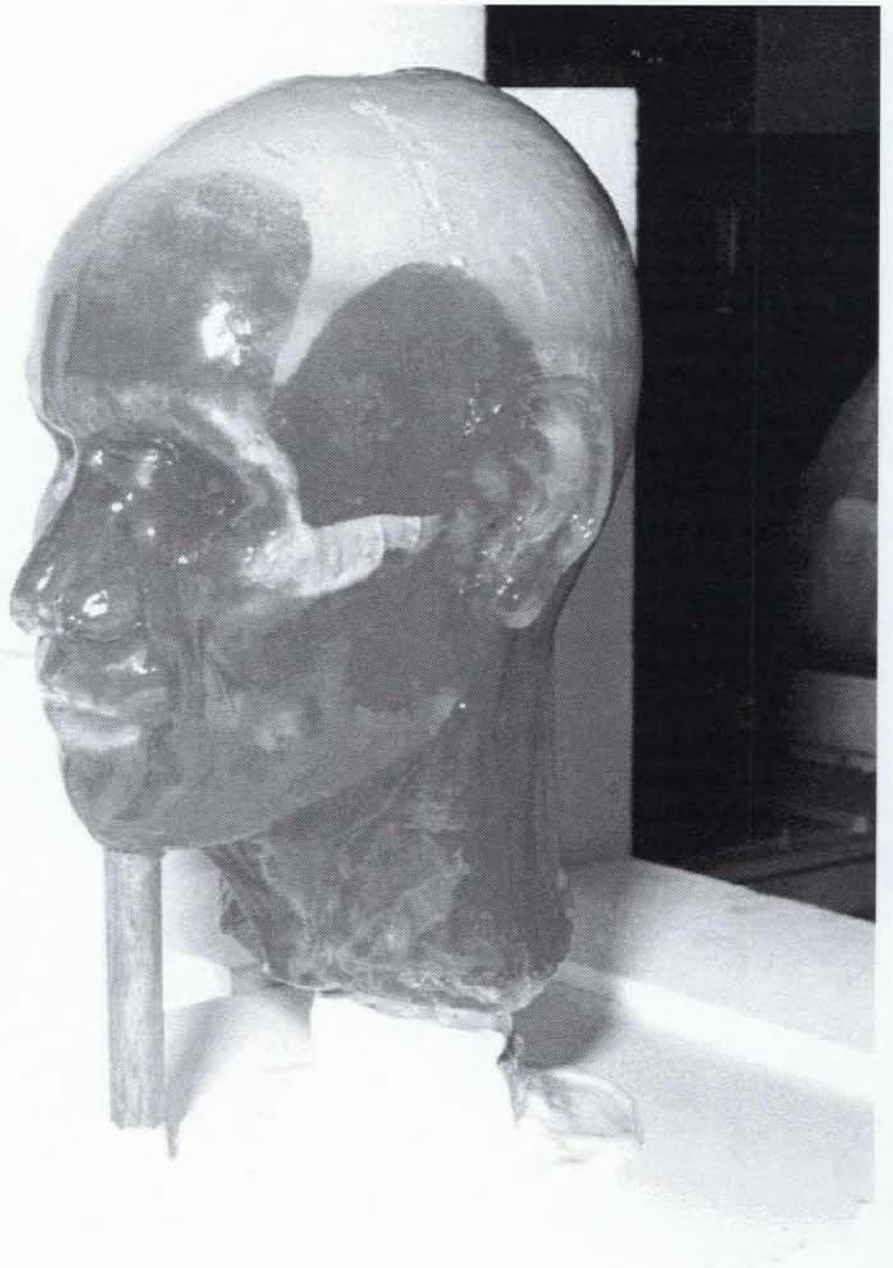

Figure 2.21: A left view of the phantom head in the dismantled styrofoam jig.

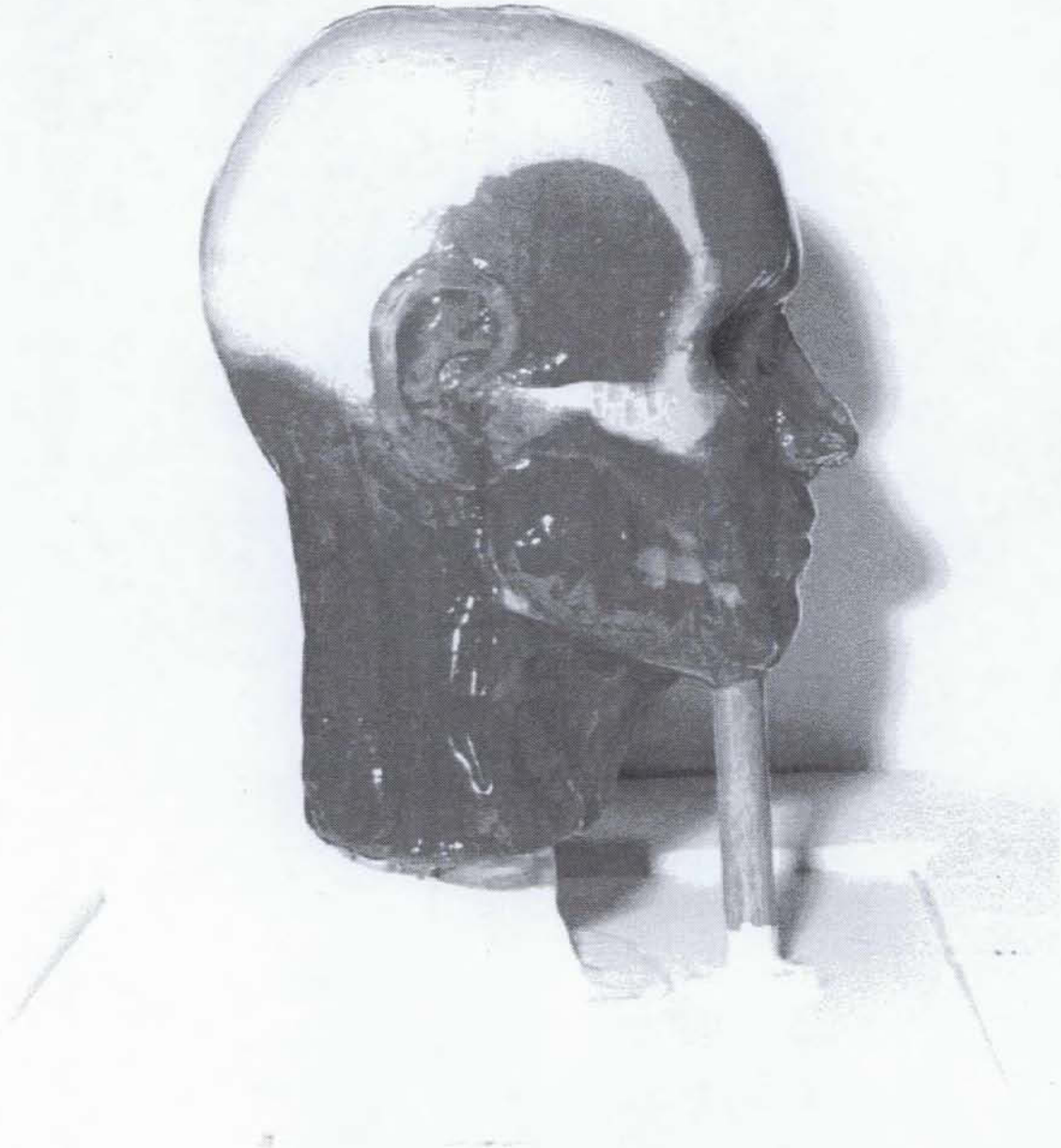

Figure 2.22: The right profile of the phantom head in the dismantled styrofoam jig.

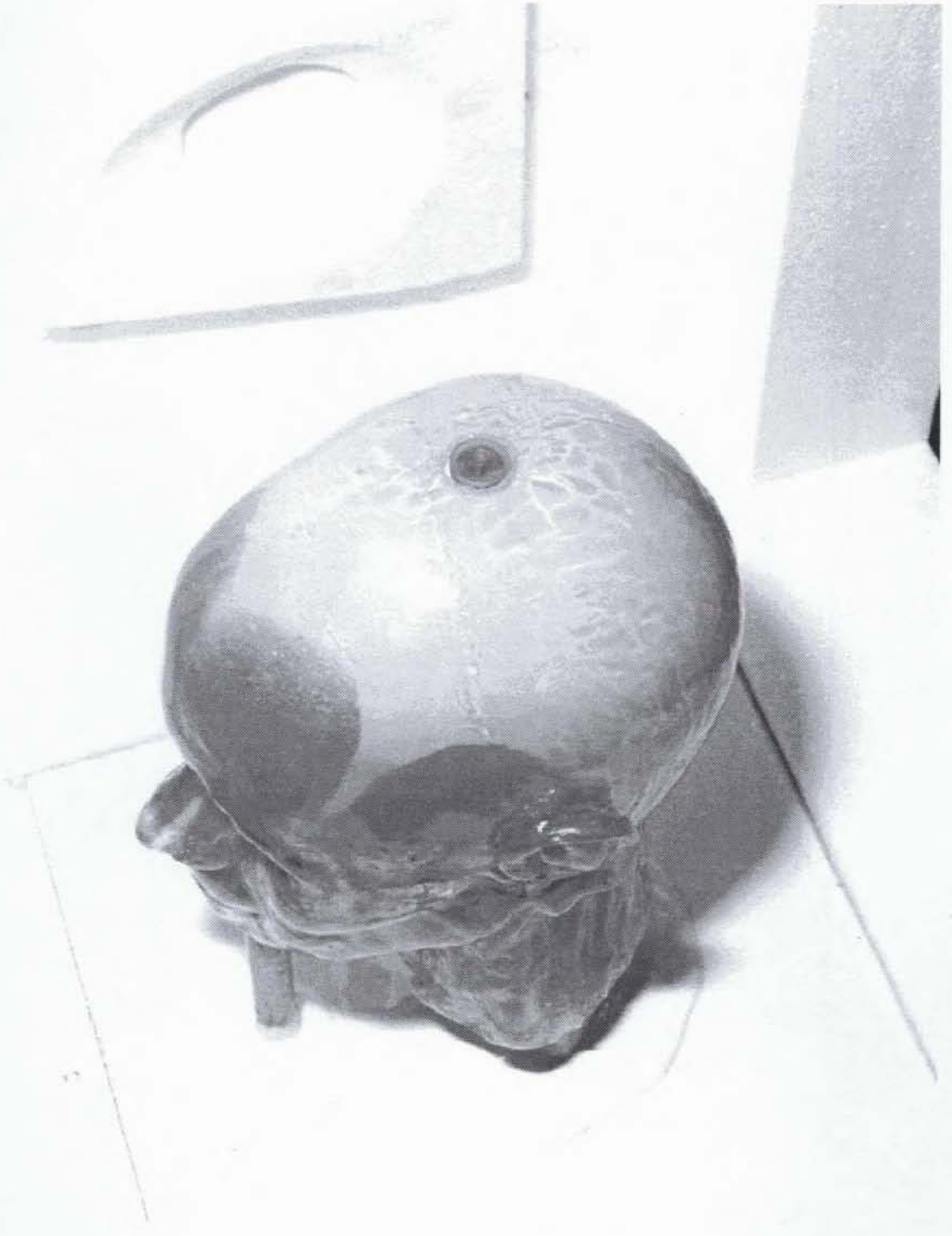

Figure 2.23: A top view of the phantom head in the dismantled styrofoam jig.

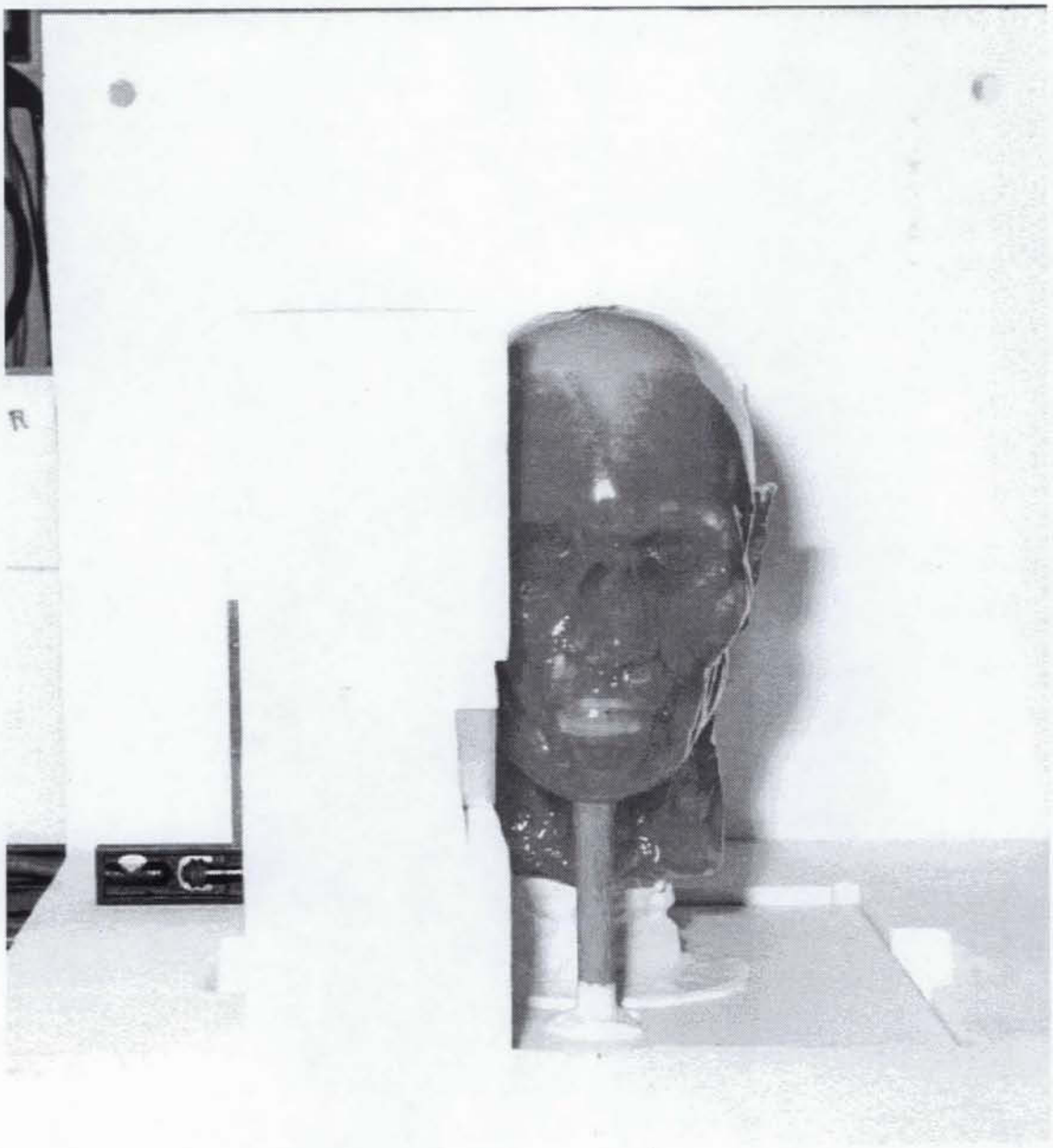

Figure 2.24: A front view of the mounting of the transmitter near the phantom head in the dismantled styrofoam jig.

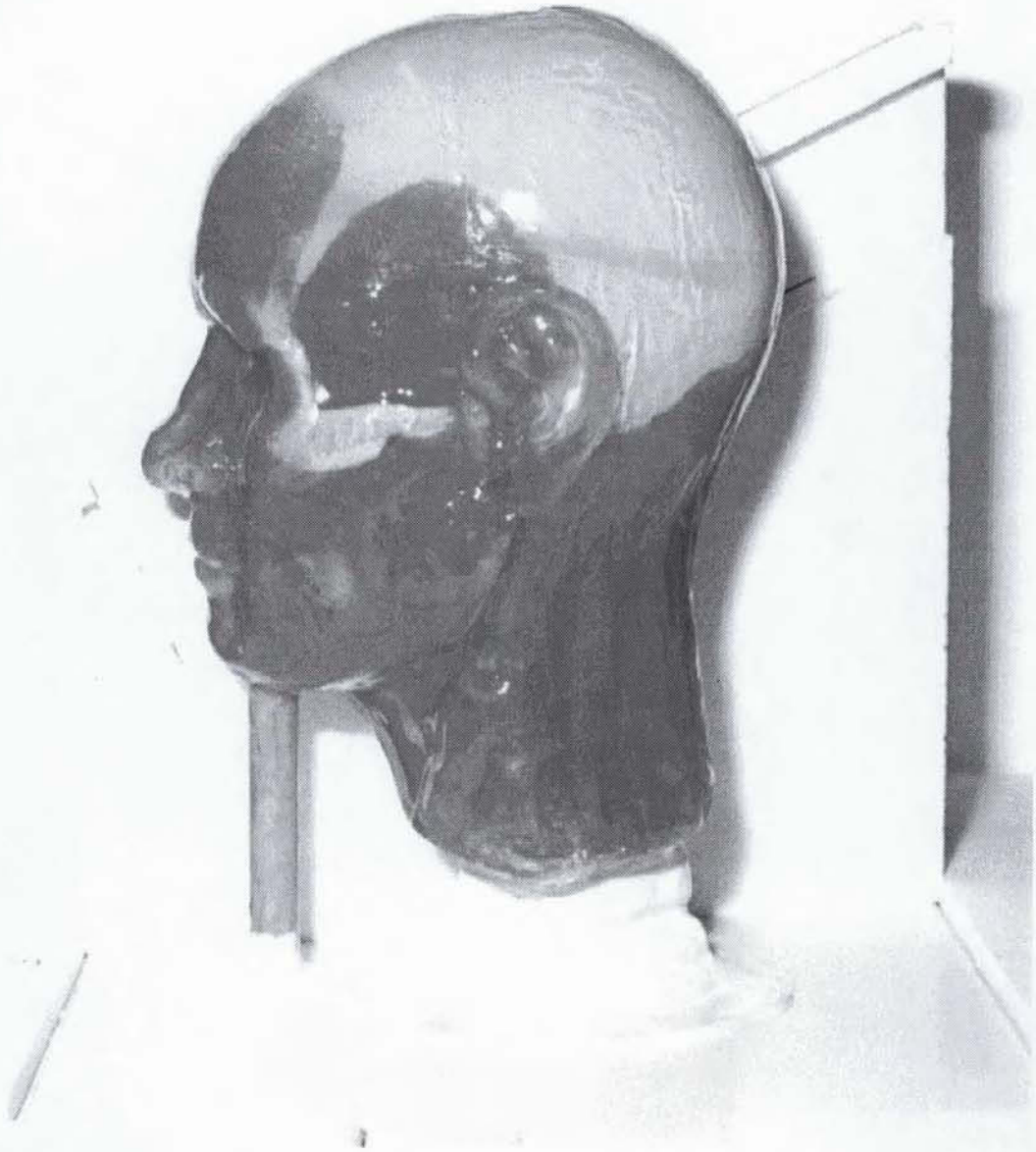

Figure 2.25: A left view of the mounting of the transmitter near the phantom head in the dismantled styrofoam jig.

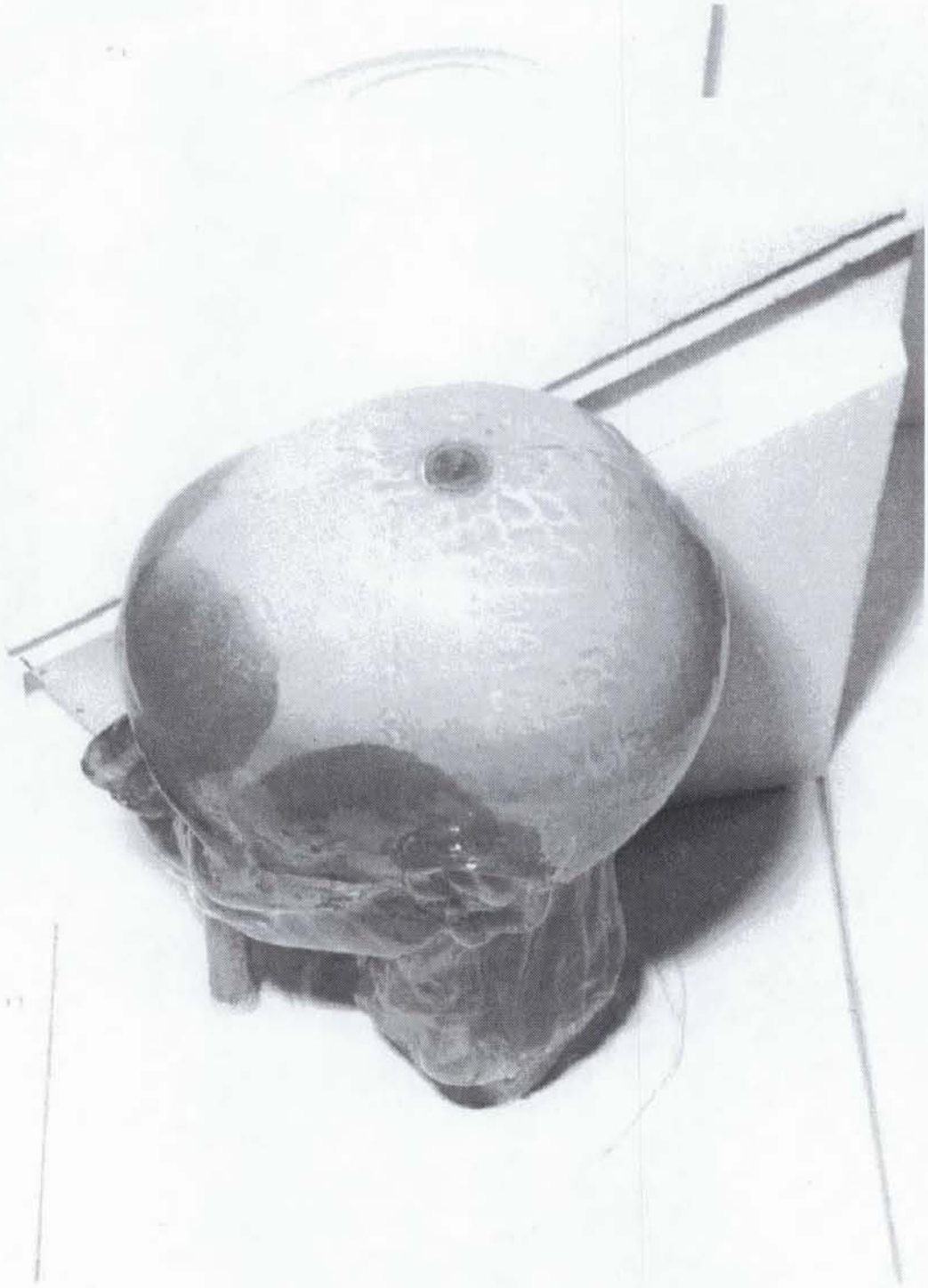

Figure 2.26: A top view of the mounting of the transmitter near the phantom head in the dismantled styrofoam jig.

Figure 2.27: A diagonal view of the mounting of the transmitter near the phantom head in the dismantled styrofoam jig.

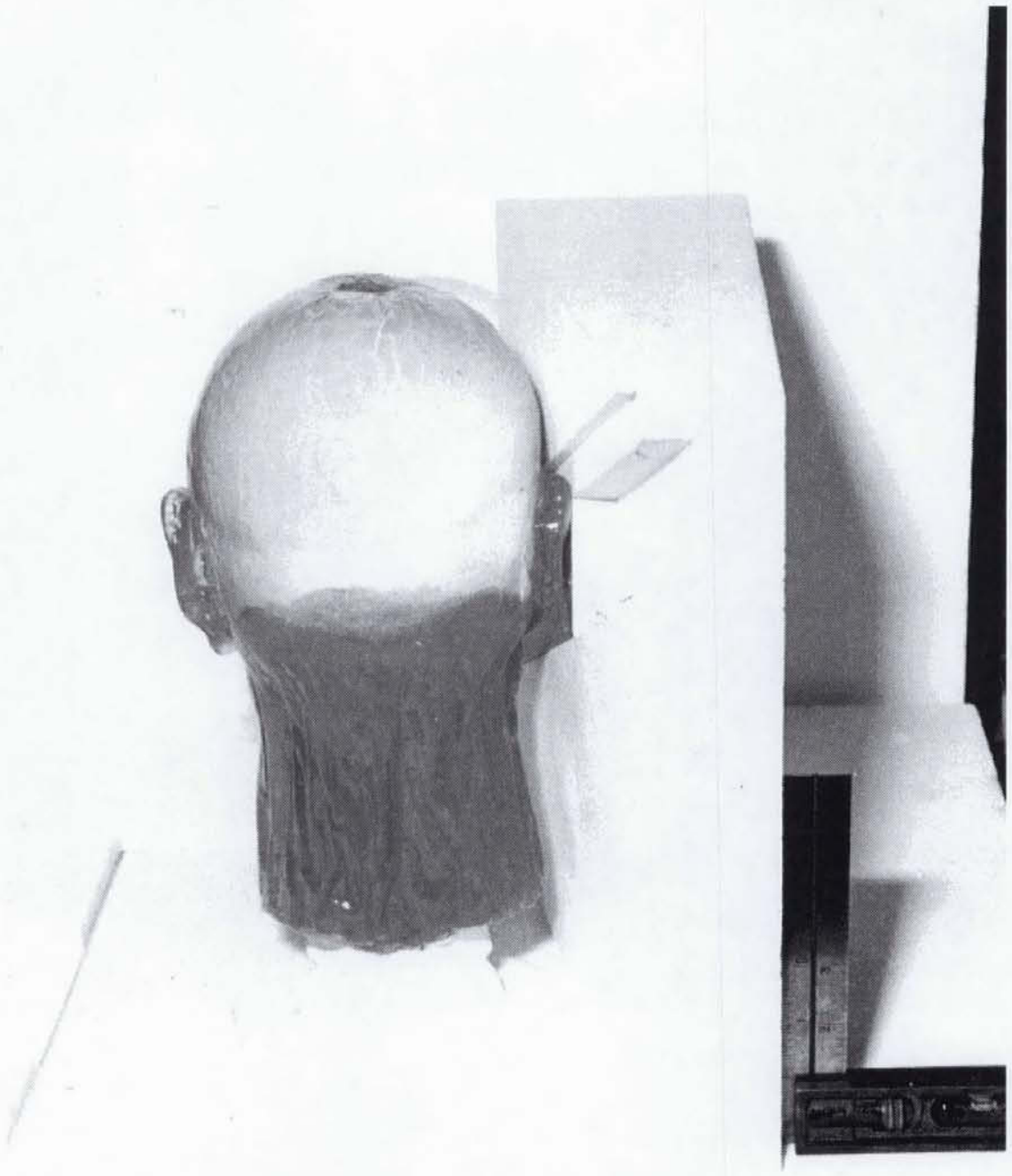

Figure 2.28: A rear view of the mounting of the transmitter near the phantom head in the dismantled styrofoam jig.

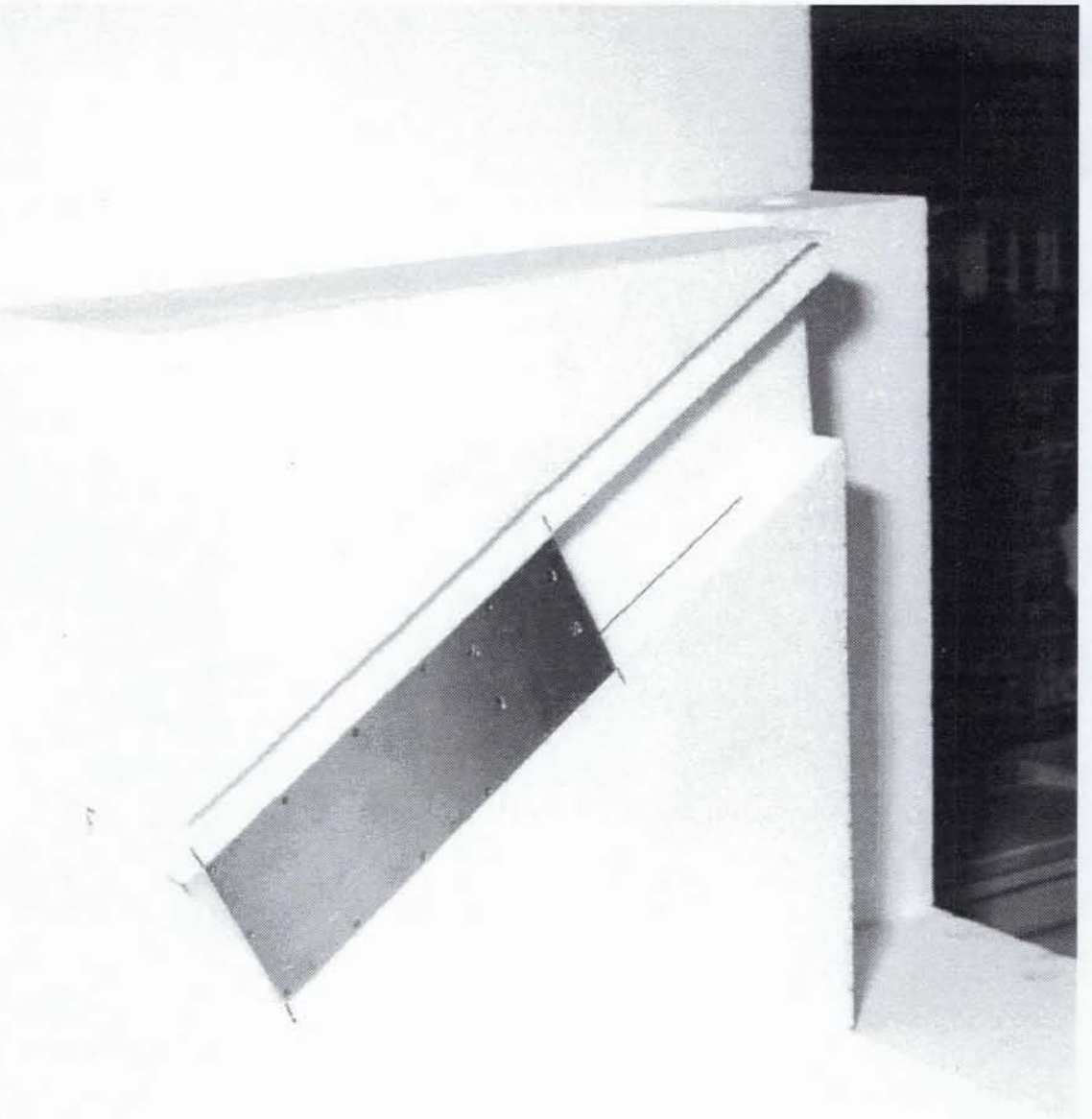

Figure 2.29: A view of the mounting of the transmitter in the dismantled styrofoam jig.

Chapter 3

Test Results

3.1 Plots

This section presents all the magnitude plots for the first, second and third tests with respect to both the measurement angle and the appropriate spherical coordinate angle, and the polar plots for the contours corresponding to 1 V/m and 3 V/m total electric field levels with respect to the appropriate spherical coordinate angle. Table 3.1 gives the description of all the runs performed herein.

3.2 Discussion

Figures 3.1 to 3.12 are plots of the data as acquired, i.e. without any processing, thus they are shown in dB rather than dBm with respect to the measurement angle. Figures 3.14 to 3.31 are rectangular plots of the data converted from the measurement angle to the appropriate spherical coordinate angle, with or without power correction. Figures 3.32 to 3.40 are polar plots of the data converted from the measurement angle to the appropriate spherical coordinate angle, with power correction. Figures 3.41 to 3.49 are polar plots of the 1 V/m and 3 V/m contour levels for the total electric field with respect to the appropriate spherical coordinate angle, with power correction.

Herein, power correction was used to eliminate the effect of the battery discharge

Table 3.1: Description of the various runs.

Run #	Orientation	Remarks
270	*Vert*	
271	*Vert*	1) absorbers leaned against the side of the heavy rail 2) padded the lower end of the control cable exposed through the large cones laid on top of the heavy rail
272	*Vert*	exact repeat of #271
273	*Edge*	lightly raining outside the chamber
274	*Edge*	exact repeat of #273
275	*Edge*	transmitter was re-levelled
276	*Edge*	1) transmitter was re-positioned 3 mm rearward 2) transmitter was re-levelled
277	*Flat*	styrofoam disk was re-aligned
278	*Flat*	exact repeat of #277
279	*HuNf*	styrofoam tower was re-levelled
280	*LuNf*	
281	*LfNd*	
282	*HuNfP*	
283	*LuNfP*	
284	*LfNdP*	styrofoam tower was slightly unlevelled in one direction
285	*Vert*	1) externally DC power supplied transmitter 2) continuous scan
286	*Vert*	1) externally DC power supplied transmitter 2) start-and-stop scan

Vert: Transmitter vertical
Edge: Transmitter on edge side
Flat: Transmitter on flat side
HuNf: Transmitter in Head-up-Nose-forward headless jig
LuNf: Transmitter in Left-ear-up-Nose-forward headless jig
LfNd: Transmitter in Left-ear-forward-Nose-down headless jig
HuNfP: Transmitter with Head-up-Nose-forward phantom head in jig
LuNfP: Transmitter with Left-ear-up-Nose-forward phantom head in jig
LfNdP: Transmitter with Left-ear-forward-Nose-down phantom head in jig

during each measurement run and to take into account the power transfer function of the network analyzer shown in Figure 3.13 in order to obtain absolute rather than relative power levels. The same linear (on a decibel scale) power correction for the battery discharge was applied to the two curves corresponding to the two polarizations of each test run. The power was corrected based on $\Delta P = P(-180^o) - P(+180^o)$ for the strongest polarization at $\pm 180^o$, as presented in Table 4.2. Some of the uncorrected plots appear to be discontinuous at the spherical coordinate angle value corresponding to the $\pm 180^o$ measurement angle values as a result of the RF power level being different at the beginning and at the end of a same run due to the battery discharge. The effect of the slow discharge is also evident from the downward shift between the three curves in Figure 3.2 which were all acquired consecutively with the same battery pack.

As expected from the similarity between the orientations of the first and second tests, we observe the following similarities between the corresponding curves when these curves are plotted with respect to a same coordinate system (the measurement angle coordinate system):

- run #272 in Figure 3.1 and run #281 in Figure 3.11;
- run #278 in Figure 3.3 and run #280 in Figure 3.9, provided that one plot is shifted by 180° to account for the physical 180° rotation difference between the two positions of the transmitter;
- run #276 in Figure 3.5 and run #279 in Figure 3.7, provided that one plot is shifted by 180° to account for the physical 180° rotation difference between the two positions of the transmitter;

These similarities, however, do not appear between the corresponding curves when these curves are plotted with respect to the appropriate spherical coordinate angle because the spherical coordinate system is not the same for both the first and the second tests, i.e. the coordinate system for the first test is with respect to the transmitter whereas the coordinate system for the second test is with respect to the phantom head.

The existence of the co-polarization and cross-polarization signals could be explained in terms of the presence of real currents induced on the various faces of the metallic case, and equivalent currents lying in the volume of the dielectric bodies surrounding the antenna. From the electromagnetic equivalence principle, the conducting surfaces of the metallic case could be replaced by equivalent surface currents and the phantom head could be replaced by equivalent volume polarization currents, all these equivalent currents being electric and existing in free space.

The effect due to the presence of the phantom head is clearly shown in Figures 3.7 to 3.12 but it is difficult to assess this effect in terms of co-polarization and cross-polarization levels because the transmitter was not perfectly vertical or horizontal in the chamber. Seen from the receive horn, the transmitter was obstructed by the phantom head in the range of measurement angle values about $+90^o$ for the Head-up-Nose-forward orientation, about 0° for the Left-ear-forward-Nose-down orientation, and about 0° for the Left-ear-up-Nose-forward orientation. In comparing the curves with and without the phantom head, one observes that the effect of the phantom head in the unobstructed region consists in filling nulls as a result of the presence of the polarization currents which produce radiation of their own (Figure 3.10 is noteworthy is that respect). On the other hand, the effect of the phantom head in the obstructed region consists in creating nulls as a result of the material (both conducting and dielectric) losses in the phantom head, or in displacing nulls as a result of the phase shift introduced by the phantom head as the wave propagates through and around the phantom head.

As expected, the dominant signal for most azimuth angles has the polarization corresponding to the orientation of the monopole antenna in the first test. In Figure 3.1, the curves for the cross-polarization signals show deep nulls at about $\pm 90^o$ because for the vertical orientation, the equivalent surface currents with the most horizontal orientation were on the top and bottom surfaces of the metallic case such that these surfaces acted as fat dipoles. Consequently, as dipoles, they produced the least radiation in the direction of their axes. As expected, the level of the curves for the cross-polarization (i.e. vertical polarization) in Figure 3.4 is much smaller than that for the co-polarization (i.e. horizontal polarization) in Figure 3.3 because for the flat orientation the equivalent surface electric currents are mostly horizontal.

In Figure 3.2, the curves for the co-polarization signals are asymmetrical because the monopole antenna is located asymmetrically on the metallic case of the transmitter. However, in Figures 3.5 and 3.6, the curves are asymmetrical about 0° even though the geometry of the transmitter is symmetrical about the origin of the coordinate system (i.e. the base of the monopole antenna), notwithstanding the presence of two small holes in the metallic cover of the transmitter.

Figures 3.41 to 3.49 show the polar plots of the contours for two values of the total electric field with respect to the appropriate spherical coordinate angle. The two values of 1 V/m and 3 V/m are approximately the values used in the immunity level assessment of equipment used by the general public in Canada.

The absolute power levels measured from the network analyzer are known from the knowledge of the relative power level measured by the network analyzer and the knowledge of the power transfer function for the network analyzer. The radiation power density at the aperture of the receive horn antenna can be computed from the knowledge of the absolute power level at the network analyzer, the knowledge of the insertion and the mismatch losses for the cables, and the knowledge of the gain for the receive horn. The cable insertion loss was measured during the 1997 test as 0.84 dB for the vertical polarization channel and 0.96 dB for the horizontal polarization channel. However, since there was no garantee that these cables were configured the same way during the 1998 test, the average value, i.e. 0.90 dB, was taken as the typical insertion loss value for each cable. The mismatch loss for the receive horn is 0.14 dB. From the knowledge of the value of 9.05 dB gain for the receive horn, the corresponding effective aperture is computed as 0.080 m^2 (see Appendix D). The radiation power density at any given point in the far-field zone can be computed from the knowledge of the radiation power density at the aperture of the receive horn and the knowledge of the free space propagation loss over the separation distance between the observation point of interest and the aperture of the receive horn. Appendix C.6 presents the source code for the FORTRAN program that computes the separation distance corresponding to the two desired total electric field levels of 1 V/m and 3 V/m.

The polar plots for the contour levels show that the shape of the 1 V/m contour is essentially a magnified version of that for the 3 V/m contour for a same orientation

since the computation was carried out by assuming that the only difference between the two contours was the $1/R$ variation of the field with the separation distance R. The effect of the presence of the phantom head is clearly seen on these plots as well.

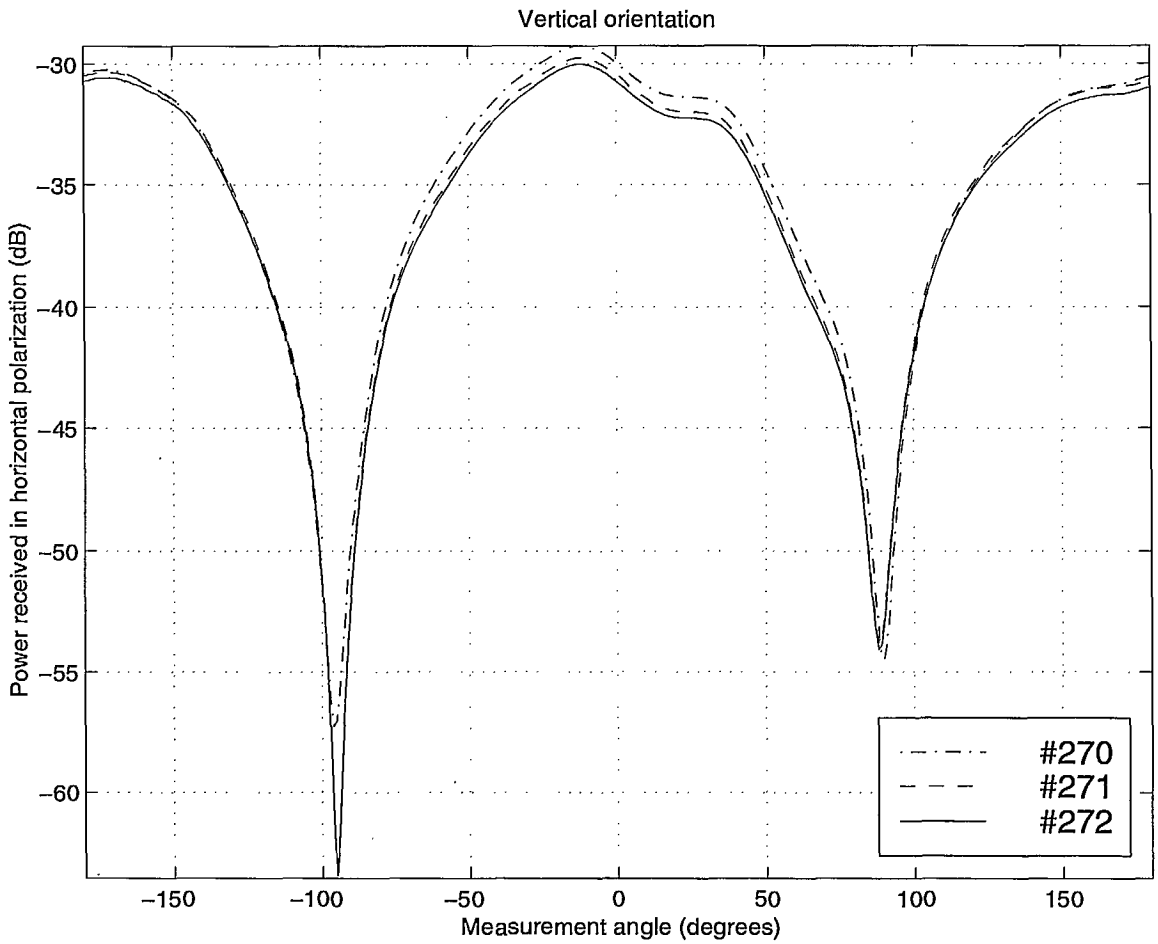

Figure 3.1: The horizontal polarization for the Vertical ($\theta = 90^o$) orientation in the first test.

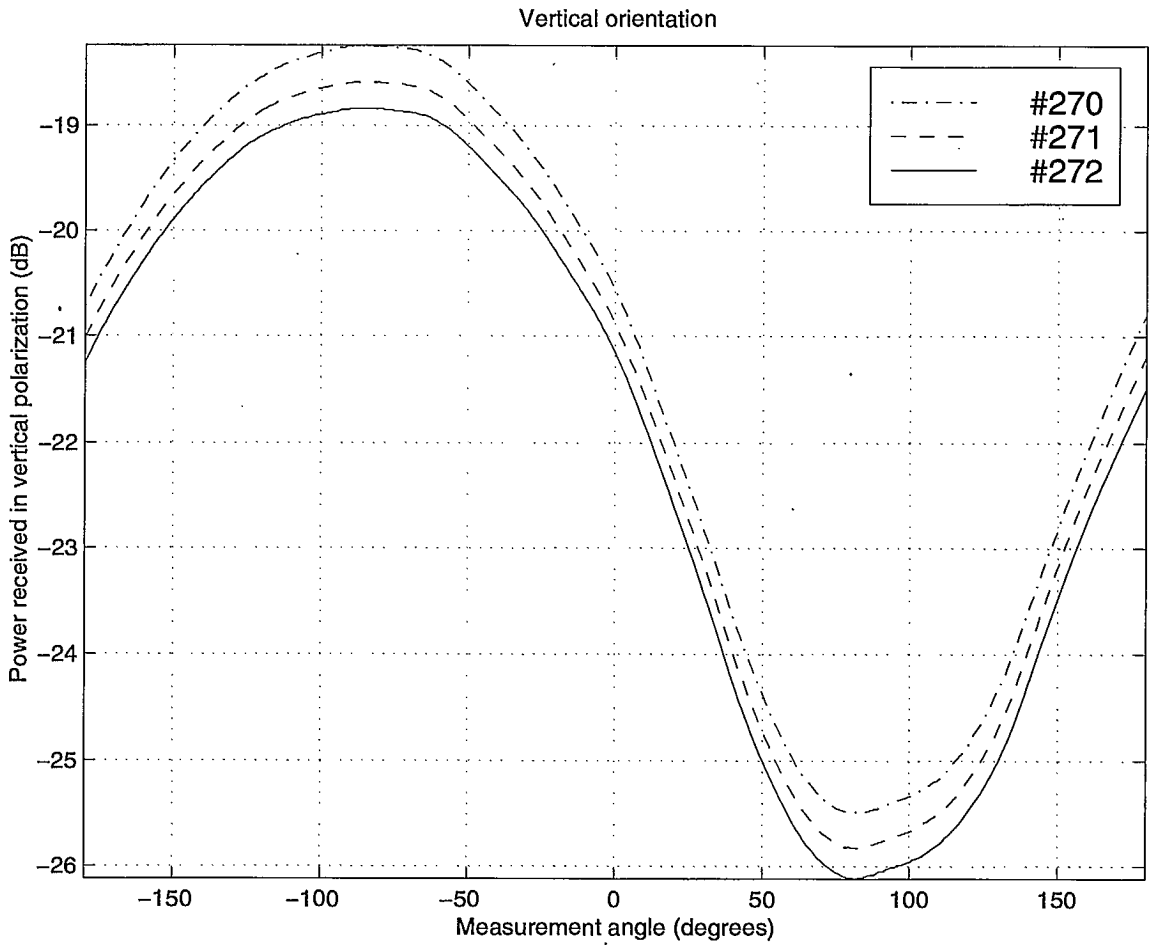

Figure 3.2: The vertical polarization for the Vertical ($\theta = 90°$) orientation in the first test.

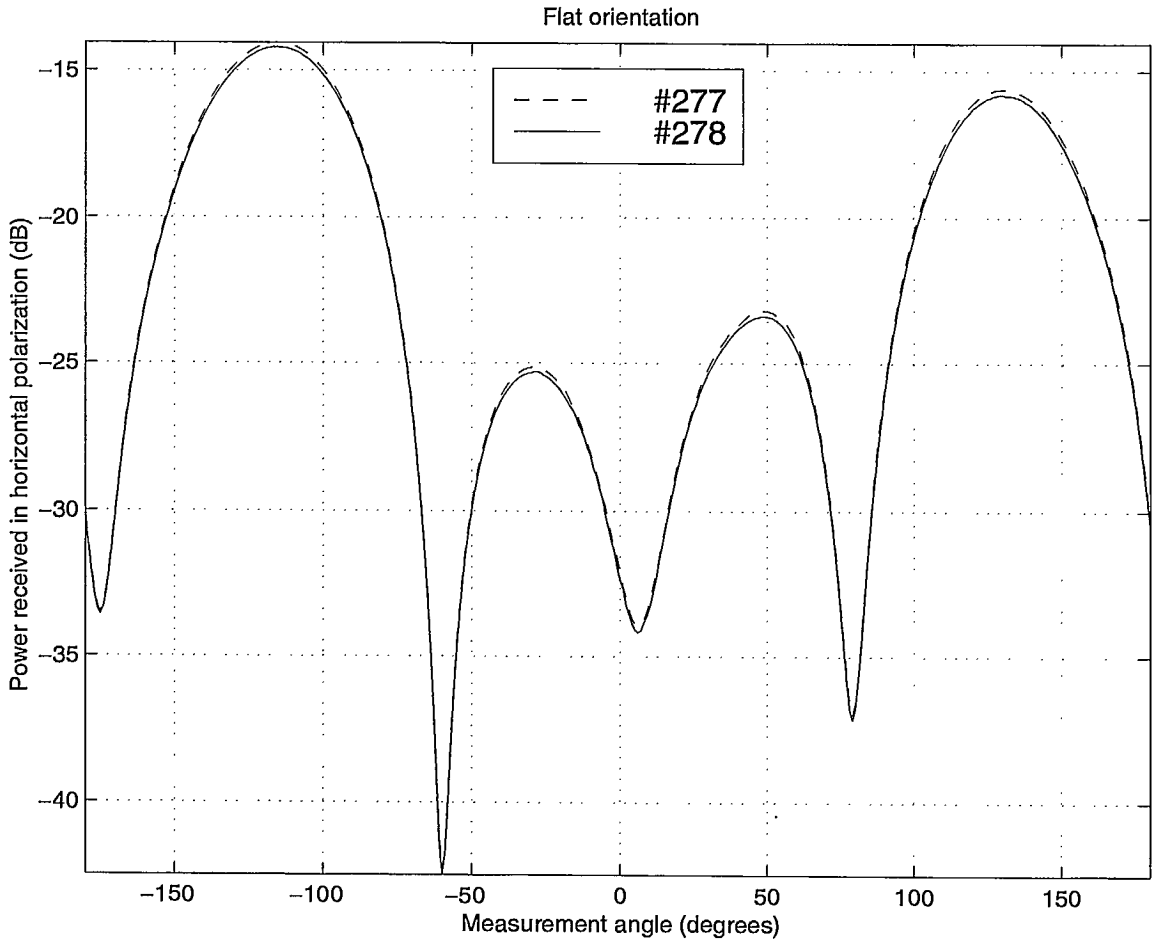

Figure 3.3: The horizontal polarization for the Flat ($\phi = 0^o$) orientation in the first test.

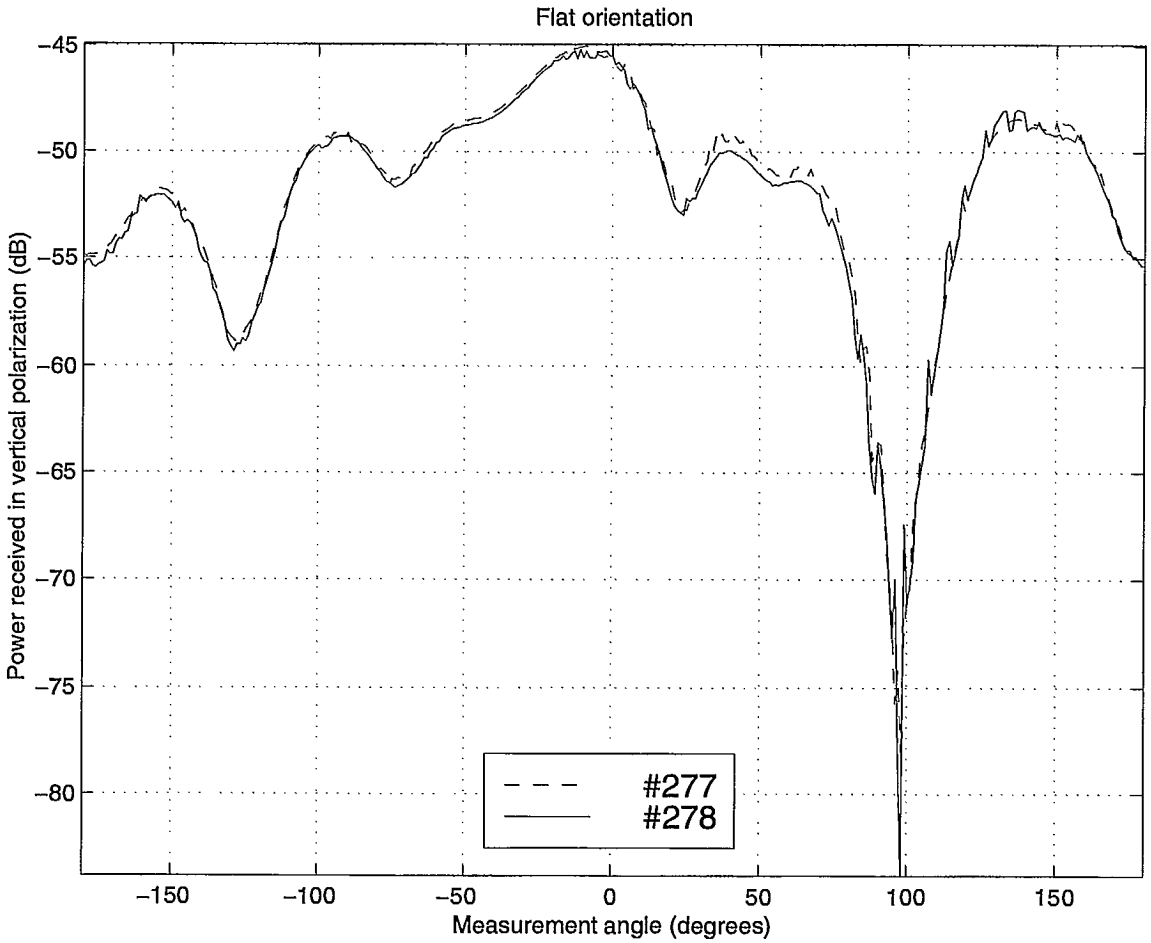

Figure 3.4: The vertical polarization for the Flat ($\phi = 0^o$) orientation in the first test.

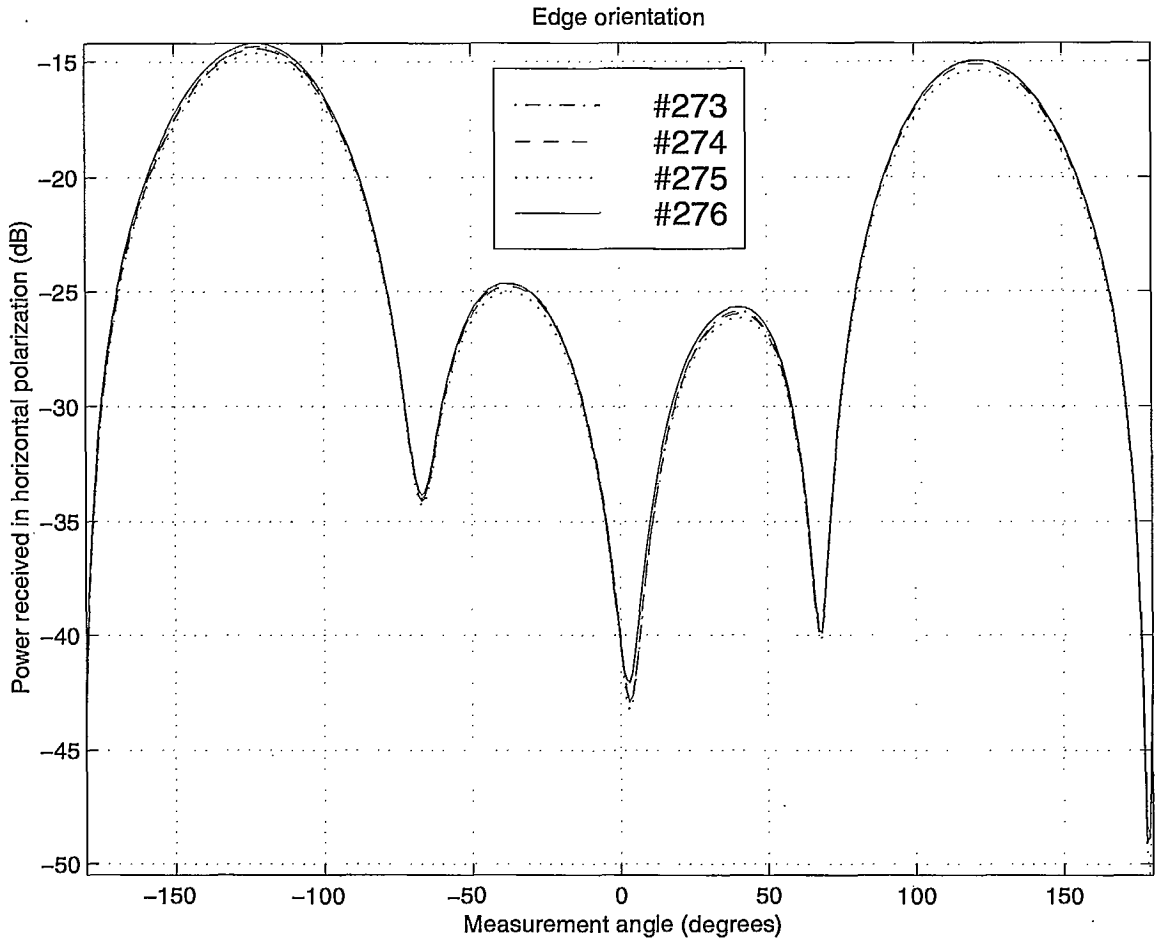

Figure 3.5: The horizontal polarization for the Edge ($\phi = 90^o$) orientation in the first test.

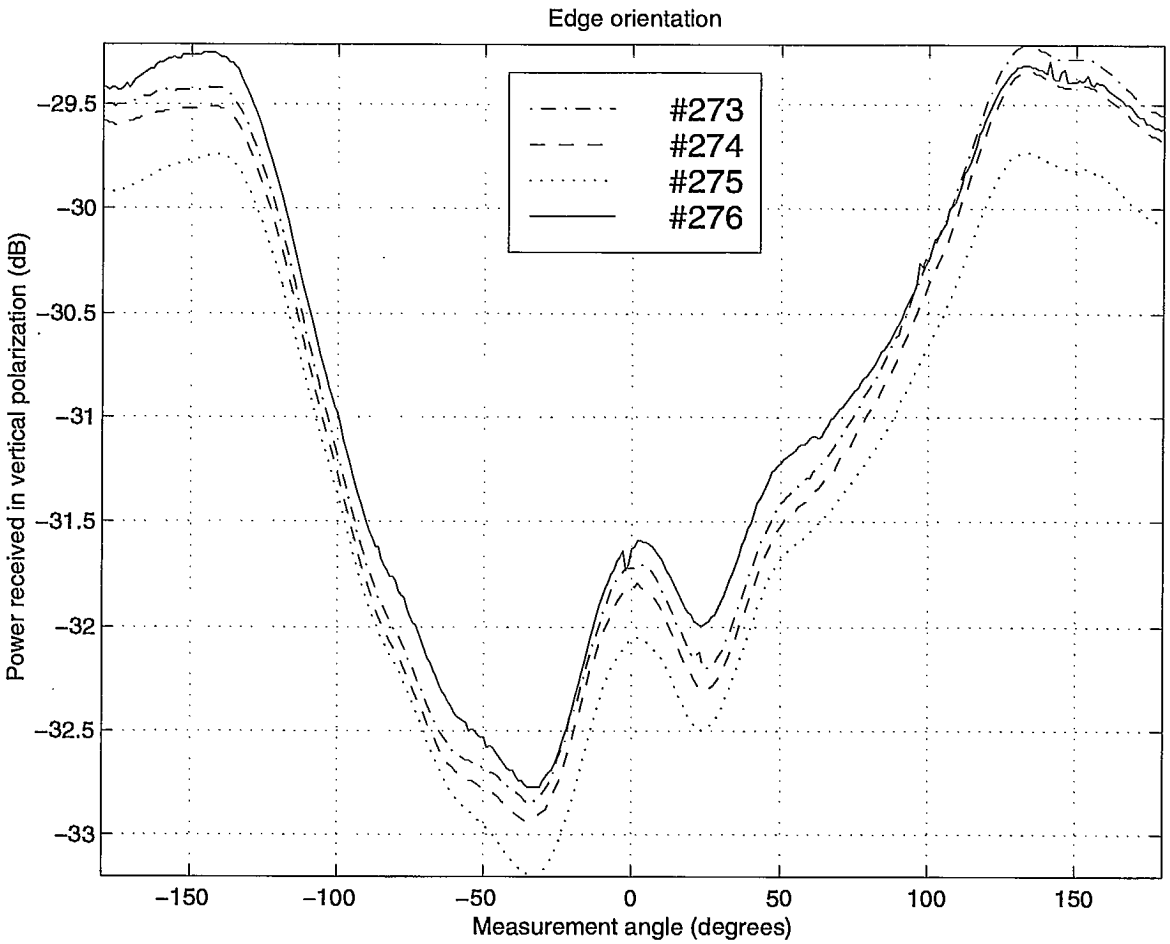

Figure 3.6: The vertical polarization for the Edge ($\phi = 90°$) orientation in the first test.

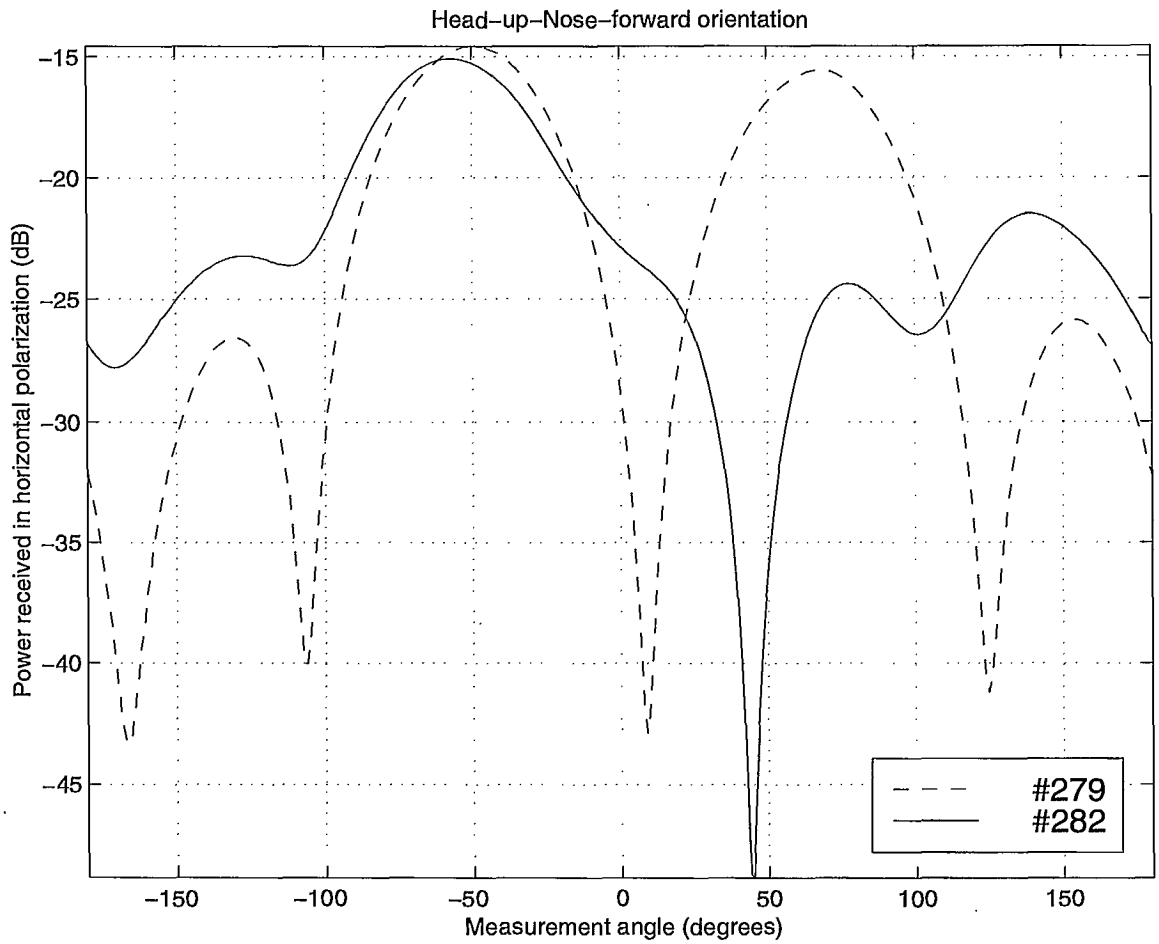

Figure 3.7: The horizontal polarization for the Head-up-Nose-forward orientation in the second and third tests.

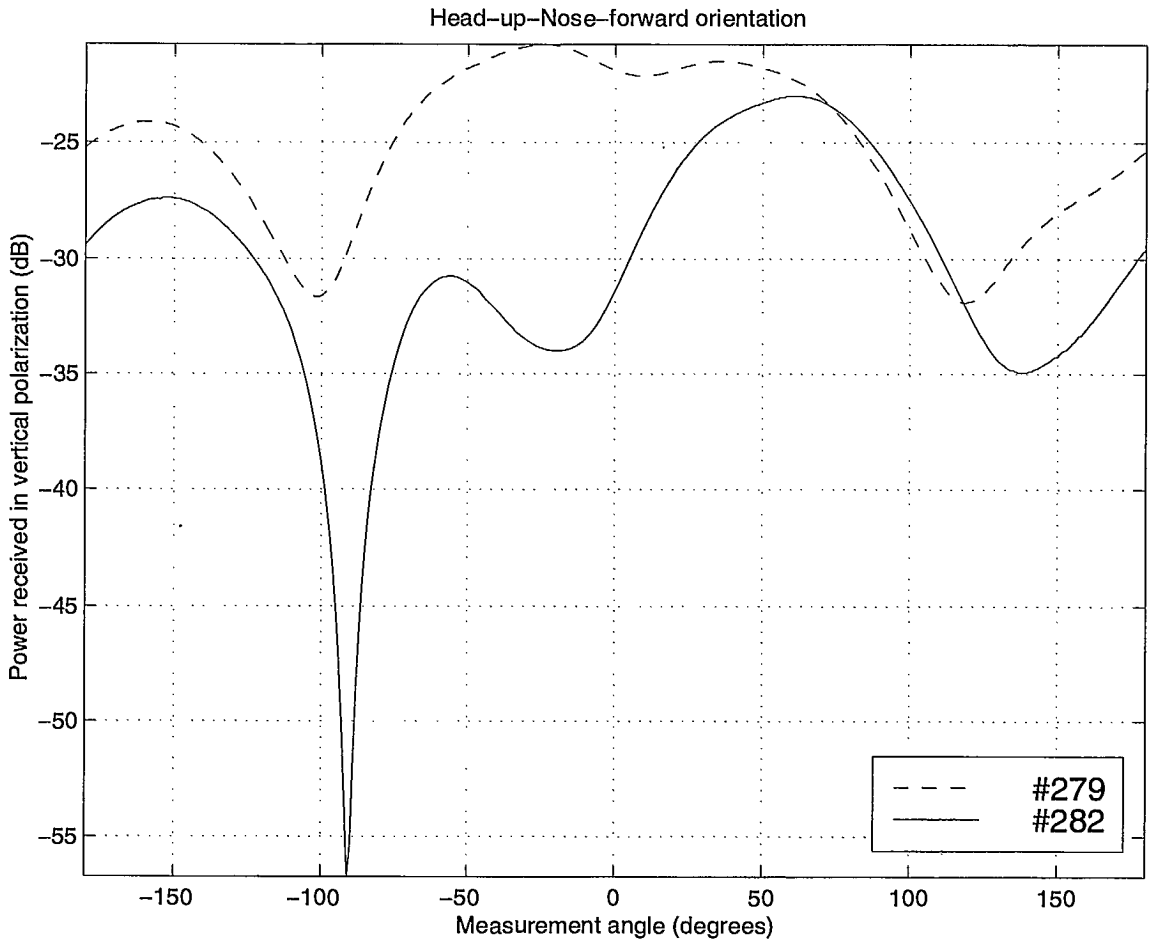

Figure 3.8: The vertical polarization for the Head-up-Nose-forward orientation in the second and third tests.

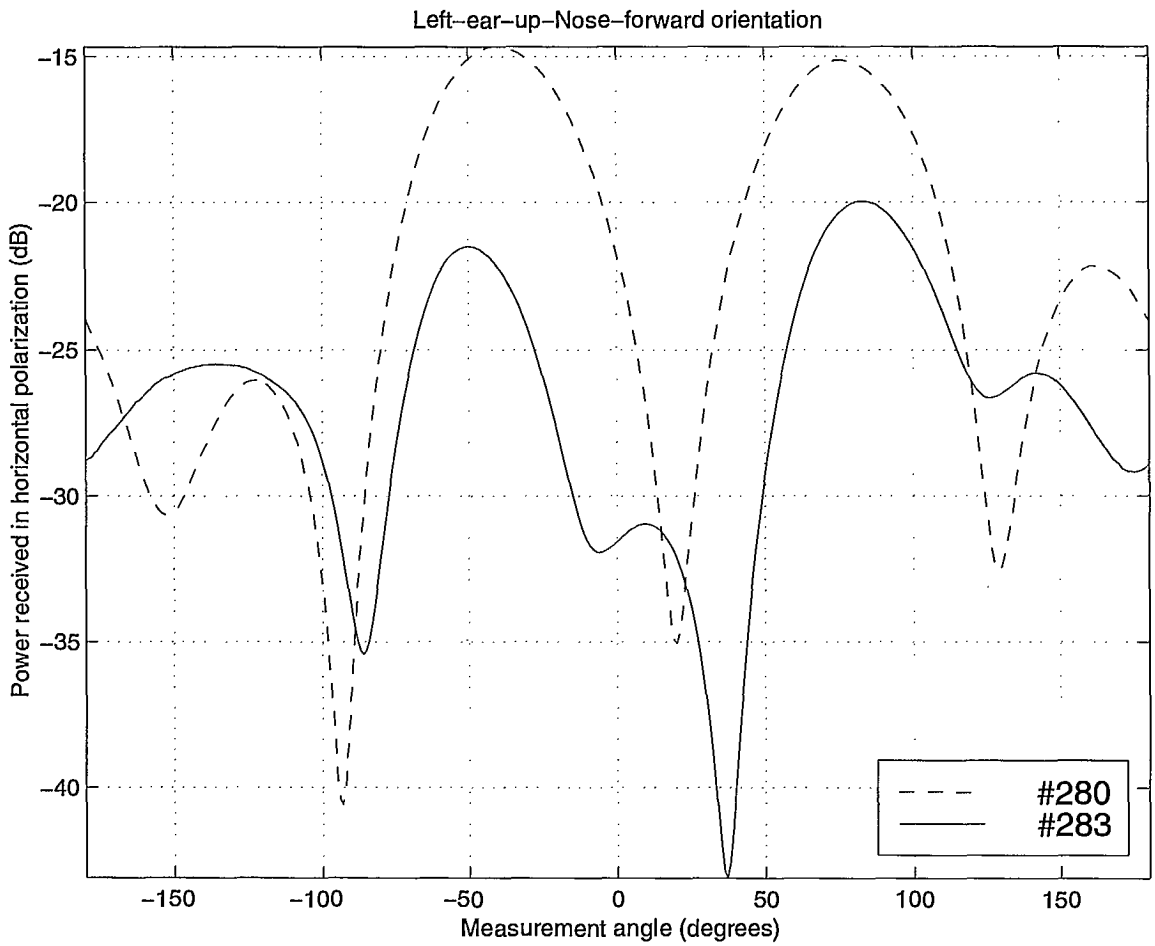

Figure 3.9: The horizontal polarization for the Left-ear-up-Nose-forward orientation in the second and third tests.

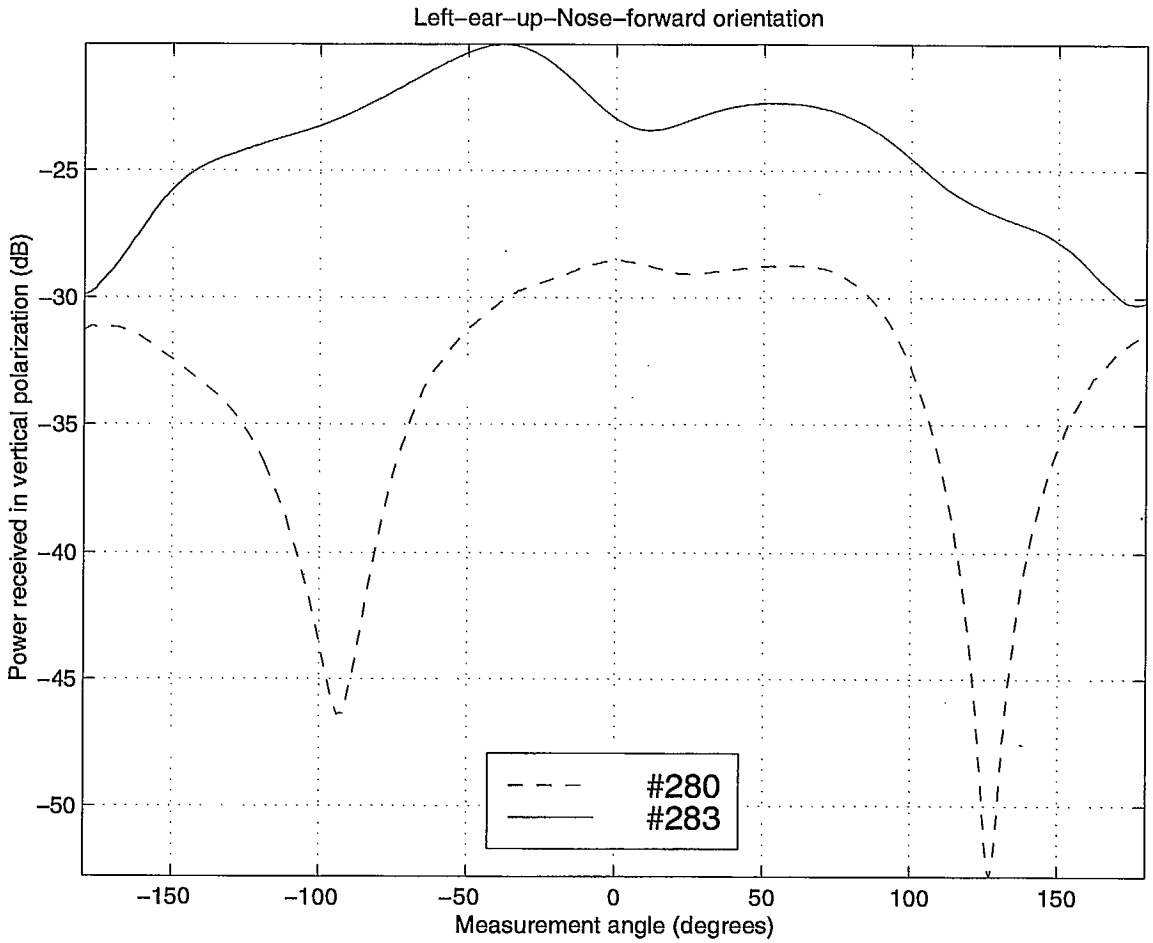

Figure 3.10: The vertical polarization for the Left-ear-up-Nose-forward orientation in the second and third tests.

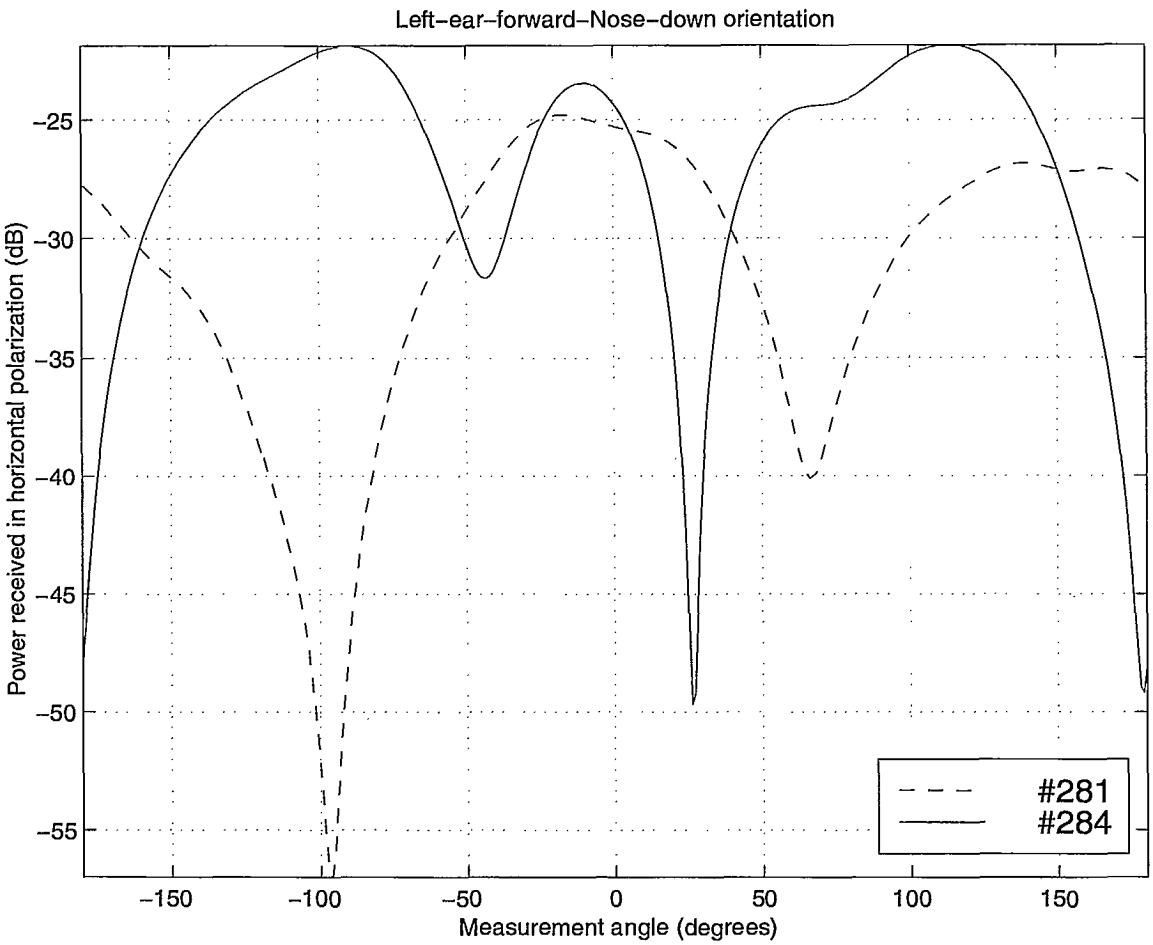

Figure 3.11: The horizontal polarization for the Left-ear-forward-Nose-down orientation in the second and third tests.

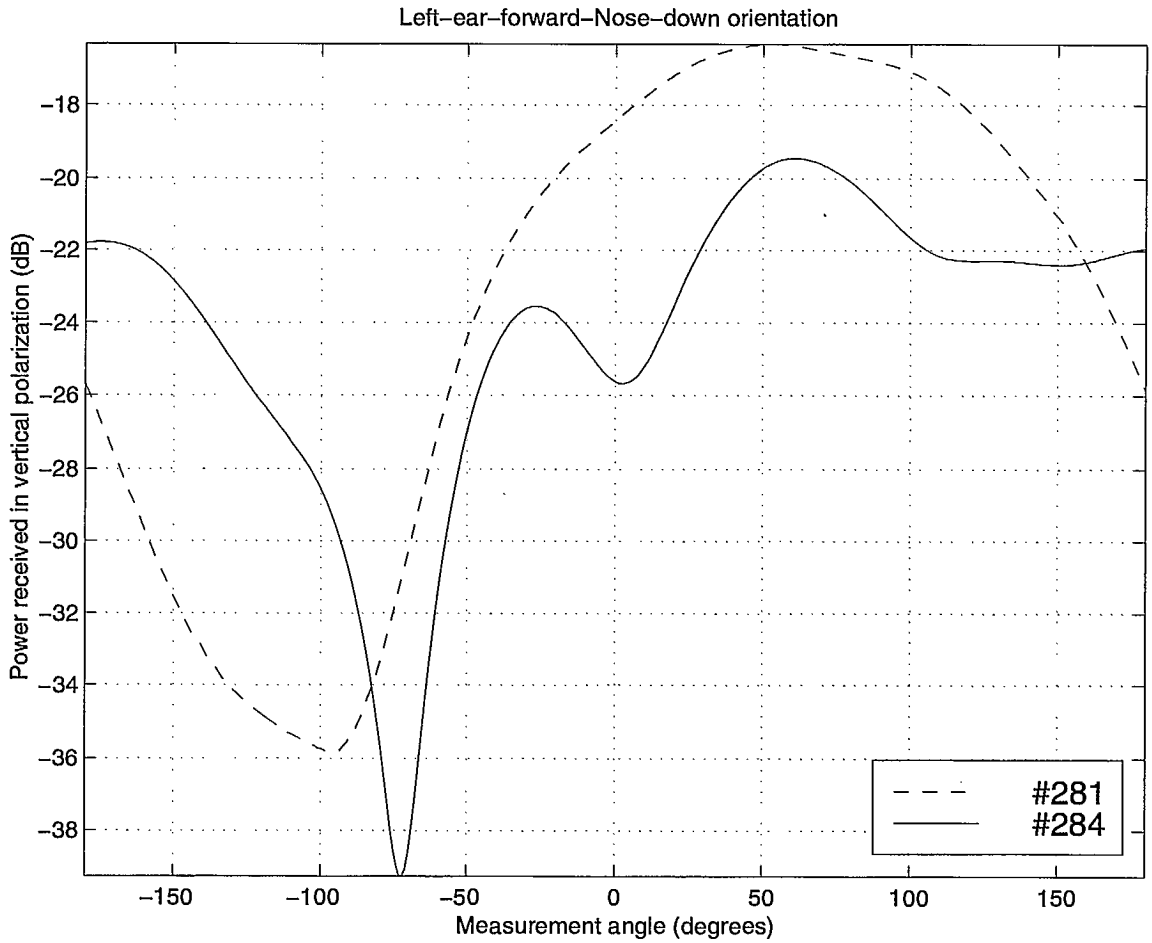

Figure 3.12: The vertical polarization for the Left-ear-forward-Nose-down orientation in the second and third tests.

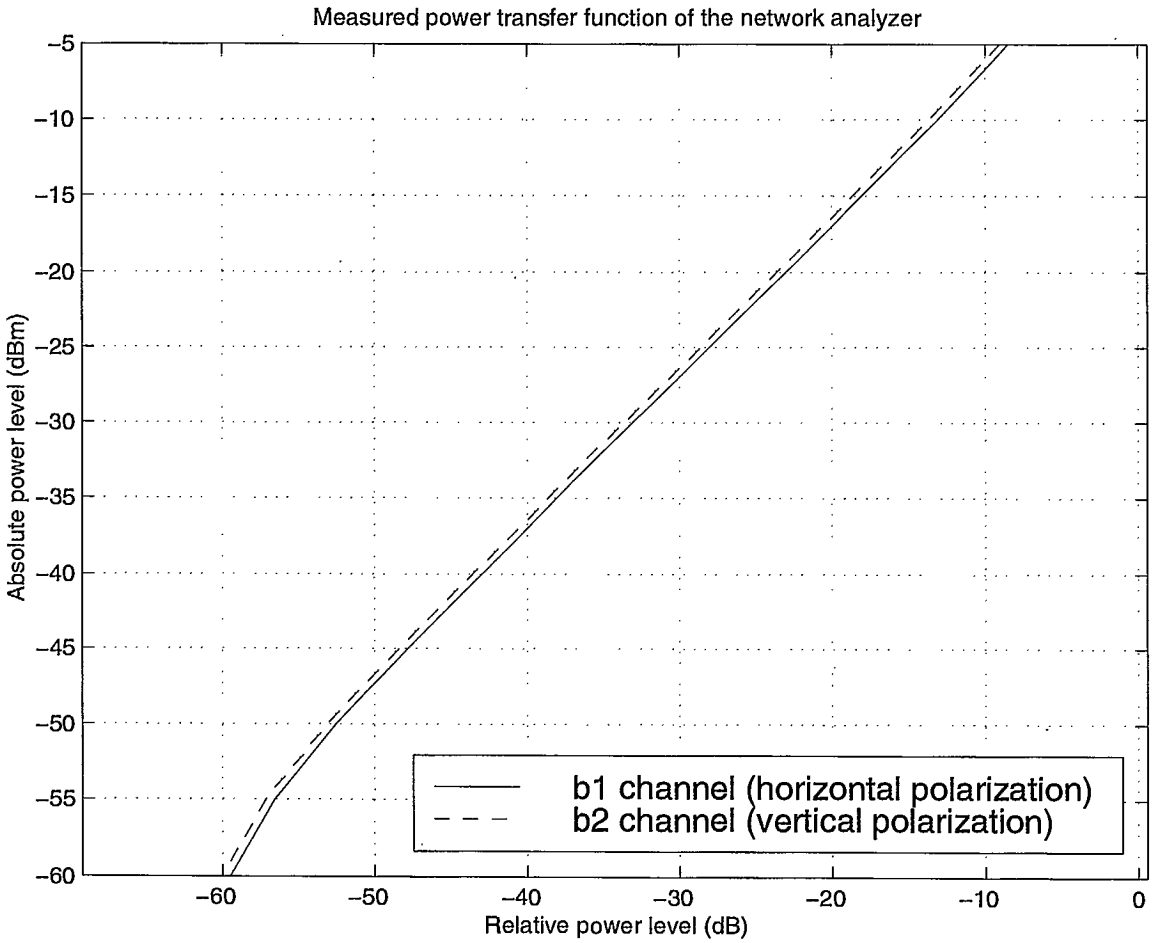

Figure 3.13: The measured power transfer function for the network analyzer.

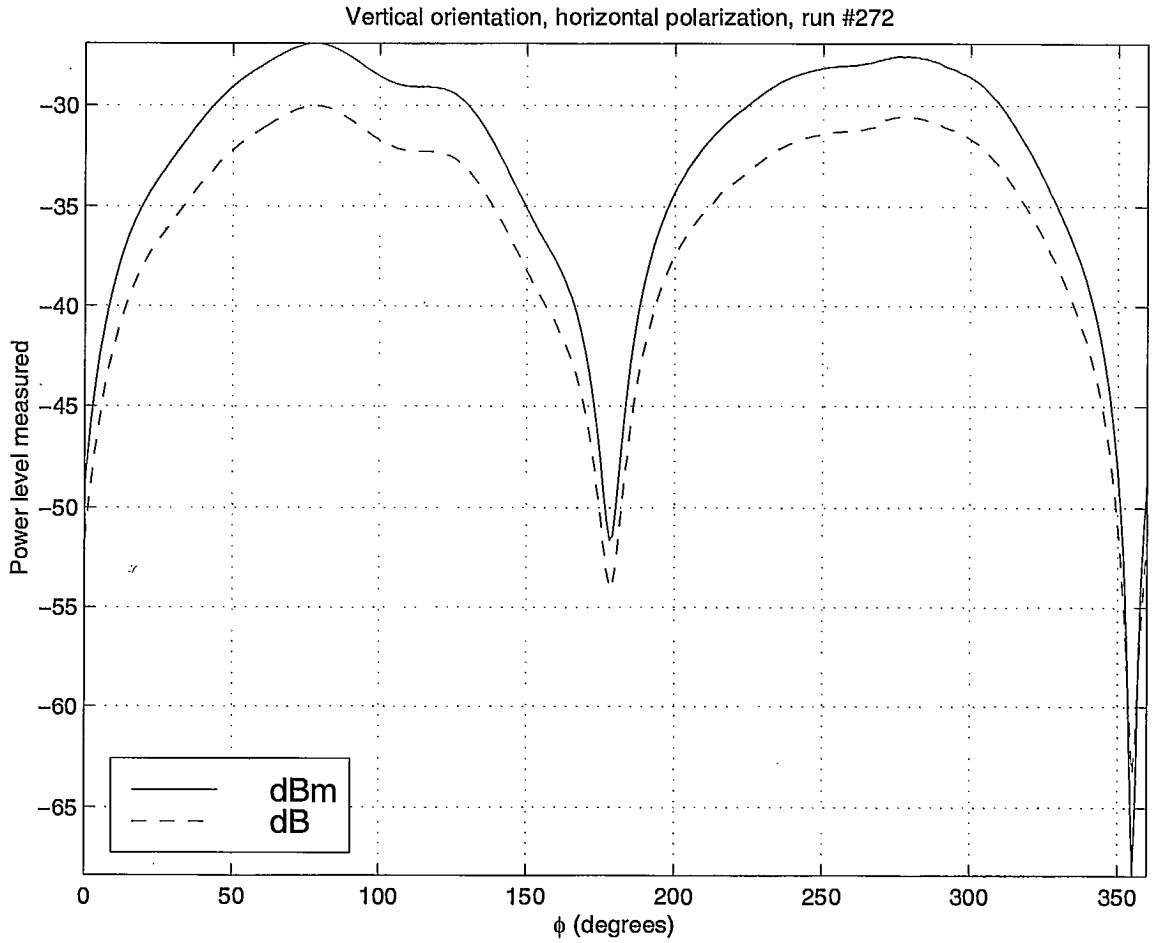

Figure 3.14: The horizontal polarization for the Vertical ($\theta = 90°$) orientation in the first test displayed with respect to the appropriate spherical coordinate rather than the measurement angle. Power correction with respect to both the battery discharge and the power transfer function of the network analyzer was applied for the curve in dBm unit.

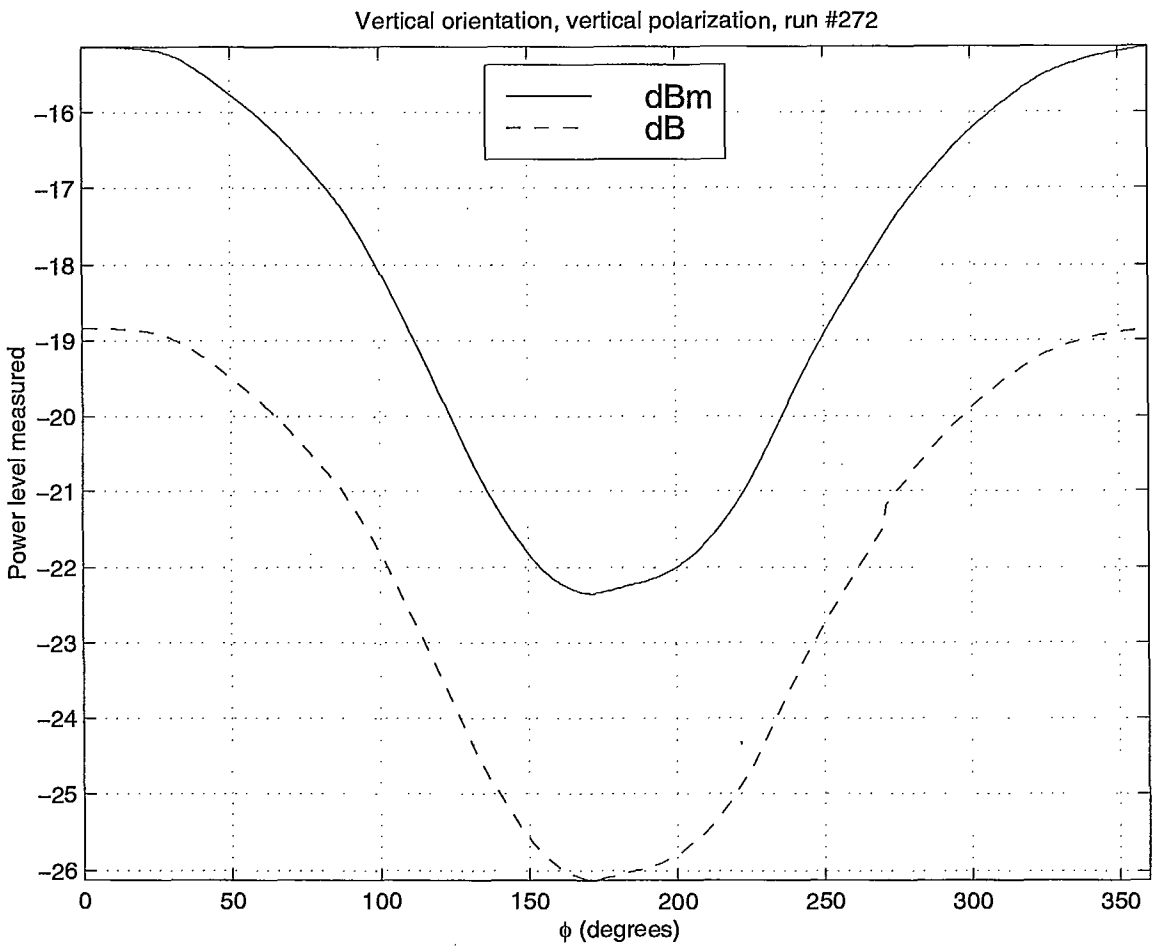

Figure 3.15: The vertical polarization for the Vertical ($\theta = 90°$) orientation in the first test displayed with respect to the appropriate spherical coordinate rather than the measurement angle. Power correction with respect to both the battery discharge and the power transfer function of the network analyzer was applied for the curve in dBm unit.

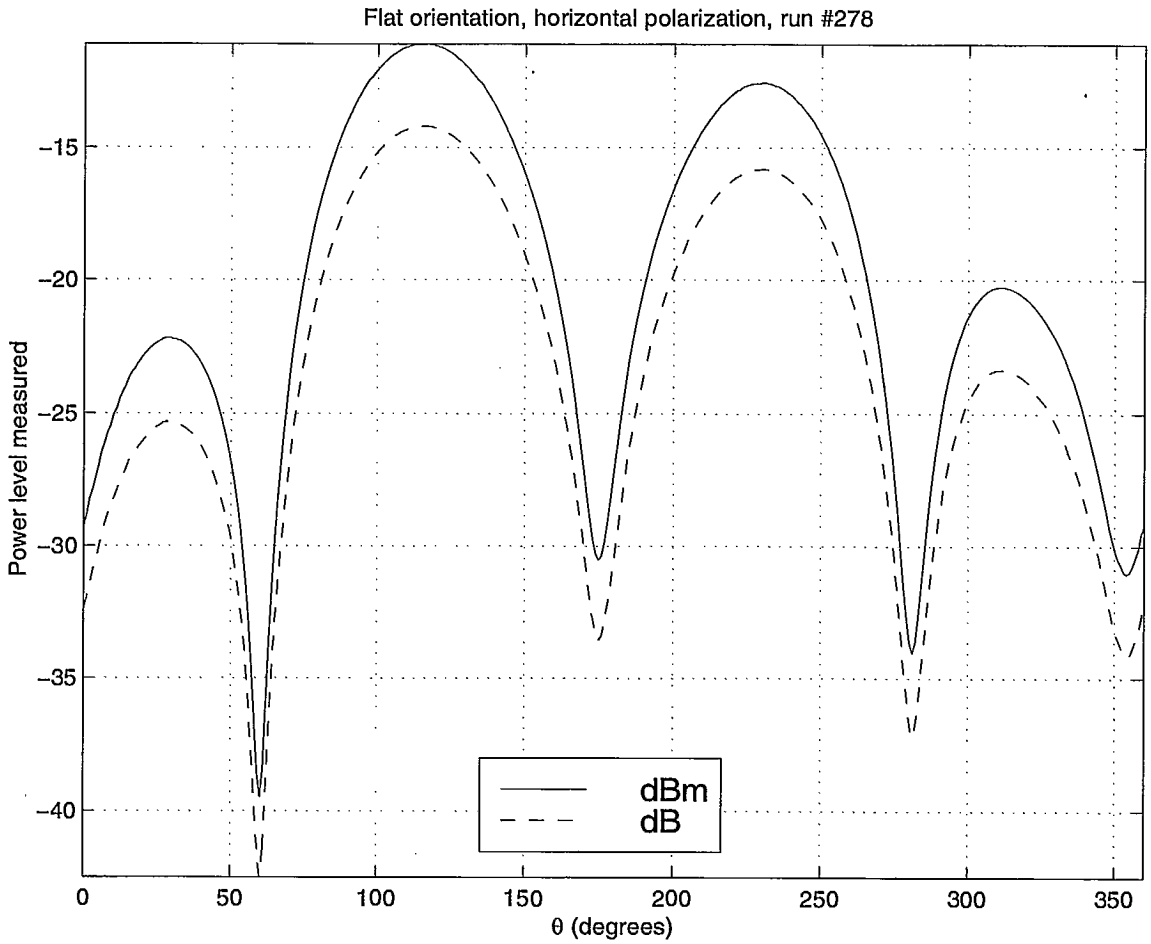

Figure 3.16: The horizontal polarization for the Flat ($\phi = 0°$) orientation in the first test displayed with respect to the appropriate spherical coordinate rather than the measurement angle. Power correction with respect to both the battery discharge and the power transfer function of the network analyzer was applied for the curve in dBm unit.

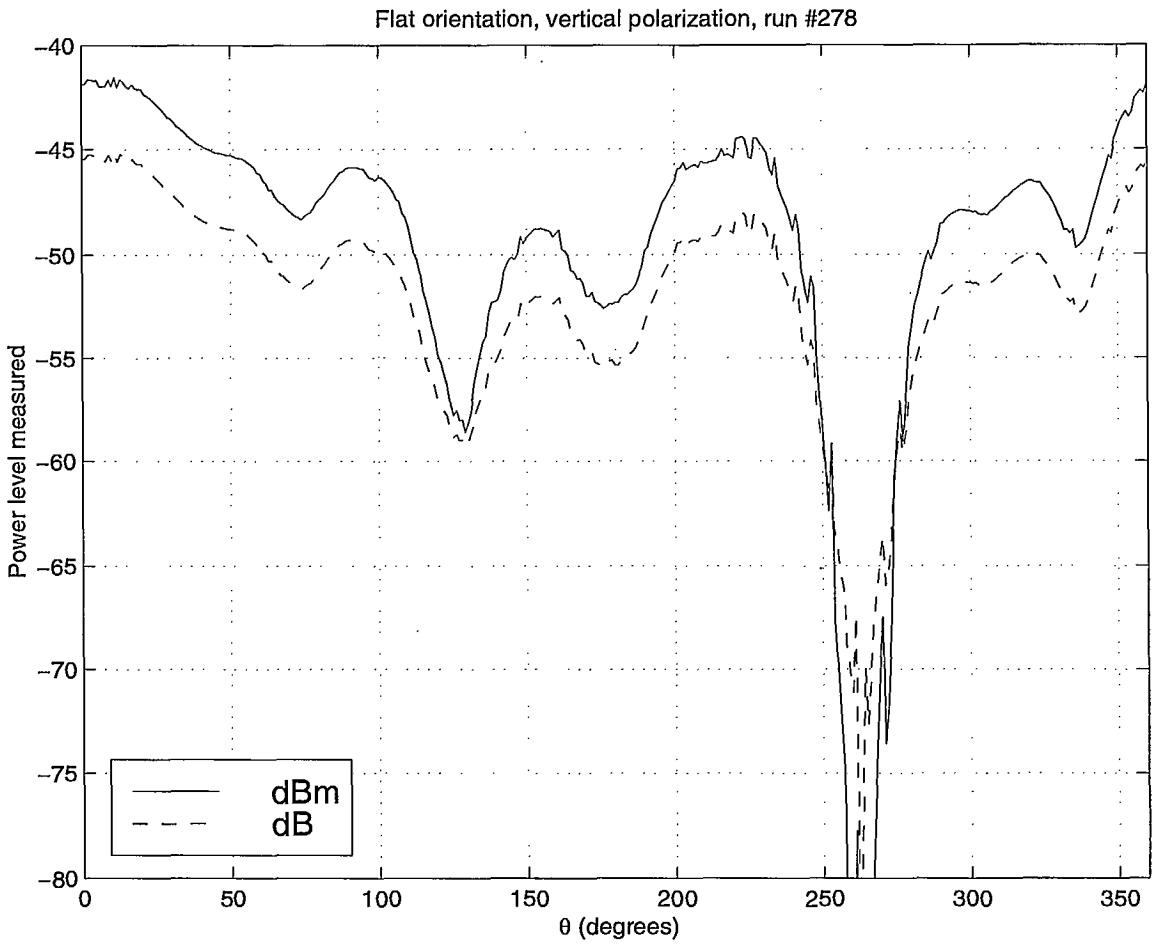

Figure 3.17: The vertical polarization for the Flat ($\phi = 0^o$) orientation in the first test displayed with respect to the appropriate spherical coordinate rather than the measurement angle. Power correction with respect to both the battery discharge and the power transfer function of the network analyzer was applied for the curve in dBm unit.

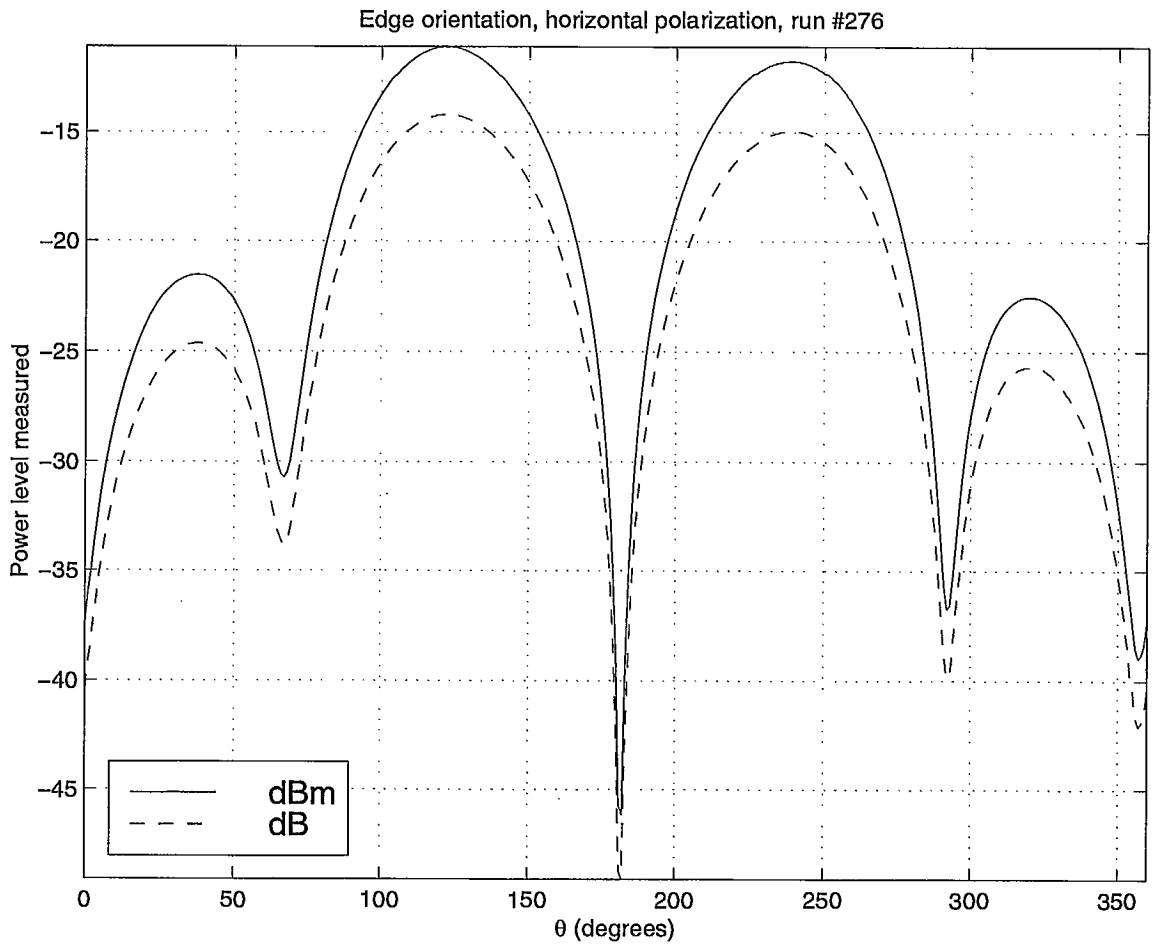

Figure 3.18: The horizontal polarization for the Edge ($\phi = 90^o$) orientation in the first test displayed with respect to the appropriate spherical coordinate rather than the measurement angle. Power correction with respect to both the battery discharge and the power transfer function of the network analyzer was applied for the curve in dBm unit.

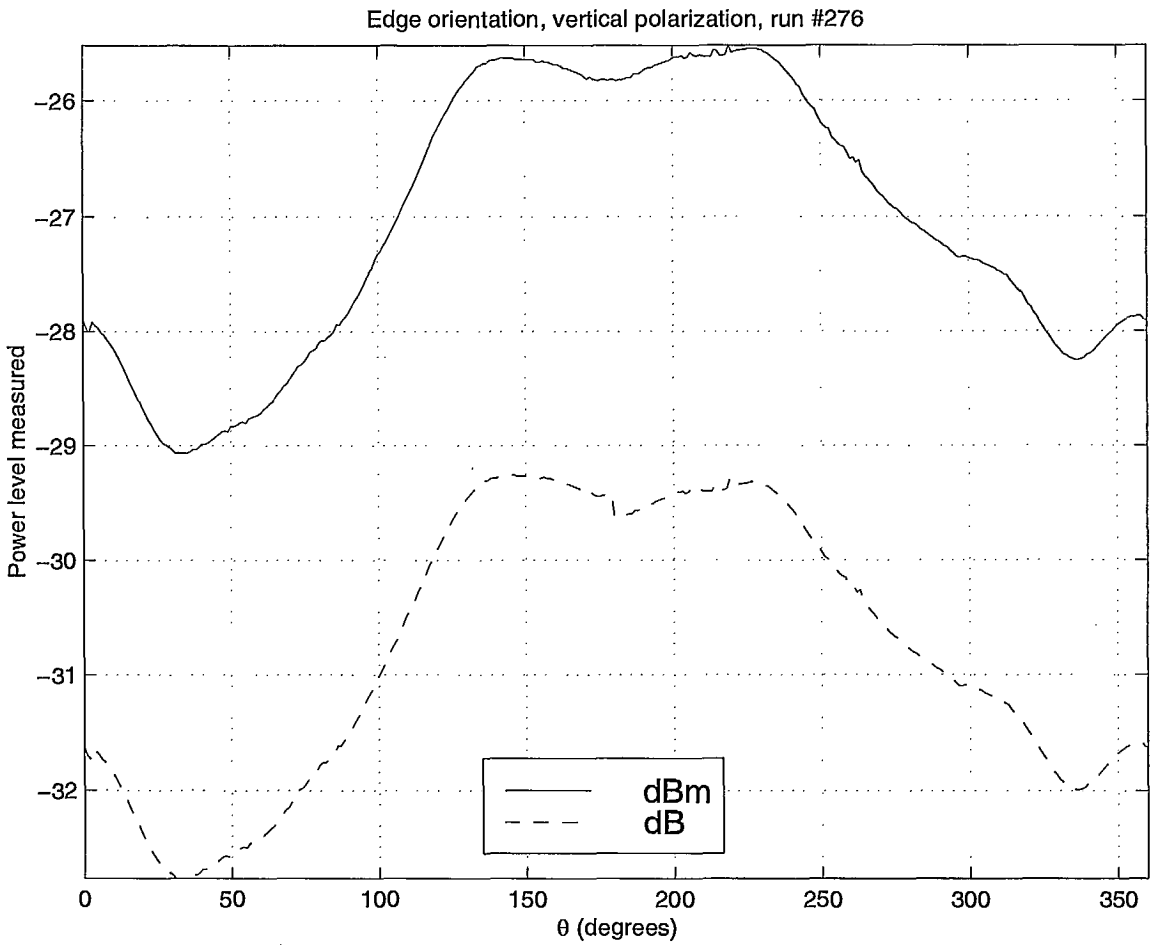

Figure 3.19: The vertical polarization for the Edge ($\phi = 90°$) orientation in the first test displayed with respect to the appropriate spherical coordinate rather than the measurement angle. Power correction with respect to both the battery discharge and the power transfer function of the network analyzer was applied for the curve in dBm unit.

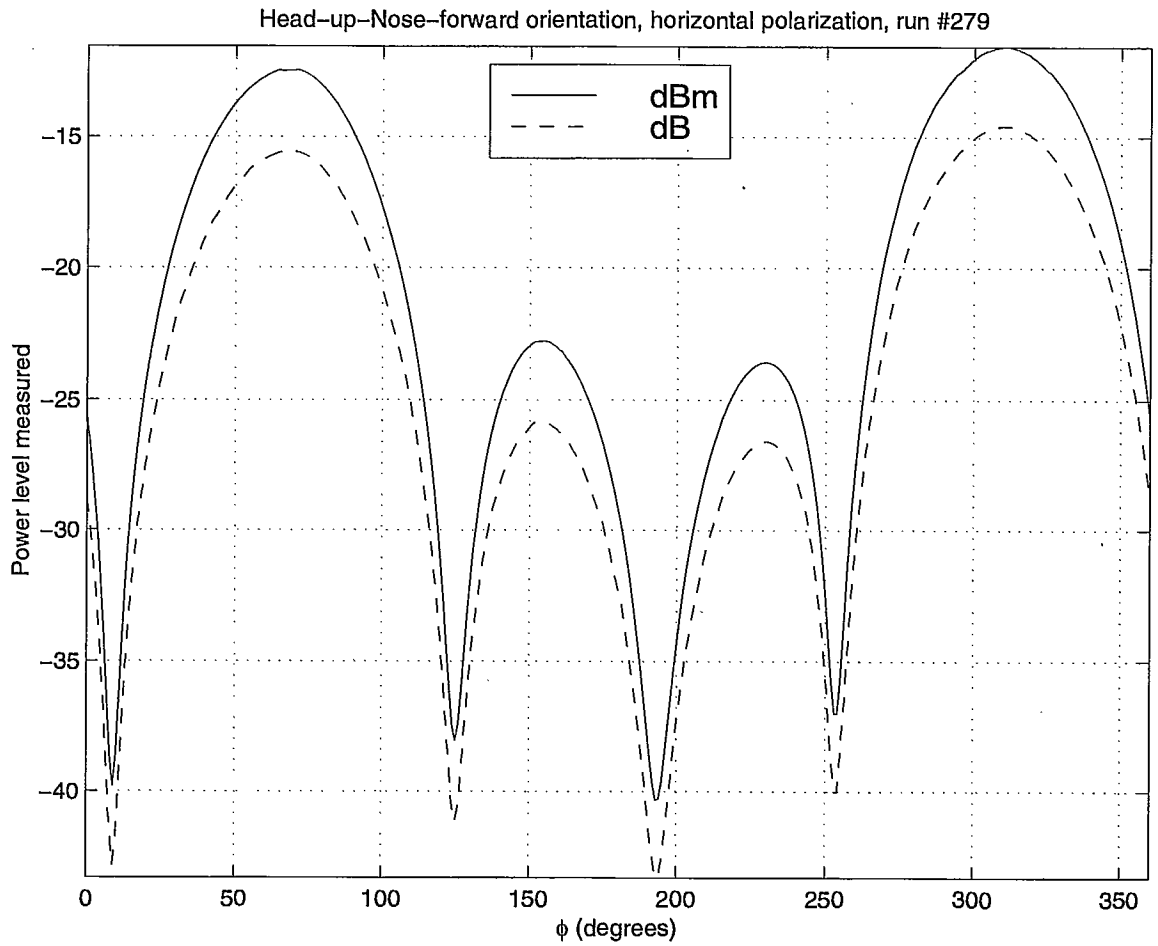

Figure 3.20: The horizontal polarization for the Head-up-Nose-forward orientation in the second test displayed with respect to the appropriate spherical coordinate rather than the measurement angle. Power correction with respect to both the battery discharge and the power transfer function of the network analyzer was applied for the curve in dBm unit.

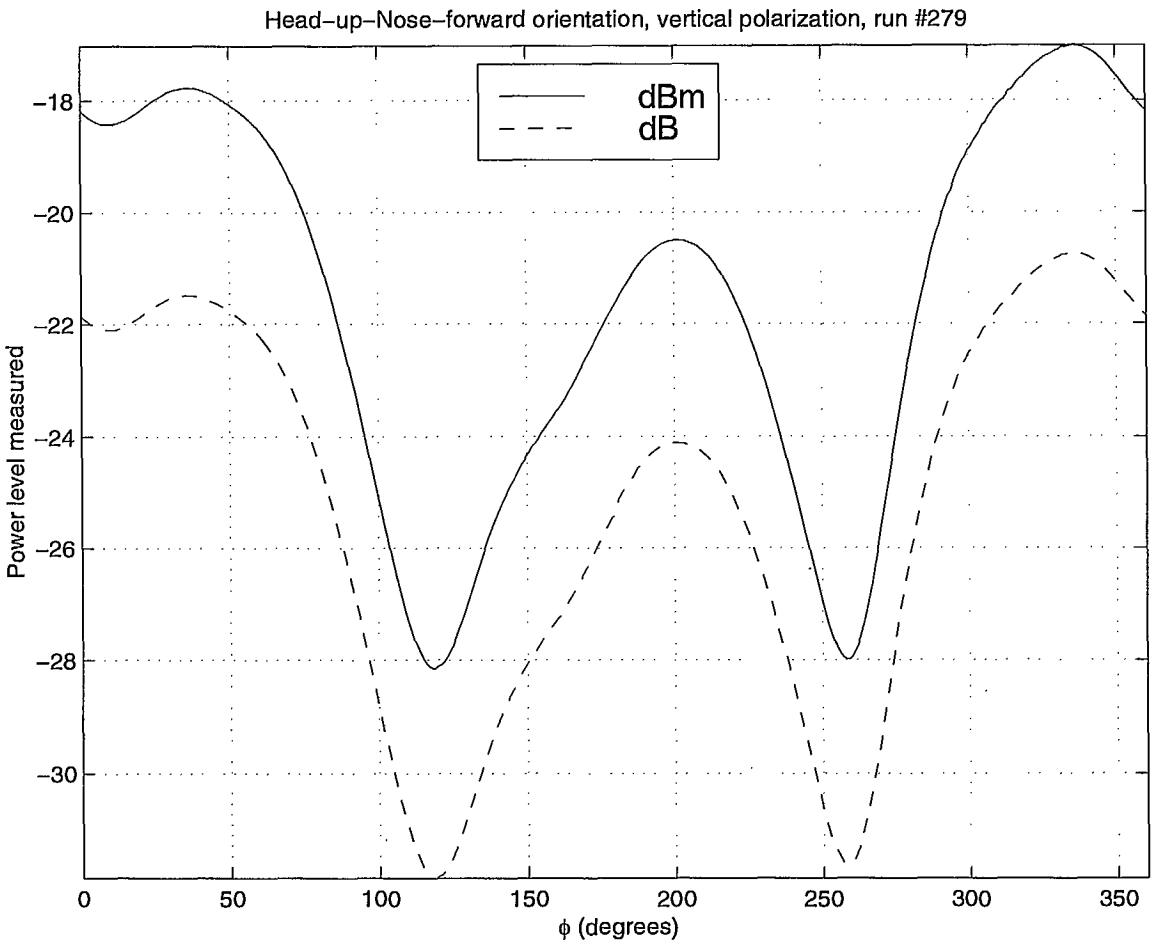

Figure 3.21: The vertical polarization for the Head-up-Nose-forward orientation in the second test displayed with respect to the appropriate spherical coordinate rather than the measurement angle. Power correction with respect to both the battery discharge and the power transfer function of the network analyzer was applied for the curve in dBm unit.

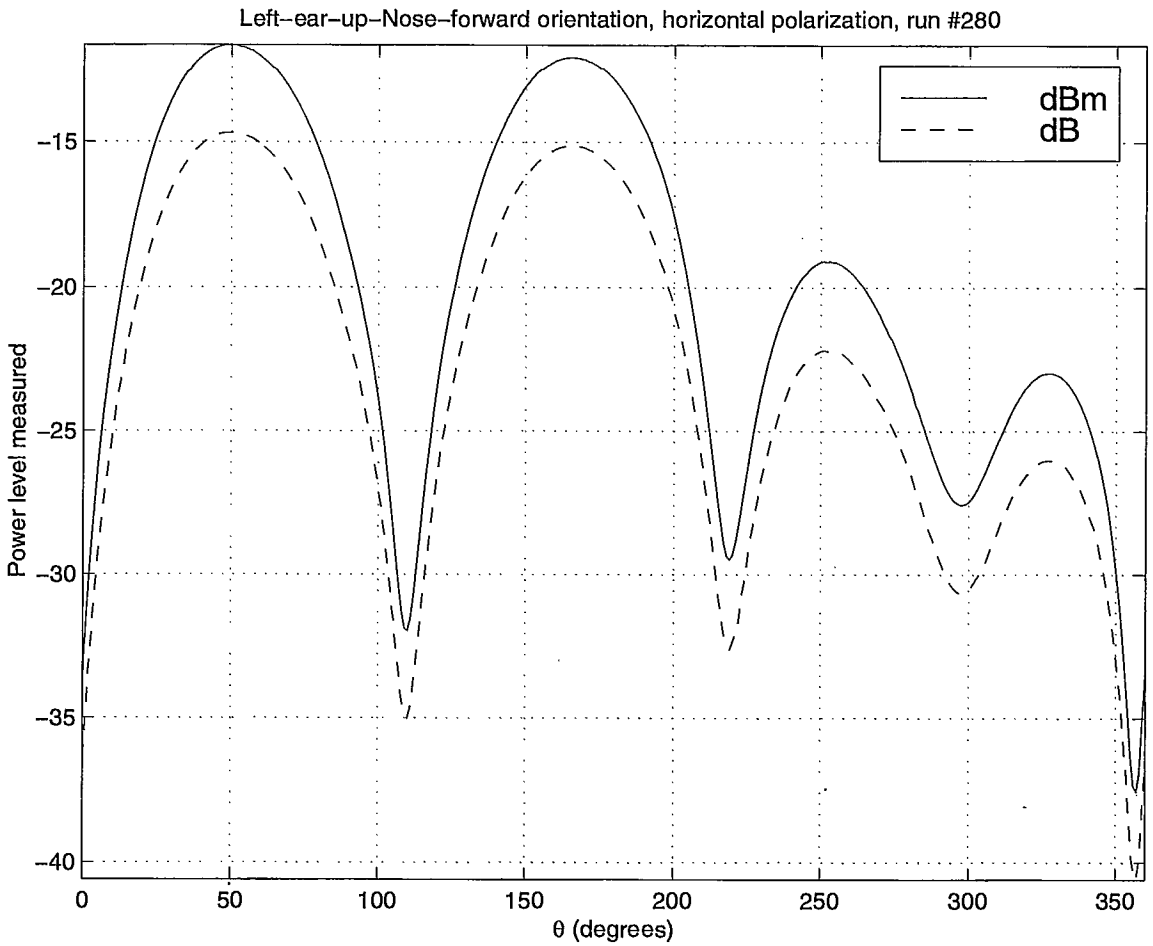

Figure 3.22: The horizontal polarization for the Left-ear-up-Nose-forward orientation in the second test displayed with respect to the appropriate spherical coordinate rather than the measurement angle. Power correction with respect to both the battery discharge and the power transfer function of the network analyzer was applied for the curve in dBm unit.

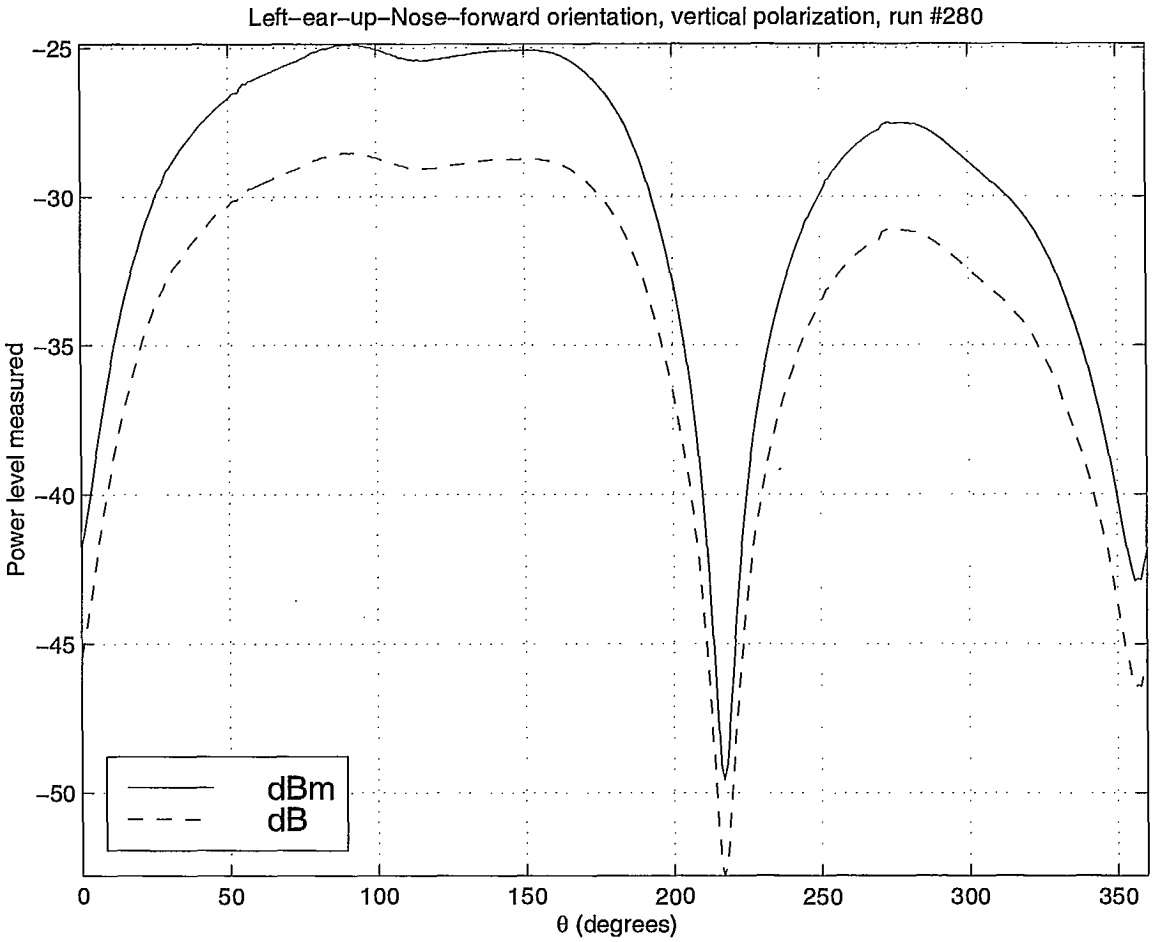

Figure 3.23: The vertical polarization for the Left-ear-up-Nose-forward orientation in the second test displayed with respect to the appropriate spherical coordinate rather than the measurement angle. Power correction with respect to both the battery discharge and the power transfer function of the network analyzer was applied for the curve in dBm unit.

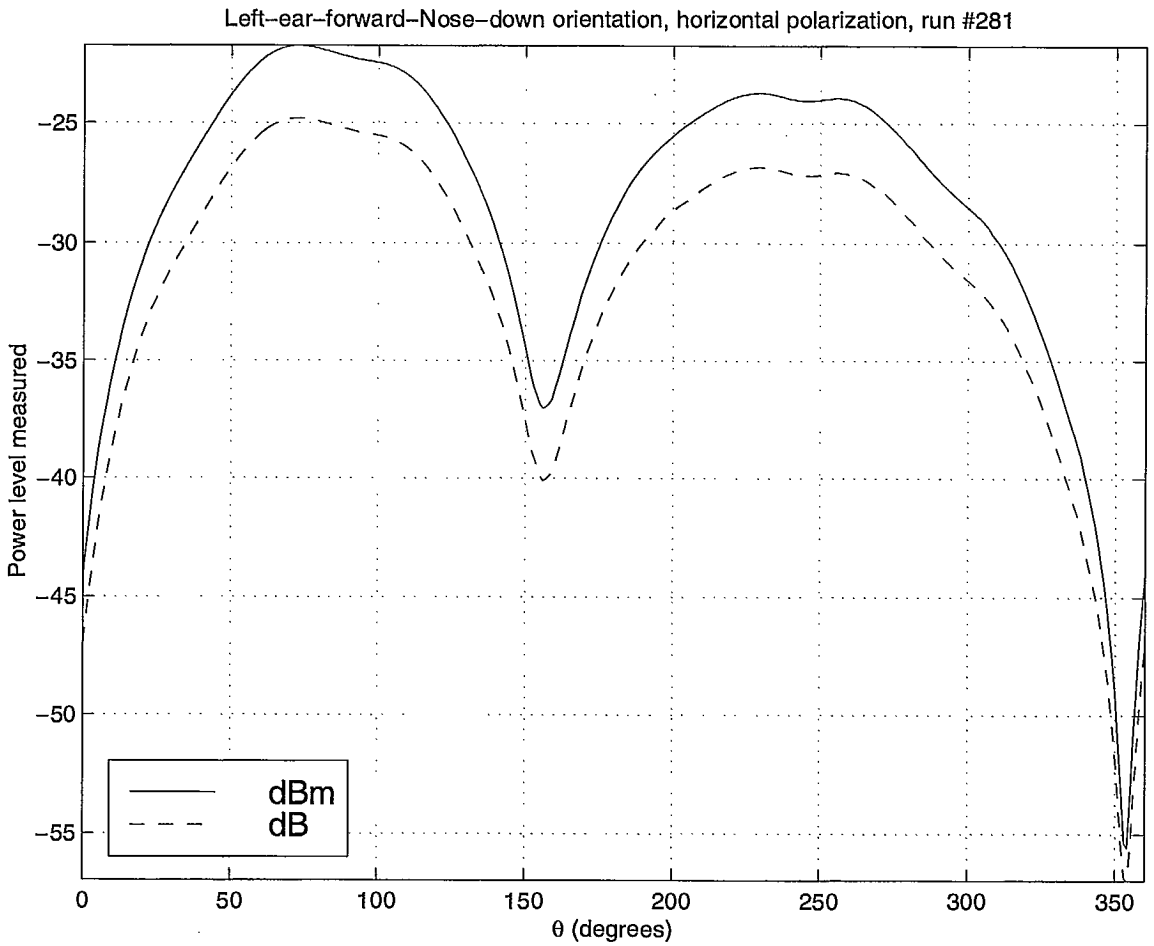

Figure 3.24: The horizontal polarization for the Left-ear-forward-Nose-down orientation in the second test displayed with respect to the appropriate spherical coordinate rather than the measurement angle. Power correction with respect to both the battery discharge and the power transfer function of the network analyzer was applied for the curve in dBm unit.

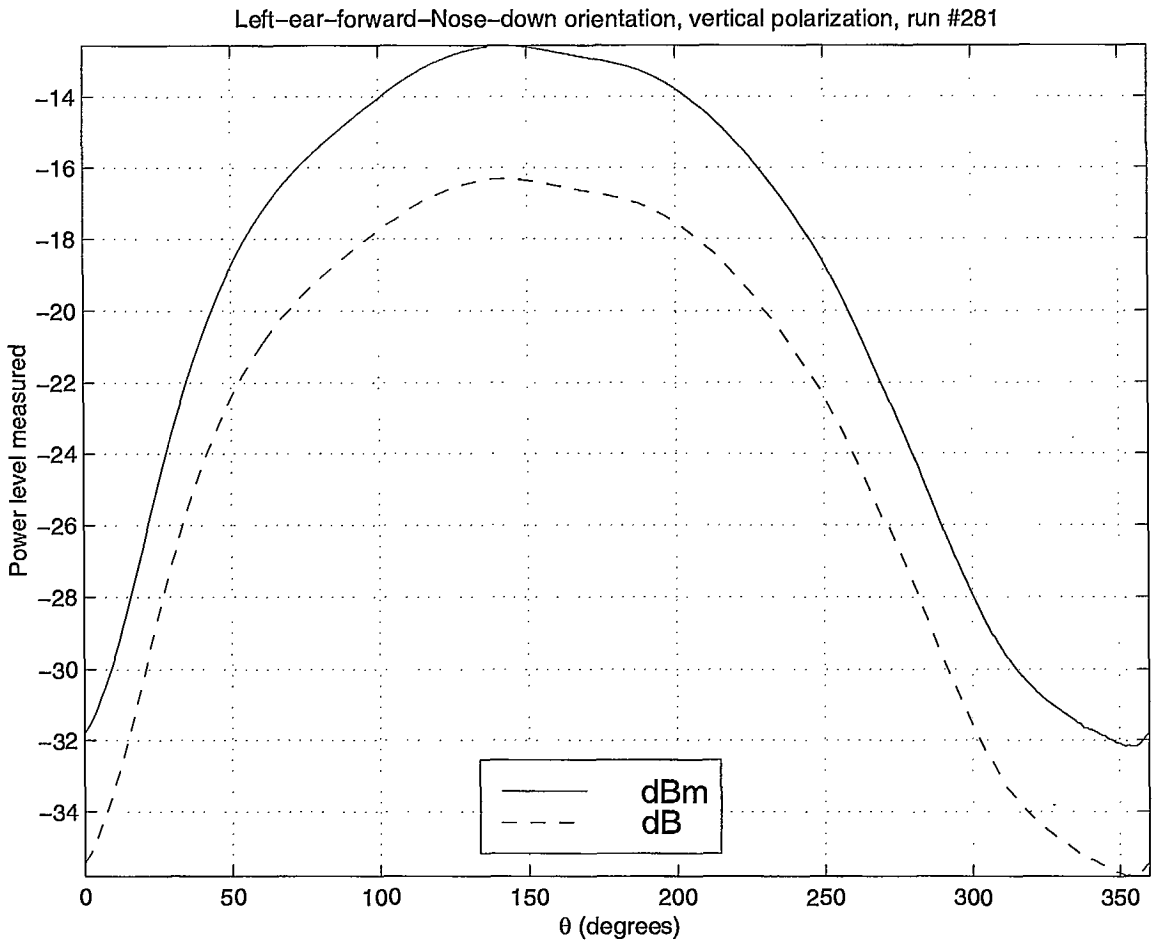

Figure 3.25: The vertical polarization for the Left-ear-forward-Nose-down orientation in the second test displayed with respect to the appropriate spherical coordinate rather than the measurement angle. Power correction with respect to both the battery discharge and the power transfer function of the network analyzer was applied for the curve in dBm unit.

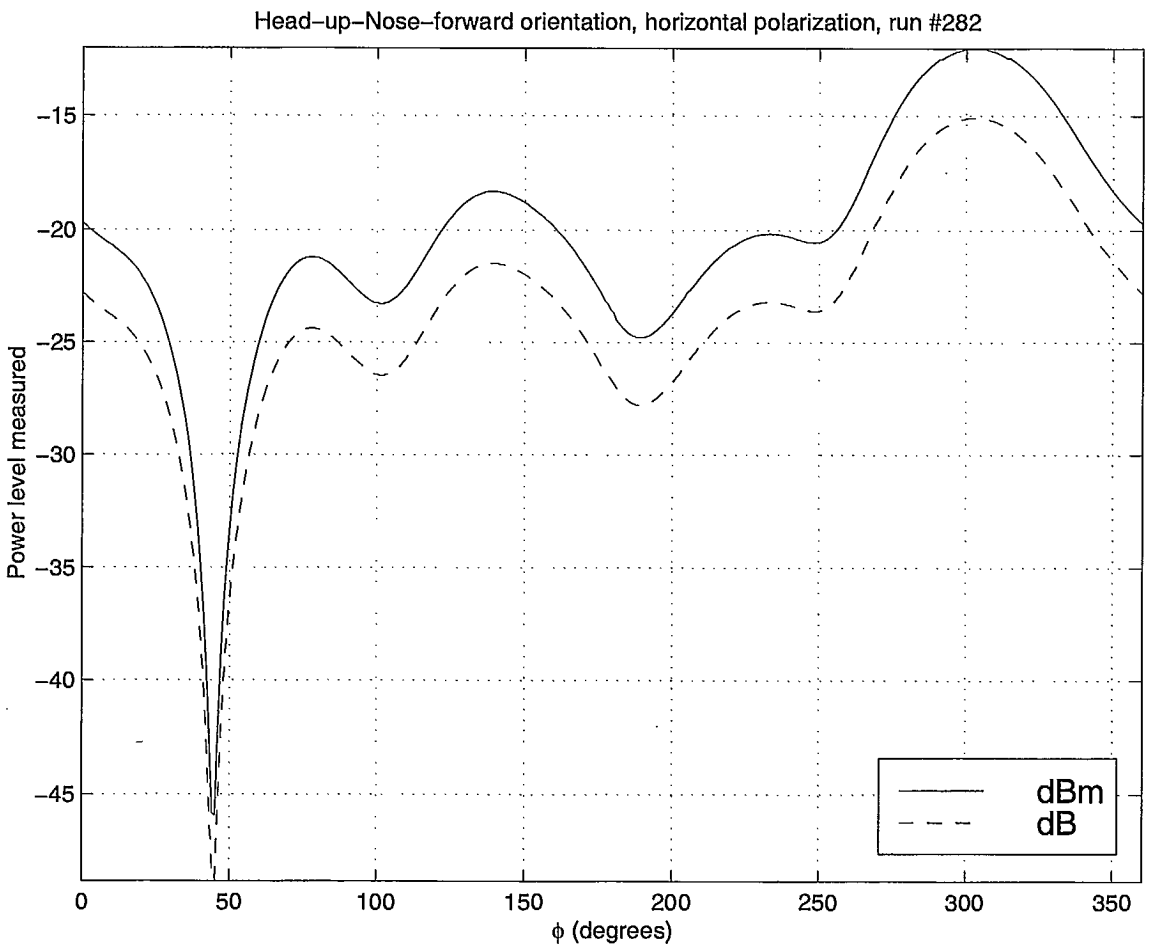

Figure 3.26: The horizontal polarization for the Head-up-Nose-forward orientation in the third test displayed with respect to the appropriate spherical coordinate rather than the measurement angle. Power correction with respect to both the battery discharge and the power transfer function of the network analyzer was applied for the curve in dBm unit.

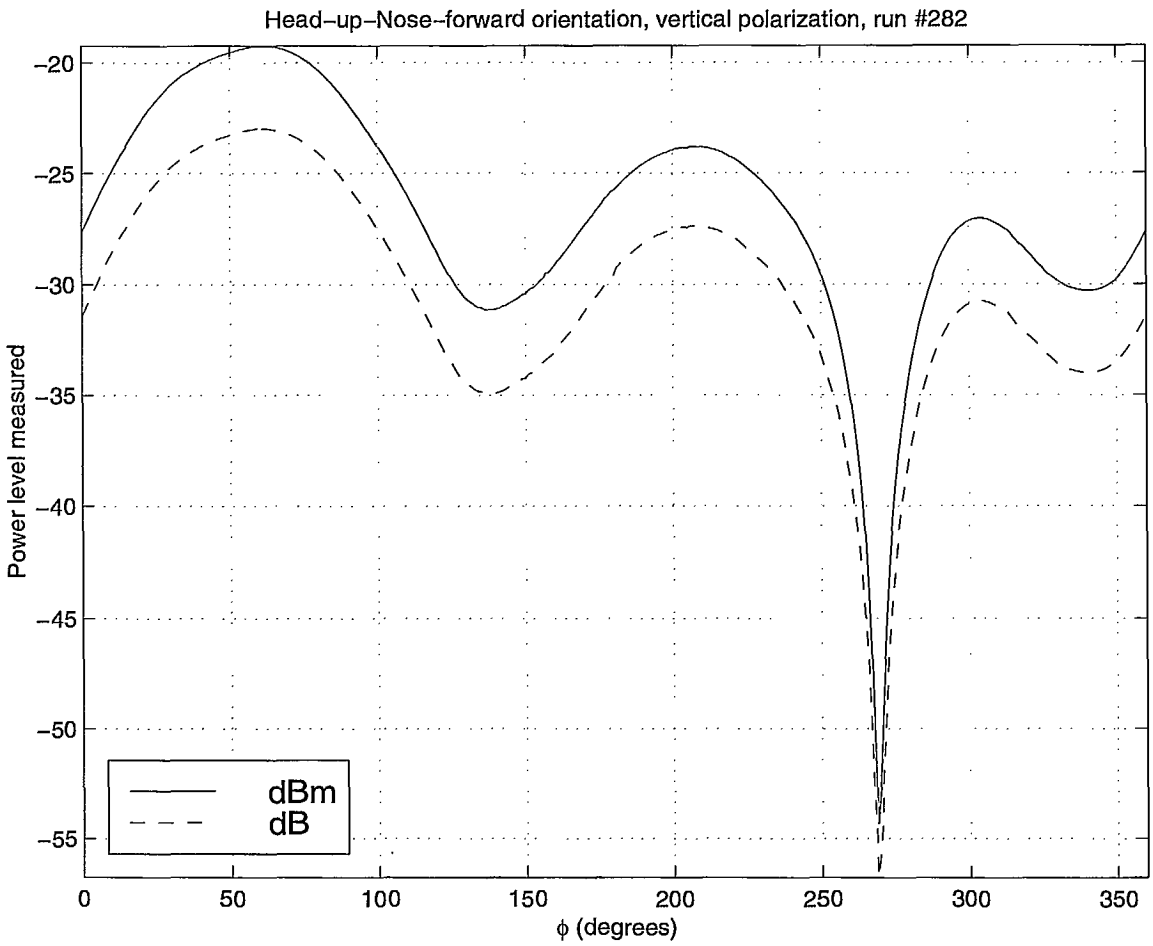

Figure 3.27: The vertical polarization for the Head-up-Nose-forward orientation in the third test displayed with respect to the appropriate spherical coordinate rather than the measurement angle. Power correction with respect to both the battery discharge and the power transfer function of the network analyzer was applied for the curve in dBm unit.

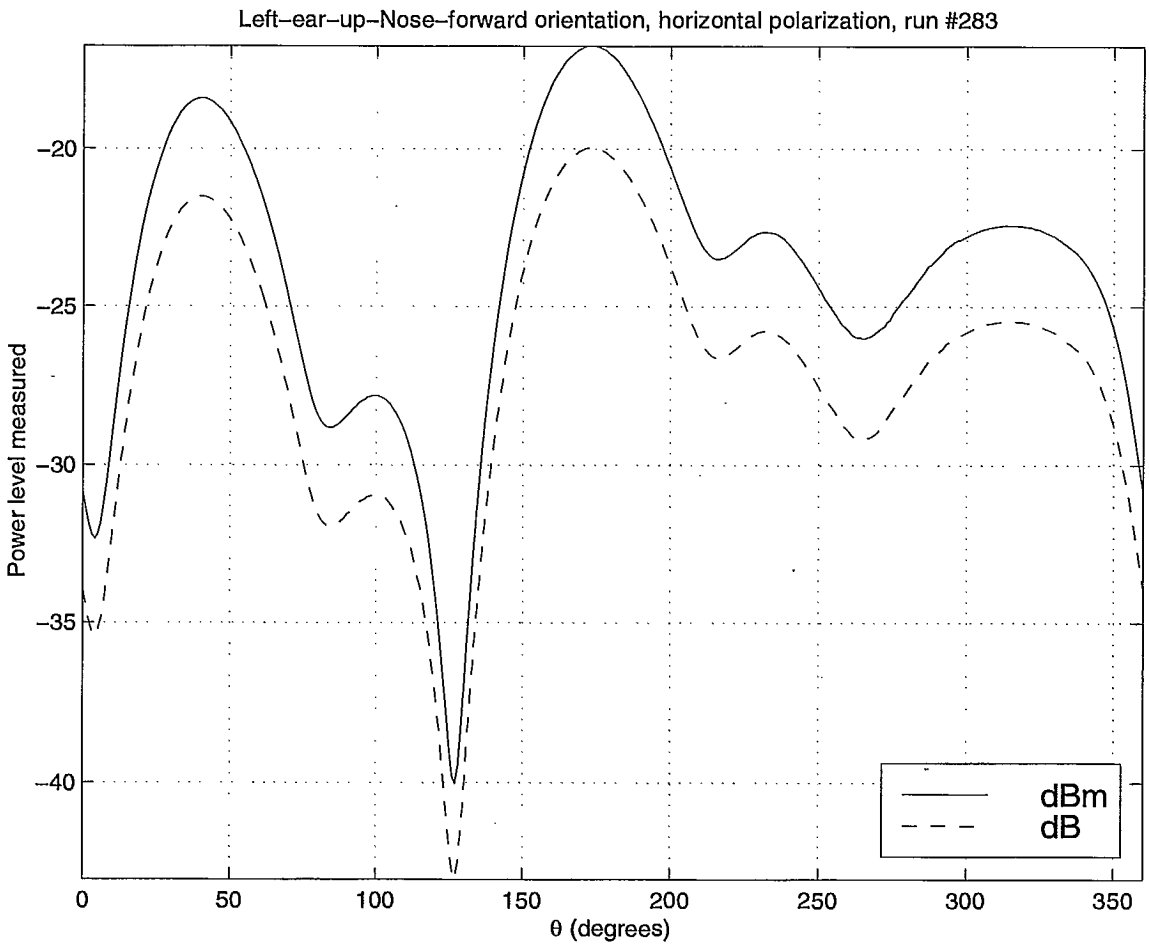

Figure 3.28: The horizontal polarization for the Left-ear-up-Nose-forward orientation in the third test displayed with respect to the appropriate spherical coordinate rather than the measurement angle. Power correction with respect to both the battery discharge and the power transfer function of the network analyzer was applied for the curve in dBm unit.

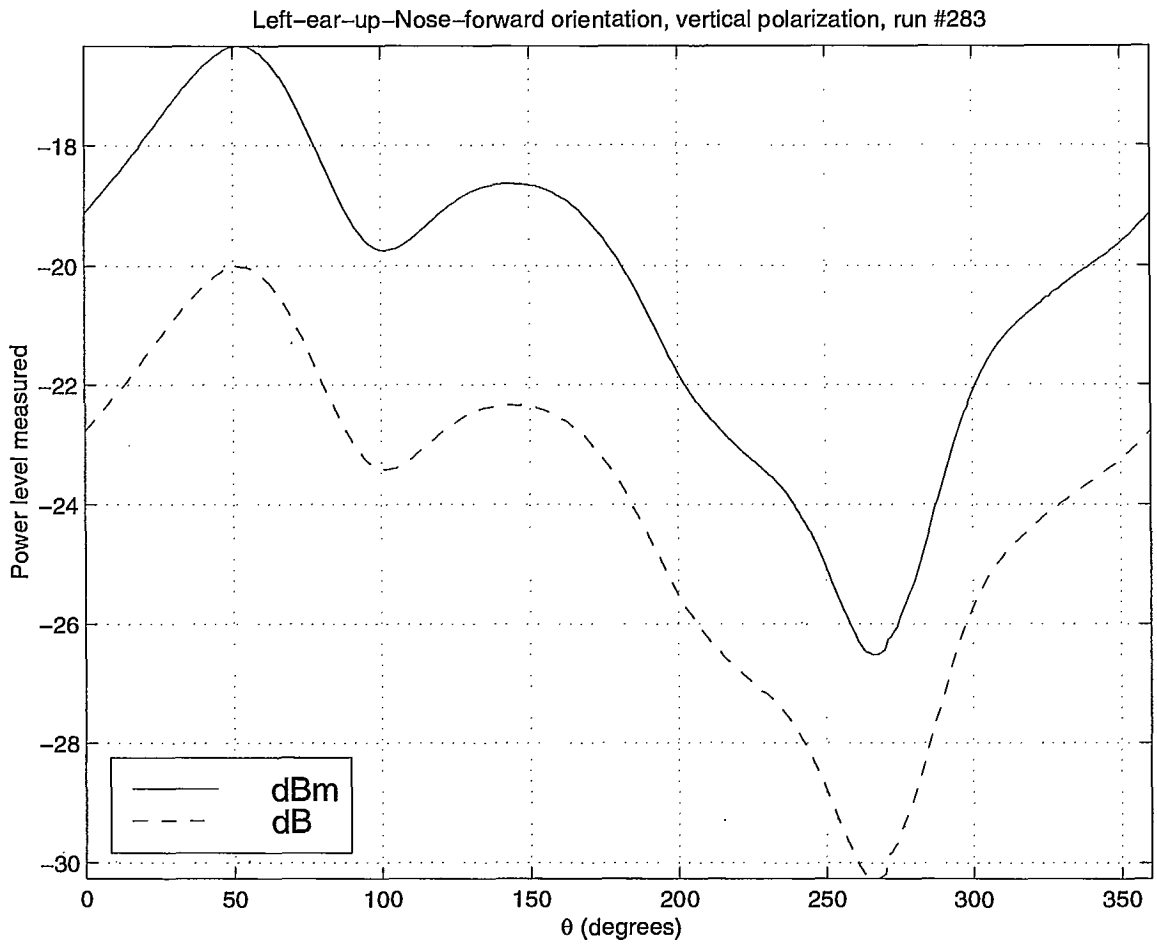

Figure 3.29: The vertical polarization for the Left-ear-up-Nose-forward orientation in the third test displayed with respect to the appropriate spherical coordinate rather than the measurement angle. Power correction with respect to both the battery discharge and the power transfer function of the network analyzer was applied for the curve in dBm unit.

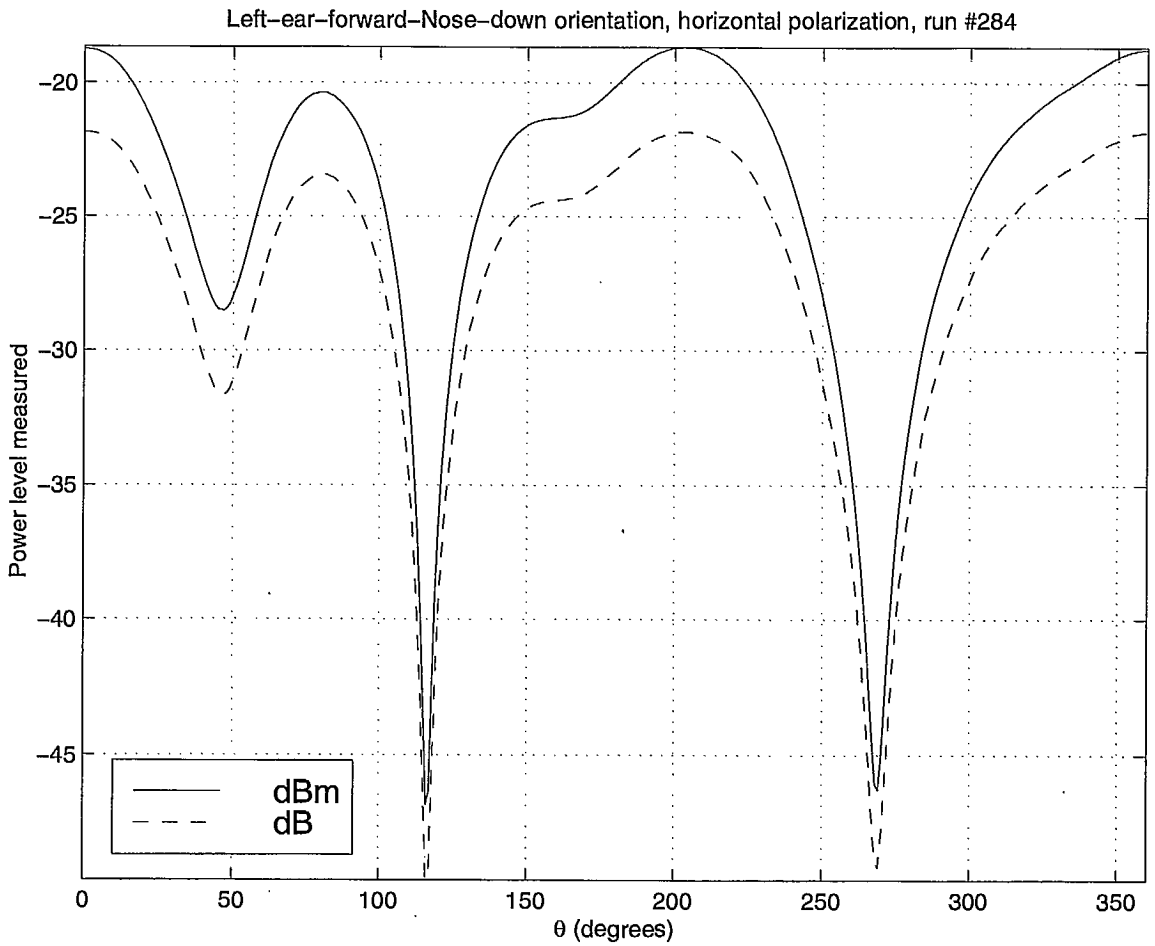

Figure 3.30: The horizontal polarization for the Left-ear-forward-Nose-down orientation in the third test displayed with respect to the appropriate spherical coordinate rather than the measurement angle. Power correction with respect to both the battery discharge and the power transfer function of the network analyzer was applied for the curve in dBm unit.

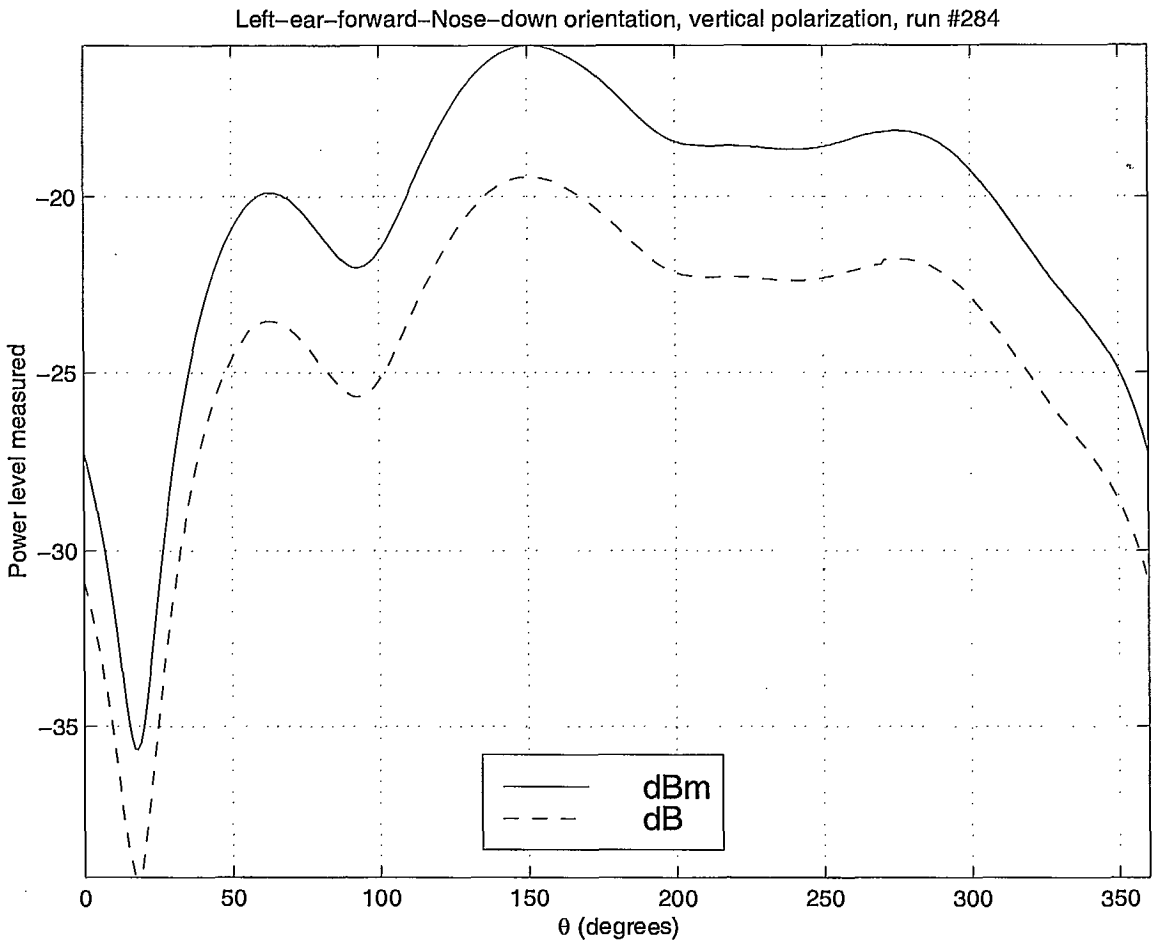

Figure 3.31: The vertical polarization for the Left-ear-forward-Nose-down orientation in the third test displayed with respect to the appropriate spherical coordinate rather than the measurement angle. Power correction with respect to both the battery discharge and the power transfer function of the network analyzer was applied for the curve in dBm unit.

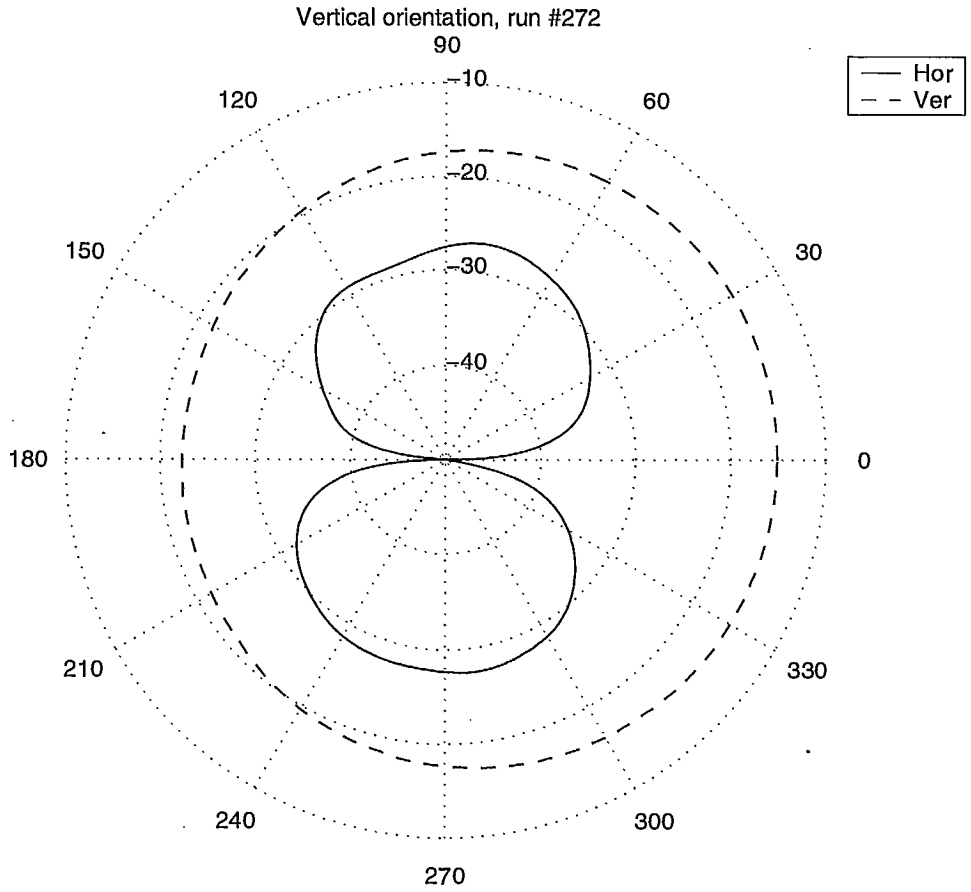

Figure 3.32: The horizontal and vertical polarizations for the Vertical orientation in the first test displayed in polar format with respect to the appropriate spherical coordinate and with power correction. The 0° and 90° directions correspond to the $\hat{x}$ and $\hat{y}$ directions, respectively. Horizontal polarization lies in the plane of the page. Vertical polarization is normal to the page.

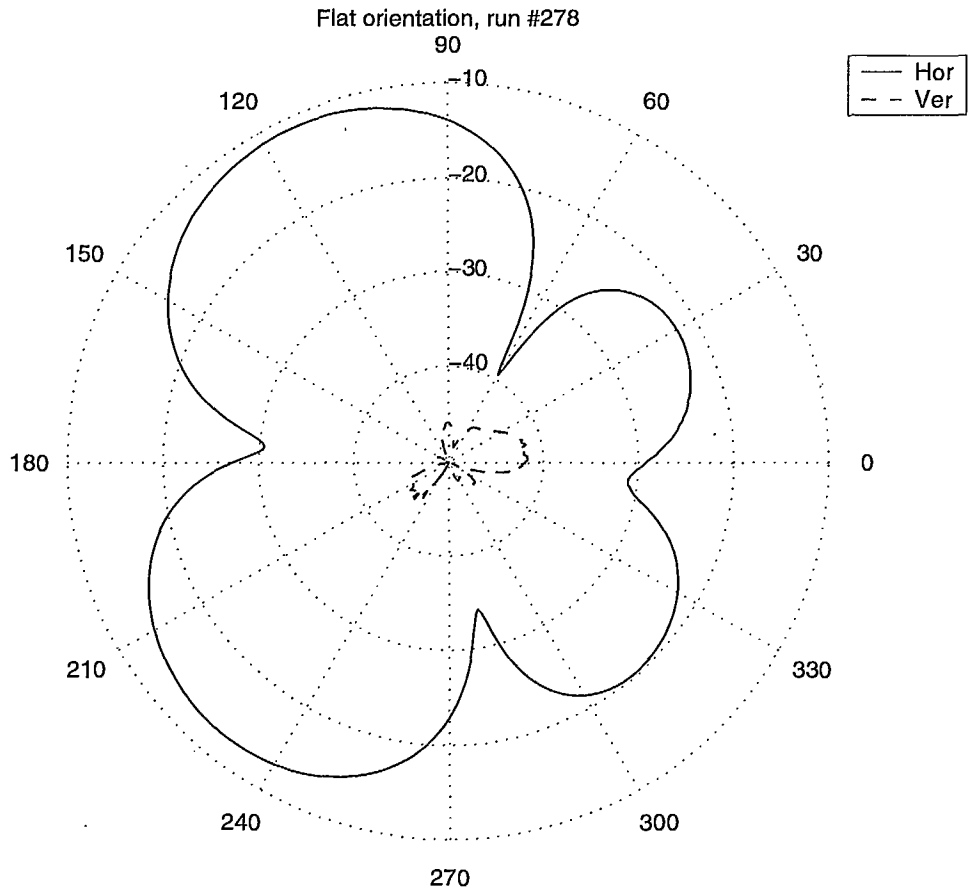

Figure 3.33: The horizontal and vertical polarizations for the Flat orientation in the first test displayed in polar format with respect to the appropriate spherical coordinate and with power correction. The 0° and 90° directions correspond to the $\hat{z}$ and $\hat{x}$ directions, respectively. Horizontal polarization lies in the plane of the page. Vertical polarization is normal to the page.

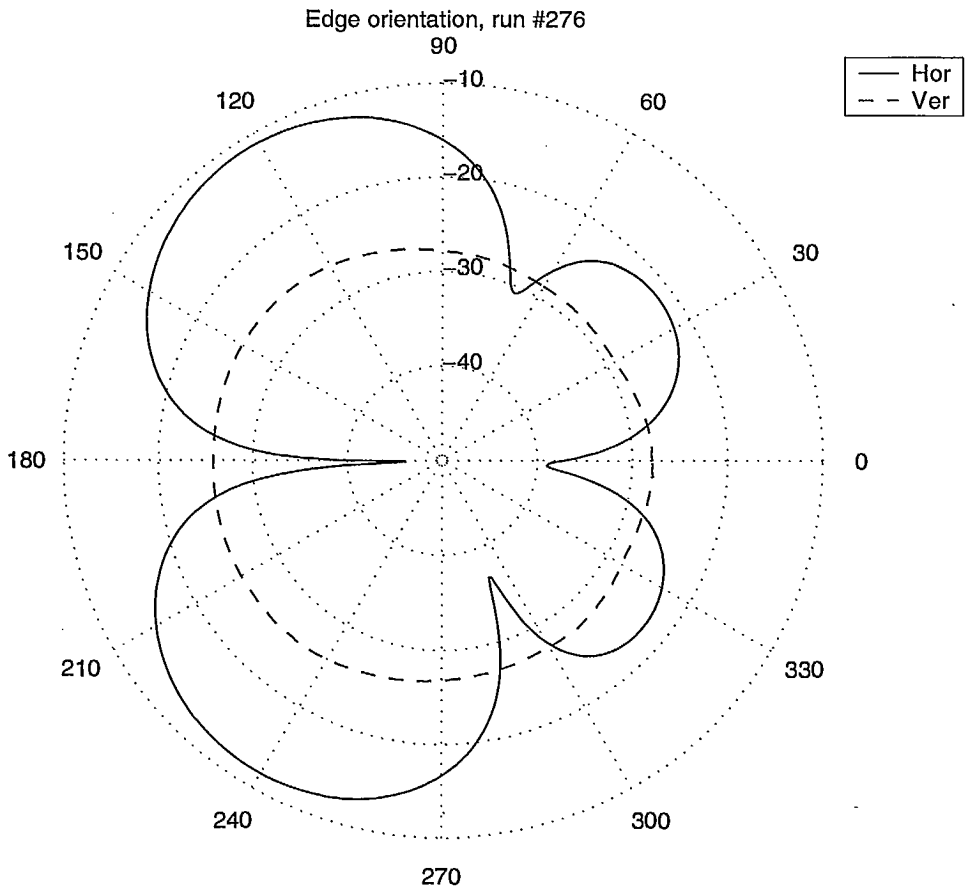

Figure 3.34: The horizontal and vertical polarizations for the Edge orientation in the first test displayed in polar format with respect to the appropriate spherical coordinate and with power correction. The 0° and 90° directions correspond to the $\hat{z}$ and $\hat{y}$ directions, respectively. Horizontal polarization lies in the plane of the page. Vertical polarization is normal to the page.

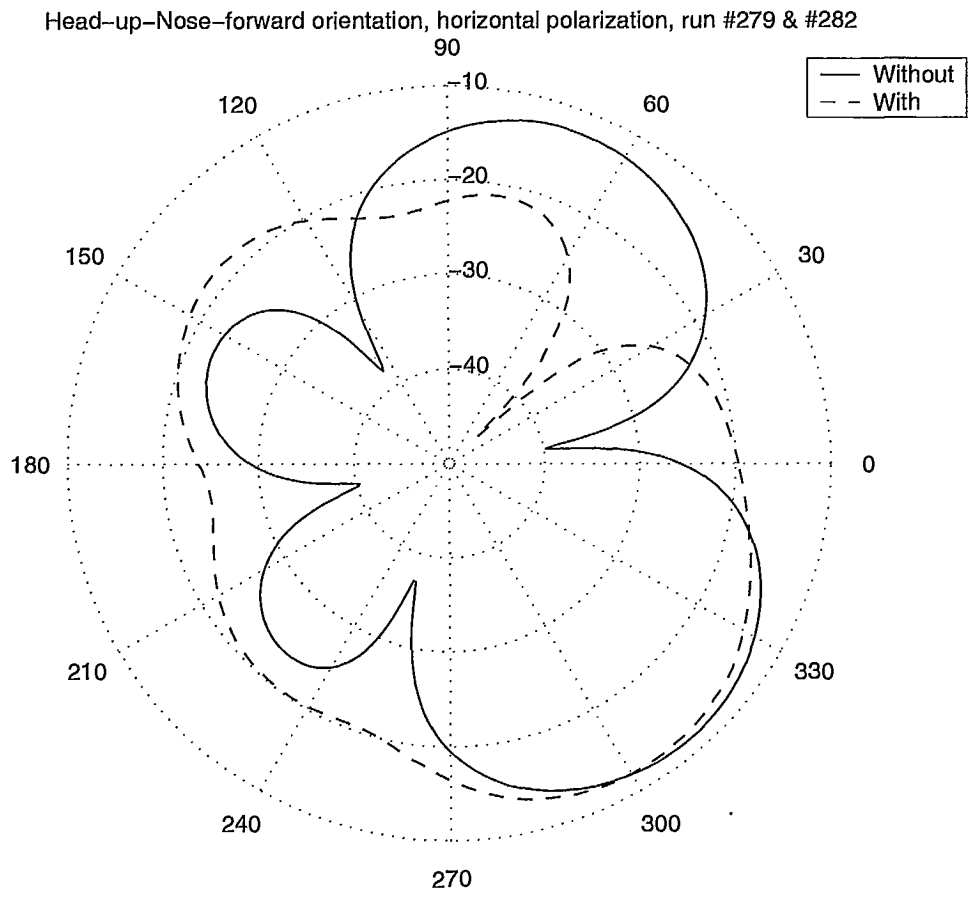

Figure 3.35: The horizontal polarization for the Head-up-Nose-forward orientation in the second (without head) and the third (with head) tests displayed in polar format with respect to the appropriate spherical coordinate and with power correction. The 0° and 90° directions correspond to the nose and left ear directions, respectively. Horizontal polarization lies in the plane of the page.

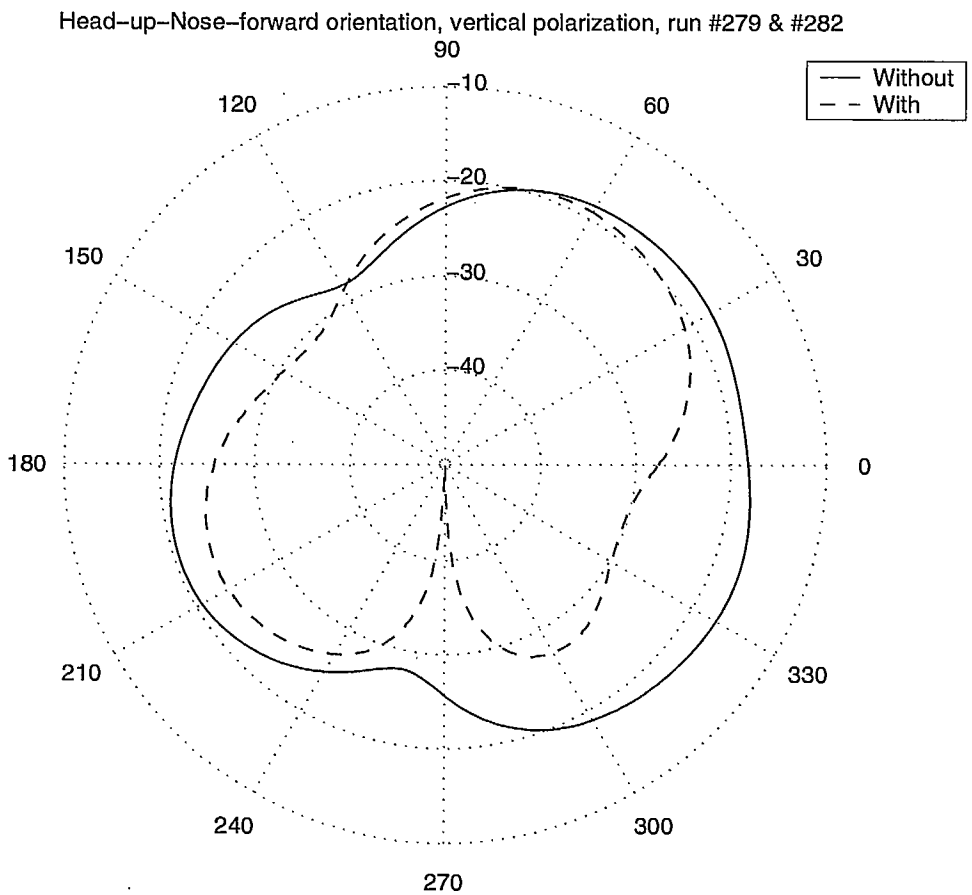

Figure 3.36: The vertical polarization for the Head-up-Nose-forward orientation in the second (without head) and the third (with head) tests displayed in polar format with respect to the appropriate spherical coordinate and with power correction. The 0° and 90° directions correspond to the nose and left ear directions, respectively. Vertical polarization is normal to the page.

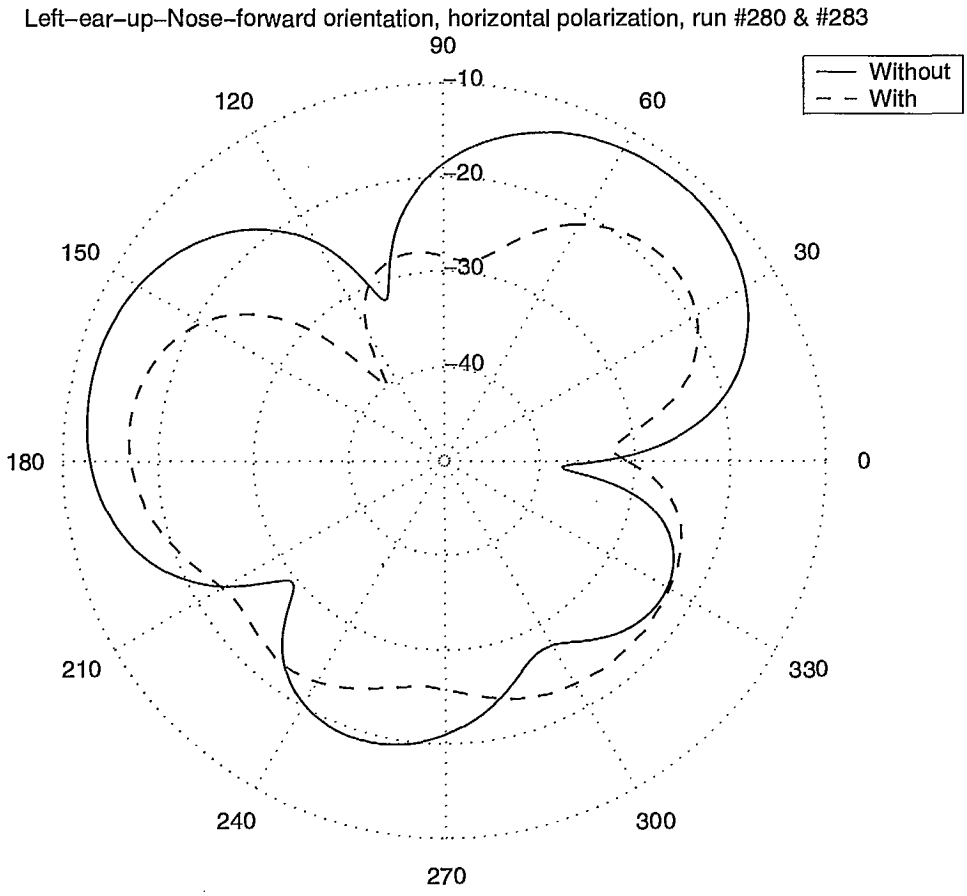

Figure 3.37: The horizontal polarization for the Left-ear-up-Nose-forward orientation in the second (without head) and the third (with head) tests displayed in polar format with respect to the appropriate spherical coordinate and with power correction. The 0° and 90° directions correspond to the top of the head and nose directions, respectively. Horizontal polarization lies in the plane of the page.

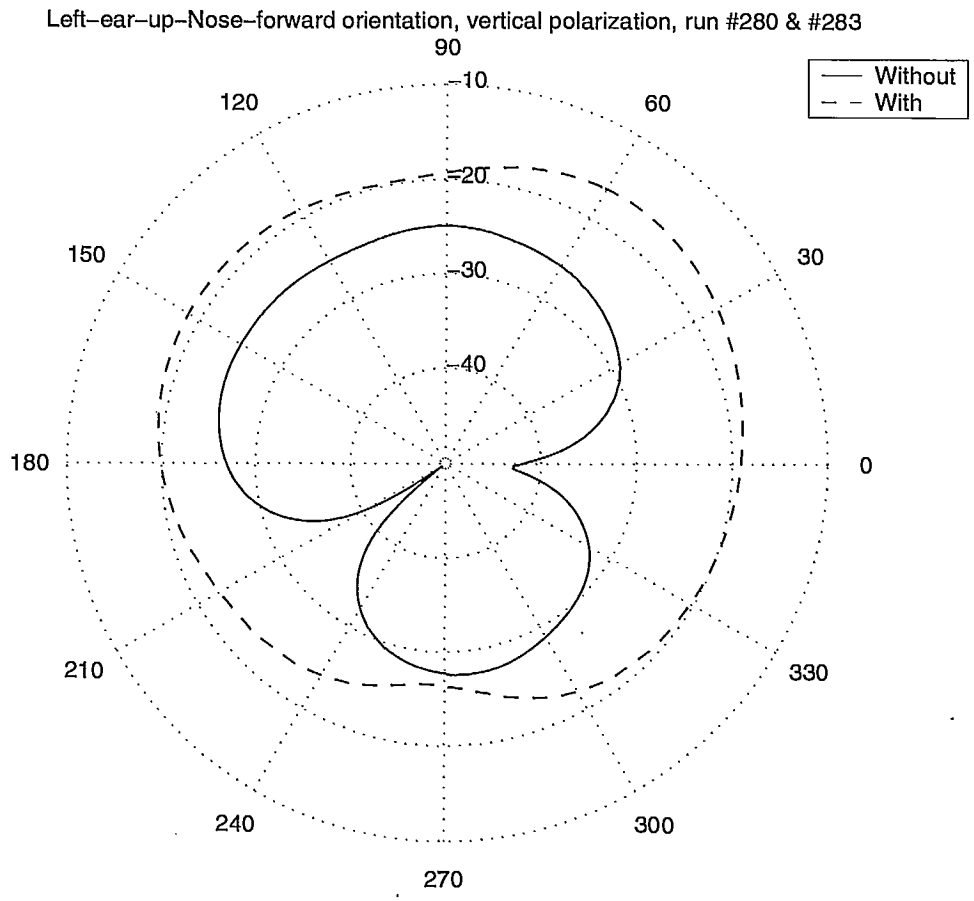

Figure 3.38: The vertical polarization for the Left-ear-up-Nose-forward orientation in the second (without head) and the third (with head) tests displayed in polar format with respect to the appropriate spherical coordinate and with power correction. The 0° and 90° directions correspond to the top of the head and nose directions, respectively. Vertical polarization is normal to the page.

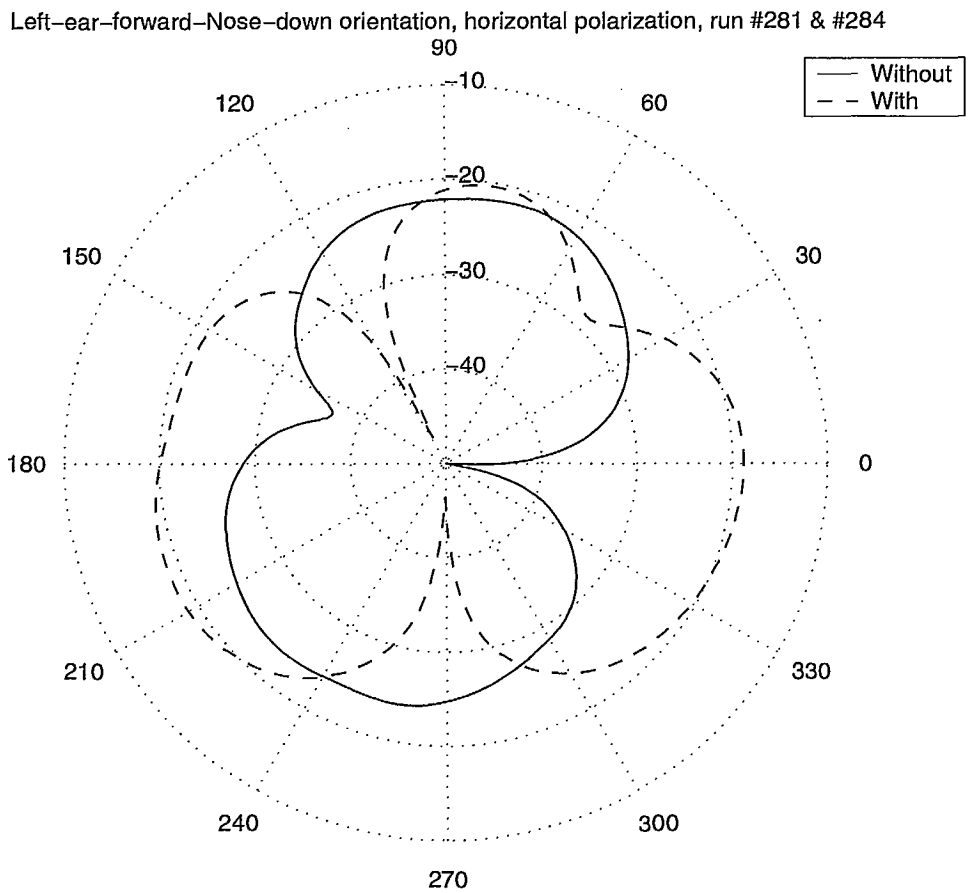

Figure 3.39: The horizontal polarization for the Left-ear-forward-Nose-down orientation in the second (without head) and the third (with head) tests displayed in polar format with respect to the appropriate spherical coordinate and with power correction. The 0° and 90° directions correspond to the top of the head and left ear directions, respectively. Horizontal polarization lies in the plane of the page.

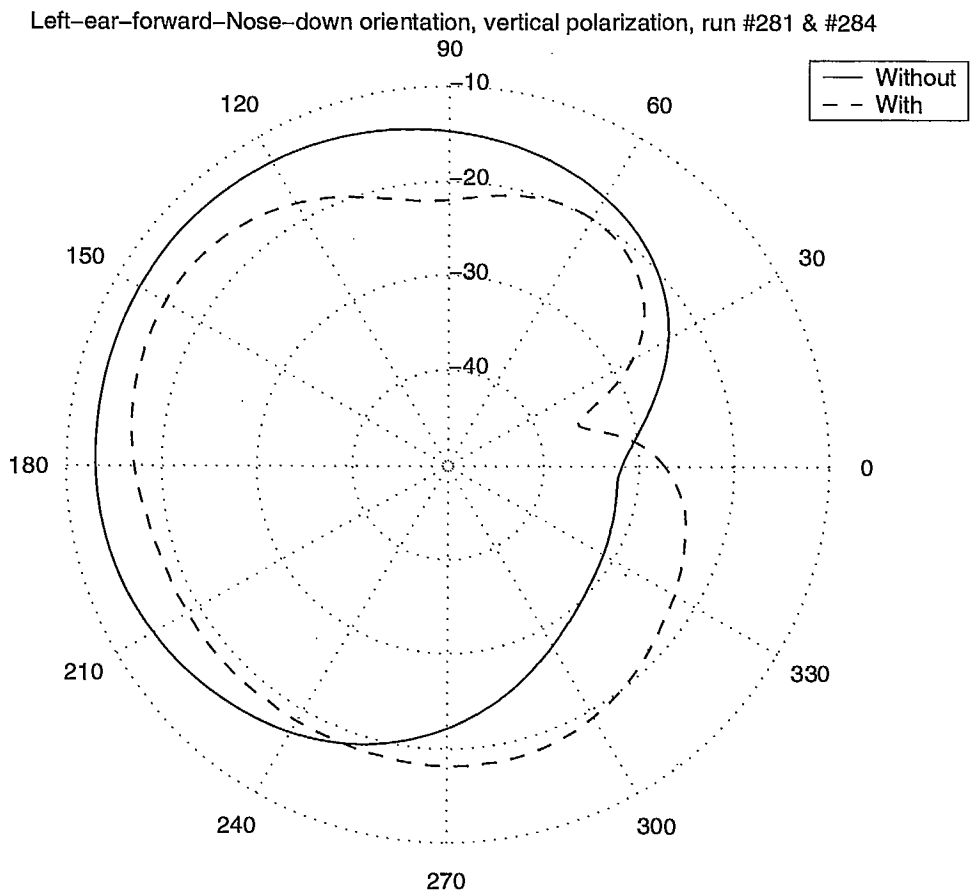

Figure 3.40: The vertical polarization for the Left-ear-forward-Nose-forward orientation in the second (without head) and the third (with head) tests displayed in polar format with respect to the appropriate spherical coordinate and with power correction. The 0° and 90° directions correspond to the top of the head and left ear directions, respectively. Vertical polarization is normal to the page.

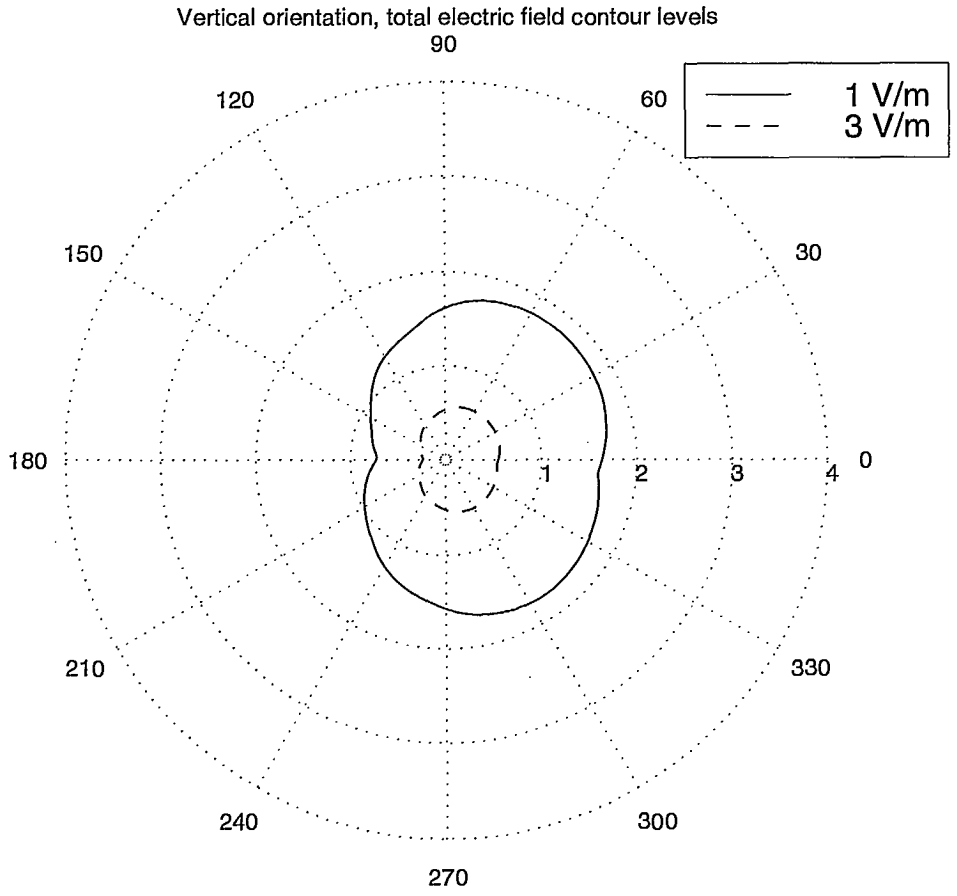

Figure 3.41: The contour for the 1 V/m and 3 V/m levels of total electric field for the vertical orientation displayed in polar format with respect to the appropriate spherical coordinate and with power correction. The 0° and 90° directions correspond to the $\hat{x}$ and $\hat{y}$ directions, respectively. The units for distance are m.

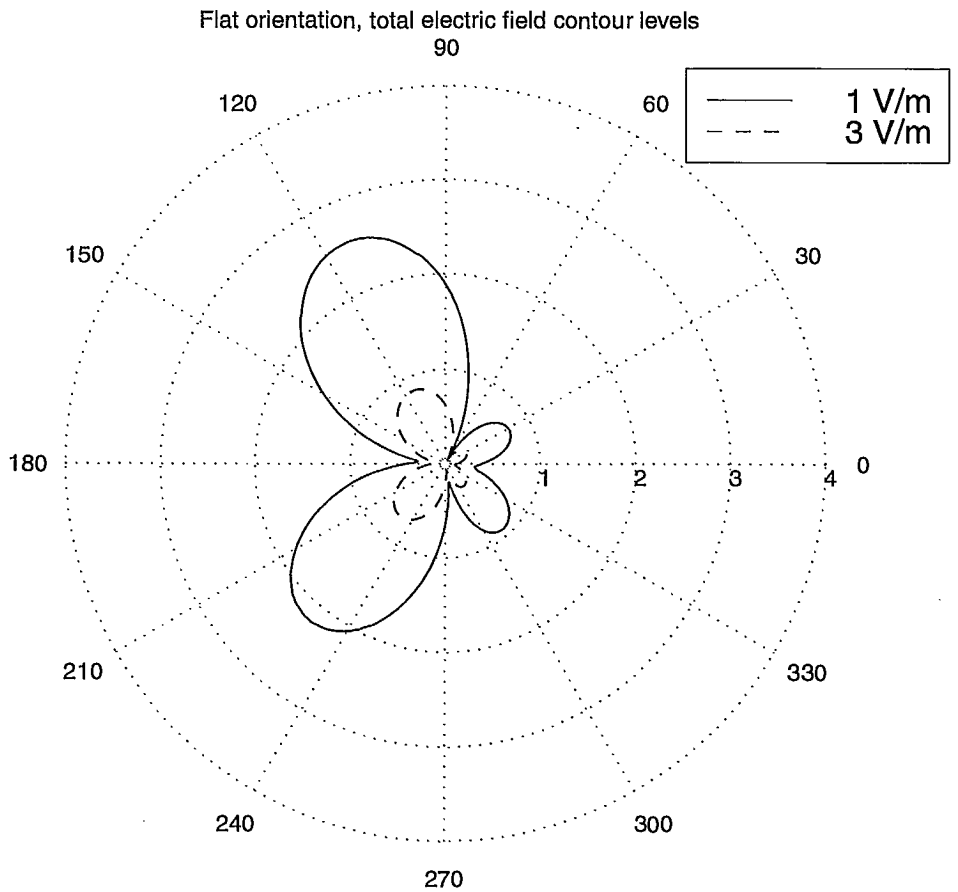

Figure 3.42: The contour for the 1 V/m and 3 V/m levels of total electric field for the flat orientation displayed in polar format with respect to the appropriate spherical coordinate and with power correction. The 0° and 90° directions correspond to the $\hat{z}$ and $\hat{x}$ directions, respectively. The units for distance are m.

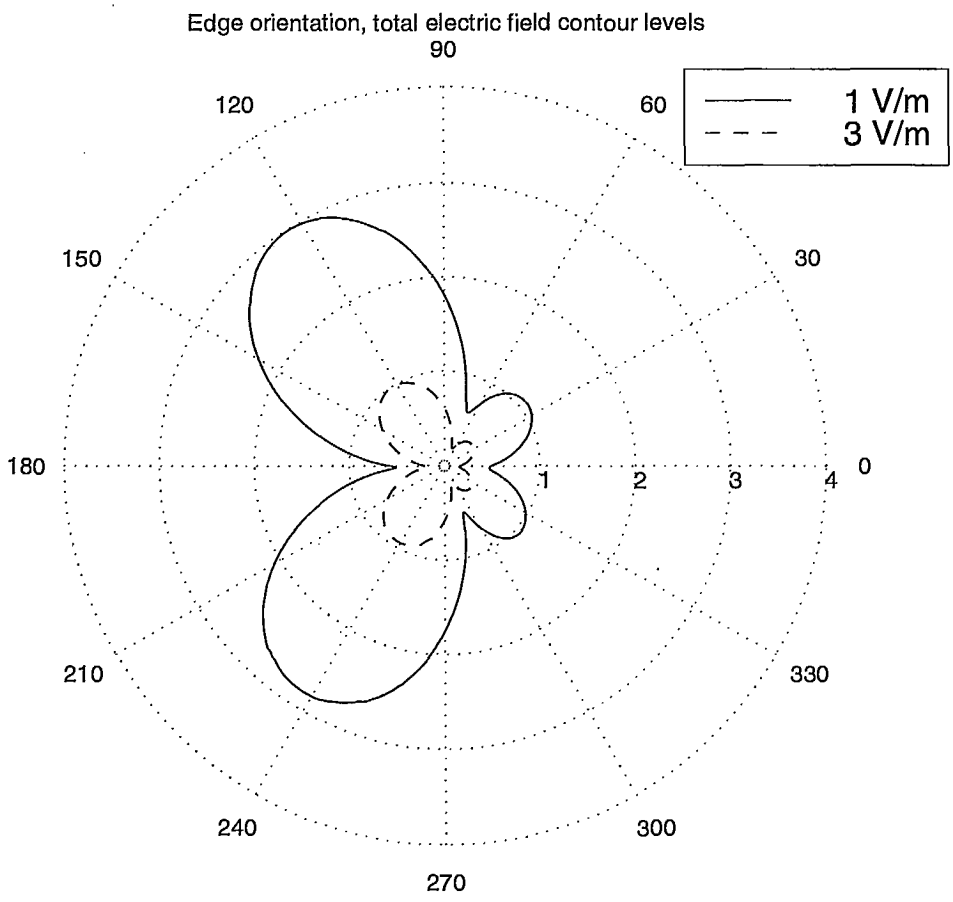

Figure 3.43: The contour for the 1 V/m and 3 V/m levels of total electric field for the edge orientation displayed in polar format with respect to the appropriate spherical coordinate and with power correction. The 0° and 90° directions correspond to the $\hat{z}$ and $\hat{y}$ directions, respectively. The units for distance are m.

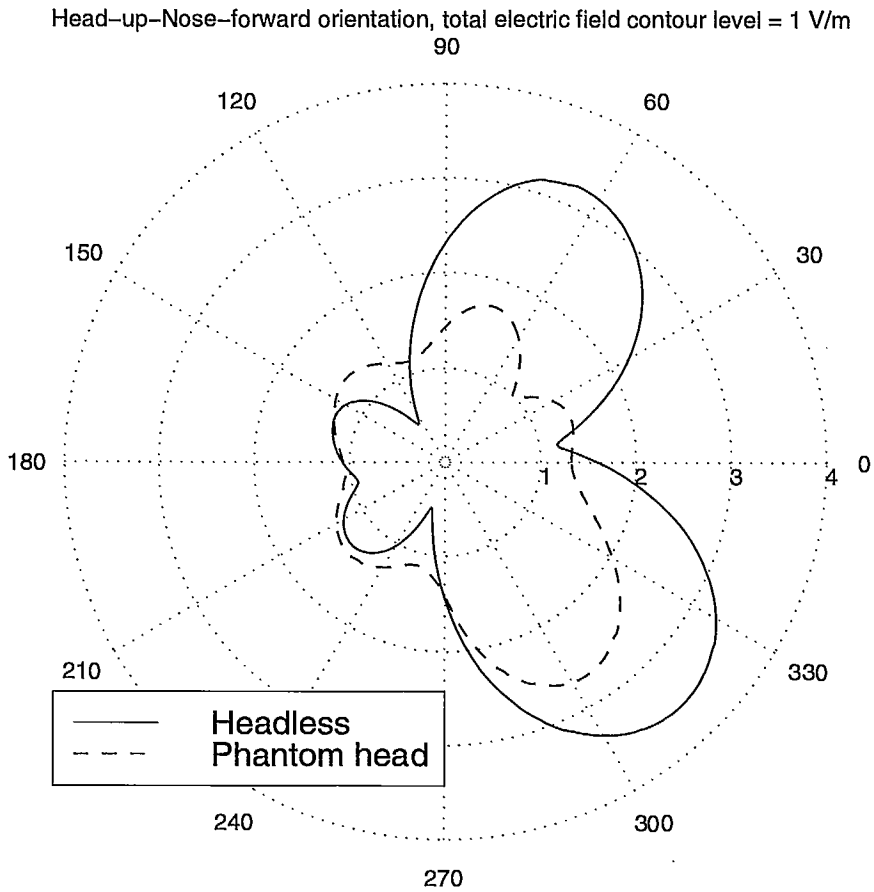

Figure 3.44: The contour for the 1 V/m level of total electric field for the Head-up-Nose-forward orientation with and without phantom head displayed in polar format with respect to the appropriate spherical coordinate and with power correction. The 0° and 90° directions correspond to the nose and left ear directions, respectively. The units for distance are m.

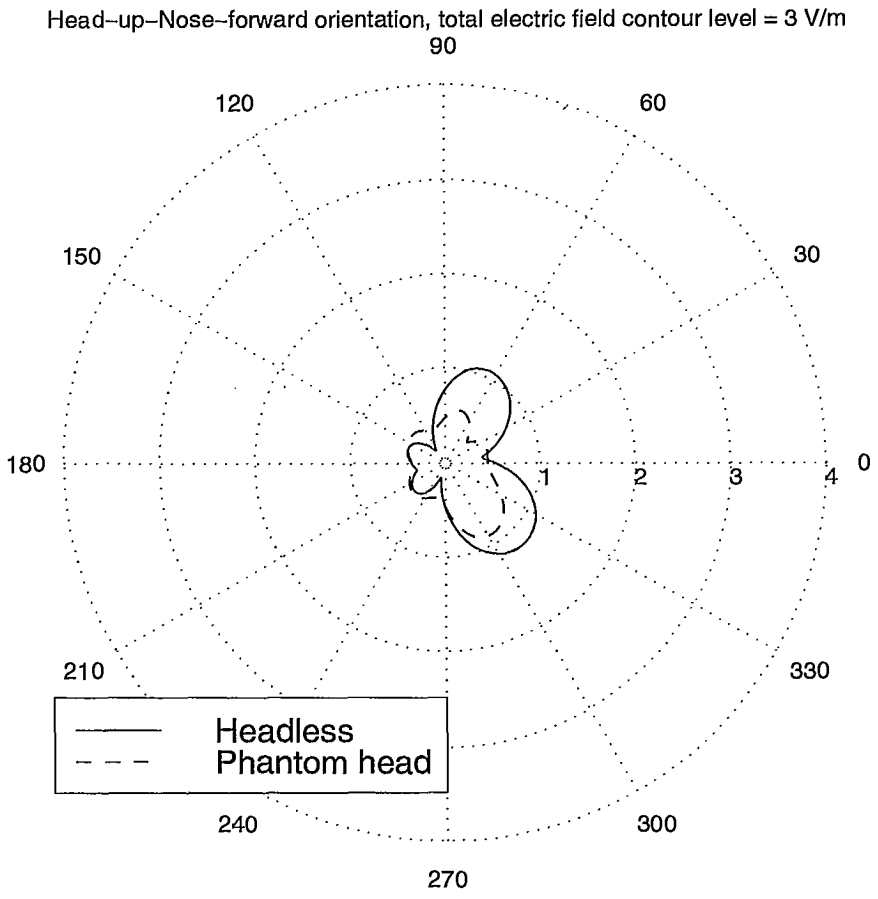

Figure 3.45: The contour for the 3 V/m level of total electric field for the Head-up-Nose-forward orientation with and without phantom head displayed in polar format with respect to the appropriate spherical coordinate and with power correction. The 0° and 90° directions correspond to the nose and left ear directions, respectively. The units for distance are m.

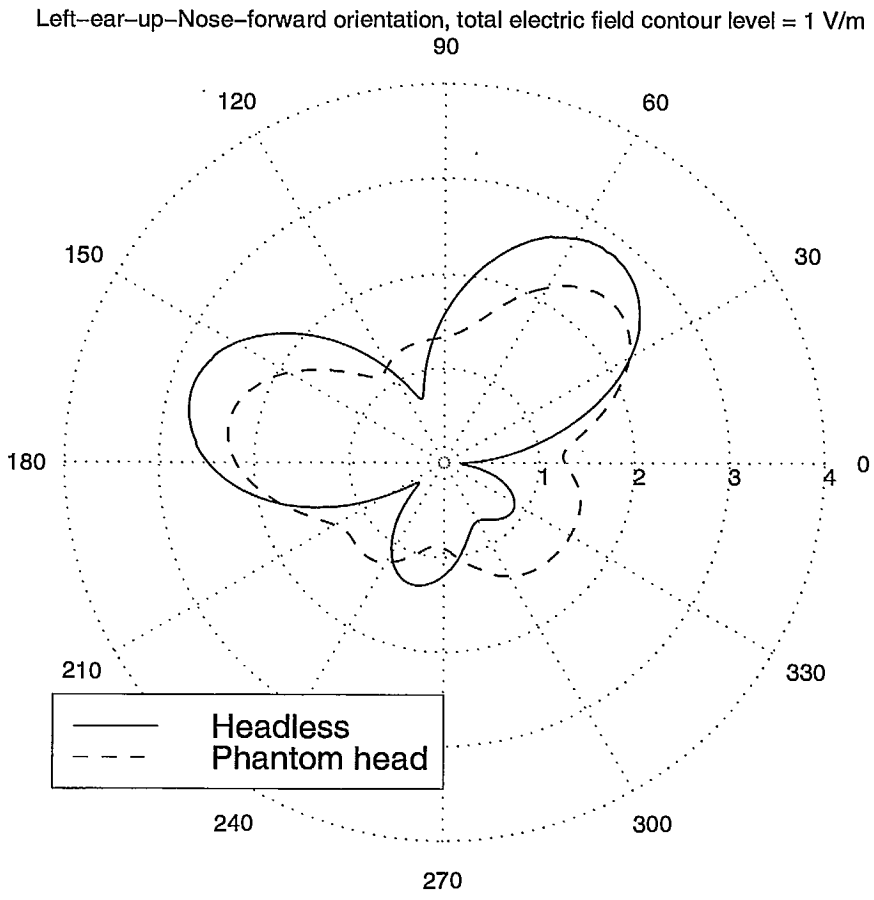

Figure 3.46: The contour for the 1 V/m level of total electric field for the Left-ear-up-Nose-forward orientation with and without phantom head displayed in polar format with respect to the appropriate spherical coordinate and with power correction. The 0° and 90° directions correspond to the top of the head and nose directions, respectively. The units for distance are m.

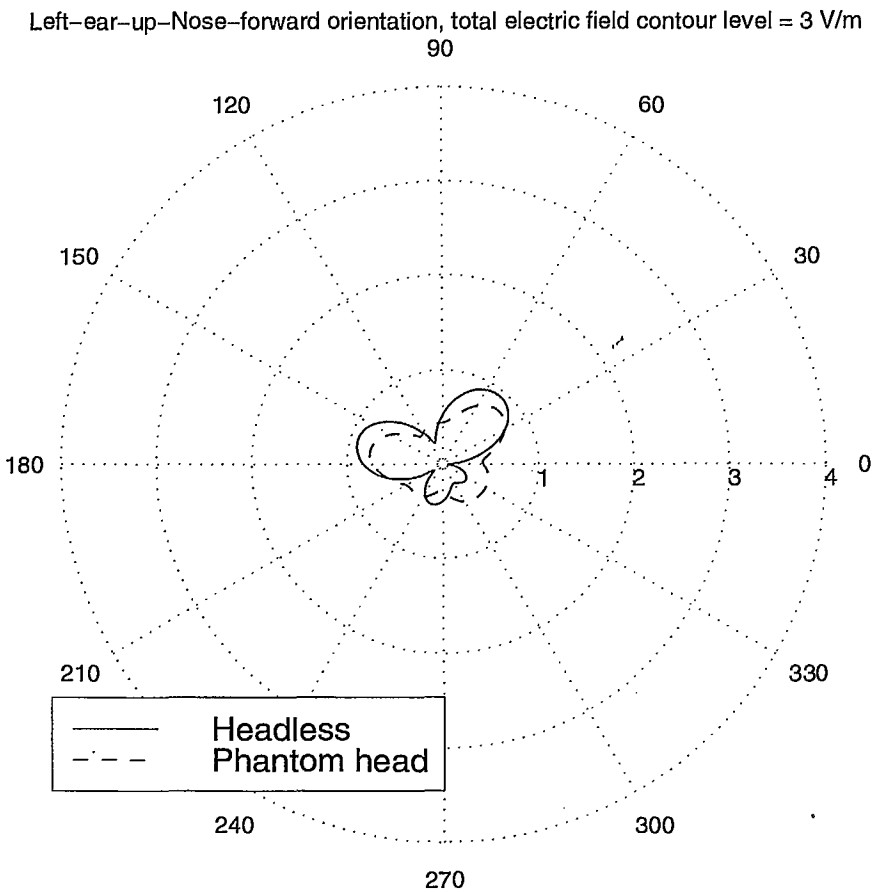

Figure 3.47: The contour for the 3 V/m level of total electric field for the Left-ear-up-Nose-forward orientation with and without phantom head displayed in polar format with respect to the appropriate spherical coordinate and with power correction. The 0° and 90° directions correspond to the top of the head and nose directions, respectively. The units for distance are m.

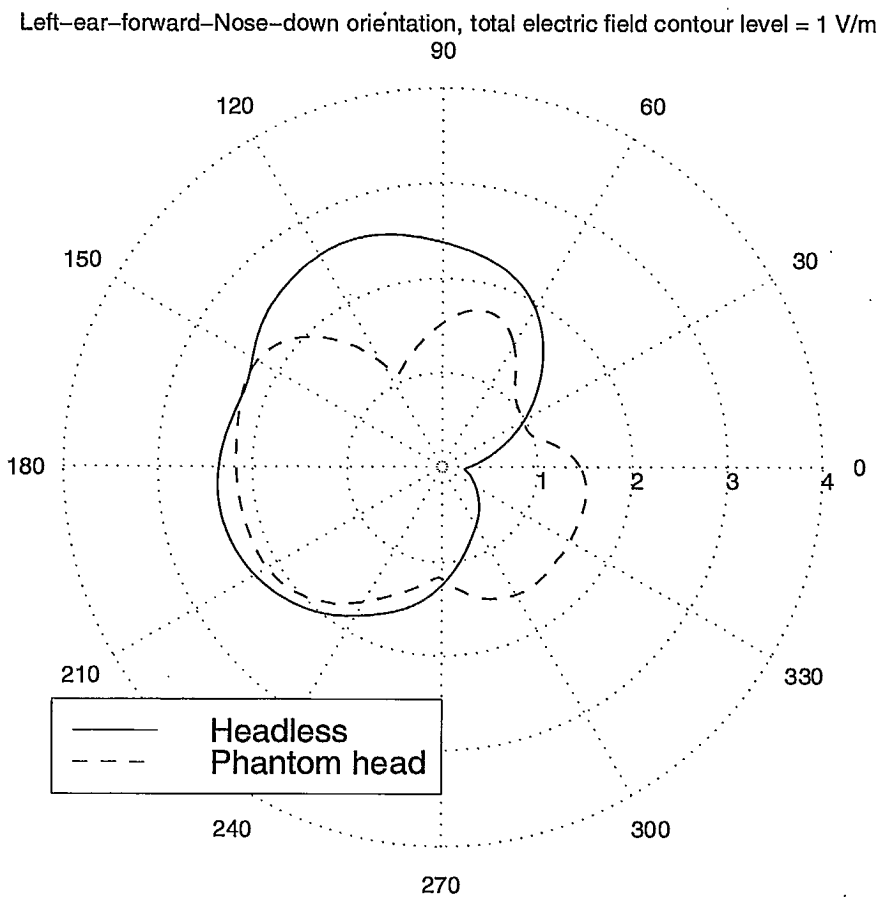

Figure 3.48: The contour for the 1 V/m level of total electric field for the Left-ear-forward-Nose-down orientation with and without phantom head displayed in polar format with respect to the appropriate spherical coordinate and with power correction. The 0° and 90° directions correspond to the top of the head and left ear directions, respectively. The units for distance are m.

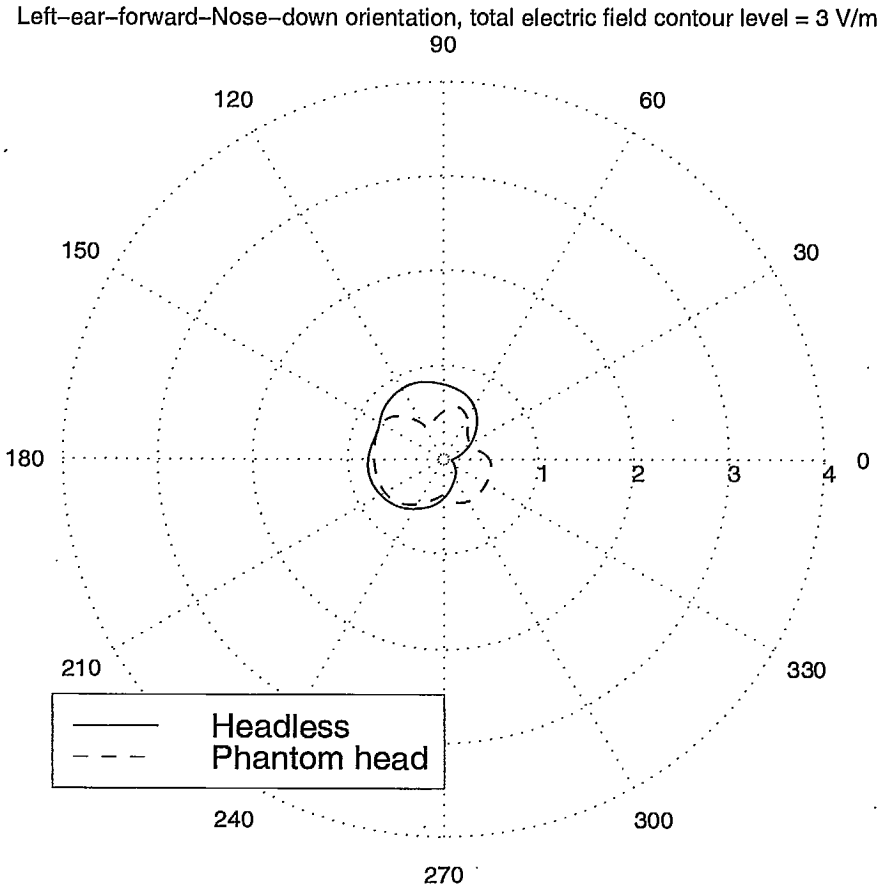

Figure 3.49: The contour for the 3 V/m level of total electric field for the Left-ear-forward-Nose-down orientation with and without phantom head displayed in polar format with respect to the appropriate spherical coordinate and with power correction. The 0° and 90° directions correspond to the top of the head and left ear directions, respectively. The units for distance are m.

Chapter 4

Sources of error

This chapter presents an attempt to quantify the effect of various sources of error affecting the measured results.

4.1 Data smearing assessment

Because of the continuous nature of the scan, the start and stop angles were recorded for every measurement point of all runs reported herein. The corresponding angular spread past the desired nominal angular value was found to be always less than about 0.17^o except on two occasions where it was 0.21^o and 0.25^o. However, the process of acquiring the data for some nominal angular value as the data collected over a range of angular values past this nominal value owing to the continuous motion of the positioner resulted in a smearing of the data for that angular value. The more variation of the signal within the time duration of the data acquisition (hence, the greater the slope of the curve), the more data smearing was incurred. The effect of this data smearing was investigated systematically by comparing the results obtained by the regular equipment setup which used the combination of a continuous scan and the averaging over 64 consecutive measurements, with the results obtained from using the combination of the start-and-stop scan and an averaging over 4096 consecutive measurements without disturbing the mechanical setup (transmitter vertical in the styrofoam disk) between the two runs. Since the combination of the start-and-stop

scan and the averaging over 4096 data values represented the most accurate measurement setup that the DFL data acquisition system could have afforded us if we had not been time restricted by the discharge of the battery packs, we present the data acquired under this combination as the reference data.

The externally DC power supplied transmitter instead of the battery operated transmitter was used here during the data smearing assessment test in order to avoid the variation in the radiated power level that would be caused by the draining of the battery. A rotary joint was also used for the DC connection through the centre of the azimuth table. The DC power supply wire was taped into place along the styrofoam tower in order to prevent any motion of the wire as the azimuth table was rotated. The fact that the presence of the DC power supply wire corrupted the radiation pattern of the transmitter by itself was not relevant to assessing the data smearing effect.

Figure 4.1 shows the difference in the power received in the horizontal polarization between the results for the continuous scan and the results for the start-and-stop scan. The variations of the curve, however, are due to both data smearing and electrical noise. Since it is reasonable to think that the data smearing depends linearly on both the scan rate of the positioner and the time duration for the data acquisition but not on the RF signal strength, as does noise, the data smearing effect could be isolated from the noise effect. This isolation was performed by applying a linear regression onto the ensemble of points representing the slope values versus the values of the difference power received for the vertical polarization (see Figure 4.5). The vertical polarization was chosen here because the corresponding difference curve was not very noisy since the signal itself always remained very strong (see Figure 4.3). The linear regression was computed by the method of least squares which, in effect, filtered out the noise. The regression was computed under the constraint of a zero intercept value since a slope value of zero should logically correspond to a data smearing value of zero. The data smearing effect was thus modeled as a proportionally linear process with characteristic value $m = 0.0334\ dB/(dB/^\circ)$. It is important to understand that the process of linear regression was performed with the data in decibels, i.e. the process did not entail converting the data from the decibel to the linear scale, performing the linear regression on the linear scale then converting back the result to the decibel

scale. Consequently, a linear regression on the decibel scale corresponds, in fact, to an exponential behaviour on the linear scale, which behaviour is very common among many systems.

From the knowledge of the slope values of the difference curve, the data smearing contribution could be computed and subtracted from the difference curve itself in order to be left with only the noise effect (see Figure 4.6 and 4.8). The slope values were numerically computed by applying onto the difference curve the centre-difference scheme for angular values in the range of $\{-179^o, +179^o\}$, the left-difference scheme for the $+180^o$ value and the right-difference scheme for the -180° value. The results are shown in Figures 4.2 and 4.4 for the horizontal and the vertical polarizations, respectively.

Inherent to the above procedure were the following assumptions:

- the linear regression process was not affected by a small amount of noise because the noise had a zero average value;
- the variation in the time duration for the data acquisition and the variation in the speed of the scan were small enough to be neglected;
- the noise in the slope curve was small enough for the computed data smearing contribution not to be significantly corrupted.

Figures 4.1 to 4.9 present the results from the data smearing and noise level assessments. A more rigorous assessment of the data smearing and the noise level would require the use of statistical analysis.

Figure 4.7 suggests that the noise level increases with an exponential-like envelope as the signal strength decreases. Figure 4.9 does not suggest as clearly an exponential-like envelope but the vertical range of the plot is very limited, covering less than 0.07 dB.

Although the noise characteristics might differ between the measurement with the externally DC power supplied transmitter and the measurement with the battery DC power supplied transmitter, the data smearing effect should nevertheless be the

same since the test setup was identical for both cases. To help us appreciate the magnitude of the error caused by the data smearing effect, we note that for the value $m = 0.0334\ dB/(dB/^o)$ and a large slope value of 3 $dB/^o$, the corresponding error would be only 0.10 dB.

It should be said that $m = 0.0334\ dB/(dB/^o) = 0.0334^o$ corresponds to half the angular spread value. This situation can be explained as follows. We wish to measure $P(\theta_1)$ in dB but in fact, due to averaging over 64 consecutive measurements for reducing the effect of the noise, we measure $\frac{1}{64}\sum_{i=1}^{64} P(\theta_i)$. Since the function $P(\theta)$ is slowly varying over the small angular spread $\Delta\theta = (\theta_{64} - \theta_1)$, we assume that the function $P(\theta)$ varies linearly with θ, i.e. $P(\theta_i) = P(\theta_1) + M(\theta_i - \theta_1)$. Hence, the actual measurement value becomes simply:

$$\frac{1}{64}\sum_{i=1}^{64} P(\theta_i) = \frac{P(\theta_1) + P(\theta_{64})}{2}$$

and the corresponding measurement error between actual and desired values becomes:

$$\epsilon = \frac{P(\theta_1) + P(\theta_{64})}{2} - P(\theta_1) = \frac{P(\theta_{64}) - P(\theta_1)}{2} = \frac{P(\theta_1) + M(\theta_{64} - \theta_1) - P(\theta_1)}{2} = \frac{M\Delta\theta}{2}$$

$$\Longrightarrow m = \frac{\epsilon}{M} = \frac{\Delta\theta}{2}$$

For $m = 0.0334^o$, the angular spread becomes $\Delta\theta = 2m = 0.0668^o$ which value should be understood to be a statistical average since angular spread values have been observed to fluctuate as seen from the difference between the stop and the start angles which, as mentioned above, was almost always found to be less than about 0.17^o.

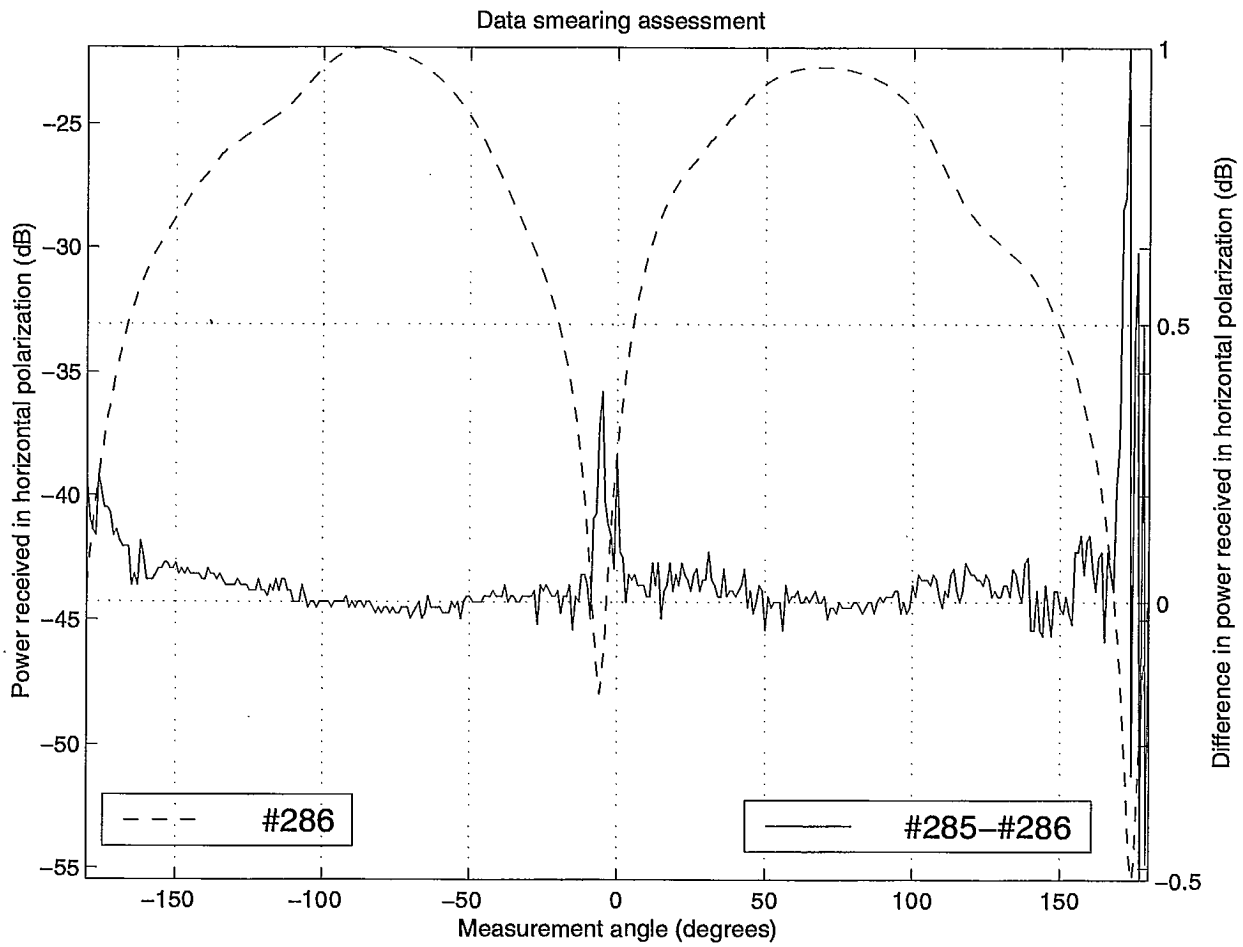

Figure 4.1: Difference between a start-and-stop scan and a continuous scan. The dashed curve shows the power received in the horizontal polarization for the start-and-stop scan whereas the solid curve shows the difference in the power received in the horizontal polarization between the continuous and the start-and-stop scans for exactly the same mechanical setup.

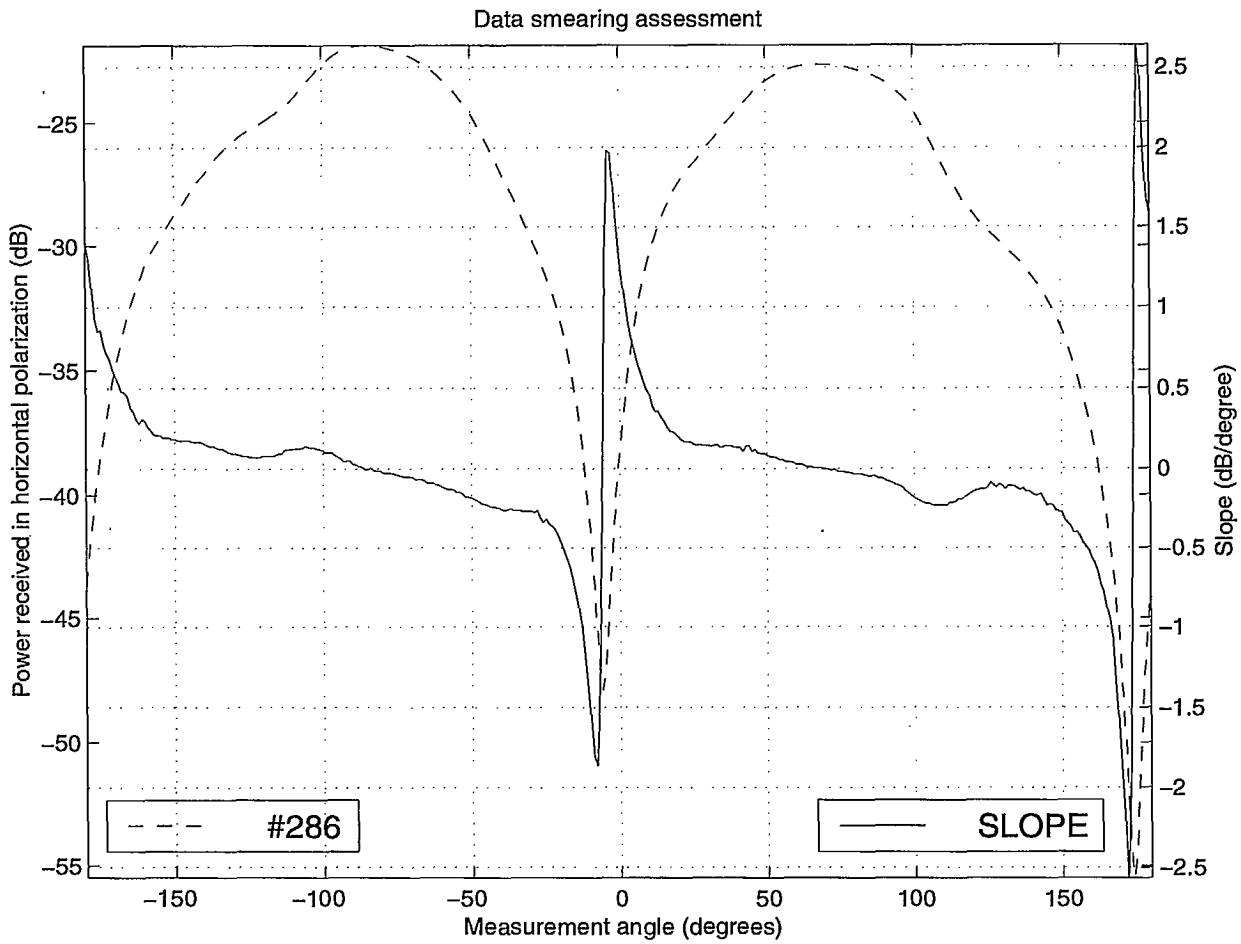

Figure 4.2: The dashed curve shows the power received in the horizontal polarization for the start-and-stop scan whereas the solid curve shows the corresponding slope of the data curve.

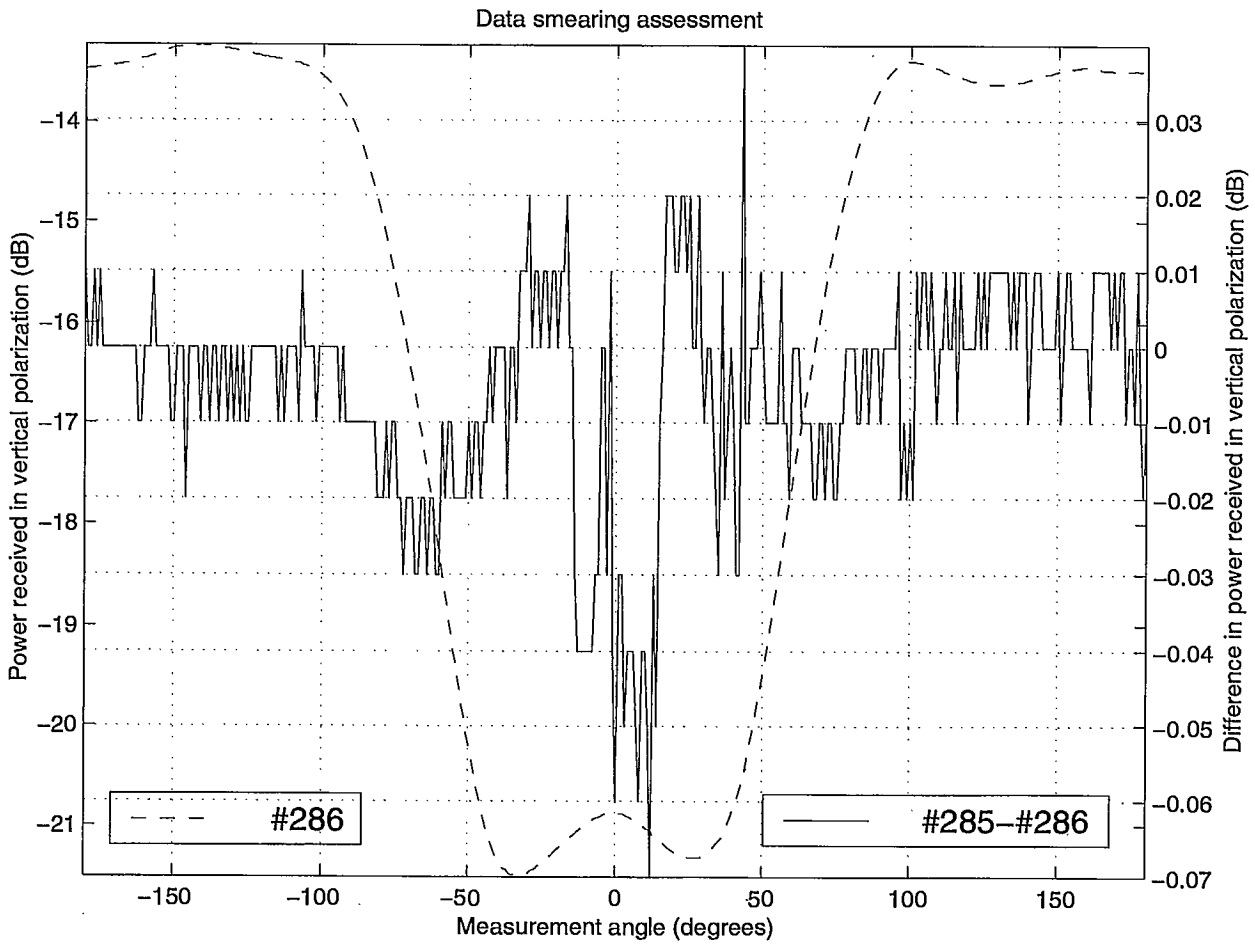

Figure 4.3: Difference between a start-and-stop scan and a continuous scan. The dashed curve shows the power received in the vertical polarization for the start-and-stop scan whereas the solid curve shows the difference in the power received in the vertical polarization between the continuous and the start-and-stop scans for exactly the same mechanical setup.

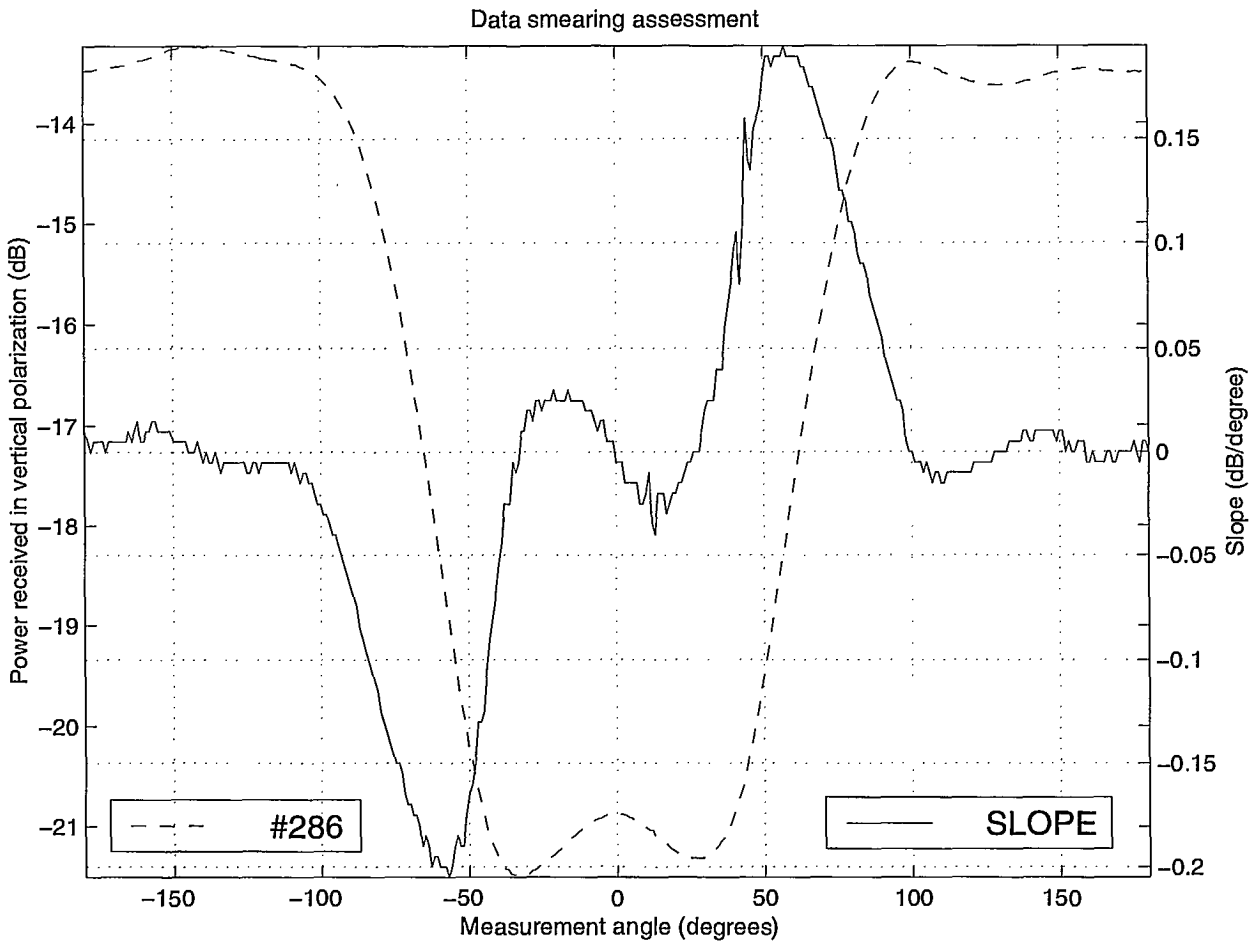

Figure 4.4: The dashed curve shows the power received in the vertical polarization for the start-and-stop scan whereas the solid curve shows the corresponding slope of the data curve.

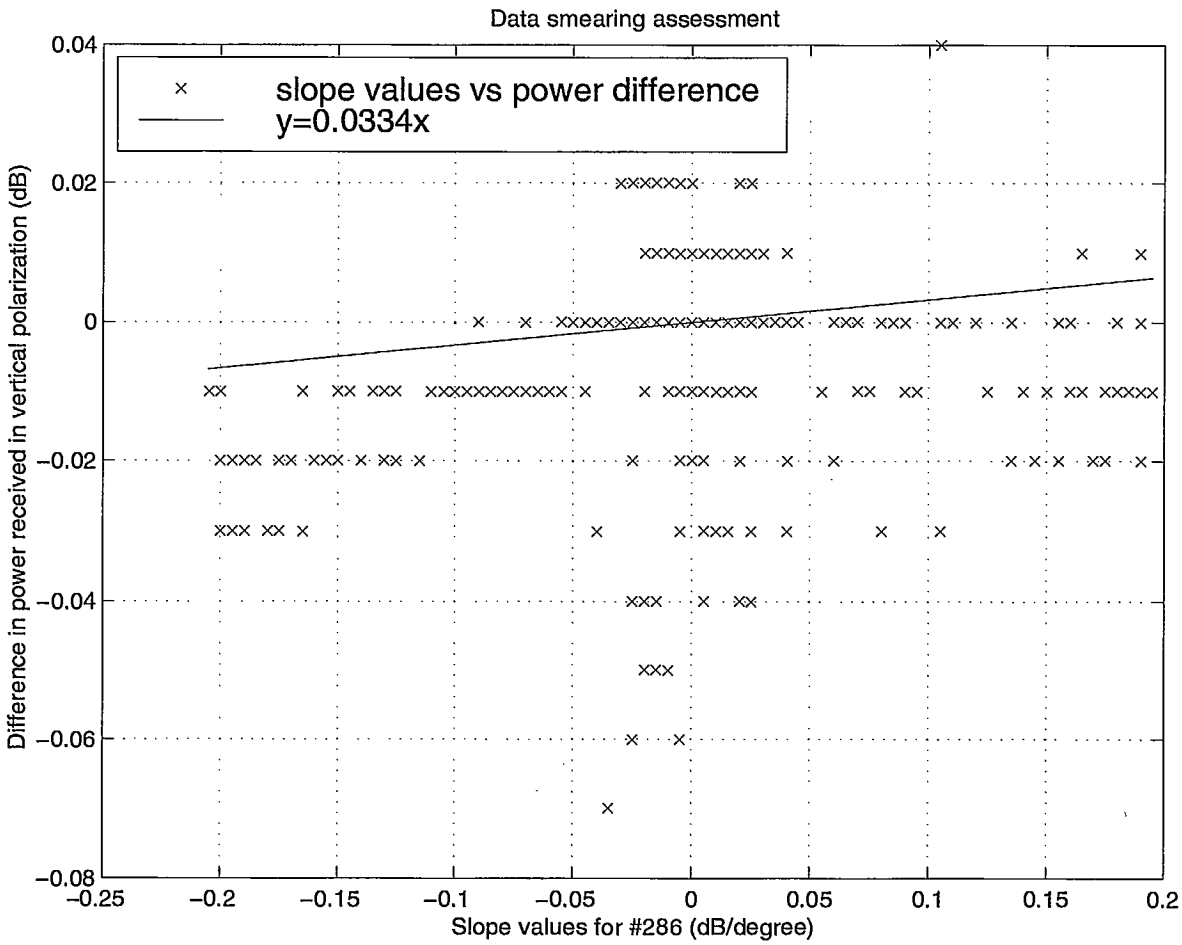

Figure 4.5: The plot corresponds to the spread distribution of the difference curve of Figure 4.3 with respect to the slope values of Figure 4.4. The solid curve corresponds to the linear regression of the distribution. Beware that since each "x" mark can possibly correspond to more than one data point, the solid curve does not necessarily appear visually satisfactory for the result of a linear regression.

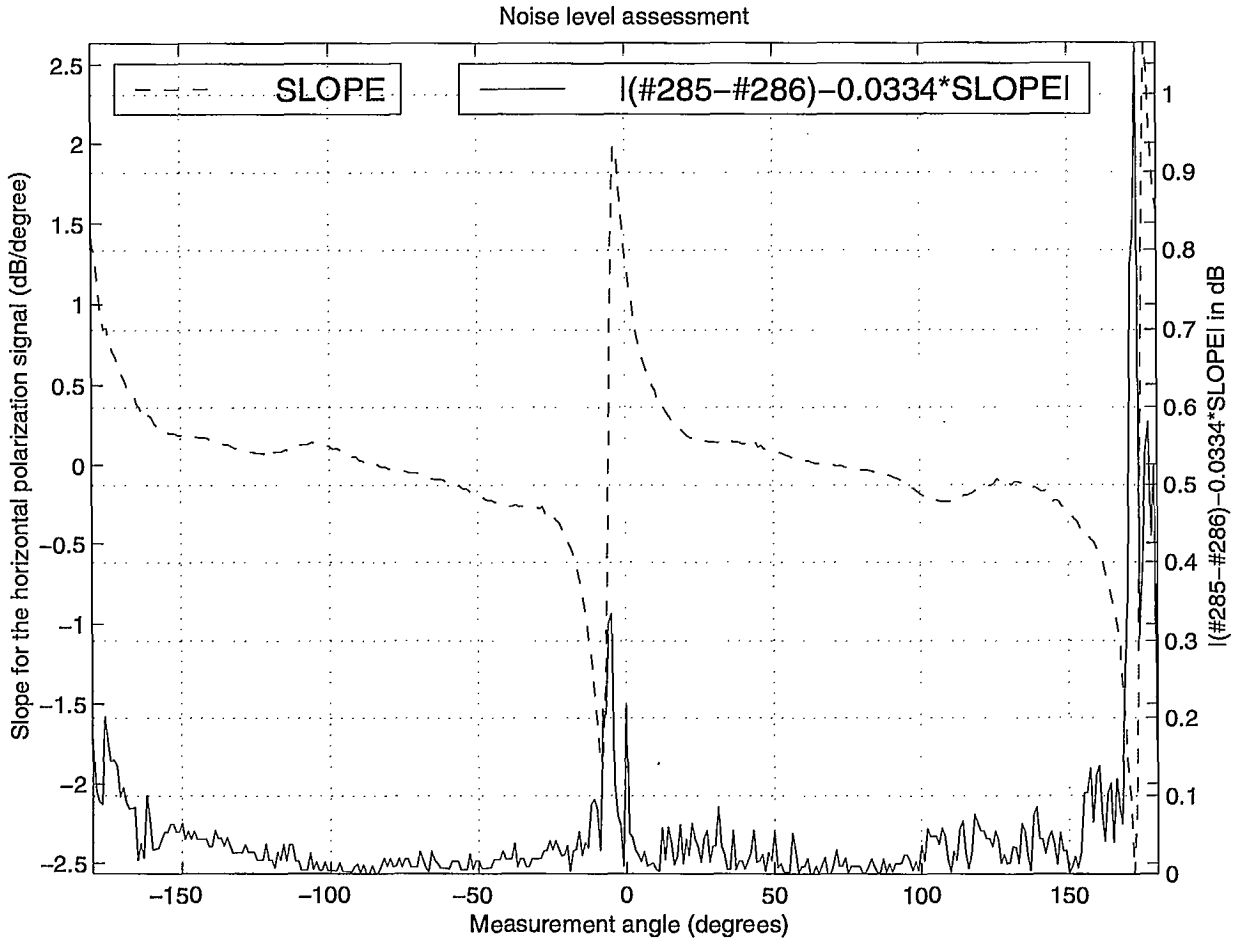

Figure 4.6: The dashed curve shows the slope corresponding to the data for the horizontal polarization. The solid curve shows the electrical noise level (absolute value) obtained after subtracting the data smearing effect from the difference curve for the horizontal polarization.

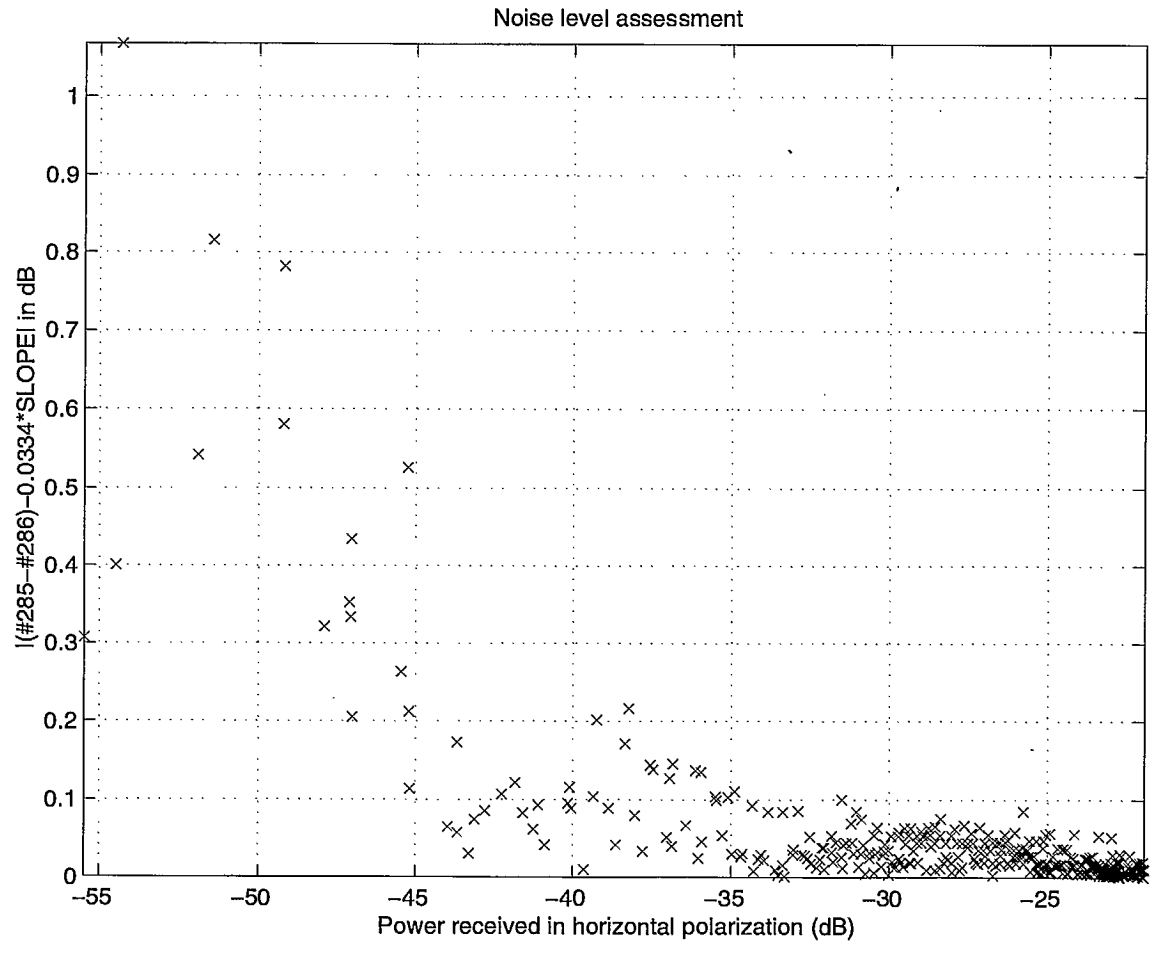

Figure 4.7: The plot shows the spread distribution of the noise amplitude of Figure 4.6 with respect to signal strength for the horizontal polarization.

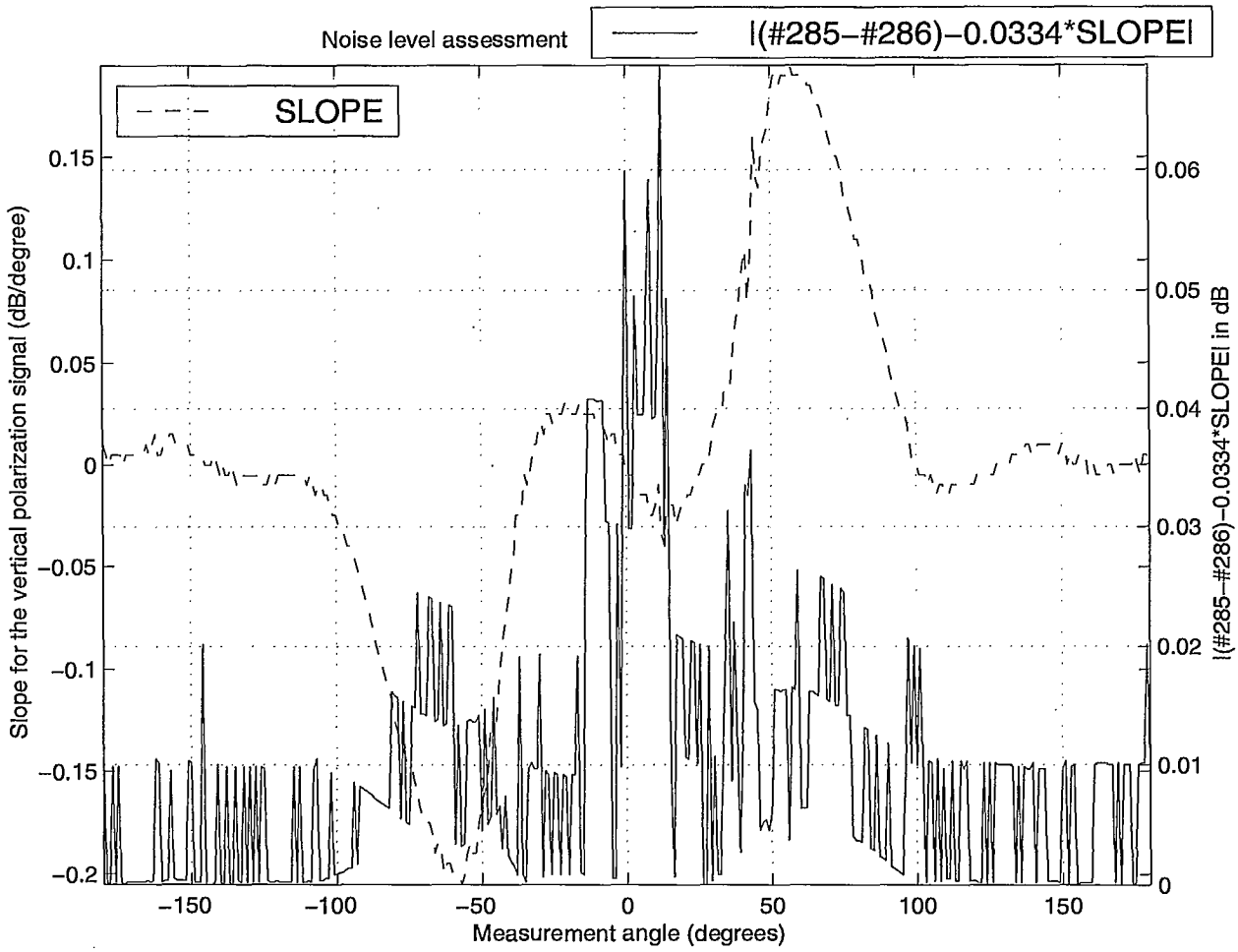

Figure 4.8: The dashed curve shows the slope corresponding to the data for the vertical polarization. The solid curve shows the electrical noise level (absolute value) obtained after subtracting the data smearing effect from the difference curve for the vertical polarization.

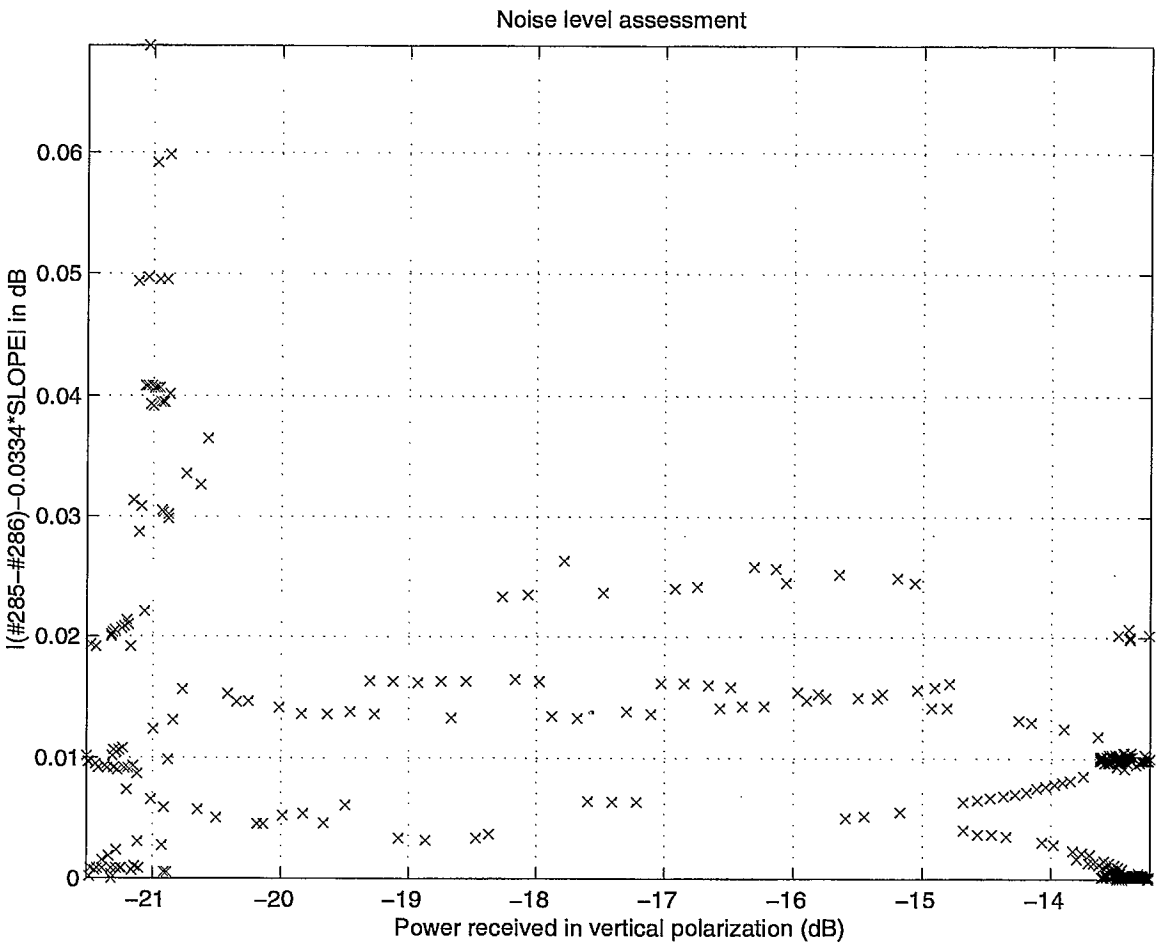

Figure 4.9: The plot shows the spread distribution of the noise amplitude of Figure 4.8 with respect to signal strength for the vertical polarization.

4.2 Repeatability assessment

In this section, the variation in repeatability due to the following factors is investigated:

- electrical noise (see Figures 4.10 to 4.19);
- a slight re-levelling of the transmitter (see Figures 4.26 to 4.29);
- a slight re-levelling and 3 *mm* rearward re-positioning of the transmitter (see Figures 4.20 to 4.24);
- a slight change to the absorbing material configuration inside the chamber (see Figures 4.30 to 4.33);
- battery DC power level variation.

4.2.1 Data variation due to electrical noise

The variations in repeatability due to the electronic measuring equipment was assessed by repeating a scan immediately without disturbing the test setup in any way. The corresponding difference curves consisting of the difference in received power between an original and its exact repeat experiments are shown in Figures 4.10 and 4.11 for the three orientations of the transmitter in the first test. No data smearing effect is present in the difference curves because the same amount of smearing occurred in both the original and its exact repeat experiments for each difference curve. However, linear regression was required on each difference curve to eliminate the power variation caused by the power drain of the battery pack so as to be left with only the noise effect. Whenever the process of linear regression did not yield the same slope value for both the horizontal and the vertical polarization curves of a same setup, the slope value was chosen as the one among the two polarization curves that provided the most satisfactory fit for that setup. Then, applying this slope value for curve-fitting the data of the polarization curve whose slope was discarded required

also to recompute the intercept value for that linear regression. Figures 4.12 shows an example of this procedure.

Let us try to account for the effect of a noise power level p in presence of the signal power level P. Assuming that the noise is additive (on the linear scale), then the measured data from the network analyser corresponds to the value:

$$10\log_{10}\left(\frac{P+p}{P_{ref}}\right) = 10\log_{10}\left(\frac{P}{P_{ref}}\right) + 10\log_{10}\left(1+\frac{p}{P}\right)$$

where P_{ref} is a reference power level (e.g. 1 mW). Assuming that the noise has a Normal probability density distribution such that the resulting sum (or difference) of two noise components is given by the square root of the sum of the square of each component, then the difference between the network analyser results for two test runs produces:

$$\begin{aligned}\Delta P &= 10\log_{10}\left(\tfrac{P_2+p}{P_{ref}}\right) - 10\log_{10}\left(\tfrac{P_1+p}{P_{ref}}\right) \\ &= 10\log_{10}\left(\tfrac{P_2}{P_{ref}}\right) - 10\log_{10}\left(\tfrac{P_1}{P_{ref}}\right) + 10\log_{10}\left(\sqrt{\left(1+\tfrac{p}{P_2}\right)^2 + \left(1+\tfrac{p}{P_1}\right)^2}\right)\end{aligned}$$

Note that the deterministic signal subtracts but the stochastic signal adds because the stochastic signal is uncorrelated in time. For $P_2 = P_1 \equiv P$, the last expression becomes:

$$\begin{aligned}\Delta P &= 10\log_{10}\left(\sqrt{2}\left(1+\tfrac{p}{P}\right)\right) \\ &= 10\log_{10}\sqrt{2} + (10\log_{10} e)\ln(1+\tfrac{p}{P}) \\ &= 10\log_{10}\sqrt{2} + (10\log_{10} e)\,\tfrac{p}{P}\left(1+\textstyle\sum_{n=1}^{\infty}\frac{(-1)^n(\frac{p}{P})^n}{n+1}\right) \\ &\approx 10\log_{10}\sqrt{2} + (10\log_{10} e)\,\tfrac{p}{P} \\ &\approx 1.5 + 4.3\tfrac{p}{P}\end{aligned}$$

where the binomial expansion for ln was used under the condition $\frac{p}{P} \leq 1$. On a graph with $Y = \Delta P$ lying on the vertical axis and $X = 10\log_{10}\left(\frac{P}{P_{ref}}\right)$ lying on the horizontal axis, the last expression becomes:

$$Y \approx 1.5 + 4.3\frac{p}{P_{ref}}10^{-\frac{X}{10}}$$

and we obtain:

$$\frac{dY}{dX} \approx -\frac{p}{P_{ref}} 10^{-\frac{X}{10}}$$

Thus, Y in dB increases exponentially as X in dB becomes more negative, and the rate of change of Y is proportional to the noise power level p.

Figures 4.13, 4.14 and 4.15 show the spread distribution of the noise data for each orientation of the transmitter in the first test. Clearly, as predicted above, the envelope increases somewhat exponentially as the signal strength decreases but surprisingly, the noise level appears to be different for different orientations (for a given polarization the rate of change of the envelope can be different for two different orientations of the transmitter as seen from Figure 4.16). Since it is not likely that the oscillator within the transmitter produced a different noise level for different orientations of the transmitter, the observation of the different noise level for different orientations suggests that something in the anechoic chamber could generate noise upon being illuminated by the radiation from the transmitter such that the level of this noise varied with the strength of the illumination. It is surmised that the top surface of the azimuth table covered with a two-dimensional array of threaded holes with 5 cm interspacing for the purpose of allowing the capability of affixing various objects onto the table might present a seemingly random scattering as the azimuth table was rotated, the table being illuminated more strongly when the transmitter was in the edge or the flat orientations. Alternatively, the source of the noise might also result from a variation of the multipath in reaching the receive horn, within the chamber as the azimuth table was rotated.

Figures 4.13 to 4.16 show that over a same range of signal strength values, the flat orientation produced by far the highest noise level whereas the vertical orientation produced the lowest level. It is also interesting to observe that the noise level for the vertical orientation is much less here than that obtained with the externally DC power supplied transmitter as part of the data smearing assessment (see Figure 4.7). It is surmised that some electrical noise was being picked up by the long DC power supply wire, that some of this noise passed through the DC supply filter to reach the oscillator inside the transmitter, and that this situation resulted in an increase of the noise level at the RF output of the oscillator.

Due to the lack of time availability of the chamber, no repeat measurements were done for the second and third tests. Thus, the data for the assessment of the electrical noise with the Head-up-Nose-forward orientation of the second test comes from a previous set of measurements, whereby the receive horn had been positioned deep within rather than at the aperture of the pyramidal extension of the chamber. Afterwards, this configuration was found to be unsatisfactory due to the presence of unwanted reflections off the metallic walls of the pyramidal extension (compare the results for run #265 in Figure 4.17 and the results for run #279 in Figure 3.7). Hence, the whole set of measurements was redone and the results are reported in this document. However, for the purpose of assessing the effect of the electrical noise, the data from the previous set of measurements could be used when the test setup remained identical between two consecutive runs.

Figure 4.19 shows that the data variation due to electrical noise for the Head-up-Nose-forward orientation of the second test is about the same as that for the edge orientation (see Figure 4.14) of the first test. This situation is reasonable since the transmitter lies mostly on its edge for the Head-up-Nose-forward orientation of the second test (compare the results for run #276 in Figure 3.5 and the results for run #279 in Figure 3.7 while also taking into account a 180° phase shift between them). This situation suggests that the noise level for the runs of the second and third tests could roughly be assumed to be about the same as that for the first test. Admittedly, this observation is based on the assumption that the noise envelope is sufficiently described by the ensemble of data points plotting the spread distribution of the noise.

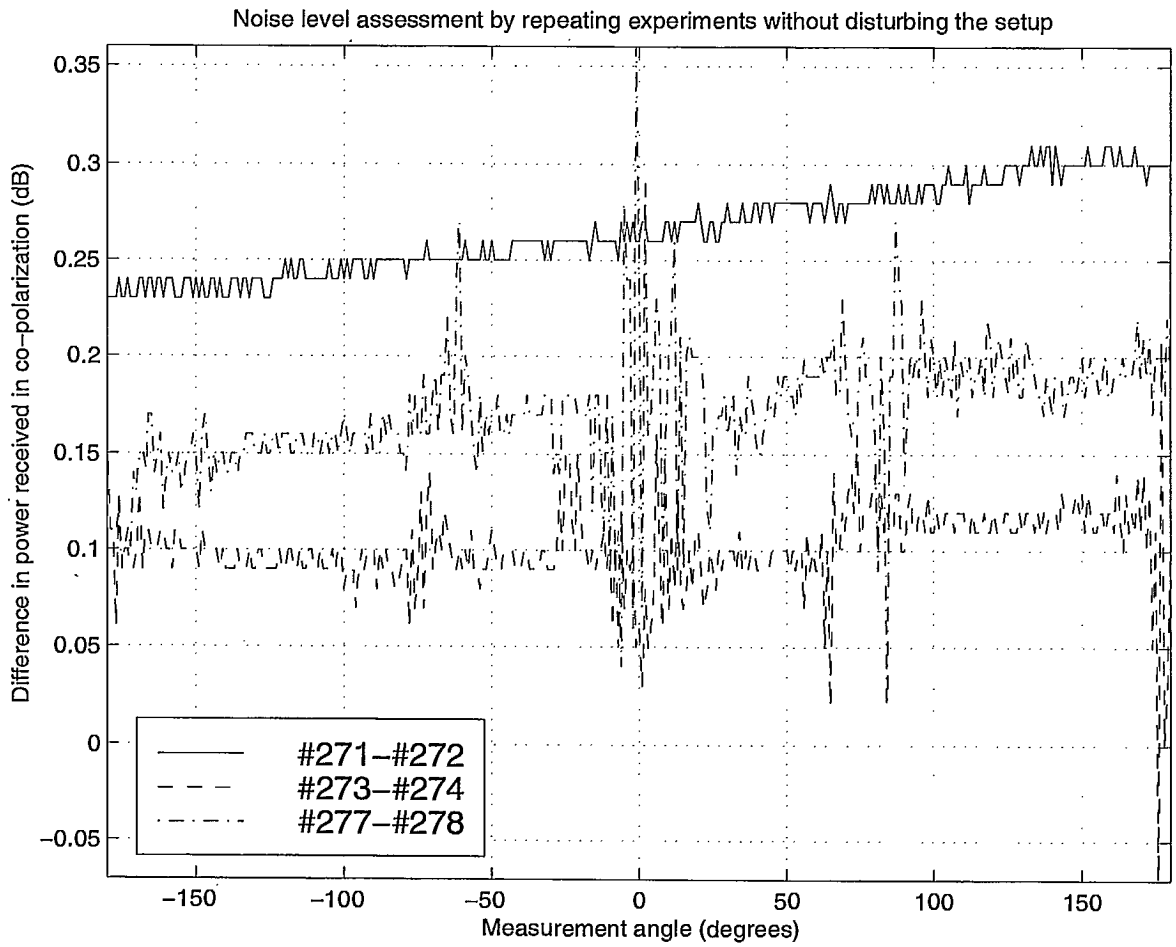

Figure 4.10: Repeatability test to assess the data variation due to electrical noise. The three plots correspond to the difference curves for the co-polarization with the transmitter in the three orientations of the first test.

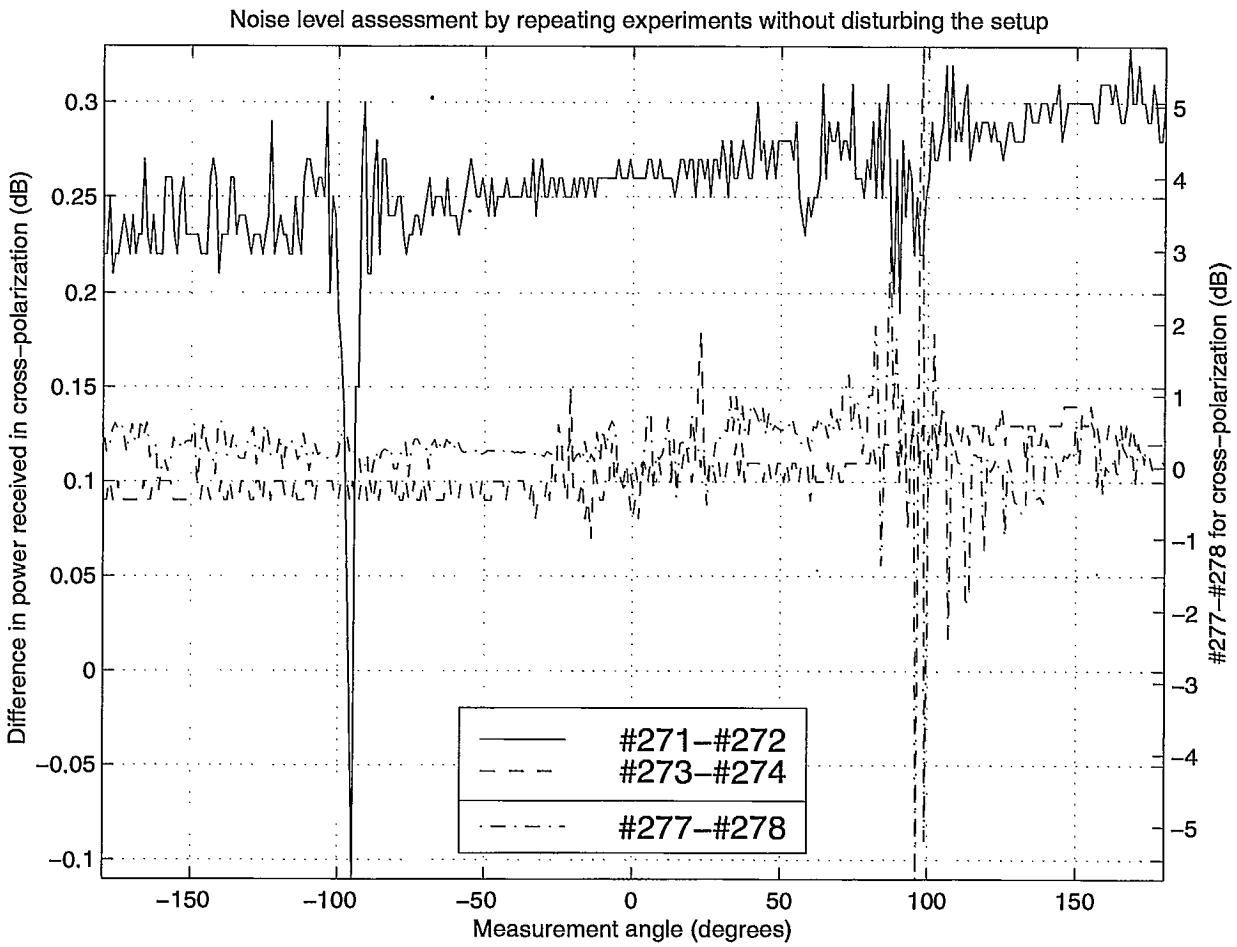

Figure 4.11: Repeatability test to assess the data variation due to electrical noise. The three plots correspond to the difference curves for the cross-polarization with the transmitter in the three orientations of the first test. A different scale shown on the right of the plot was used for the flat orientation (#277-#278).

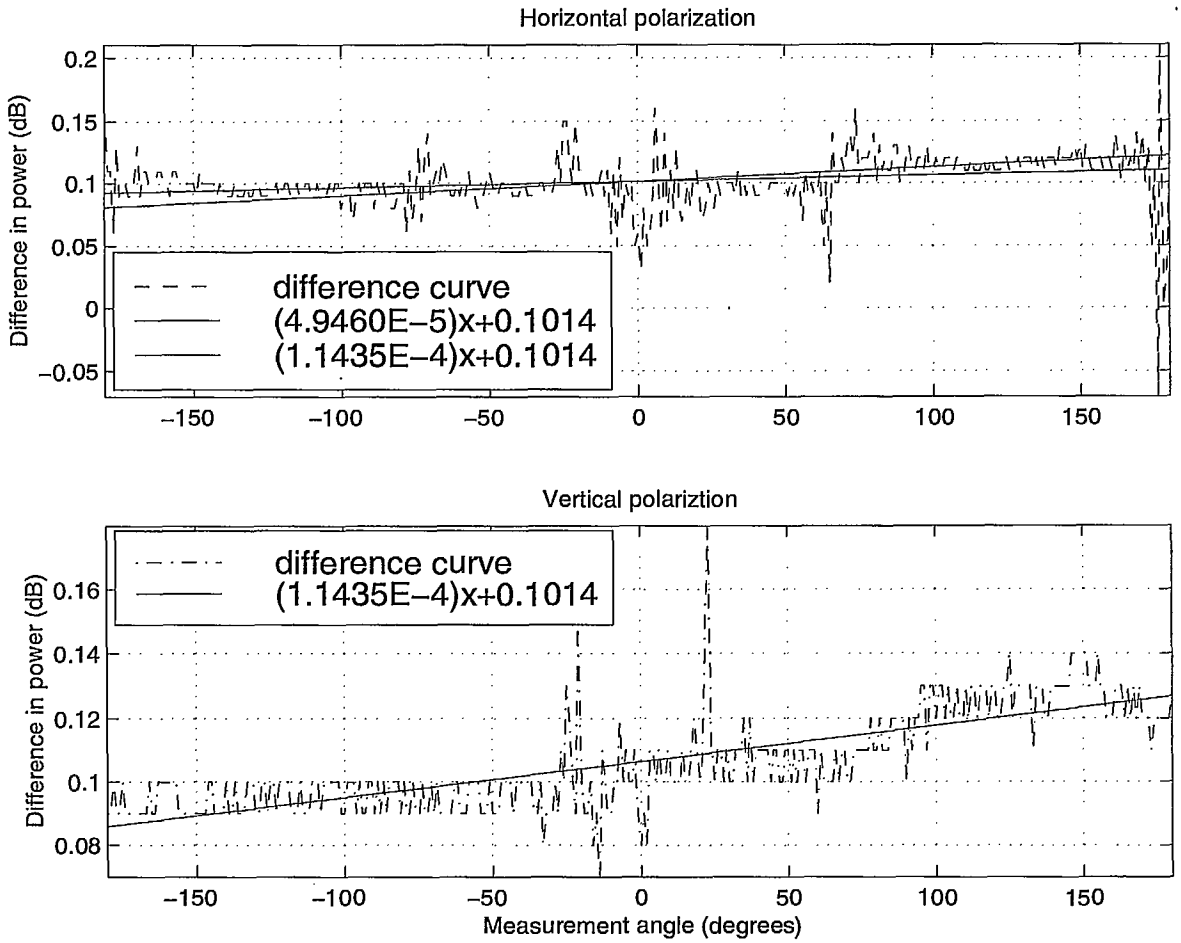

Figure 4.12: The top plot shows the results from two different linear regressions on the difference curve for the horizontal polarization with the transmitter in the edge orientation of the first test. The initial result with slope $m = 4.9460E - 5$ is seen to be less than fully satisfactory whereas the result with slope $m = 1.1435E - 4$ obtained from the linear regression for the vertical polarization shown in the bottom plot is seen to be more satisfactory.

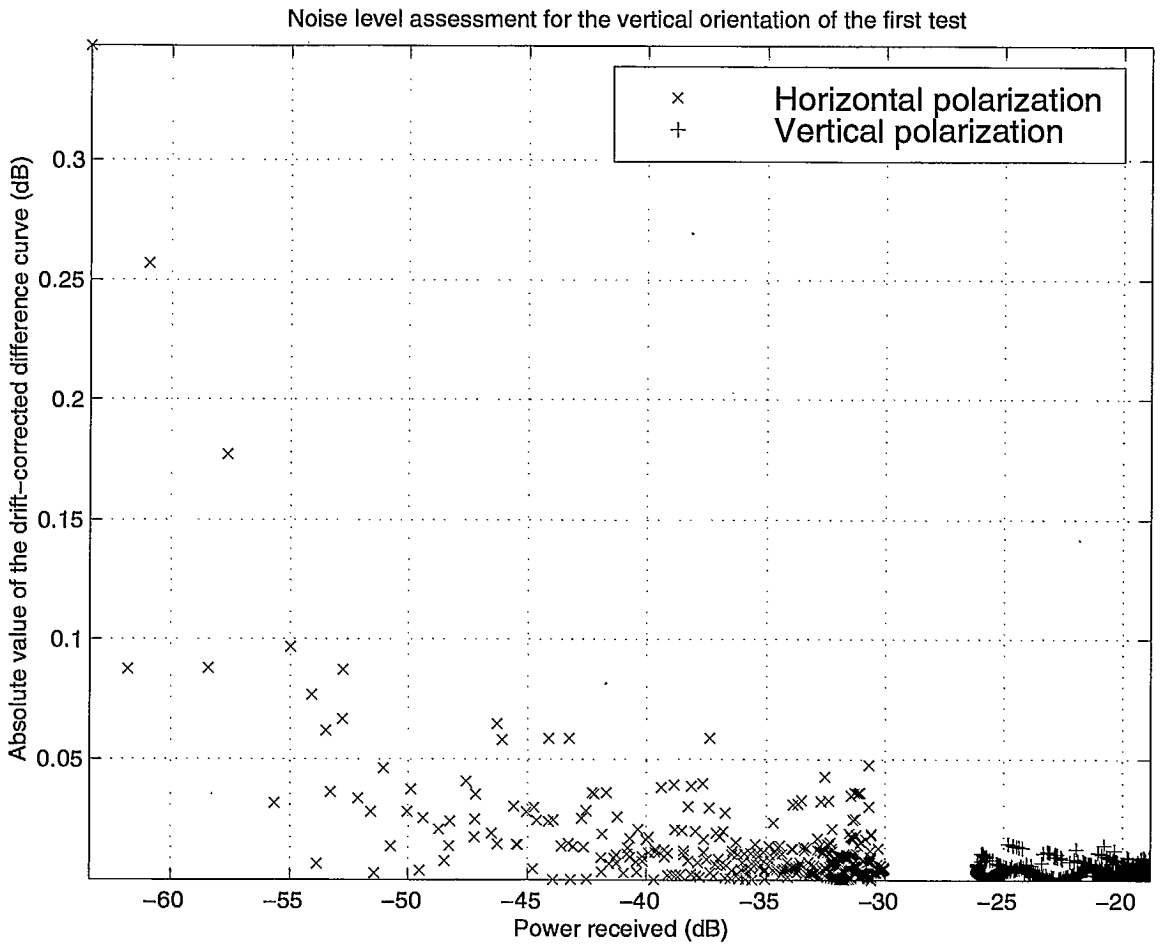

Figure 4.13: The plot shows the spread distribution of the noise amplitude with respect to signal strength for the vertical orientation of the transmitter in the first test.

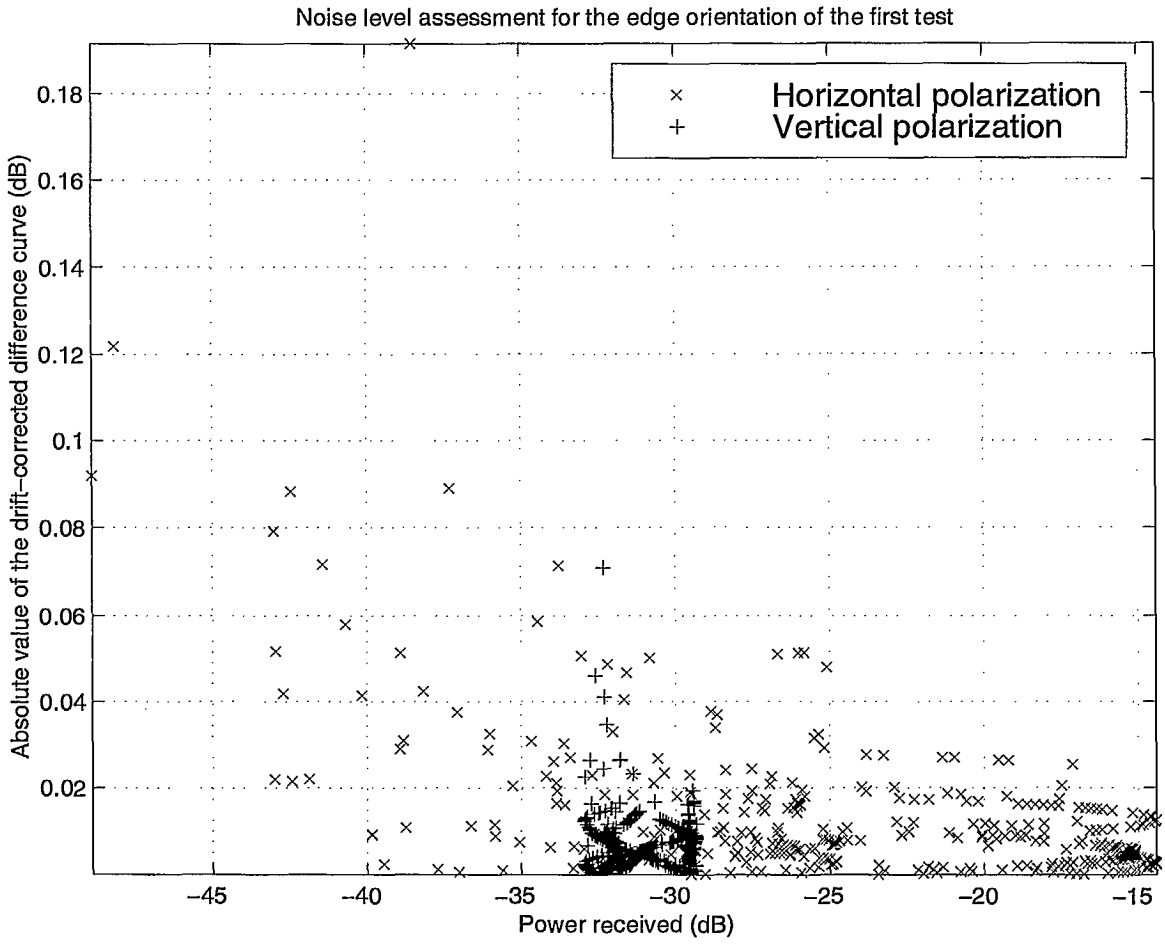

Figure 4.14: The plot shows the spread distribution of the noise amplitude with respect to signal strength for the edge orientation of the transmitter in the first test.

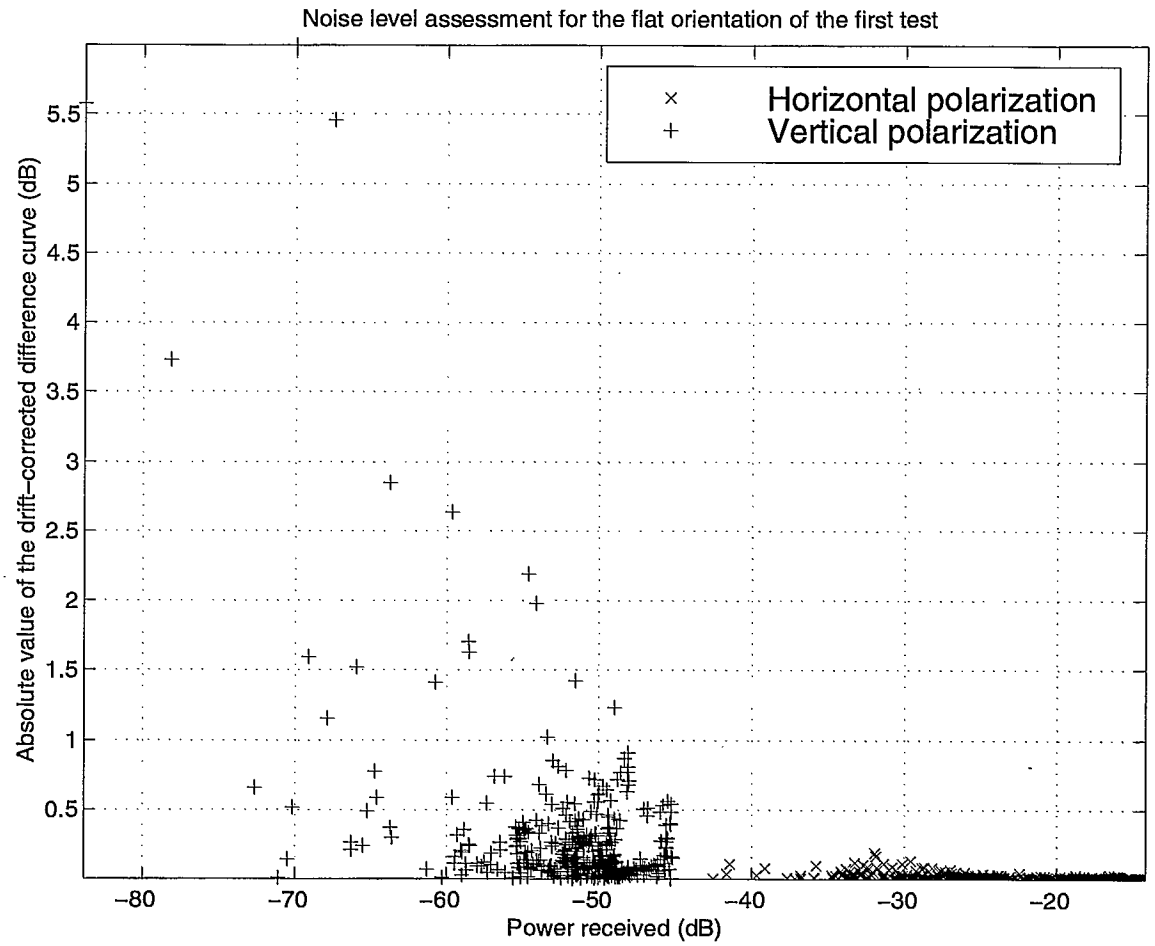

Figure 4.15: The plot shows the spread distribution of the noise amplitude with respect to signal strength for the flat orientation of the transmitter in the first test.

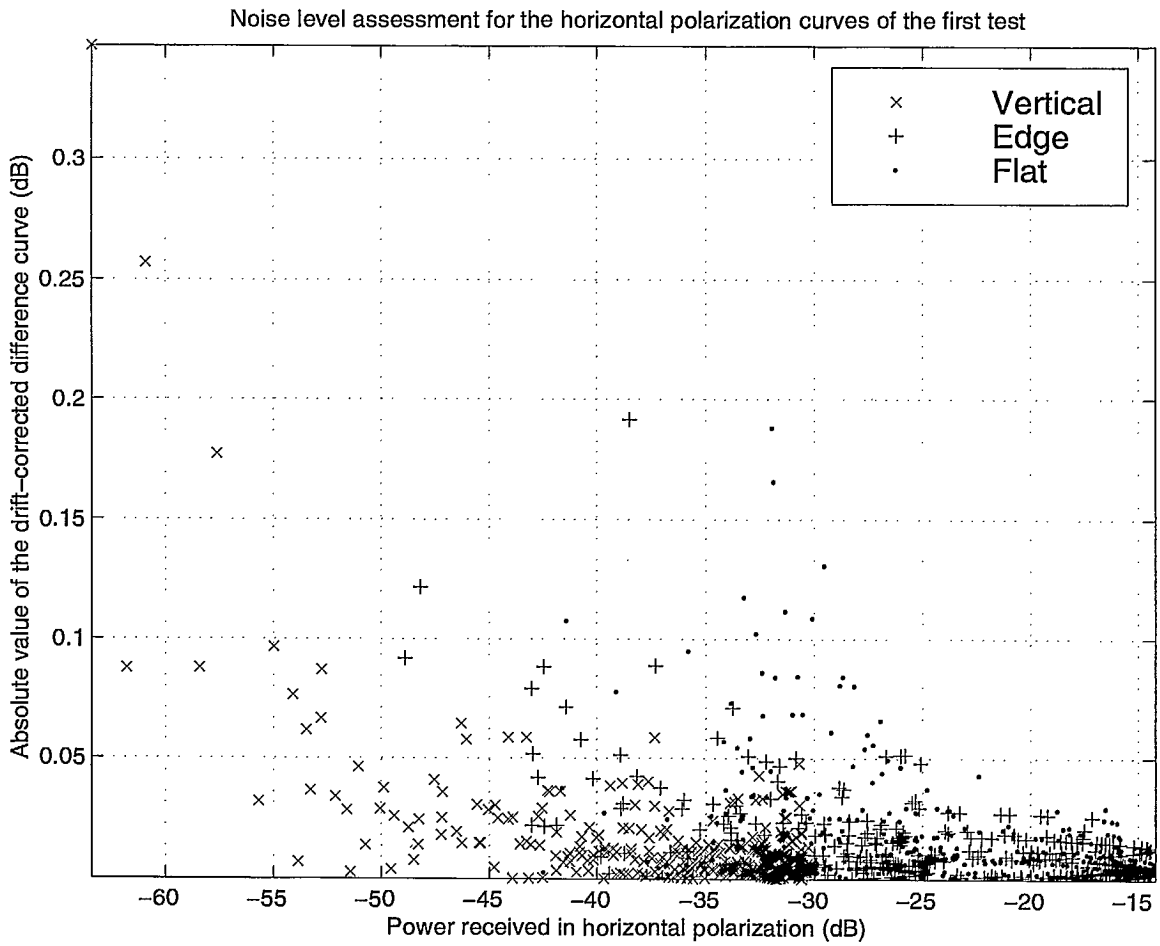

Figure 4.16: The plot shows the spread distribution of the noise amplitude with respect to signal strength for the horizontal polarization for the three orientations of the transmitter in the first test.

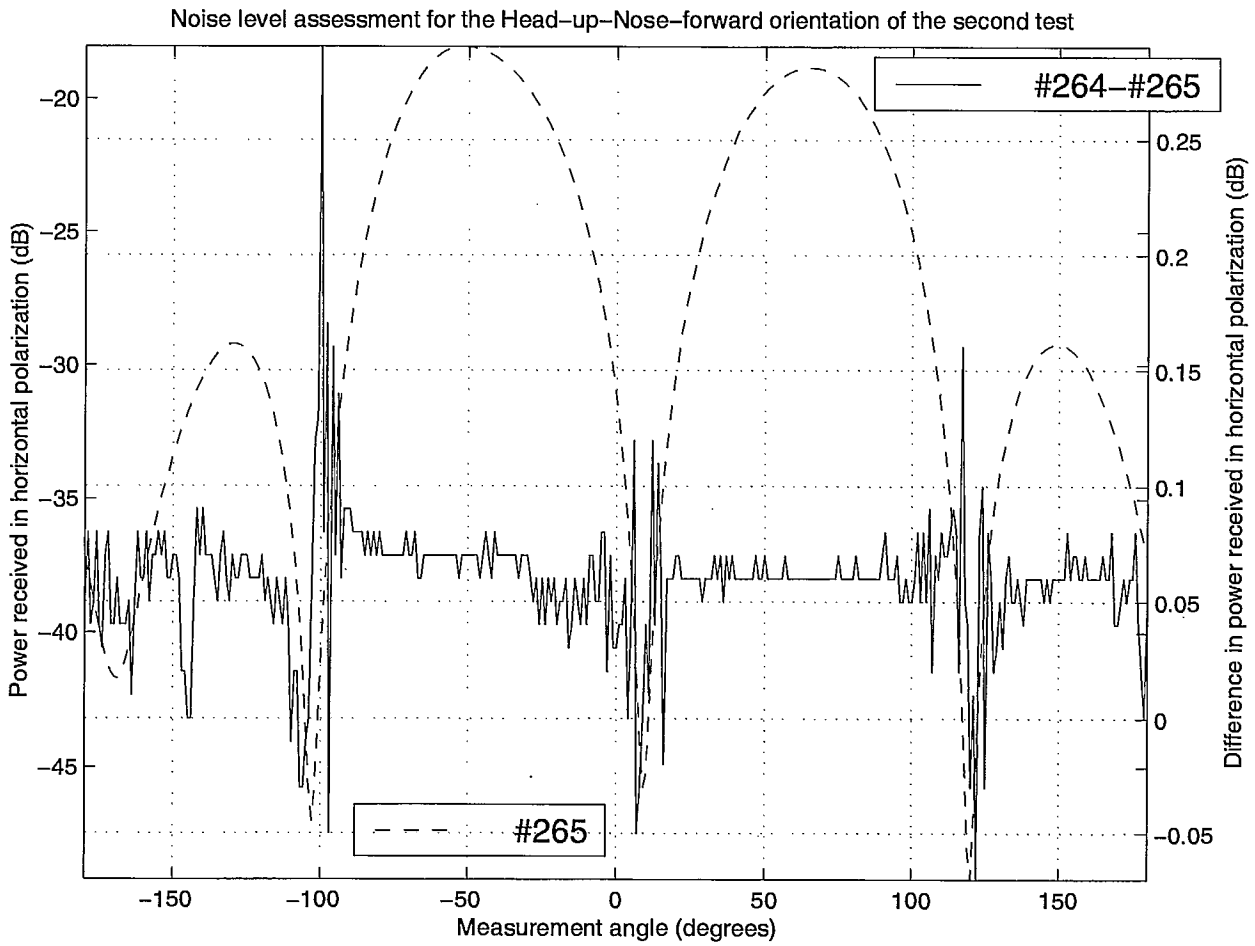

Figure 4.17: Repeatability test to assess the data variation due to electrical noise. The plot corresponds to the difference curve for the horizontal polarization with the Head-up-Nose-forward orientation of the second test.

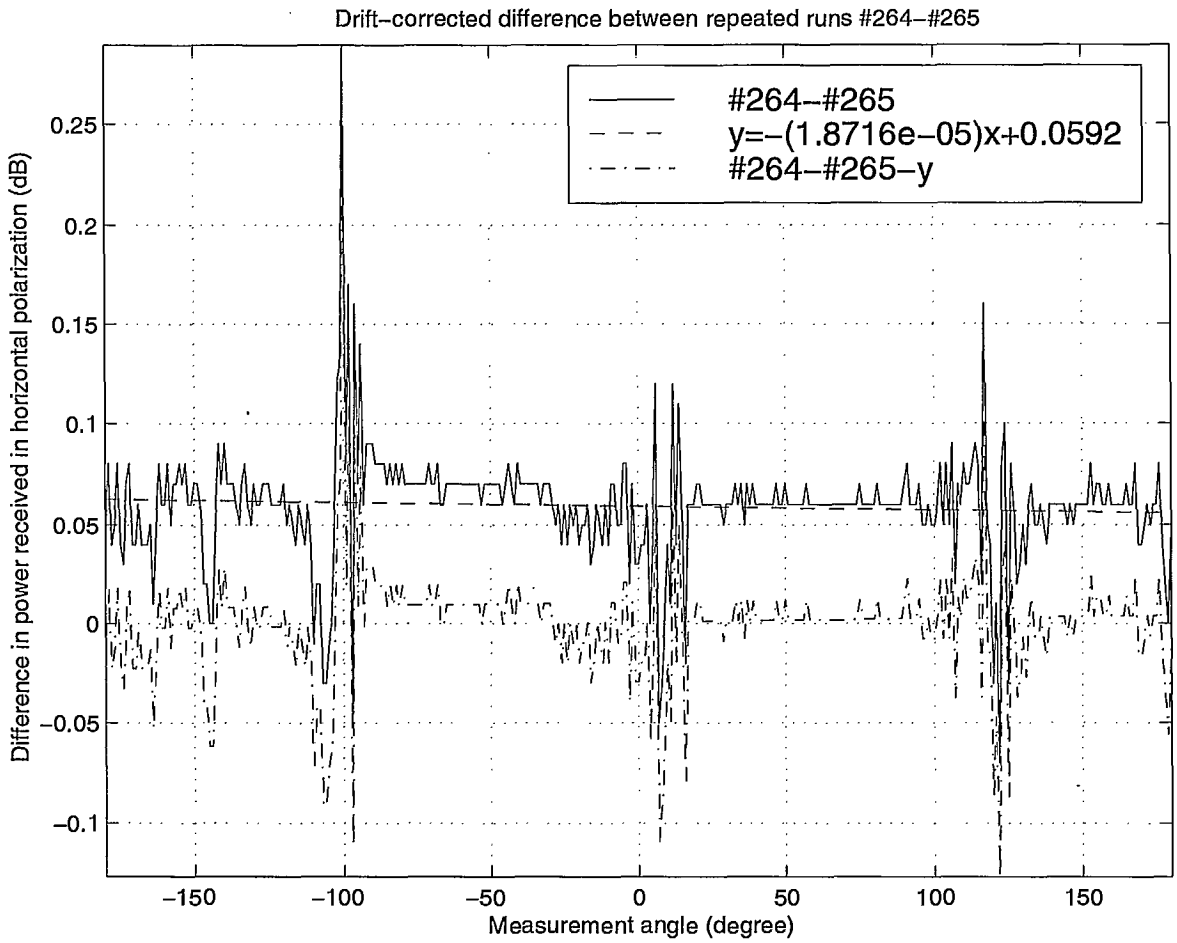

Figure 4.18: Repeatability test to assess the data variation due to electrical noise for the horizontal polarization with the Head-up-Nose-forward orientation of the second test. The plot shows the result of applying drift correction for taking out the data variation caused by the draining of the battery.

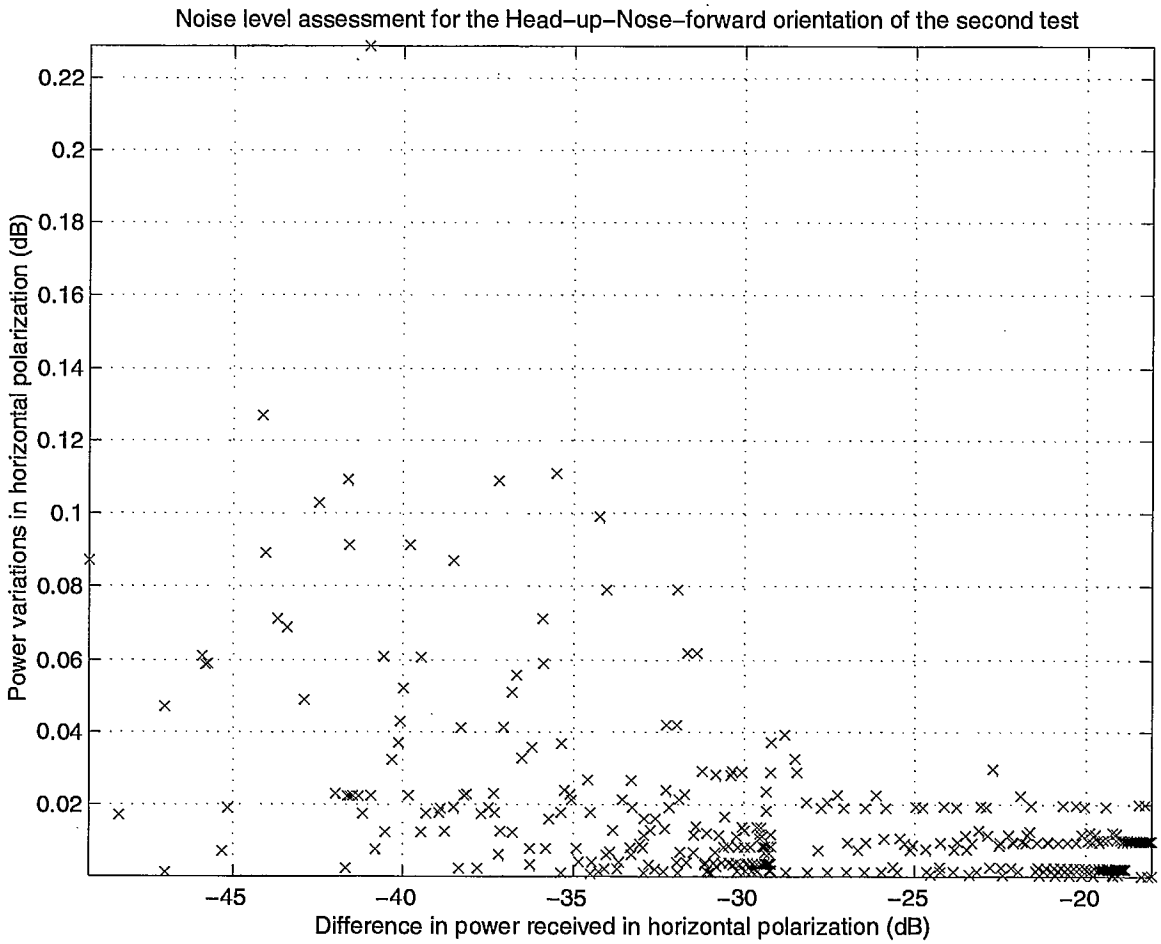

Figure 4.19: The plot shows the spread distribution of the noise amplitude with respect to signal strength for the horizontal polarization of the Head-up-Nose-forward orientation in the second test.

4.2.2 Data variation due to re-positioning and re-levelling the transmitter

Figure 4.20 shows the results from various data processing steps for run #276.

Figure 4.21 shows that the variation in the vertical polarization due to the combination of re-positioning and re-levelling the transmitter is not noise-like and lies significantly above the envelope for noise alone by up to about 0.16 dB. Figure 4.24 shows that the spread distribution for the horizontal polarization has an envelope that is much larger than that for the noise alone, while Figure 4.23 shows clearly the presence of a non-noise-like component in the difference curve. The difference can be as large as about 1 dB in deep nulls of the pattern.

This difference is reminiscent of the result obtained from taking the difference between two identical but slightly shifted patterns. Figure 4.25 shows the result for a 1° shift in either direction. A smaller shift would result in an even smaller difference. However, comparison between Figures 4.23 and 4.25 suggests that the shift would need to vary differently in both amplitude and direction over various angular ranges. This situation suggests that in terms of the complete radiation pattern existing on the observation sphere centred about the D.U.T., the radiation pattern corresponding to one measurement would be slightly distorted with respect to that corresponding to the other measurement such that the shift would vary in both amplitude and direction.

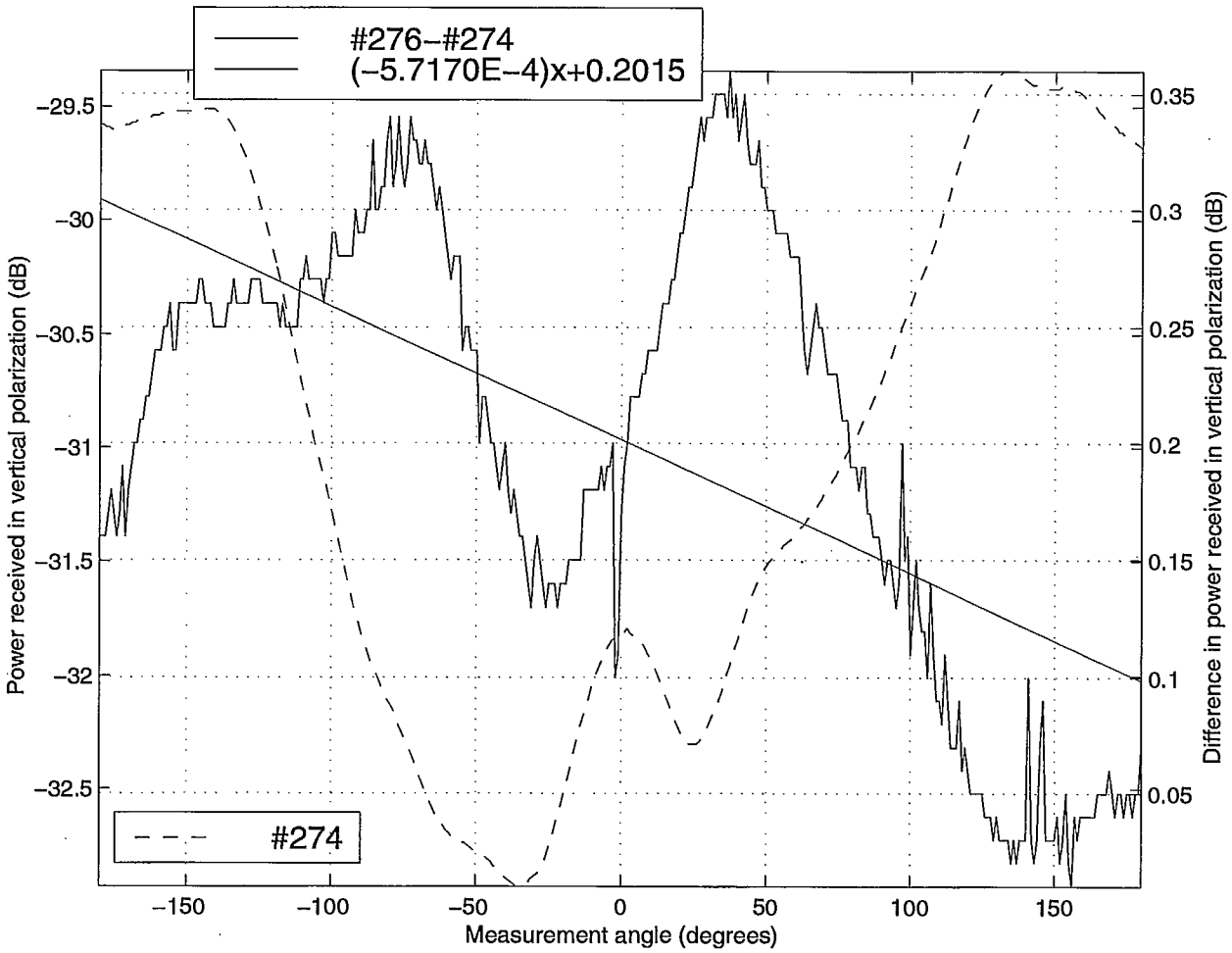

Figure 4.20: Variation of the vertical polarization data due to the combination of electrical noise, changing the battery pack, re-positioning the transmitter 3 mm rearward and re-levelling the transmitter in the edge orientation of the first test.

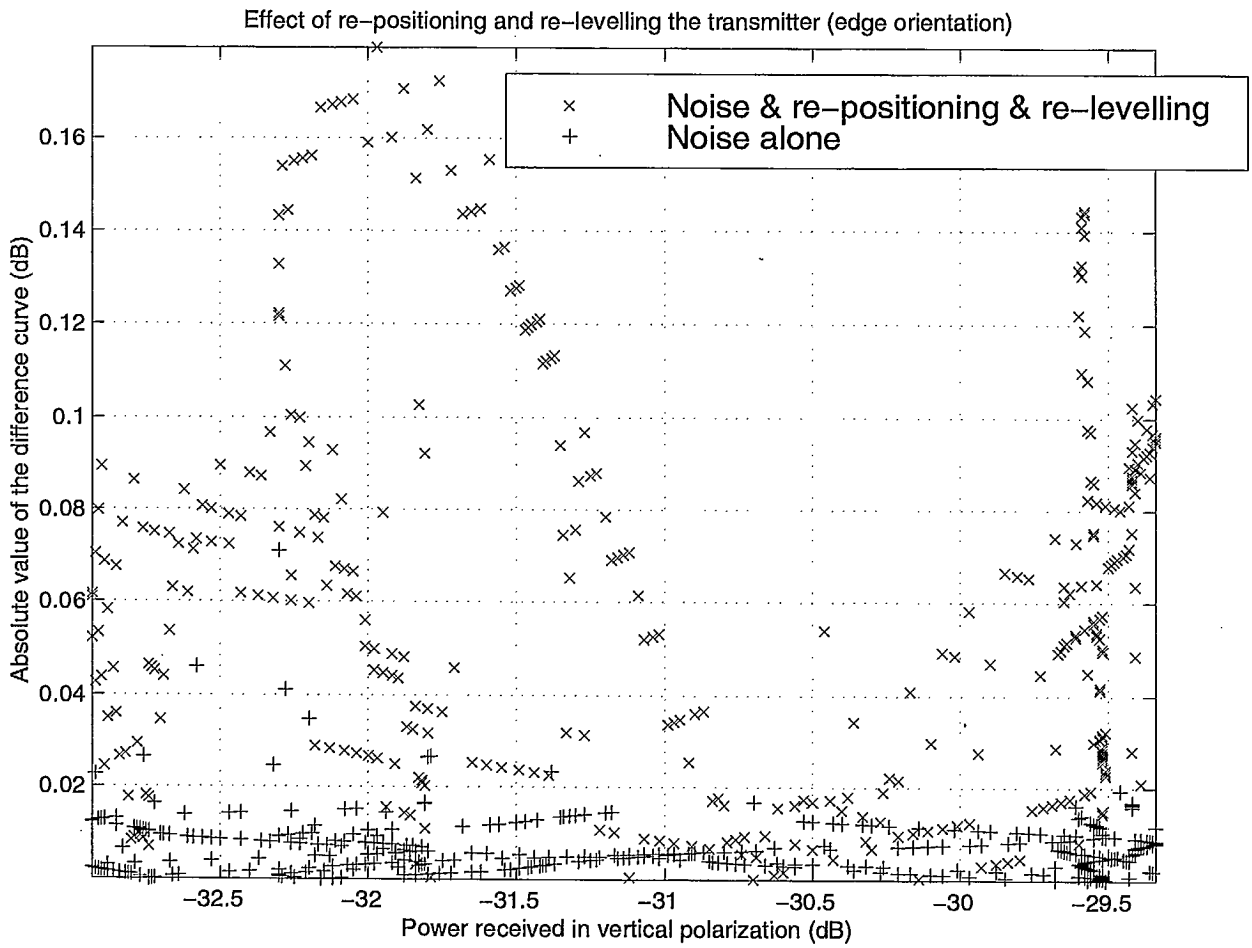

Figure 4.21: The plot shows the spread distribution of the drift-corrected data corresponding to Figure 4.20 with respect to signal strength.

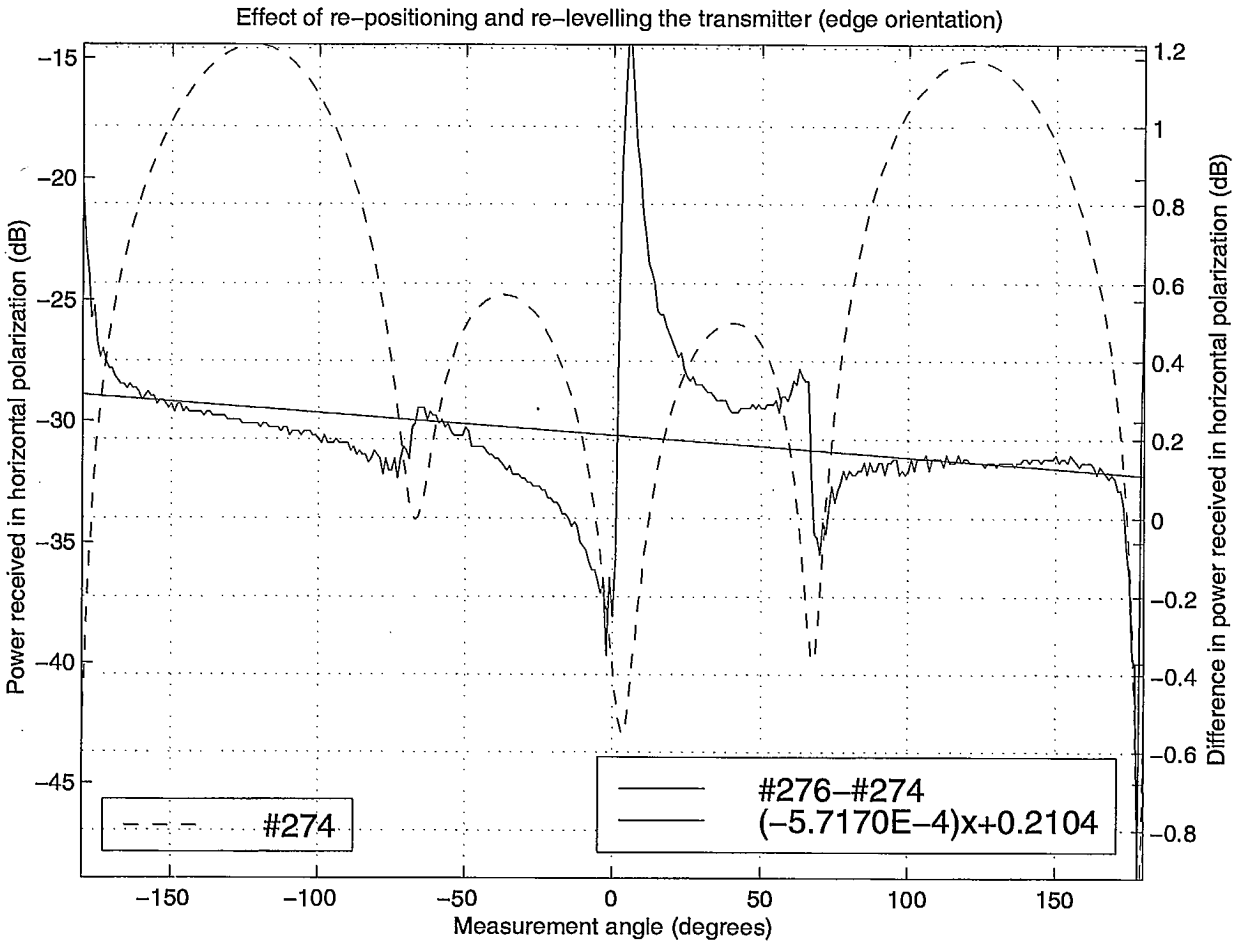

Figure 4.22: Variation of the horizontal polarization data due to the combination of electrical noise, changing the battery pack, re-positioning the transmitter 3 *mm* rearward and re-levelling the transmitter for the edge orientation of the first test.

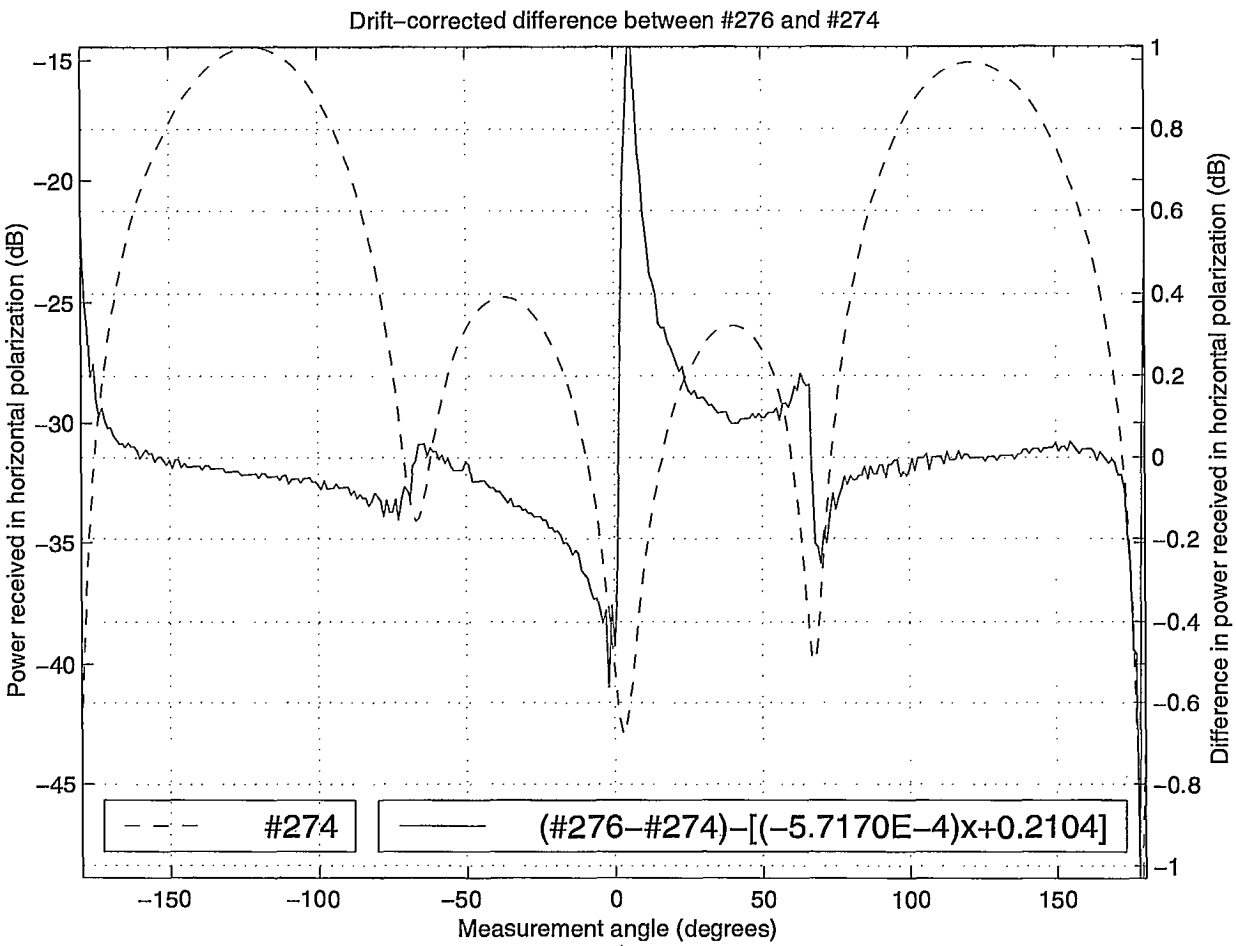

Figure 4.23: Drift correction of Figure 4.22 to eliminate the variation caused by the drainage of the battery pack.

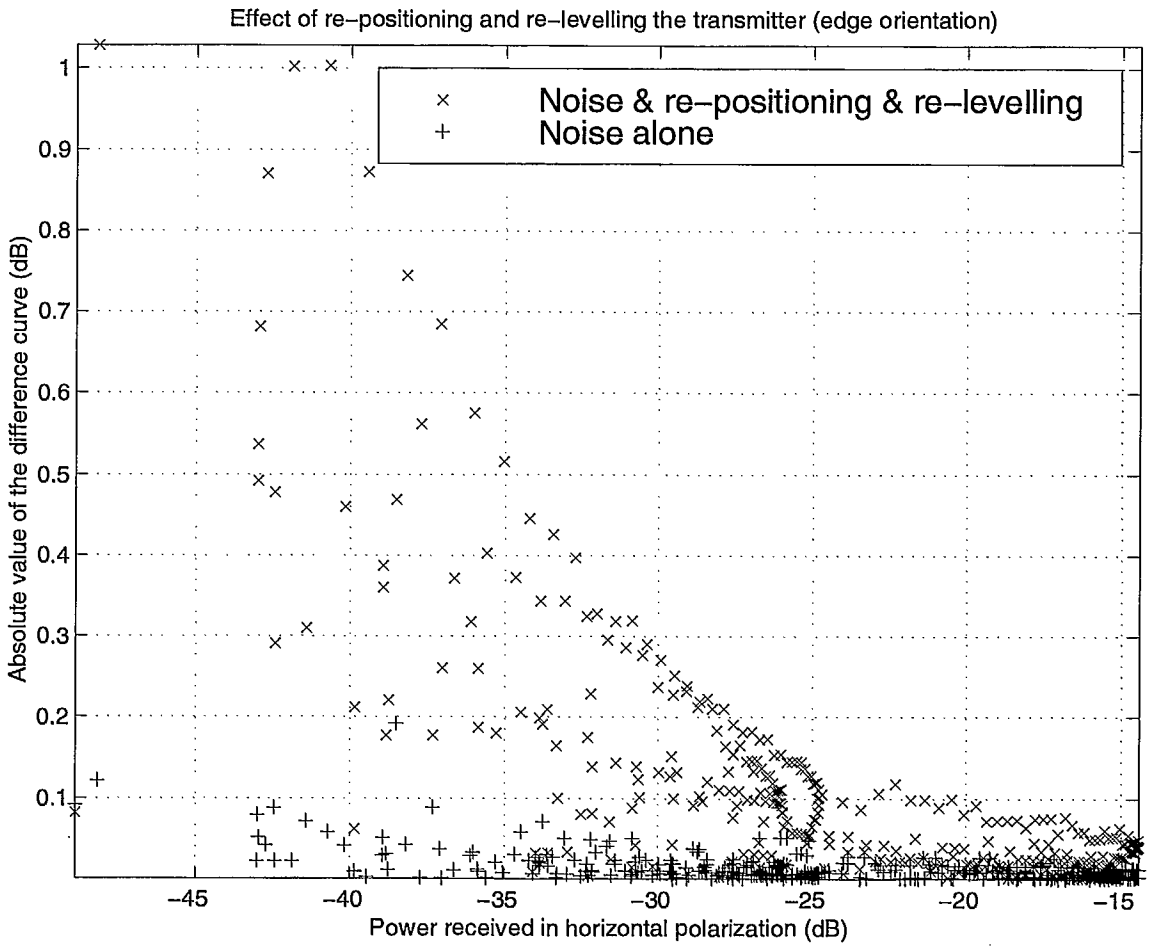

Figure 4.24: The plot shows the spread distribution of the data in Figure 4.23 with respect to signal strength.

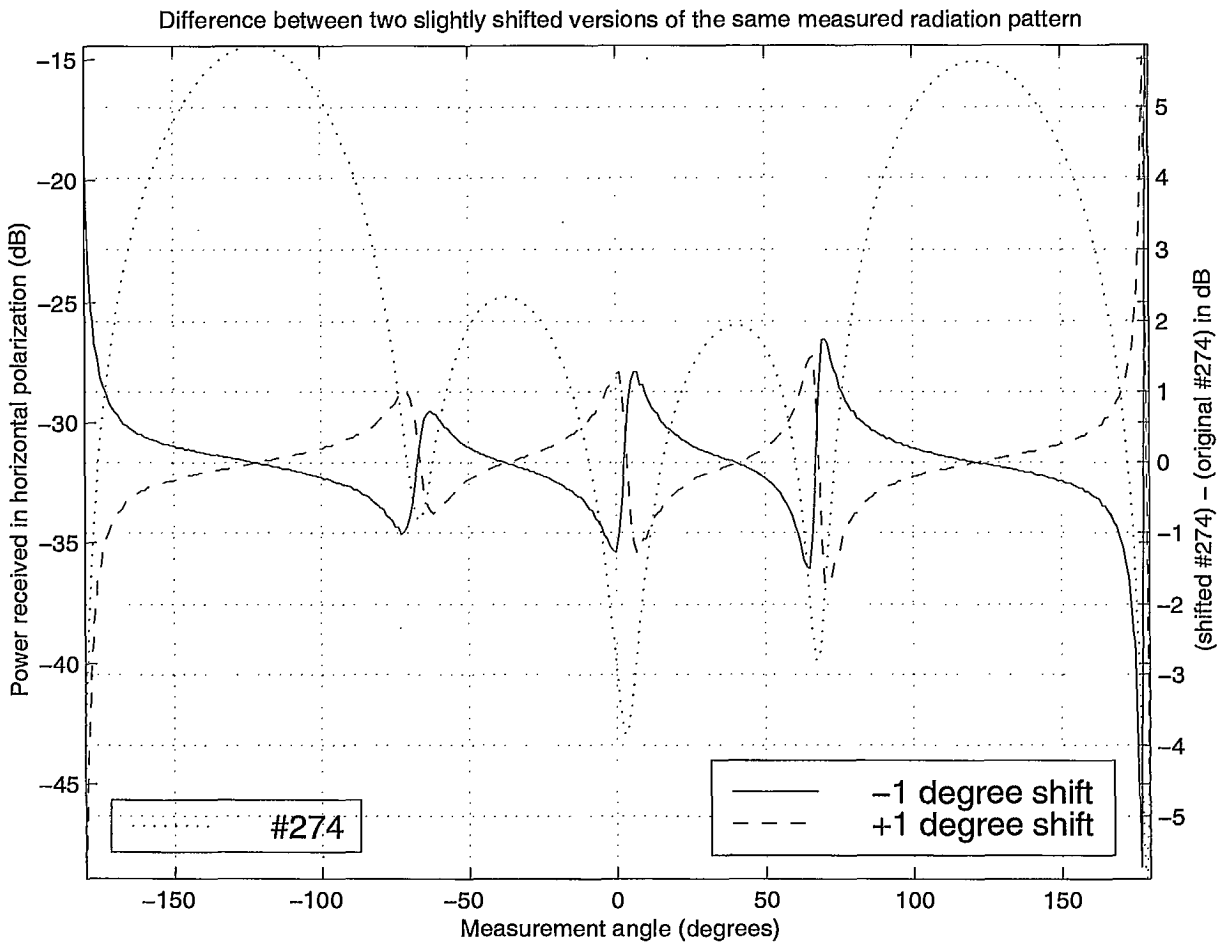

Figure 4.25: Difference between two slightly shifted versions of the same radiation pattern measured with the transmitter in the edge orientation of the first test.

4.2.3 Data variation due to re-levelling the transmitter

Figure 4.26 shows the results from various data processing steps for run #275.

Figure 4.27 shows that the variation in the vertical polarization due to slightly re-levelling the transmitter is not noise-like and lies significantly above the envelope for noise alone by up to about 0.18 dB. Although Figure 4.29 shows that the spread distribution for the horizontal polarization has an envelope that is about the same as that for the noise alone, however, Figure 4.28 shows clearly the presence of a non-noise-like component in the difference curve. The difference can be as large as about 1.2 dB in deep nulls of the pattern. Although the values of 0.18 dB and 1.2 dB corresponding to re-levelling are similar to the values of 0.16 dB and 1.0 dB corresponding to the combination of re-positioning and re-levelling, however, a comparison between Figure 4.24 and 4.29 suggests that re-levelling causes a lesser error than the combination of re-positioning and re-levelling, as expected.

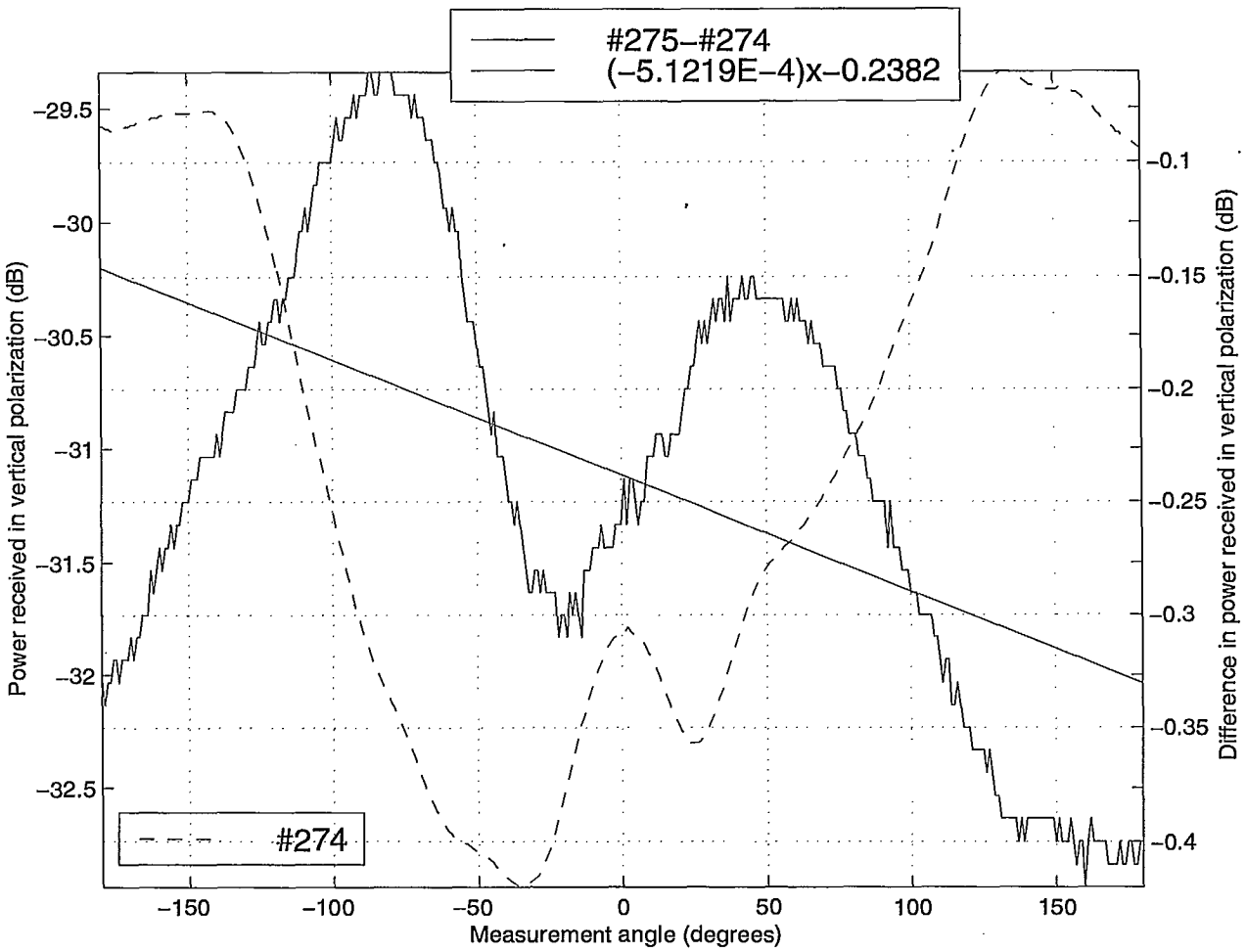

Figure 4.26: Variation of the vertical polarization data due to the combination of electrical noise, variation in the battery DC power level and a slight re-levelling of the transmitter in the edge orientation of the first test.

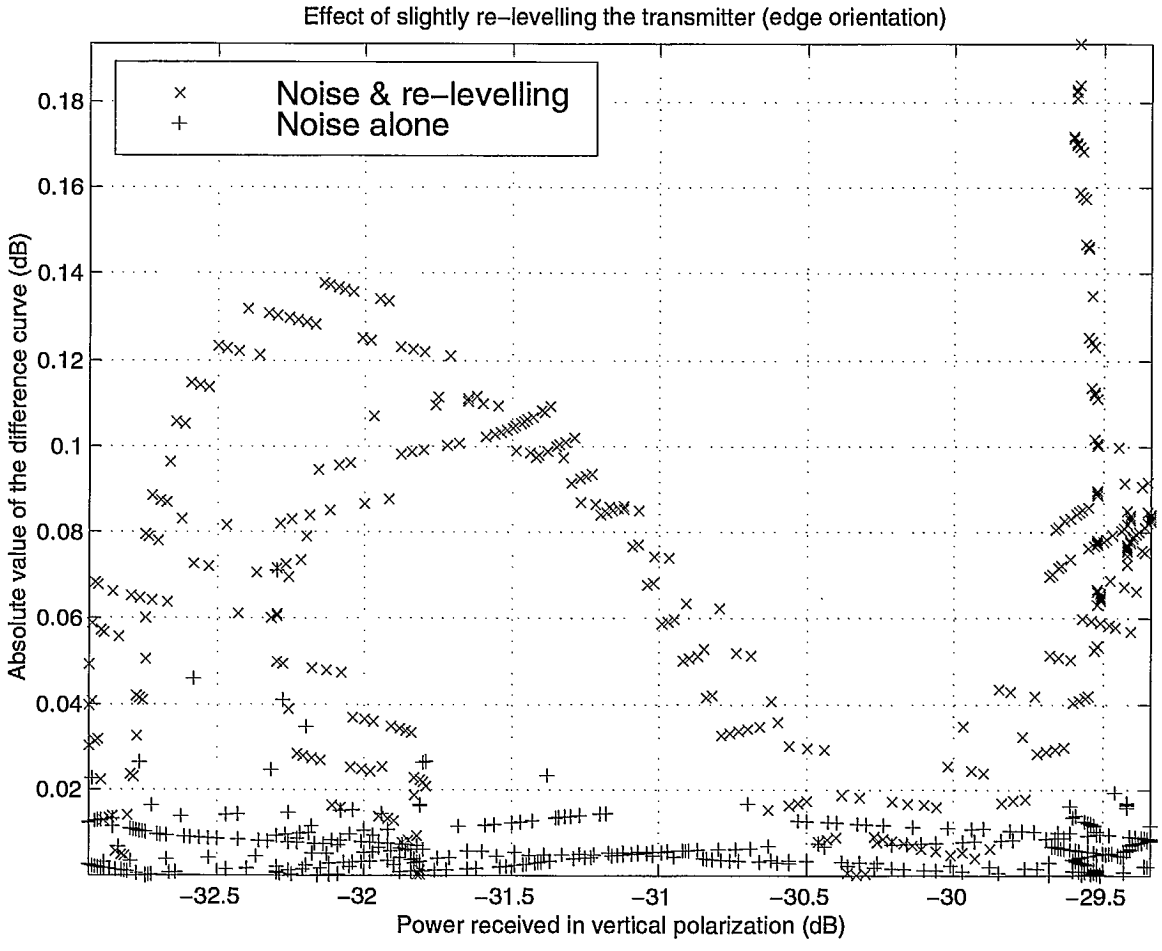

Figure 4.27: The plot shows the spread distribution of the drift-corrected data corresponding to Figure 4.26 with respect to signal strength.

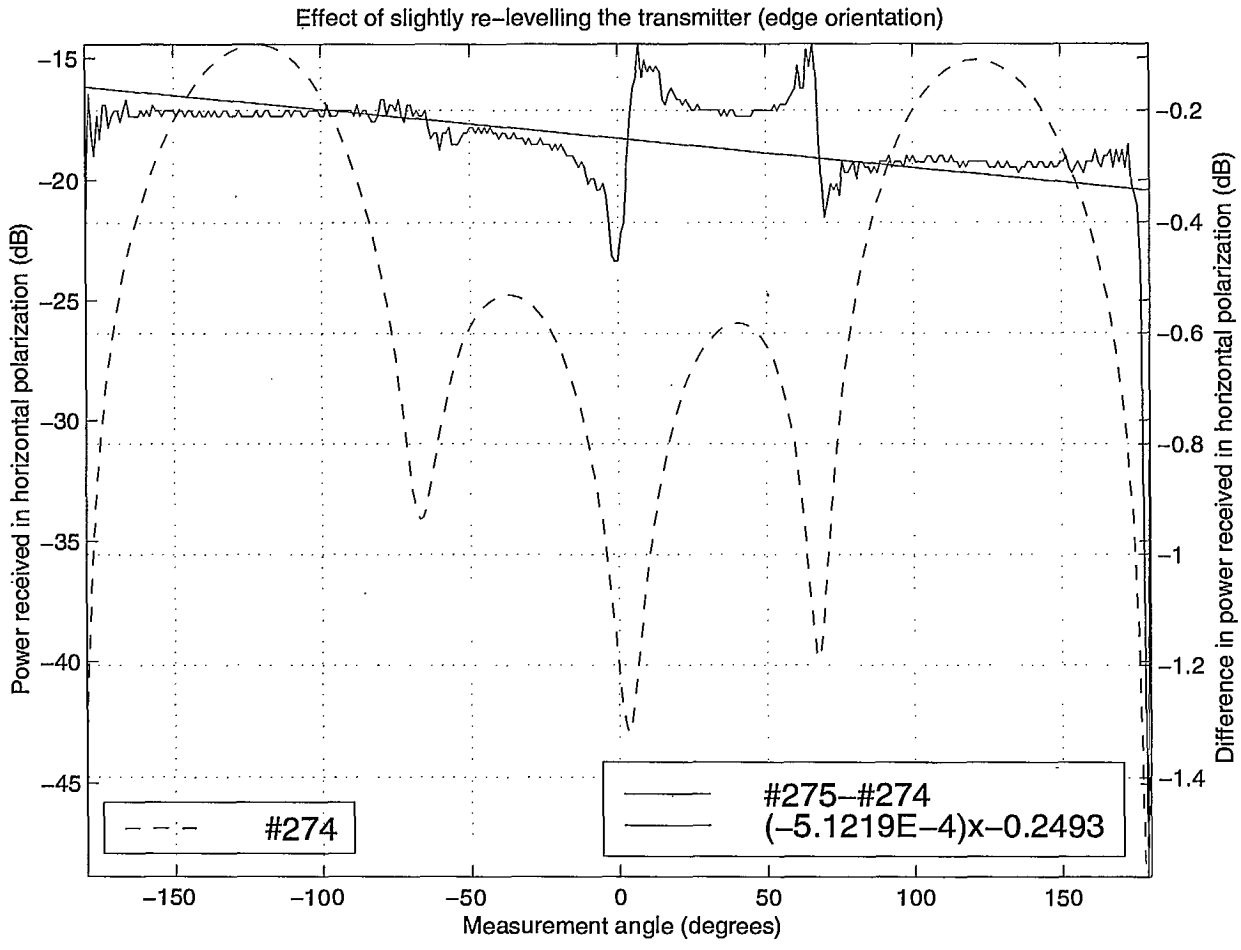

Figure 4.28: Variation of the horizontal polarization data due to the combination of electrical noise, variation in the battery DC power level and a slight re-levelling of the transmitter for the edge orientation of the first test.

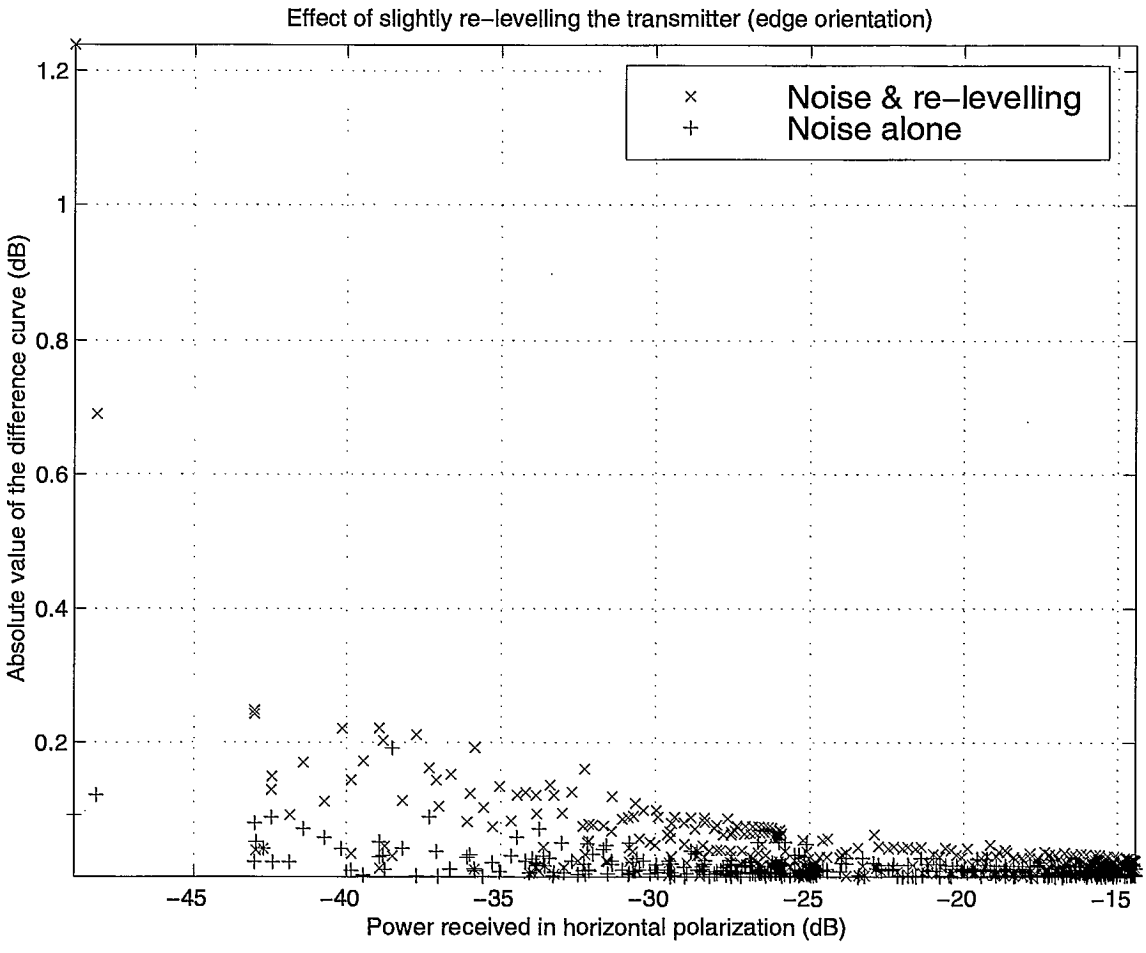

Figure 4.29: The plot shows the spread distribution of the drift-corrected data corresponding to Figure 4.28 with respect to signal strength.

4.2.4 Data variation due to re-positioning some absorber

Figure 4.30 shows the results from various data processing steps for run #271.

Figure 4.31 shows the variation in the vertical polarization due to the combination of padding the lowermost end of the control cable hanging from the ceiling, and re-positioning the absorbing cones beside the heavy rail such that the cones leaned at about 45° angle against the side of the heavy rail. The variation is seen to be non-noise-like and to lie significantly above the envelope for noise alone by up to about $0.03\ dB$. Figure 4.33 shows that the spread distribution for the horizontal polarization is non-noise-like with an envelope that is much larger than that for the noise alone. Figure 4.32 shows clearly the presence of a non-noise-like component in the difference curve. The difference can be as large as about $6\ dB$ in deep nulls of the pattern.

The difference is again reminiscent of the result obtained from taking the difference between two identical but slightly shifted patterns. Figure 4.34 shows the result for a 3° shift in either direction. A smaller shift would result in an even smaller difference. However, comparison between Figures 4.32 and 4.34 suggests that the shift would need to vary differently in both amplitude and direction over various angular ranges. It is surprising to see that minor changes made to some absorbing material away from the styrofoam tower had such a noticeable effect on the cross-polarization pattern.

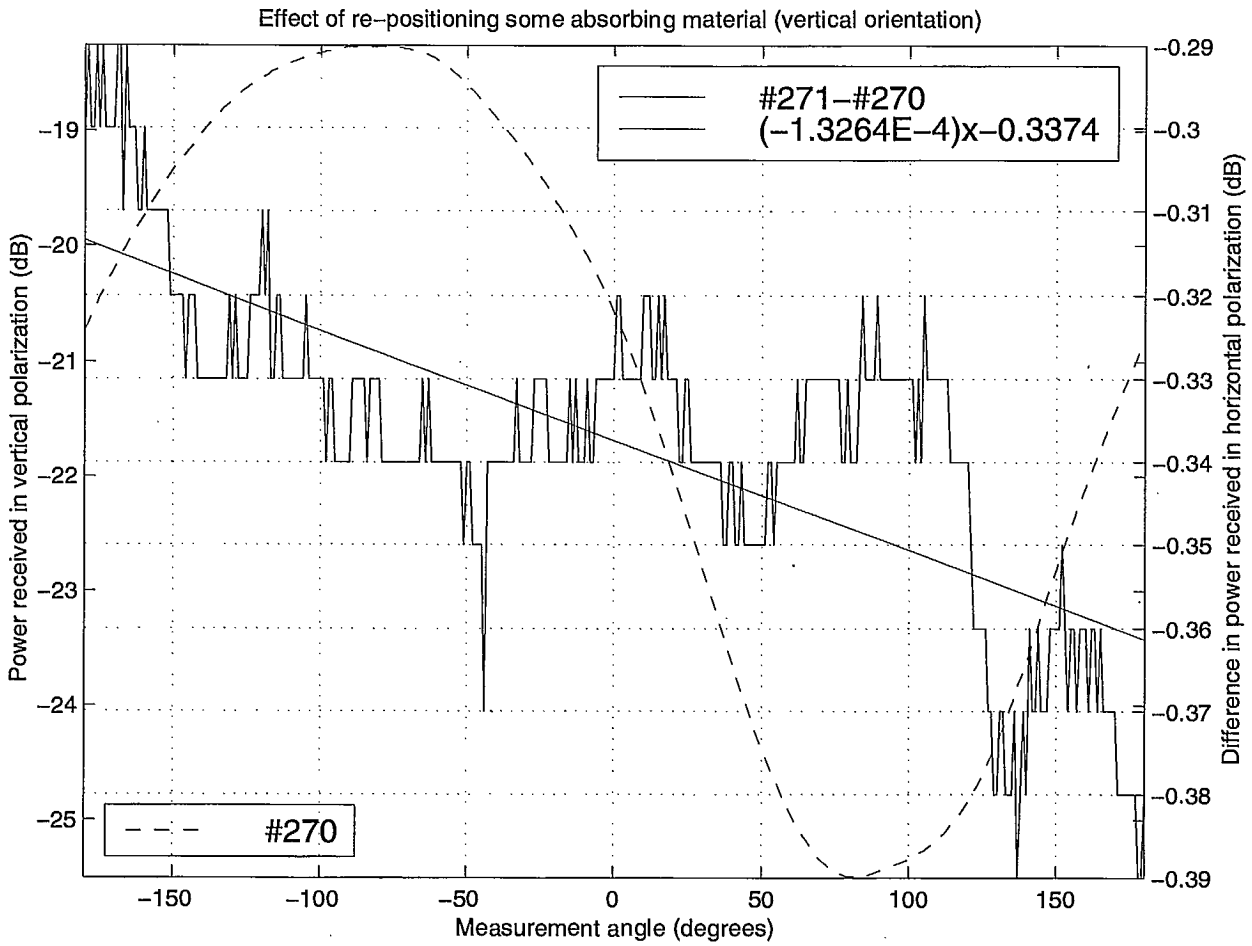

Figure 4.30: Variation of the vertical polarization data due to leaning the absorbers against the side of the heavy rail and to adding absorbing material around the lower end of the control cable that was exposed through the large absorbing cones laid on top of the rail. The transmitter was in the vertical orientation of the first test.

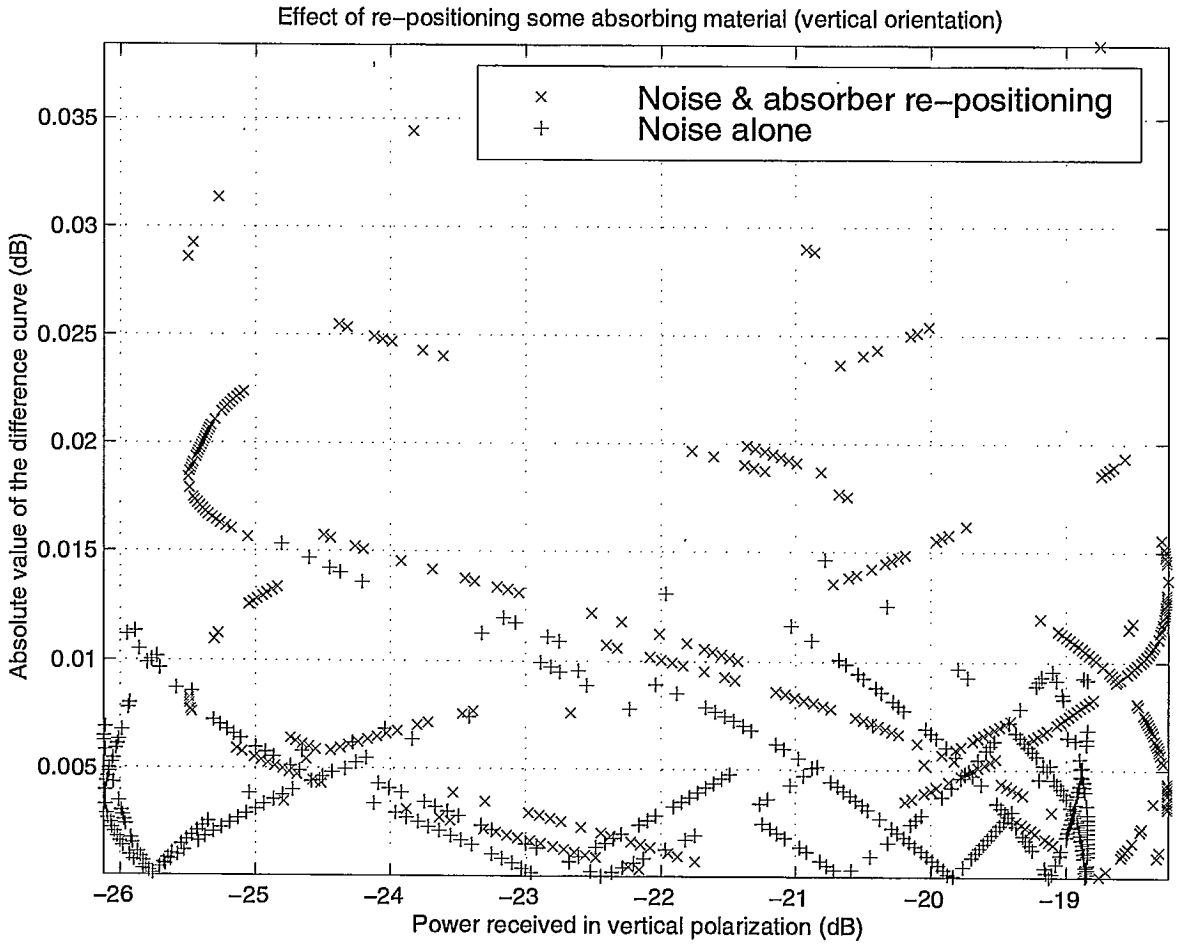

Figure 4.31: The plot shows the spread distribution of the drift-corrected data corresponding to Figure 4.30 with respect to signal strength.

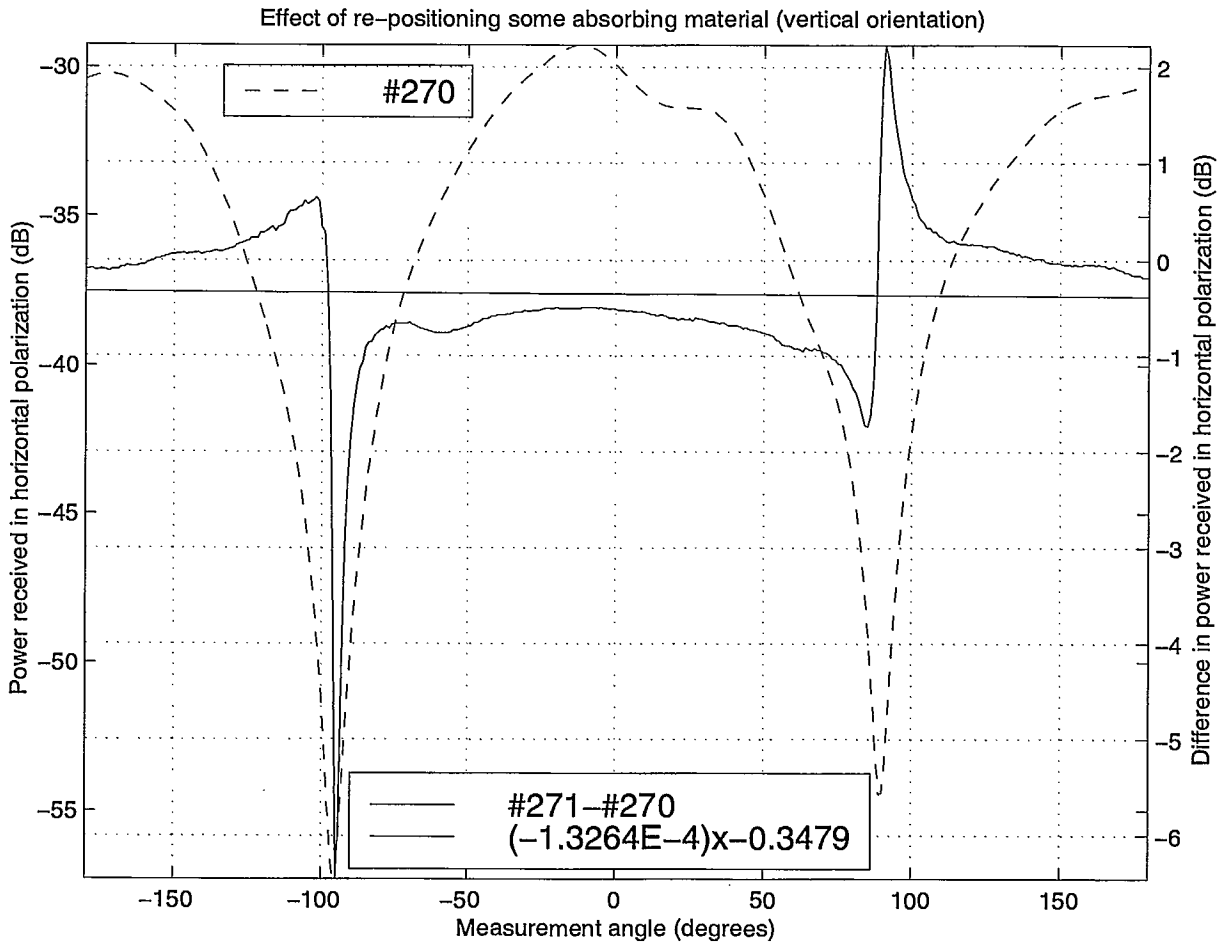

Figure 4.32: Variation of the horizontal polarization data due to leaning the absorbers against the side of the heavy rail and to adding absorbing material around the lower end of the control cable that was exposed through the large absorbing cones laid on top of the rail. The transmitter was in the vertical orientation of the first test.

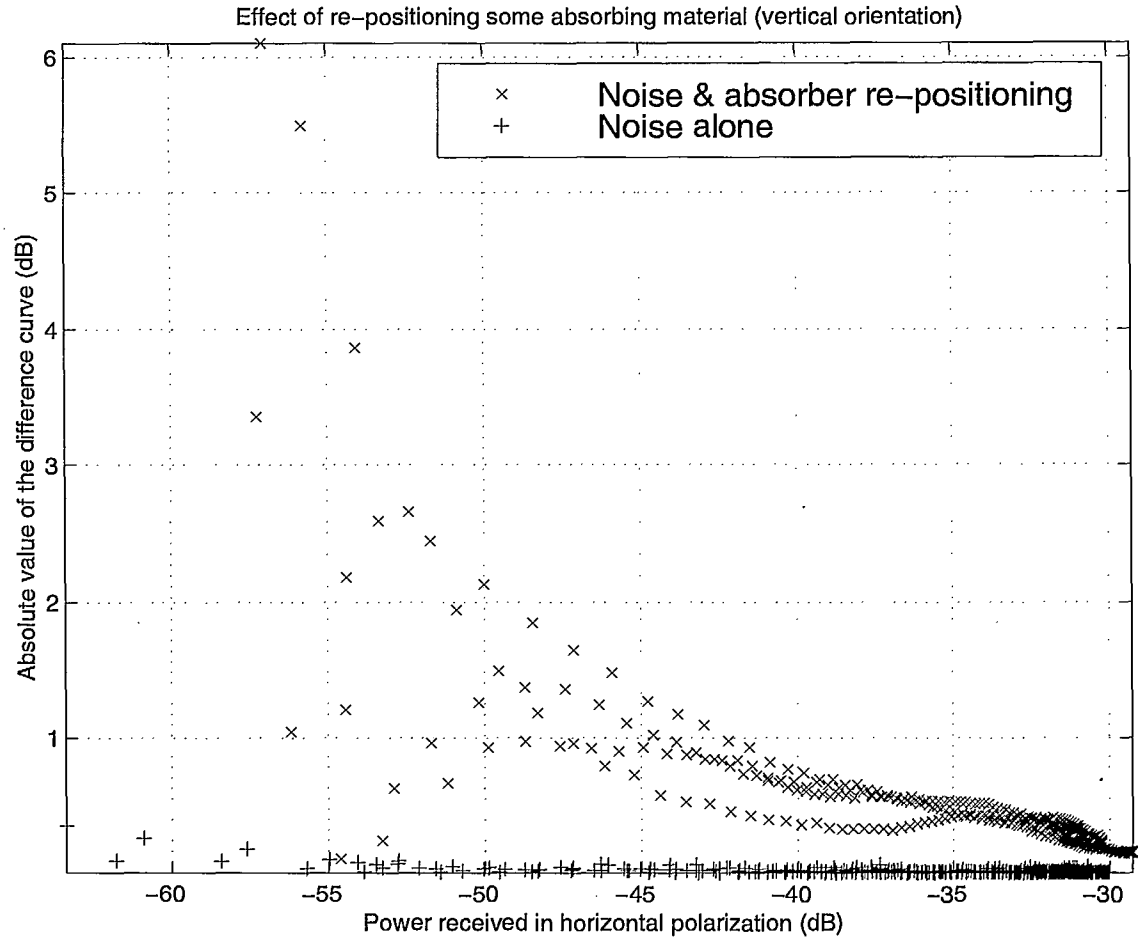

Figure 4.33: The plot shows the spread distribution of the drift-corrected data corresponding to Figure 4.32 with respect to signal strength.

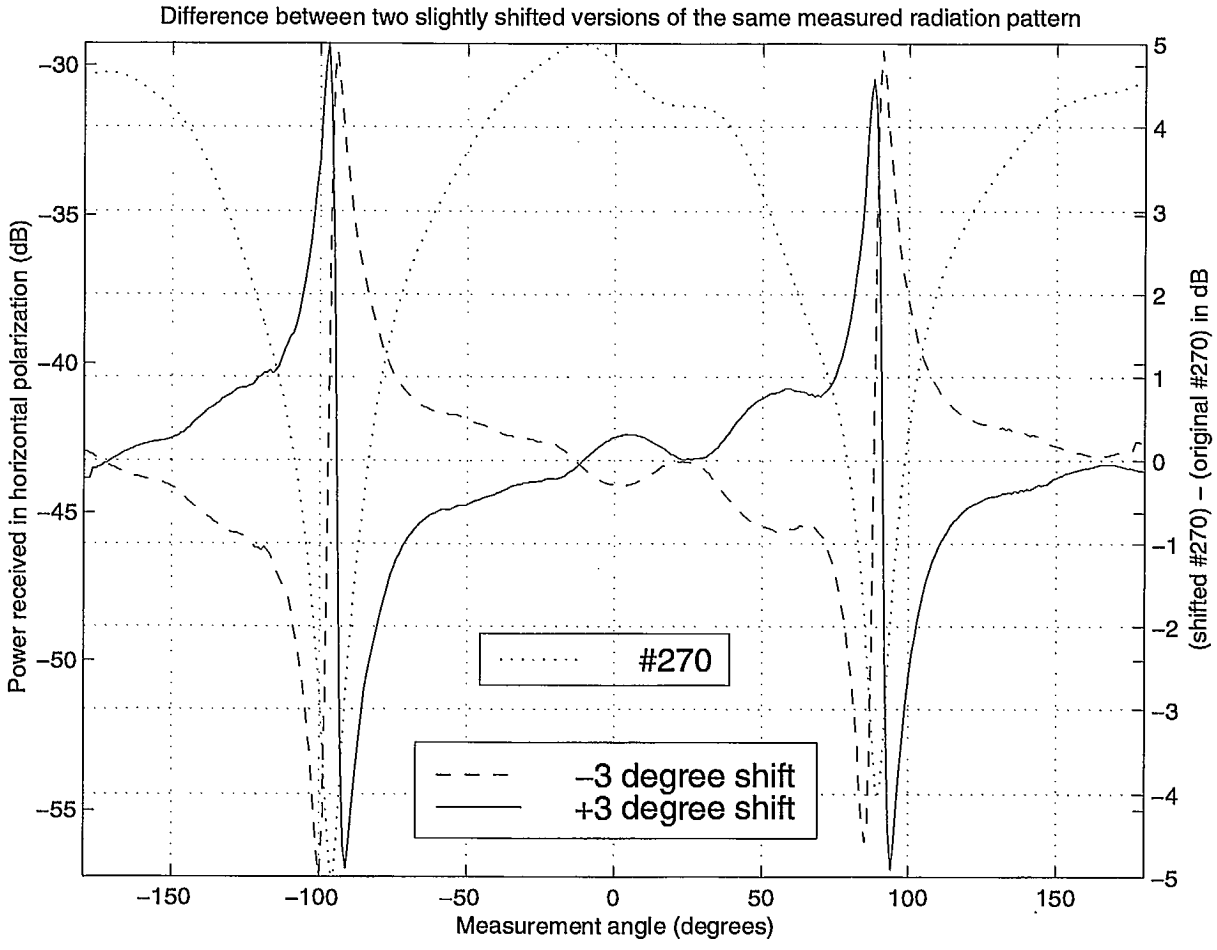

Figure 4.34: Difference between two slightly shifted versions of the same radiation pattern measured with the transmitter in the vertical orientation of the first test.

4.2.5 Data variation due to the battery DC power level variation

The data for the power generated by the very same oscillator working into a 50 Ω resistive load from a cold state at the beginning of the measurement set was measured as per Table 4.1.

The power radiated by the transmitter alone could then be estimated as P_{in} from Table 4.1 less the return loss corresponding to the impedance mismatch between the 50 Ω output impedance of the oscillator and the input impedance of the monopole antenna radiating in free space, transformed through the length of the coaxial cable connecting the antenna to the oscillator. The value of this return loss was estimated to be about 1.01 dB (see Appendix B of reference [1]). Similarly, the radiated power could also be estimated in the third test, provided that the return loss was known when the monopole antenna radiated in the presence of the phantom head.

The above information, however, provided only an estimate of the variation of the radiated power level during a measurement run because of the time delay and the temperature cooling that took place between the time that a run ended and the time that the cover of the transmitter was removed for checking the battery voltage. A better gauge for assessing the variation of the radiated power level during a measurement run was obtained by taking the difference between the radiated power levels measured at the azimuth angles of -180° and $+180^o$ since these two angles corresponded to the same point in space. Using the externally DC power supplied transmitter, the variation of the radiated power levels between the results at -180° and $+180^o$ was found to be no more than 0.02 dB for the co-polarization signal and thus, the variation of the radiated power level during a measurement run with the battery operated transmitter was then reliably estimated from the difference between the power level at -180° and the power level at $+180^o$, notwithstanding the additional variation due to electrical noise. However, the variation of the radiated power level between the results at -180° and $+180^o$ does not come out to be necessarily the same for the two polarizations in a same run. This situation is thought to owe mostly to the facts that:

1. the signal strength and the slope values at $\pm 180^o$ can be widely different between the two polarizations and thus, the corresponding noise level and data smearing would accordingly be significantly different between the two polarizations;

2. electrical noise introduced a random variation as part of the measurement results.

The finite resolution of the positioner, being as good as about 0.007^o, is not thought to be a significant cause for the variation between the results at -180° and $+180^o$. The difference in the received power level between -180° and $+180^o$ for the strongest polarization (not necessarily the co-polarization) measured at these angle values is shown in Table 4.2. The strongest polarization was used in order to minimize the possible corruption of the data by the electrical noise whose detrimental effect increased stongly as the signal level became smaller. Linear power correction with respect to the battery discharge was applied to each plot on the decibel scale according to the difference $\Delta P = P(-180^o) - P(+180^o)$ shown in Table 4.2.

4.3 Measurement error budget

Table 4.3 presents a summary of the error assessment for the measurements herein.

Table 4.1: RF Power level from the oscillator as a function of DC power supply voltage, for the oscillator working into a 50 Ω resitive load. The transmitter started from a cold state for the 16.51 V data point.

DC Voltage (V)	Power level P_{in} (dBm)
16.51	20.34
16.41	20.17
16.31	20.00
16.20	20.00
16.11	20.00
16.00	19.84
15.91	19.67
15.80	19.67
15.70	19.67
15.61	19.50
15.51	19.50
15.40	19.50
15.31	19.50
15.20	19.50
15.00	19.34
14.50	19.00
14.00	18.67
13.50	18.17
13.00	18.00
12.50	17.67
12.00	17.17
11.50	16.84
11.00	16.17
10.50	15.34
10.00	14.50

Table 4.2: The difference in received power level between -180° and $+180^o$ for the strongest polarization measured at these angles.

File #	Orientation	DC supply	$\Delta P(dB)$	$P(+180^o)(dB)$	Polarization
270	*Vert*	Bat. C	0.09	-20.81	vertical
271	*Vert*	Bat. C	0.17	-21.19	vertical
272	*Vert*	Bat. C	0.24	-21.49	vertical
273	*Edge*	Bat. A	0.06	-29.55	vertical
274	*Edge*	Bat. A	0.10	-29.68	vertical
275	*Edge*	Bat. A	0.18	-30.08	vertical
276	*Edge*	Bat. B	0.19	-29.61	vertical
277	*Flat*	Bat. B	0.09	-30.32	horizontal
278	*Flat*	Bat. B	0.17	-30.51	horizontal
279	*HuNf*	Bat. C	0.14	-25.36	vertical
280	*LuNf*	Bat. C	0.07	-24.05	horizontal
281	*LfNd*	Bat. C	0.14	-25.85	vertical
282	*HuNfP*	Bat. A	0.07	-26.92	horizontal
283	*LuNfP*	Bat. A	0.14	-28.94	horizontal
284	*LfNdP*	Bat. A	0.12	-21.94	vertical
285	*Vert*	Ext.	0.02	-13.49	vertical
286	*Vert*	Ext.	0.00	-13.48	vertical

$\Delta P = P(-180^o) - P(+180^o)$
Bat.: Battery pack
Ext.: External power supply
Vert: Transmitter vertical
Edge: Transmitter on edge side
Flat: Transmitter on flat side
HuNf: Transmitter in Head-up-Nose-forward headless jig
LuNf: Transmitter in Left-ear-up-Nose-forward headless jig
LfNd: Transmitter in Left-ear-forward-Nose-down headless jig
HuNfP: Transmitter with Head-up-Nose-forward phantom head in jig
LuNfP: Transmitter with Left-ear-up-Nose-forward phantom head in jig
LfNdP: Transmitter with Left-ear-forward-Nose-down phantom head in jig

Table 4.3: Summary of the measurement errors.

Error type	Error estimate
Battery discharge	$\leq 0.24\ dB$
Data smearing	$\leq 0.17^o$ angular spread $0.0334\ dB/(dB/^o)$ error $\Longrightarrow 0.10\ dB$ for a $3\ dB/^o$ slope
Centring	$\leq 3\ mm \Longrightarrow 0.05^o$ during a run of the first test $\leq 6\ mm \Longrightarrow 0.10^o$ during a run of the second/third test $\approx 1\ mm$ due to tolerance in machining the styrofoam jig
Alignment	$\leq 1.90^o$ due to alignment during a run of the first test $\leq 1^o$ due to drawing the alignment lines on the top surface of the styrofoam disk $\leq 0.5^o$ due to positioning the transmitter vertically in the slightly oversized slot of the styrofoam disk $\leq 0.11^o$ due to alignment during a run of the second/third test $\leq 0.4^o$ due to drawing the alignment lines on the six surfaces of the styrofoam jig
Electrical noise	exponential-like envelope with these values in the deepest null: $0.35\ dB$ for co-polarization of any orientation $0.3\ dB$ for cross-polarization of *Vert* or *LfNd* $1.2\ dB$ for cross-polarization of *Edge*, *LuNf* or *HuNf* $6.0\ dB$ for cross-polarization of *Flat*
Vert: Transmitter vertical *Edge*: Transmitter on edge side *Flat*: Transmitter on flat side *HuNf*: Transmitter in Head-up-Nose-forward headless jig *LuNf*: Transmitter in Left-ear-up-Nose-forward headless jig *LfNd*: Transmitter in Left-ear-forward-Nose-down headless jig	

Chapter 5

Data Comparison

This chapter presents the results from comparing the 1998 measured data with the FDTD predicted data, and the results from comparing the 1998 measured data with the 1997 measured data. The 1998 measured data was used as the reference for both the FDTD predicted data and the 1997 measured data, over the measurement range of -180° to $+180^o$ for both polarizations.

5.1 FDTD predicted vs 1998 measured data for the first and second tests

5.1.1 Generalities

The measured data for the first test were those for runs #272, #278 and #276 for the vertical, the flat and the edge orientations, respectively, as each one is believed to have been acquired with the best alignment among all runs of the first test pertaining to the same respective orientation. The predicted values were obtained from FDTD simulations with the version 4.03 of Remcom's XFDTD software (see reference [4]).

5.1.2 FDTD simulation

A total of four different models were investigated:

- transmitter modeled without holes;
- transmitter modeled with two holes;
- transmitter modeled with two holes and with its monopole antenna shortened by 1 cell;
- transmitter modeled with two holes and with its monopole antenna lengthened by 1 cell.

The motivation for taking into account the presence of the two small circular holes through which pass the plastic lever of the power switch and the red plastic lens of the low power warning LED stems from the fact that the presence of these holes should disturb the distribution of the induced current on the surface of the metallic cover. From the polarizability theory for electrically small apertures (see reference [5, p. 191]), the radiation from a small hole can be approximated by the radiation from the combination of one electric dipole positioned in the circular aperture in a direction normal to the plane of the aperture, and one magnetic dipole positioned in the circular aperture in a direction tangential to the aperture. The electric field radiation from such a hole would be significant in the direction normal to the aperture owing to the radiation from the equivalent magnetic dipole, and in a direction parallel to the aperture owing to the radiation from the equivalent electric dipole. The two neighbouring holes can be regarded as the elements of a two element array with its two elements fed nearly in phase. The radiation from this array is thus the product of the element factor and the array factor (neglecting the effect of the mutual coupling between the two elements). The small holes would thus produce a significant amount of radiation in the hemisphere centred about the holes. These holes faced directly the receive horn at $+90^o$ azimuth angle for the edge orientation, and $\pm 180^o$ azimuth angle for the vertical orientation.

The motivation for taking into account the variation of the length of the monopole antenna by one cell stems from the fact that the process of forcing to zero the electric field component E_z tangential to the metallic wire incurs an ambiguity of one cell in modeling the length of the wire which parameter is critical for a resonant antenna.

Figures 5.1 and 5.2 present the model used in conjunction with the XFDTD403 software (see reference [4]) to compute the predicted data. All predicted data were obtained with a cell size of 2.205 mm, a time step of 4.246 ps, the use of the Liao's absorbing boundary condition and a minimum of 15 white cells between the outer boundary and any point of the transmitter (except for the case of modelling the monopole antenna with 41 instead of 40 cells thus leaving only 14 white cells between the tip of the antenna and the closest point to the absorbing boundary). The computational space was $95 \times 79 \times 187$ cells. The monopole antenna was excited at its base with 1 V/m point source. The monopole antenna was modeled with 39, 40 and 41 cells for the cases of the shortened, normal and lengthened antenna, respectively. The FDTD simulation model did not include the presence of the styrofoam blocks for holding the transmitter into place. Owing to the cartesian nature of the Yee lattice used to discretize space within the XFDTD403 software, the small circular holes were modeled as square apertures with 2 cells on a side. The convergence of the XFDTD403 simulation results was verified for a cell size of 2.94 mm by means of displaying with a color coded map the difference in the E_x, E_y and E_z magnitudes over the $\phi = 0^o$ principal plane in the near-field zone between the simulation results for 2.94 mm and 0.98 mm cell sizes. Therefore, the convergence for the XFDTD403 simulation results with the smaller grid size of 2.205 mm was a fortiori verified.

The far field for each case was computed from the graphical user's interface of the XFDTD403 software in the three principal planes and for the two polarizations of interest. In comparing the 1998 measured data with the FDTD predicted data for the second test, the predicted data came from the same simulation as the predicted data for the first test except that the direction of observation was computed by coordinate transformation (see Appendix B). Proceeding in that manner rather than performing another FDTD simulation with the transmitter model tilted in the computational space permitted to keep the transmitter aligned with the Yee lattice of the FDTD simulation space in order to avoid some staircase approximation.

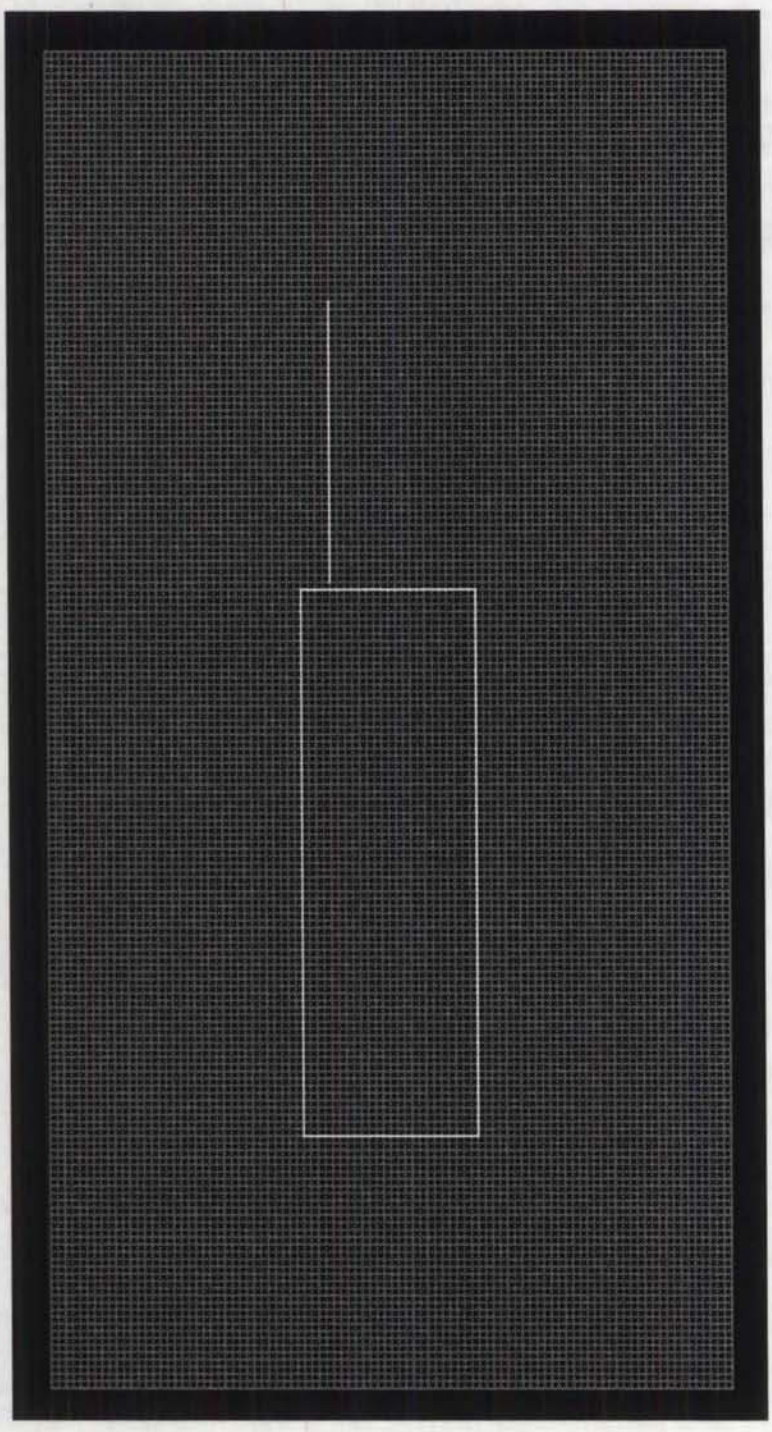

Figure 5.1: Model of the transmitter used in conjunction with the XFDTD403 software to compute the predicted data. The model shown here has the monopole antenna being 40 cells long.

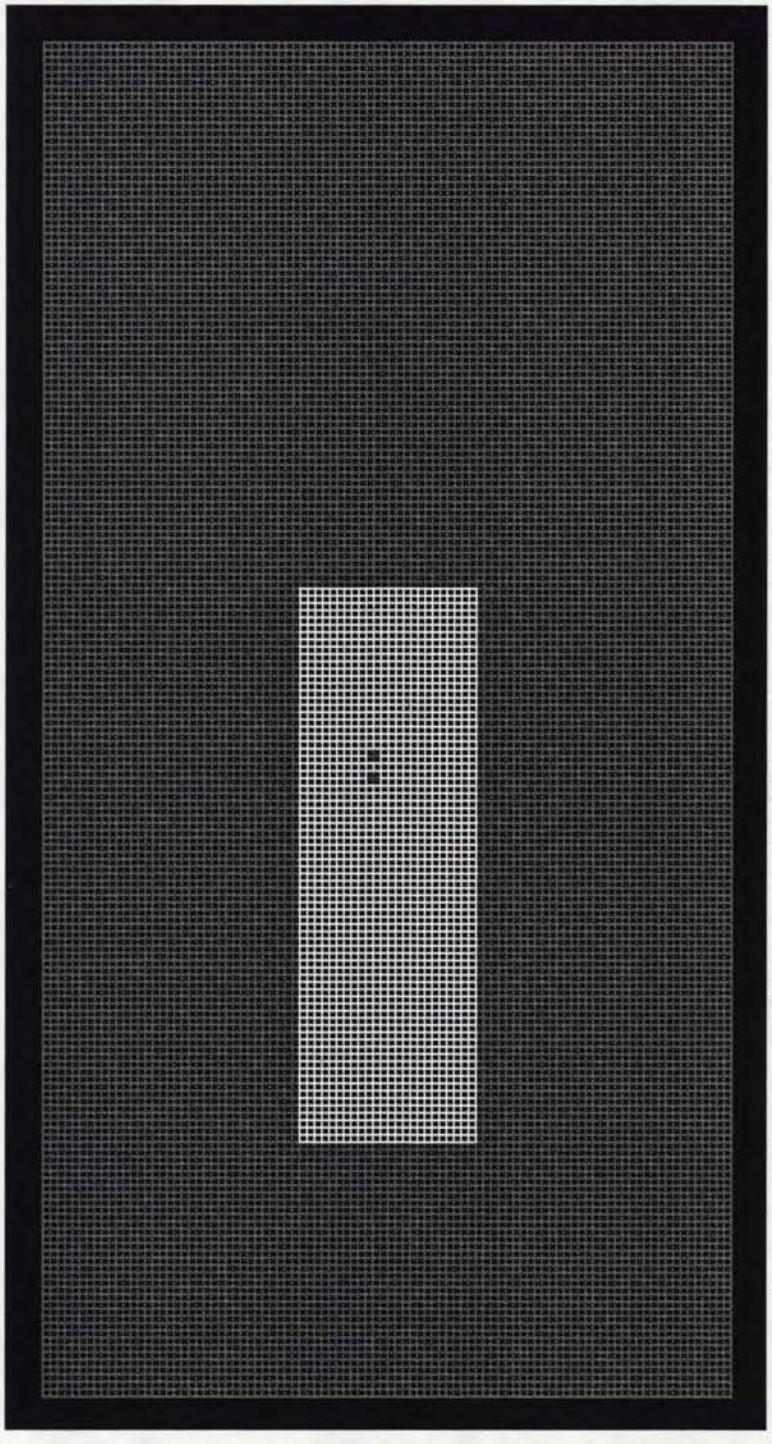

Figure 5.2: A detail of the model for the metallic cover of the transmitter showing the presence of the two small holes modelled as two square holes with 2 cells on a side.

5.1.3 Results

This section presents all the magnitude plots (see Figures 5.3 to 5.14) and Table 5.1 presents the corresponding numerical values resulting from comparing measured (in dBm) and predicted (in dBi) data. The comparison is based on applying a scaling factor (see Appendix C) to the data under comparison in order to account for the difference between the radiated power level for the experiment with data under comparison and the radiated power level for the 1998 test. However, different values of the scaling factor were allowed for the two polarizations of a same run even though both polarizations drew their energy from the same power source, either a delta gap field source in the simulation or a local oscillator in the experimental setup. Admittedly, the justification for this choice stemmed more from a desire to improve the result of the comparison than from the application of some physical principle at work.

The value of the scaling factor might also have varied between different runs because the battery packs were either changed between runs or discharging at different rates during consecutive runs. The same linear (on a decibel scale) power correction with respect to the battery discharge was applied to both polarizations of every curve of measured data according to $\Delta P = P(-180^o) - P(+180^o)$ for the strongest polarization at $\pm 180^o$, as presented in Table 4.2. Power correction with respect to the power transfer function of the network analyzer was also applied to the data herein.

A variable offset angle was also added to the angle of the data under comparison. The value of this offset was so selected as to minimize the absolute value of the difference between the data under comparison and the 1998 measured data. The total error shown in Table 5.1 refers to the average error value per degree that would be obtained if the error were uniformly distributed over the data ensemble. The averaging of the error was computed on the linear scale and the result was converted to dB. The total error value is used as an indicator of goodness of fit when comparing different cases, and thus, more importance was attached to its relative variation over the cases being compared than to its absolute value.

The results of the comparison are shown in decibels but it is important to understand that the process of finding the angle offset value that minimized the error

between the measured and the predicted co-polarization curves was performed by first converting each curve from the decibel to the linear scales so as not to distort the minimization process. Since the data for both polarizations were acquired simultaneously from a dual polarization quad-ridge horn, the same adjustment value was used for both polarizations of a same run. In order to search for the minimum error value with a resolution finer than the 1° resolution used to acquire the measured data and to compute the predicted data, each sequence of data was parabolically interpolated so as to produce a resolution of 0.2^o.

For the results of the second test, coordinate transformation was used to obtain the predicted data in the coordinated system of the chamber. The coordinate transformation accounted for the transmitter being translated away from the centre of the styrofoam jig, and tilted with respect to the rotation axis of the azimuth table. The coordinate transformation accounted also for the offset angle incurred by the finite separation distance between the centre of the styrofoam jig and the aperture of the receive horn.

The code for finding the scaling factor, for performing the power correction with respect to the battery discharge, and for minimizing the error was written in FORTRAN77 and can be found in Appendix C.1. The code for interpolating was also written in FORTRAN77 and can also be found in Appendix C.2. The code for performing the power correction with respect to the transfer function of the network analyzer was written in FORTRAN and can be found in Appendix C.5.

The results of performing the above data processing is shown in Table 5.1 and Figures 5.3 to 5.14.

Table 5.1: Summary of the pertinent numerical values obtained from the process of comparing the FDTD predicted and the 1998 measured data for the first test.

Cases	Offset	Scaling factor (dB)		Total error ($dB/°$)	
	(°)	Horizontal	Vertical	Horizontal	Vertical
Vert1	-5.6	15.3757	16.7480	-6.2251	+5.5020
Vert2	-5.8	15.5589	16.7473	-6.5703	+6.2125
Vert2 $\star$	+2.0	16.4957	16.7435	+3.6034	+4.1446
Vert2S	-6.2	15.5989	16.7925	-6.3616	+5.3542
Vert2L	-5.6	15.4312	16.6745	-5.6609	+5.7427
Flat1	+1.4	15.9699	-58.3973	+9.3616	+3.6443
Flat2	+1.6	15.8442	37.8594	+8.3804	+3.6369
Flat2S	+1.0	15.9782	42.4856	+10.3387	+3.6881
Flat2L	+1.6	15.8512	47.0860	+8.2515	+3.6768
Edge1	-0.4	15.2111	15.1462	+6.2611	+3.3146
Edge2	-0.4	15.2386	15.1800	+6.2336	+2.5056
Edge2S	-0.4	15.2583	15.2721	+7.7154	+3.5416
Edge2L	-0.2	15.2131	15.0742	+5.7146	+2.2503
HuNf	-0.6	14.9892	15.8549	+8.9872	+8.4613
LuNf	-0.4	15.5063	14.8899	+7.5449	+2.0112
LfNd	-0.6	16.0687	15.2157	-3.2809	+11.1738

Vert: vertical orientation
Flat: flat orientation
Edge: edge orientation
1: transmitter without holes; monople being 40 cells long
2: transmitter with holes; monopole being 40 cells long
2S: transmitter with holes; monopole shortened by 1 cell
2L: transmitter with holes; monopole lengthened by 1 cell
$\star$: with error minimization done on vertical polarization

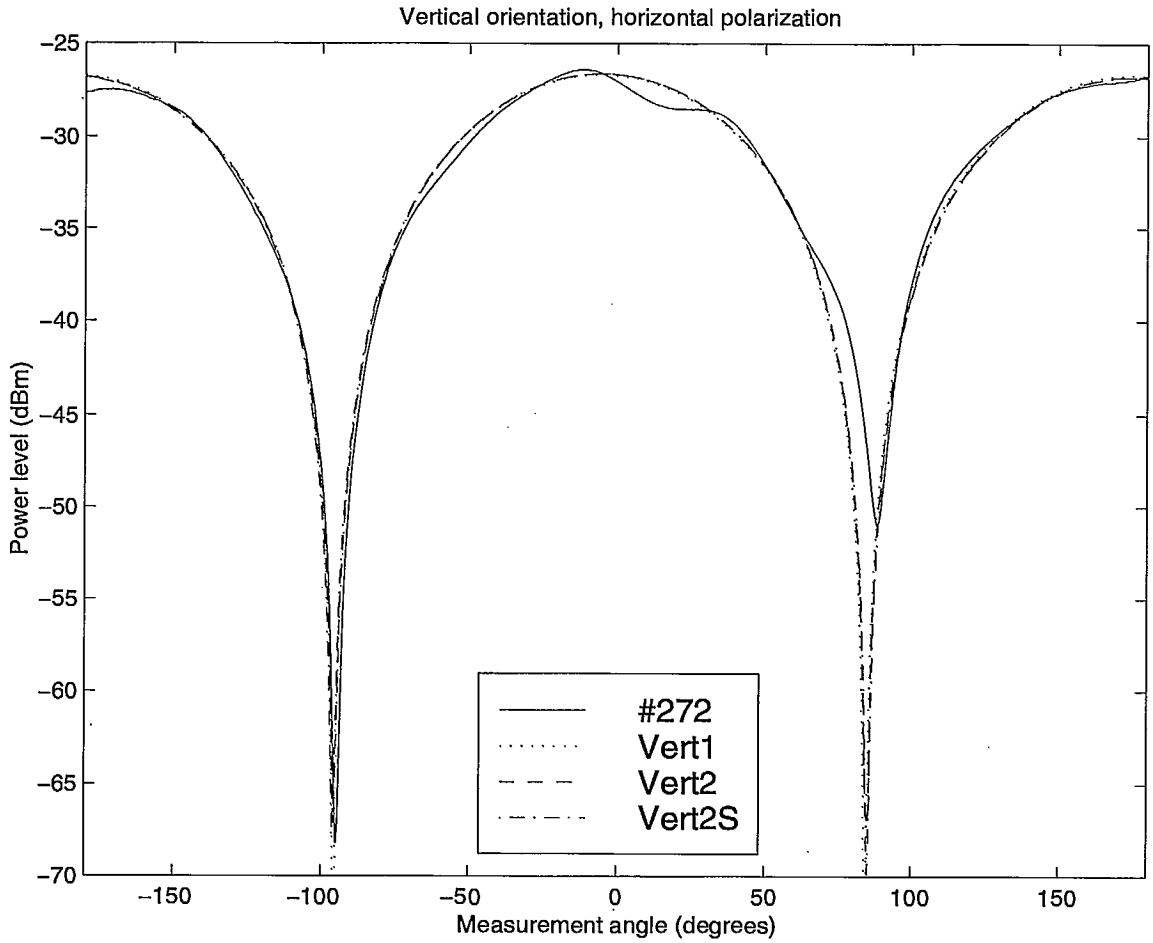

Figure 5.3: Comparison between the magnitudes of the FDTD predicted and the 1998 measured data of horizontal polarization for the vertical orientation of the first test.

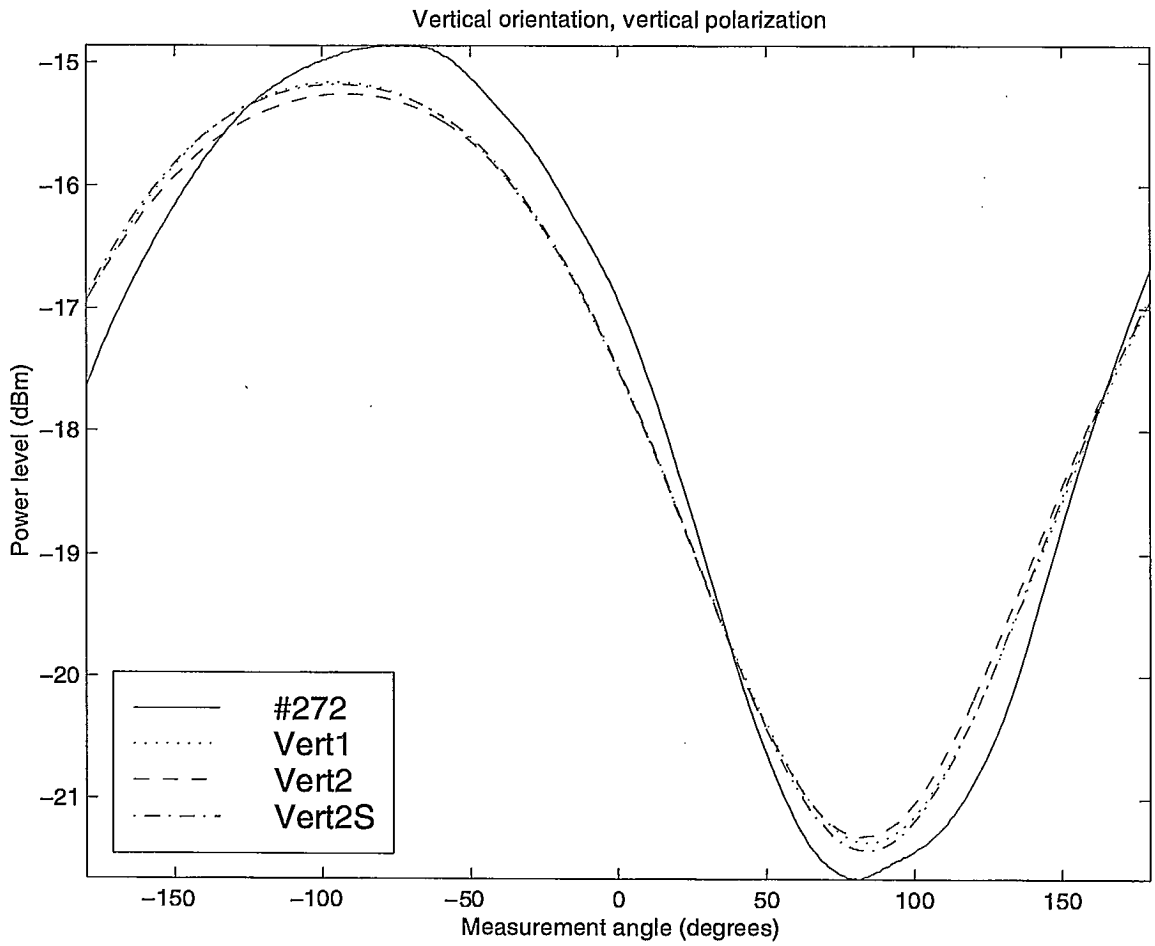

Figure 5.4: Comparison between the magnitudes of the FDTD predicted and the 1998 measured data of vertical polarization for the vertical orientation of the first test.

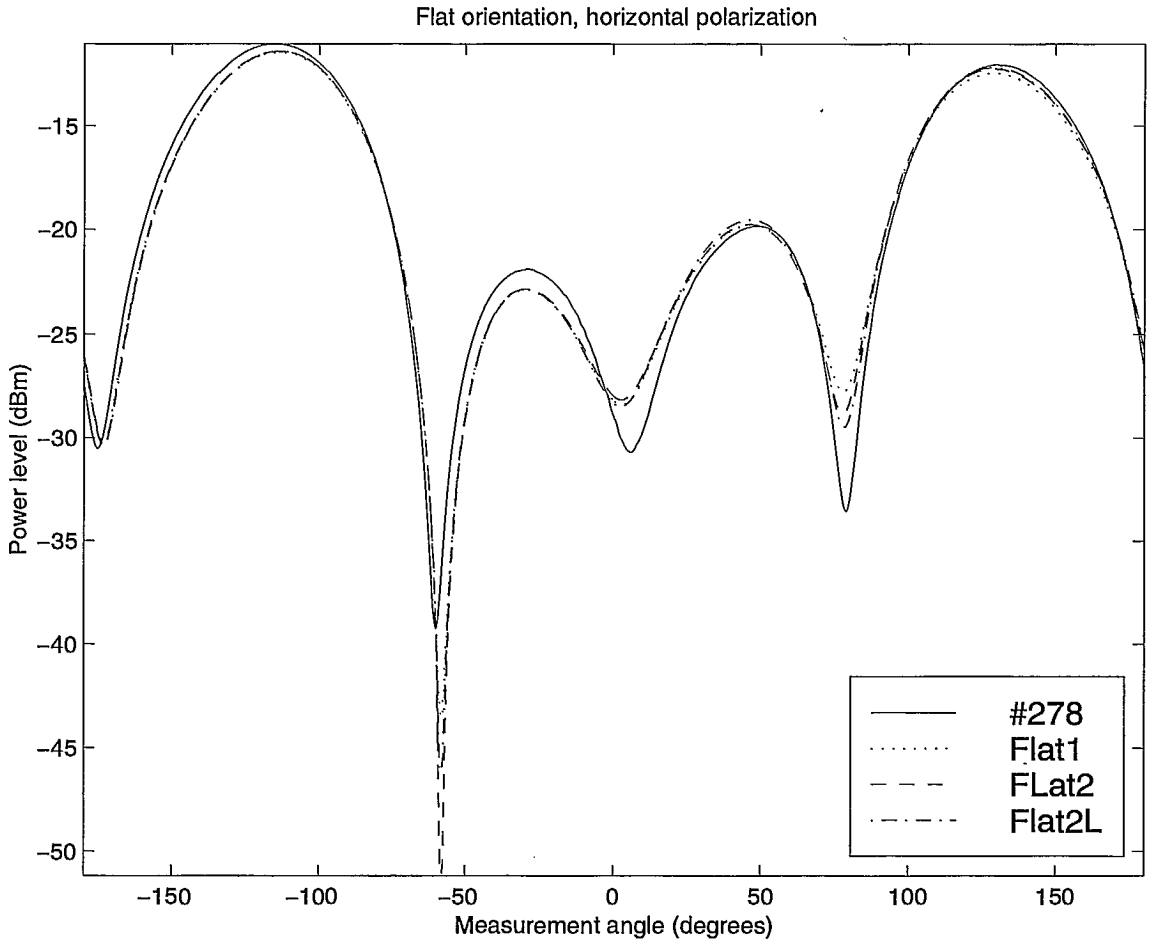

Figure 5.5: Comparison between the magnitudes of the FDTD predicted and the 1998 measured data of horizontal polarization for the flat orientation of the first test.

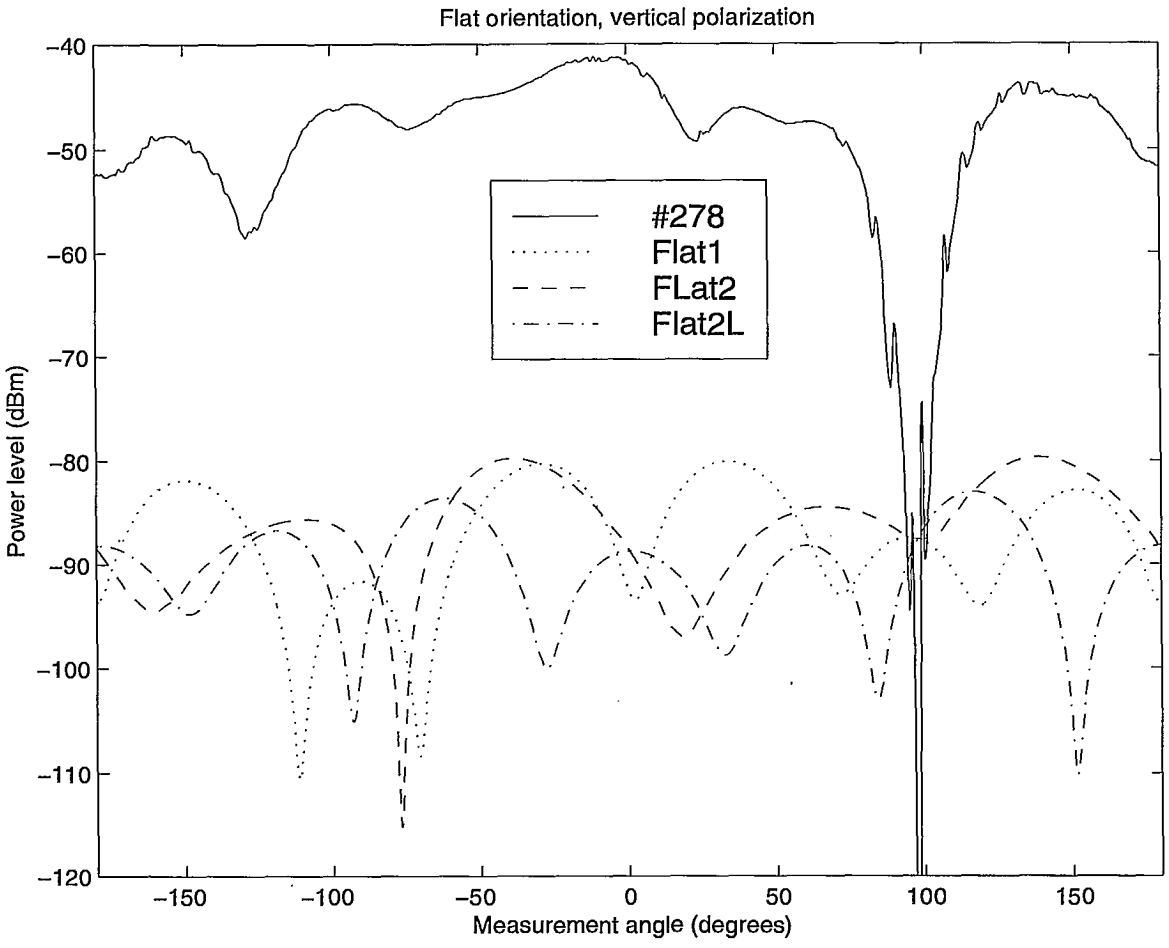

Figure 5.6: Comparison between the magnitudes of the FDTD predicted and the 1998 measured data of vertical polarization for the flat orientation of the first test.

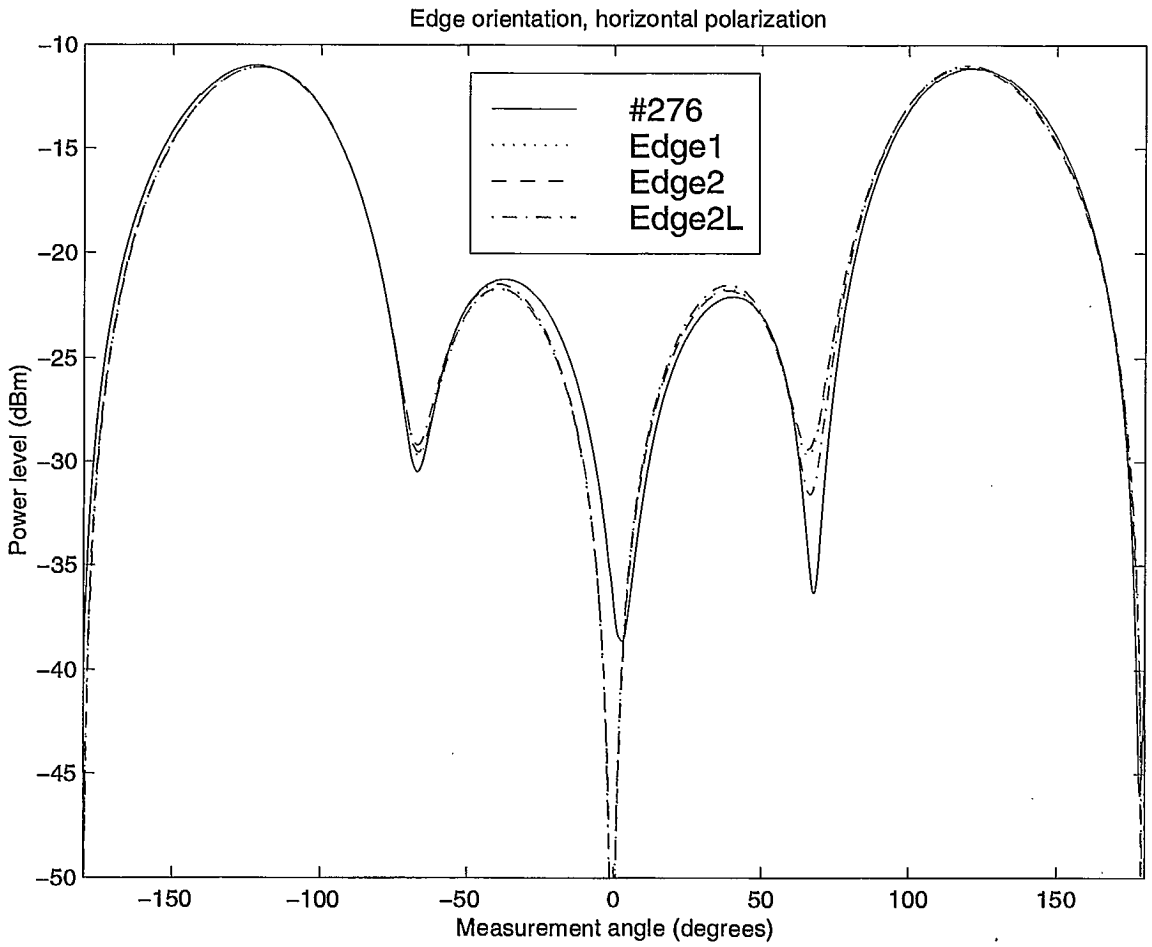

Figure 5.7: Comparison between the magnitudes of the FDTD predicted and the 1998 measured data of horizontal polarization for the edge orientation of the first test.

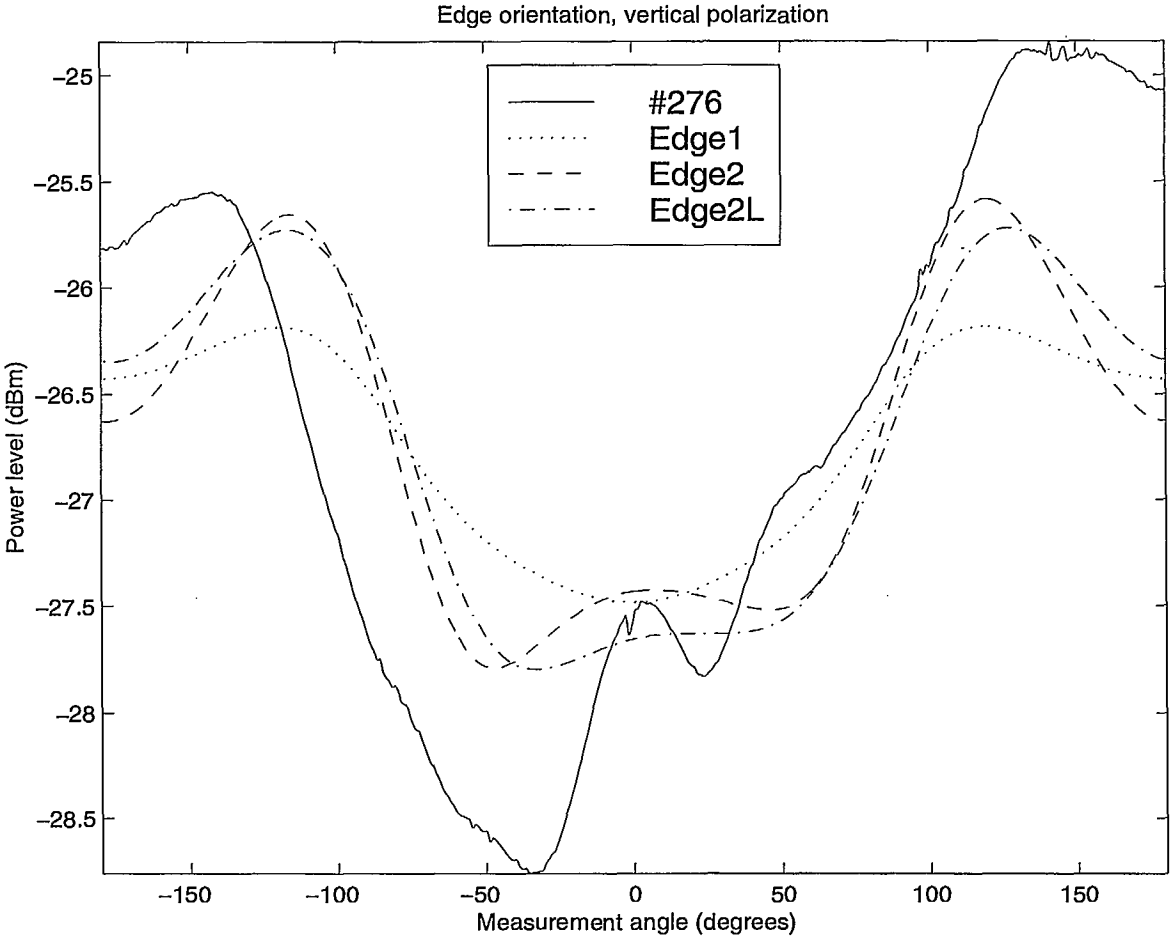

Figure 5.8: Comparison between the magnitudes of the FDTD predicted and the 1998 measured data of vertical polarization for the edge orientation of the first test.

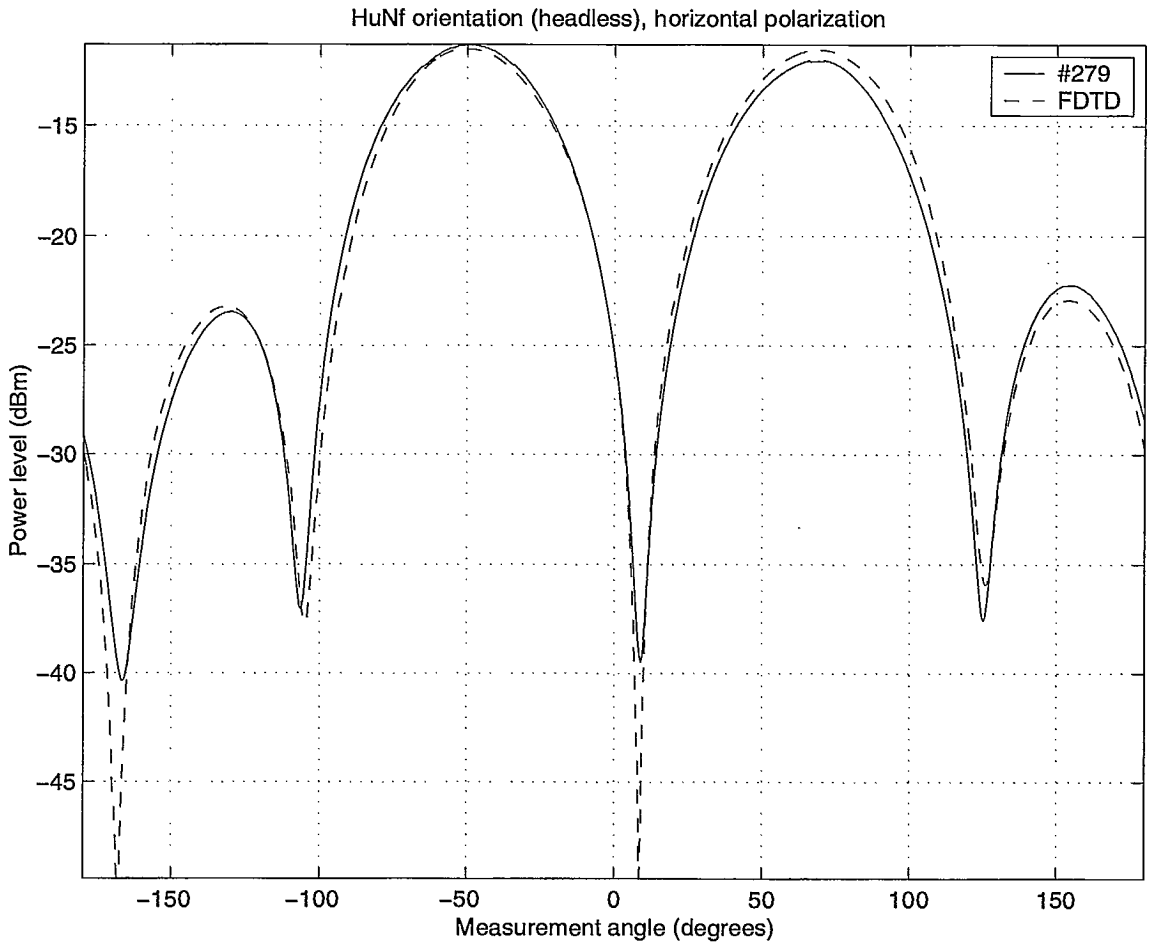

Figure 5.9: Comparison between the magnitudes of the FDTD predicted and the 1998 measured data of horizontal polarization for the Head-up-Nose-forward orientation of the second test.

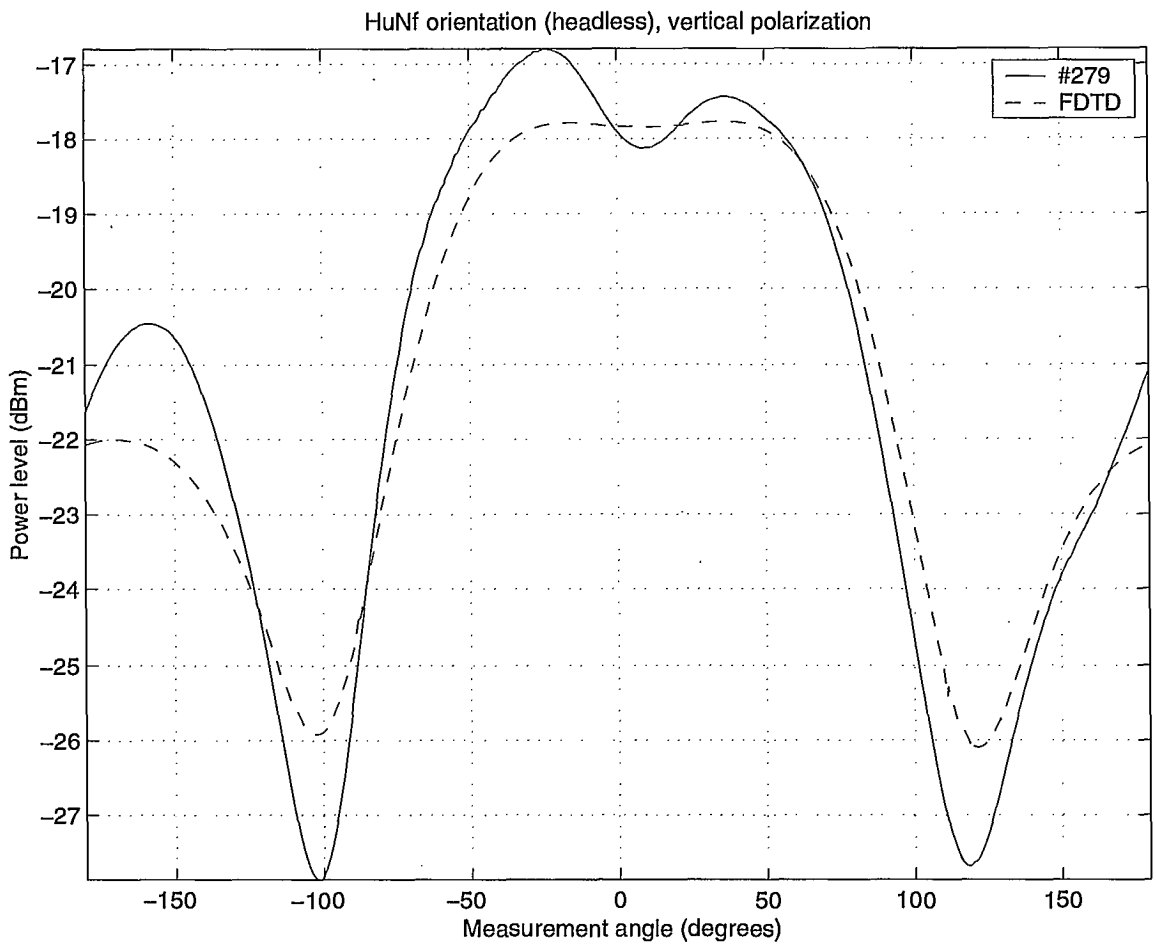

Figure 5.10: Comparison between the magnitudes of the FDTD predicted and the 1998 measured data of vertical polarization for the Head-up-Nose-Forward orientation of the second test.

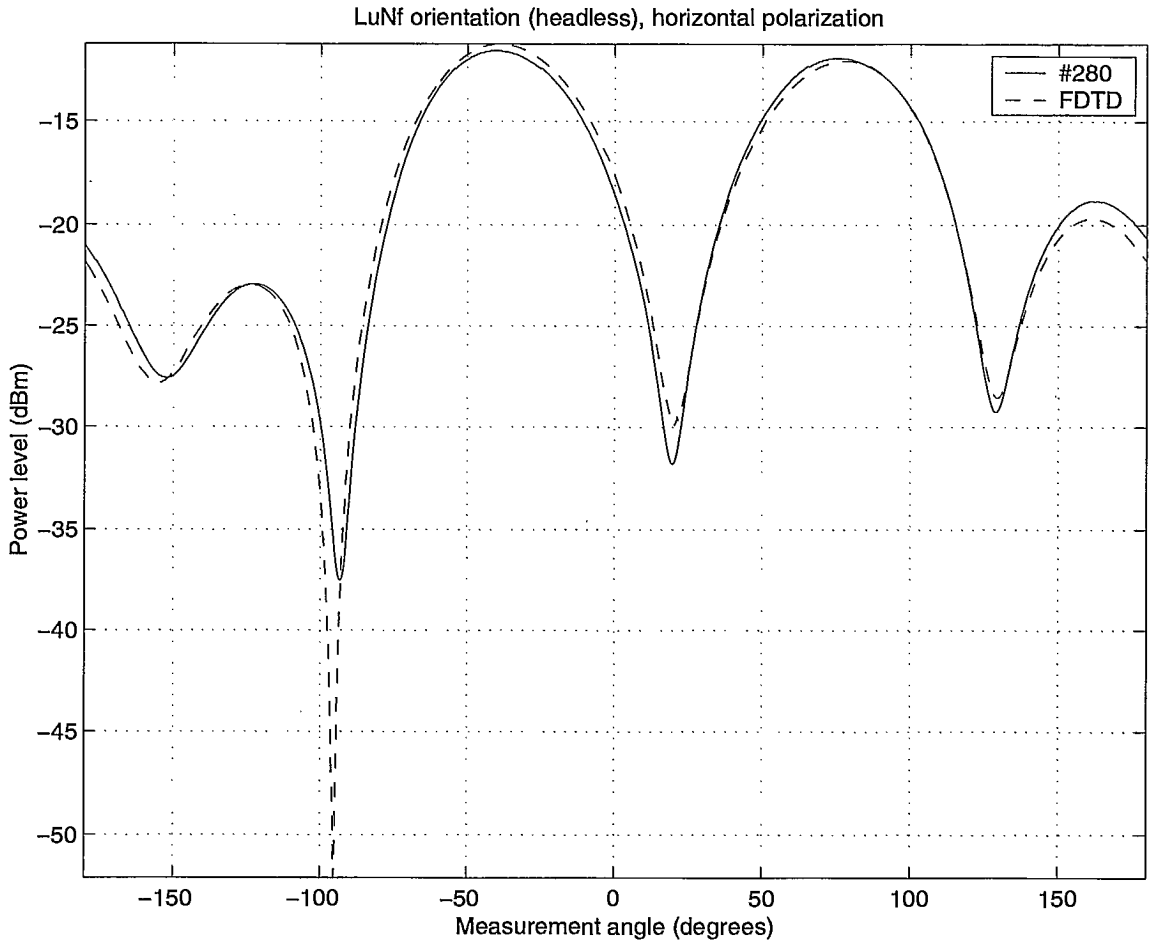

Figure 5.11: Comparison between the magnitudes of the FDTD predicted and the 1998 measured data of horizontal polarization for the Left-ear-up-Nose-forward orientation of the second test.

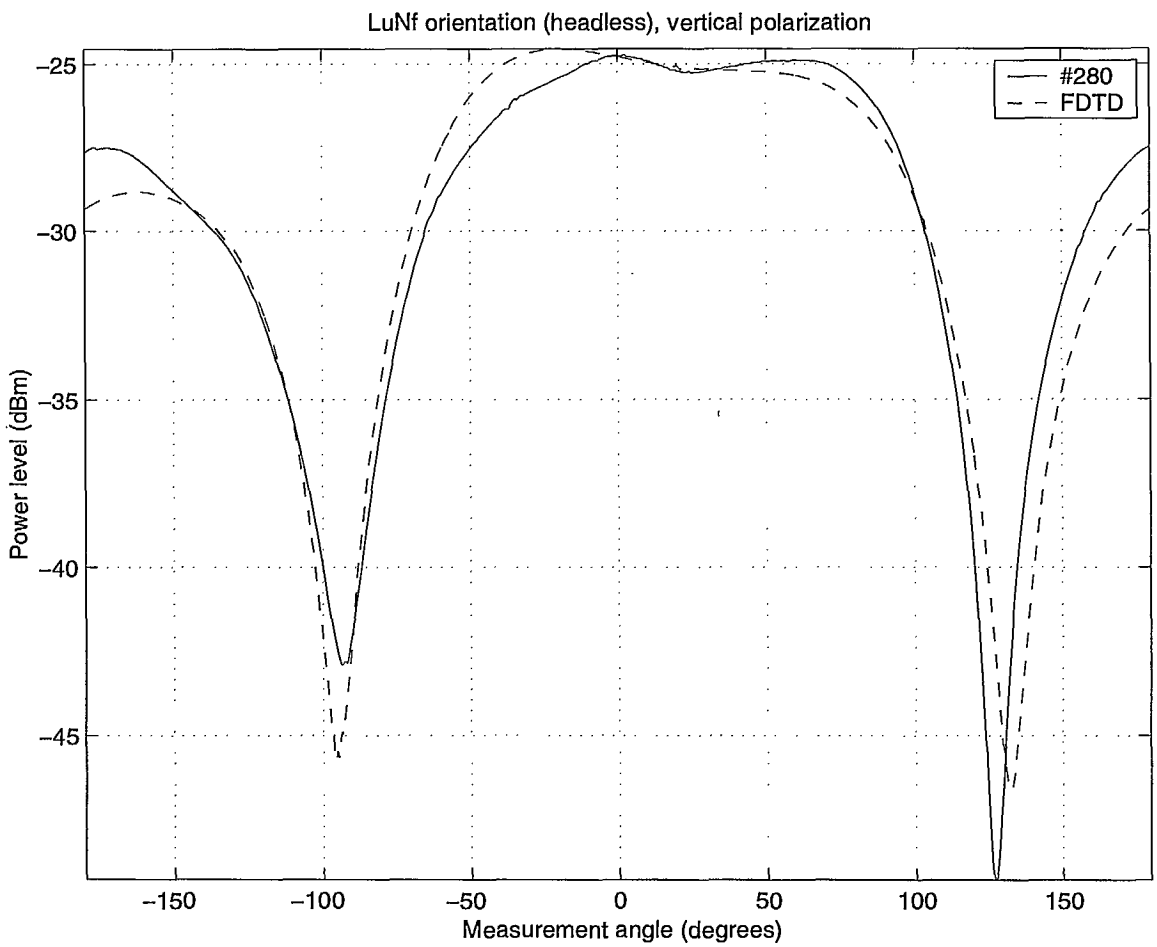

Figure 5.12: Comparison between the magnitudes of the FDTD predicted and the 1998 measured data of vertical polarization for the Left-ear-up-Nose-forward orientation of the second test.

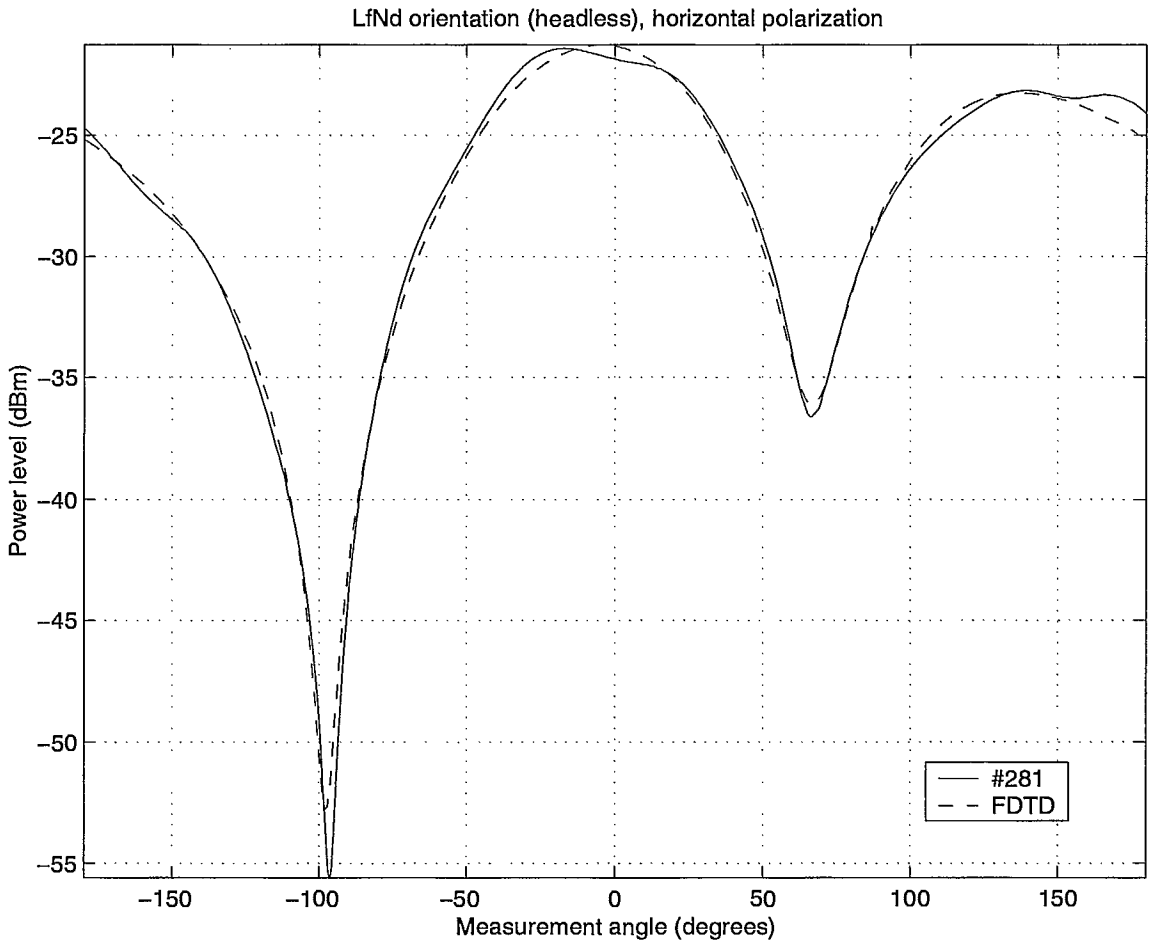

Figure 5.13: Comparison between the magnitudes of the FDTD predicted and the 1998 measured data of horizontal polarization for the Left-ear-forward-Nose-down orientation of the second test.

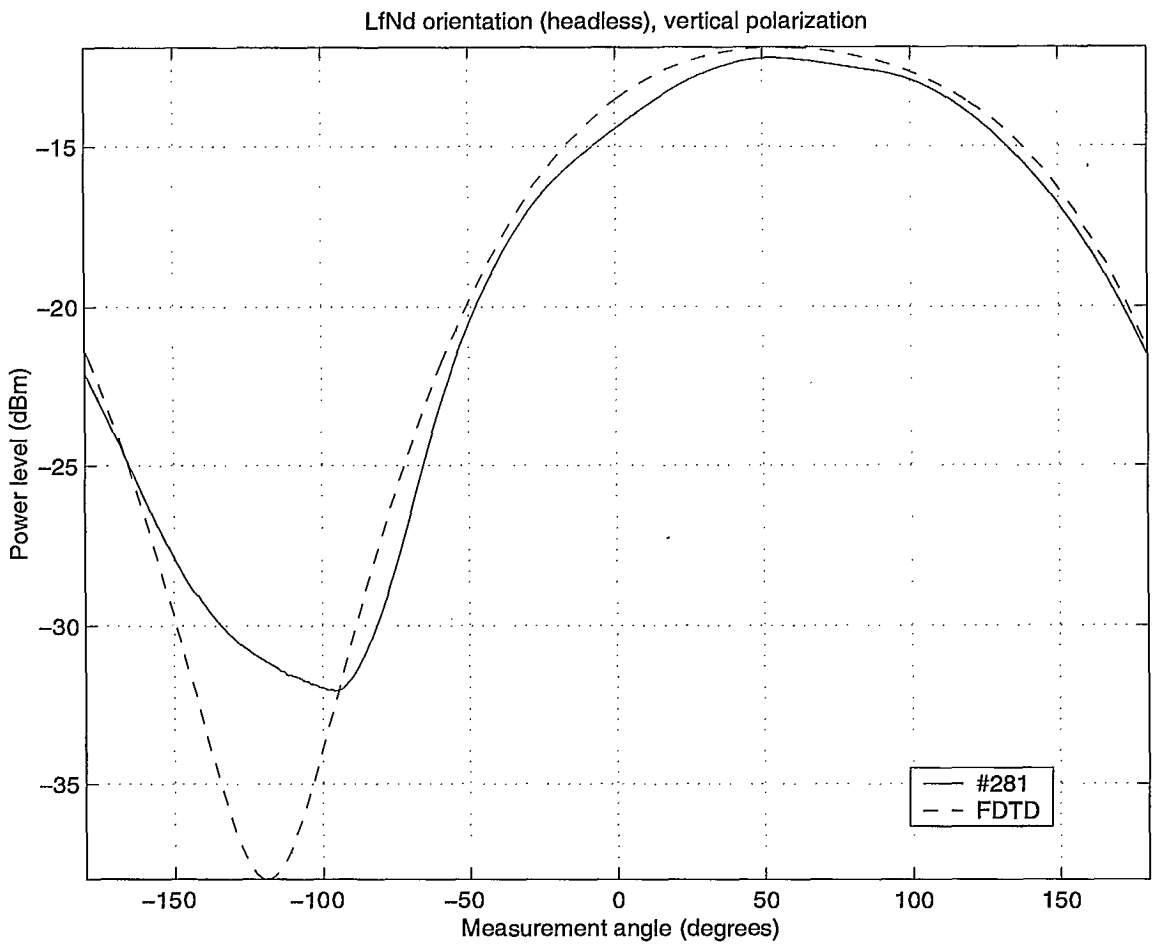

Figure 5.14: Comparison between the magnitudes of the FDTD predicted and the 1998 measured data of vertical polarization for the Left-ear-forward-Nose-down orientation of the second test.

5.1.4 Discussion

Figures 5.3 to 5.8 presented the results from comparing the measured data with the predicted data for the following cases:

- transmitter modeled without holes;
- transmitter modeled with two holes;
- transmitter modeled with two holes and with its monopole antenna lengthened or shortened by 1 cell, depending on which case produced the smaller error when minimizing the error on the horizontal polarization.

For the transmitter alone, the comparison held well for all curves except the cross-polarization (i.e. vertical polarization) for the flat orientation (see Figure 5.6). The discrepancy owes simply to the fact that the chamber did not have a cross-polarization purity sufficient to measure accurately a cross-polarization level as low as that for the predicted data of the flat orientation. This fact accounts also for the large difference between the values 15.9699 dB and -58.3973 dB for the scaling factors of the horizontal and vertical polarizations for the case *Flat1* in Table 5.1. The effect of some electrical noise is also apparent from the erratic behaviour of some plots of the measured data.

Figure 5.8 shows also some discrepancy but the scale of the plot is highly magnified. However, this discrepancy cannot be attributed to noise alone because the discrepancy has a definite rather than a noisy pattern. Figure 5.3 shows a big dent in the measured radiation pattern at about $+25^o$ and some loss of depth for the null at $+90^o$. Figure 5.7 shows some discrepancy for the null about $+65^o$ where the measured null is almost 7 dB deeper than any predicted null. The reason for such a strong break in the symmetry of the measured radiation pattern cannot be imputed to the presence of the two small holes nor to the effect of electrical noise but it could be imputed to the fact that the antenna was not perfectly straight nor perfectly vertical.

The angular adjustment corresponding to minimizing the difference between the predicted and the measured data of the horizontal polarization for the vertical orientation was obtained as -5.8^o (see Table 5.1). This value lies clearly outside the $\pm 1.9^o$ alignment tolerance given in Table 4.3. This situation suggests an excess error of about 3.9^o. A careful measurement of the angles performed on the disk itself could account for only less than 1° error for drawing the alignment lines on the top surface of the disk, and for less than 0.5^o error for positioning the transmitter in the slightly oversized slot of the styrofoam disk. However, the remaining error might be due to the minimization process since different adjustment values could be obtained from applying the minimization process on the vertical rather than the horizontal polarization. For instance, for the case corresponding to *Vert2v* (see Figures 5.15, 5.16 and Table 5.1), the adjustment values of -5.8^o and $+2.0^o$ were obtained from applying the minimization process on the horizontal and vertical polarizations, respectively, thus representing a variability of 7.8^o between them. Of course, since the data for both polarizations are acquired simultaneously from a dual polarization quad-ridge horn, one should expect to have the same adjustment value for both polarizations of a same run. Although the minimization process was performed on the horizontal polarization because the latter presented sharp features for discriminating against misalignment, one could argue that it should be more important to perform the minimization process on the co-polarization which, for the vertical orientation, is the vertical rather than the horizontal polarization.

It should also be said that the predicted results might be slightly inaccurate themselves since the model used as part of the FDTD simulation was only an idealized representation of the actual experiment setup. For instance, the physical monopole antenna was sligltly curved, off vertical and shorter than its corresponding simulation model. Reference [7] shows that a small departure in the position of the tip of the otherwise perfectly straight monopole antenna can bring about a significant amount of cross-polarization level. For a departure value of 1, 2, and 3 mm, the cross-polarization level for the flat orientation was obtained in reference [7] as $-41.2\ dB$, $-35.2\ dB$ and $-31.7\ dB$, respectively. The value of 1 mm corresponds approximately to the departure value measured. Furthermore, reference [6, pp. 19] shows that the depth and placement of some minima in the results from a FDTD simulation of the transmitter in free space varies with the cell size; differences of up to 2.6 dB and 1°

were observed between the 4.41 mm and the 2.205 mm cell size simulation results. Furthermore, reference [6, p. 29] shows also that, by comparing the near field result for a wire grid model of the transmitter in free space computed by NEC-4, and the far field result for a 4.41 mm cell size model for the transmitter in free space computed by FDTD, a separation distance of 3.30 m between the D.U.T. and the receive horn can lead to errors as large as 3.9 dB in the depth of some minima. Note, however, that the far field results generated by FDTD in references [6] and [7] corresponded to the observation direction angles for an infinite separation distance, i.e. no correction was made to the observation direction angle for taking into account the variation in observation angle incurred by the finite separation distance when the transmitter did not lie on the rotation axis of the azimuth table.

The smallest value of total error on the horizontal polarization (see Table 5.1) is obtained for the cases *Vert2*, *Flat2L* and *Edge2L* for the vertical, flat and edge orientations, respectively. The smallest value of total error on the vertical polarization is obtained for the cases *Vert2S*, *Flat2* and *Edge2L* for the vertical, flat and edge orientations, respectively. This situation suggests that a better match is always obtained between measured and predicted data when the predicted data incorporates the effect of the two small holes. However, the need for vaying the length of the monopole antenna is not as clearly demonstrated. The physical antenna length was measured as 87.77 mm (although the drawings called for 88.2 mm) whereas the simulated length was either 39, 40 or 41 cells long which corresponded to 86.00 mm, 88.20 mm and 90.41 mm, respectively.

For the case of the second test (see Figures 5.9 to 5.13), the agreement between the FDTD results and the measurement results is good and the angular adjustment values are within the uncertainty range mentioned in Table 4.3.

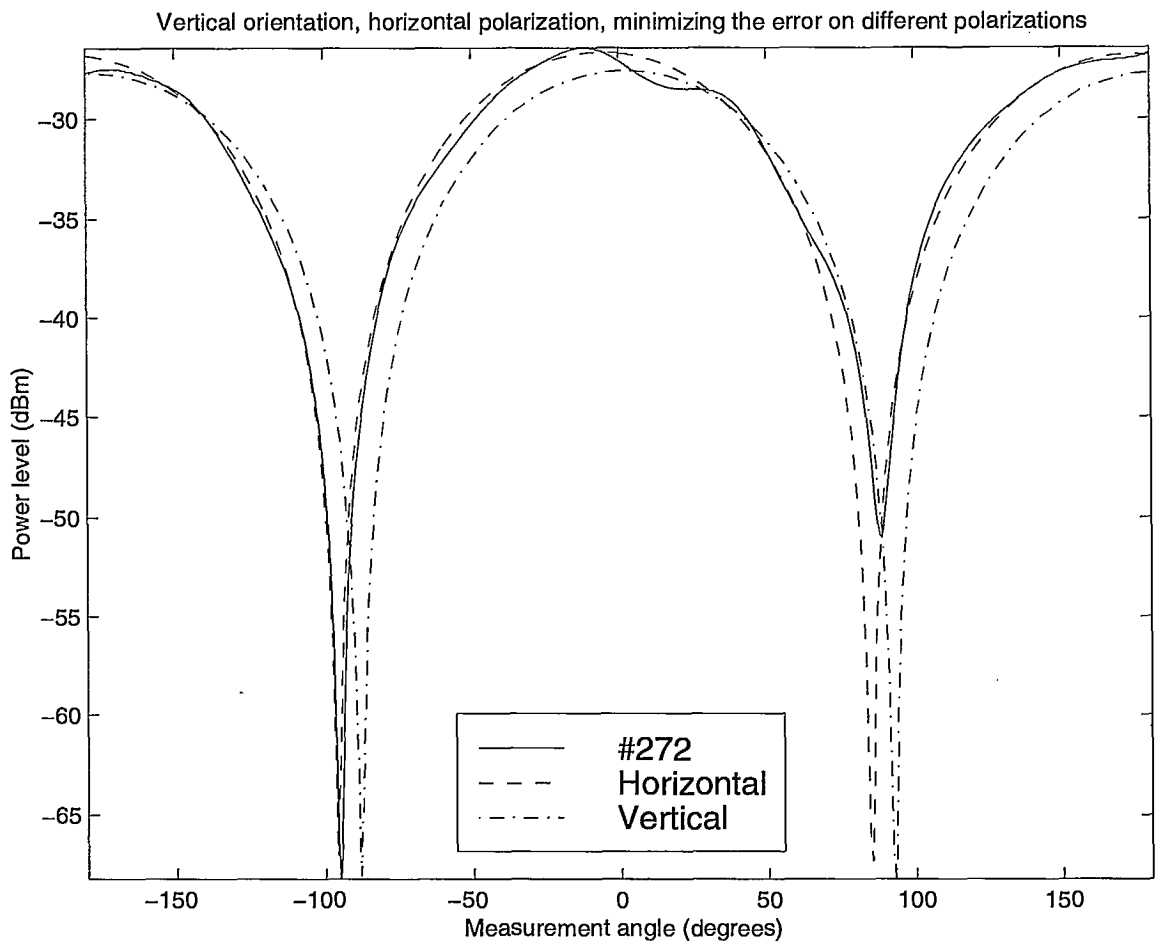

Figure 5.15: Comparison between the magnitudes of the FDTD predicted and the 1998 measured data of horizontal polarization for the case corresponding to *Vert2* when minimizing the difference between the predicted and the measured data of the vertical and the horizontal polarizations.

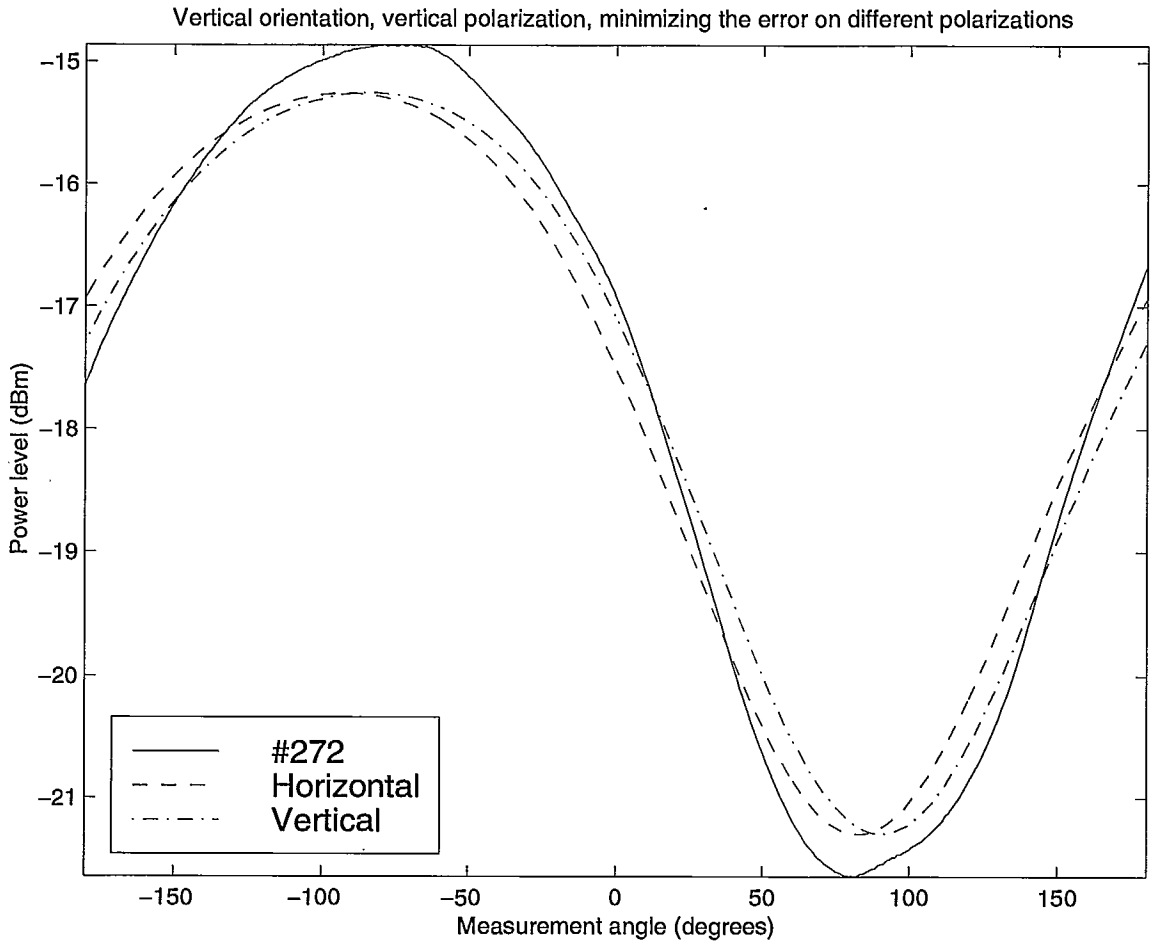

Figure 5.16: Comparison between the magnitudes of the FDTD predicted and the 1998 measured data of vertical polarization for the case corresponding to *Vert2* when minimizing the difference between the predicted and the measured data of the vertical and the horizontal polarizations.

5.2 1998 measured data vs 1997 measured data

5.2.1 Generalities

This section presents a comparison between the measured data reported in reference [1] and the corresponding measured data from the 1998 measurement for the vertical, flat and edge orientations. The following differences should be noted between the two test setups:

- the monopole antenna required to be resoldered between the first test of the 1997 measurement session and the first test of the 1998 measurement session as a result of the wire antenna having been hit accidentally. Consequently, the length of the monopole antenna might have have been slightly different between the two measurement sessions.

- A new styrofoam tower with a large uniform rectangular rather than a small tapered circular cross-section was used in the last mechanical setup in order to accomodate the large styrofoam jig housing the transmitter and the phantom head. As a result, the new tower left more surface area of the metallic azimuth table electromagnetically exposed, although the centre strip and the periphery of the table were well covered with a stack of absorbing material totalling a height of no less than 40 cm. However, since the horizontal orientation of the antenna resulted in a strong illumination of the top surface of the metallic azimuth table for the edge and the flat orientations, such a difference in the electromagnetically exposed surface area of the top surface of the upper azimuth table might have had a significant effect.

- the received horn was repositioned in the aperture of the pyramidal extension since the chamber had been used with other setups in the intervening year between the two measurements;

- the control cable for the crane was lined up with absorbing material oriented toward the azimuth table, rather than left uncovered and pushed snugly between the cones of the absorbers on the side wall of the chamber;

- the four huge absorbing pieces covering the monorail directly over the azimuth table were repositioned as a result of having been displaced from using the crane during the intervening year;

- a large obsolete metallic support bracket near the camera was removed and the metallic support bracket of the camera was covered with absorbing material as part of the last anechoic chamber setup; however, no record of the orientation of the camera was systematically kept throughout any test other than the assurance of leaving it undisturbed between repeated consecutive runs;

- a lamp affixed to the rear wall in a corner of the chamber was removed and the associated electrical socket was covered with absorbing material;

- new absorbing walk-on cubes forming a tower over 2 m high was added near the access door of the chamber to hide the door as part of the last anechoic chamber setup;

- two large transformers were removed from their anchoring site on the outside surface of the front wall of the chamber in order to avoid a possible contamination of the work environment by PCB contained within these transformers if leakage were to occur; as the bolts went through the chamber wall and the nuts laid on the inside of the chamber, the process of removing the transformers had required to remove temporarily some absorbing material. After performing run #276, it was discovered that one horizontal metallic bolt about 15 cm long had been left uncovered. Some absorbing material was then used to cover the bolt. Since the uncovered bolt was located in a lower front corner of the chamber, on the front wall which houses also the receive horn that faces the centre of the chamber, there was no line of sight between this bolt and the receive horn. However, indirect scattering off the uncovered bolt remained a possibility.

5.2.2 Results

Figures 5.17 to 5.22 present the comparison for the first test between the 1997 measured data, the 1998 measured data and the data predicted by XFDTD403. The FDTD predicted data used here corresponds to that presented earlier in section 5.1.3

for the transmitter model including the presence of the two small holes and featuring the normal length monopole antenna. However, the comparison was carried out without correcting the power level of the measured data for taking into account the transfer function of the network analyzer because this function was not measured for the 1997 calibration time frame. Consequently, the values for *Vert2, Flat2* and *Edge2* in Table 5.2 differ from those in Table 5.1. Moreover, the curves for both measured data sets are in dB rather than dBm (the curve for the FDTD predicted data is again in dBi) and the comparison with the FDTD predicted data is intended only as a guide.

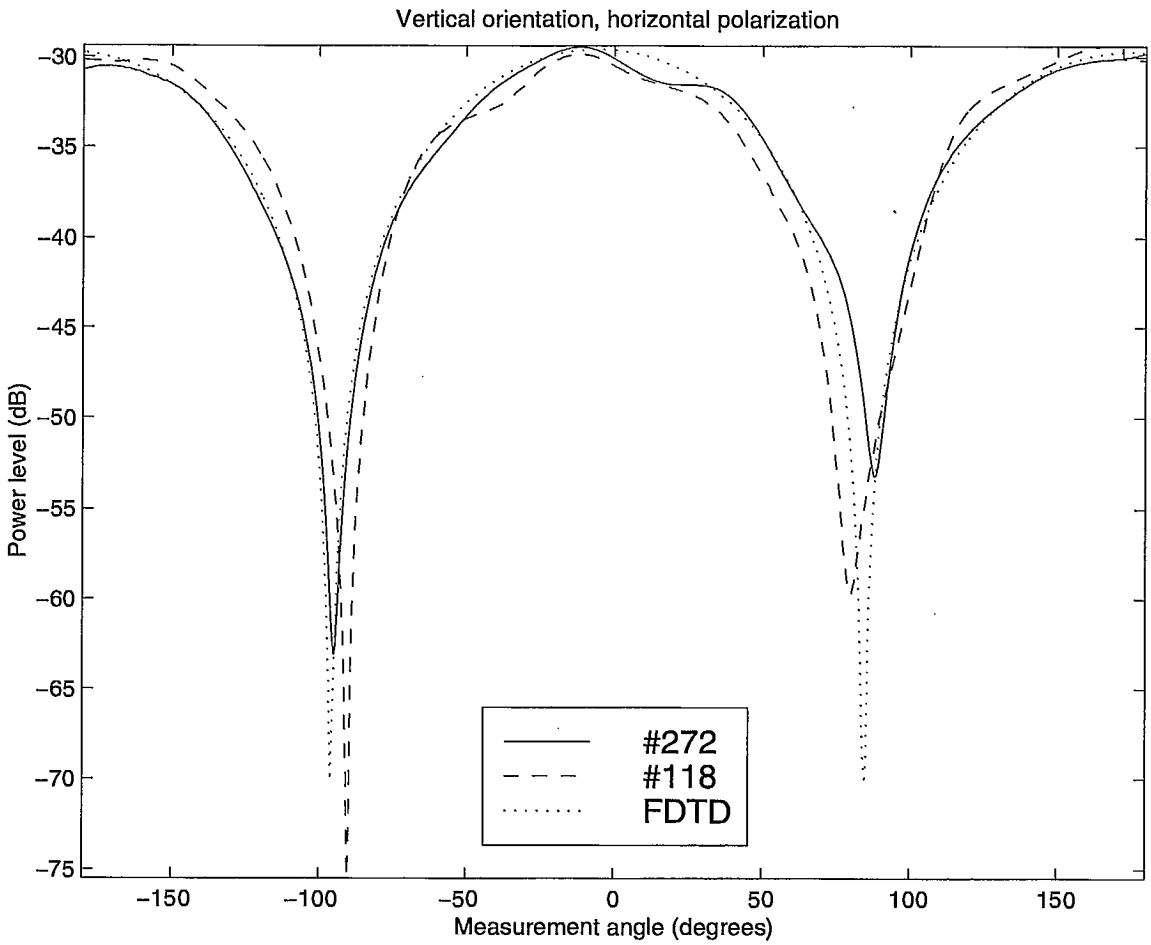

Figure 5.17: Comparison between the magnitudes of the FDTD predicted data, the 1997 measured data and the 1998 measured data in the horizontal polarization for the vertical orientation of the first test.

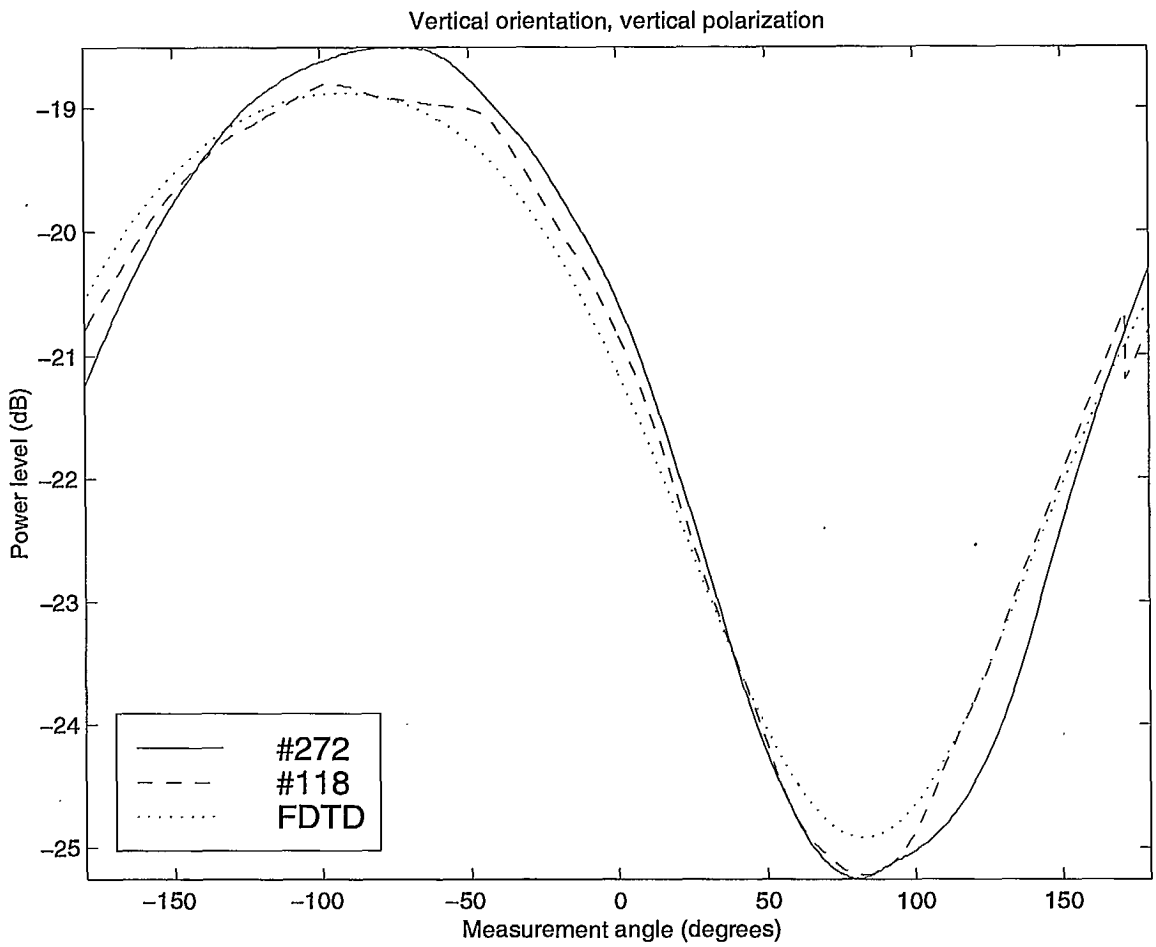

Figure 5.18: Comparison between the magnitudes of the FDTD predicted data, the 1997 measured data and the 1998 measured data in the vertical polarization for the vertical orientation of the first test.

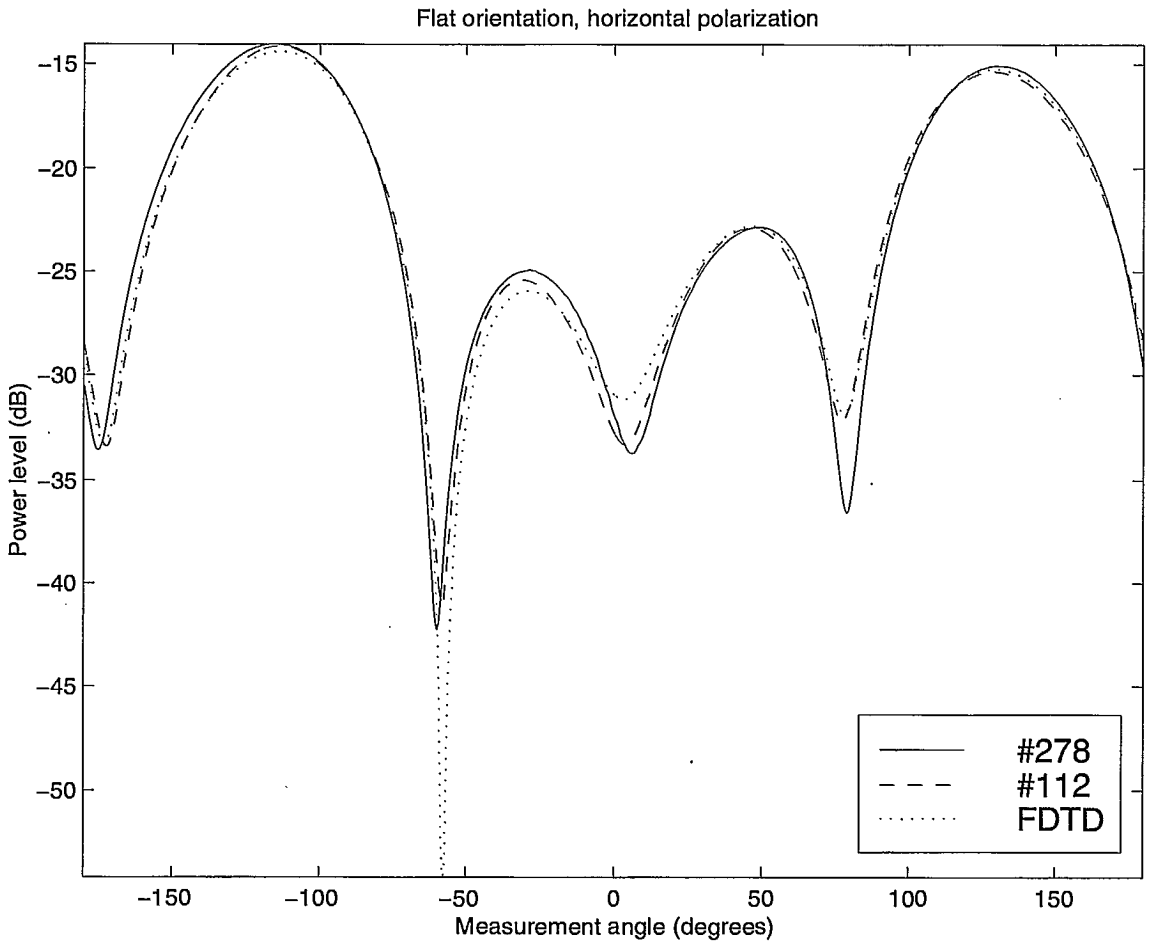

Figure 5.19: Comparison between the magnitudes of the FDTD predicted data, the 1997 measured data and the 1998 measured data in the horizontal polarization for the flat orientation of the first test.

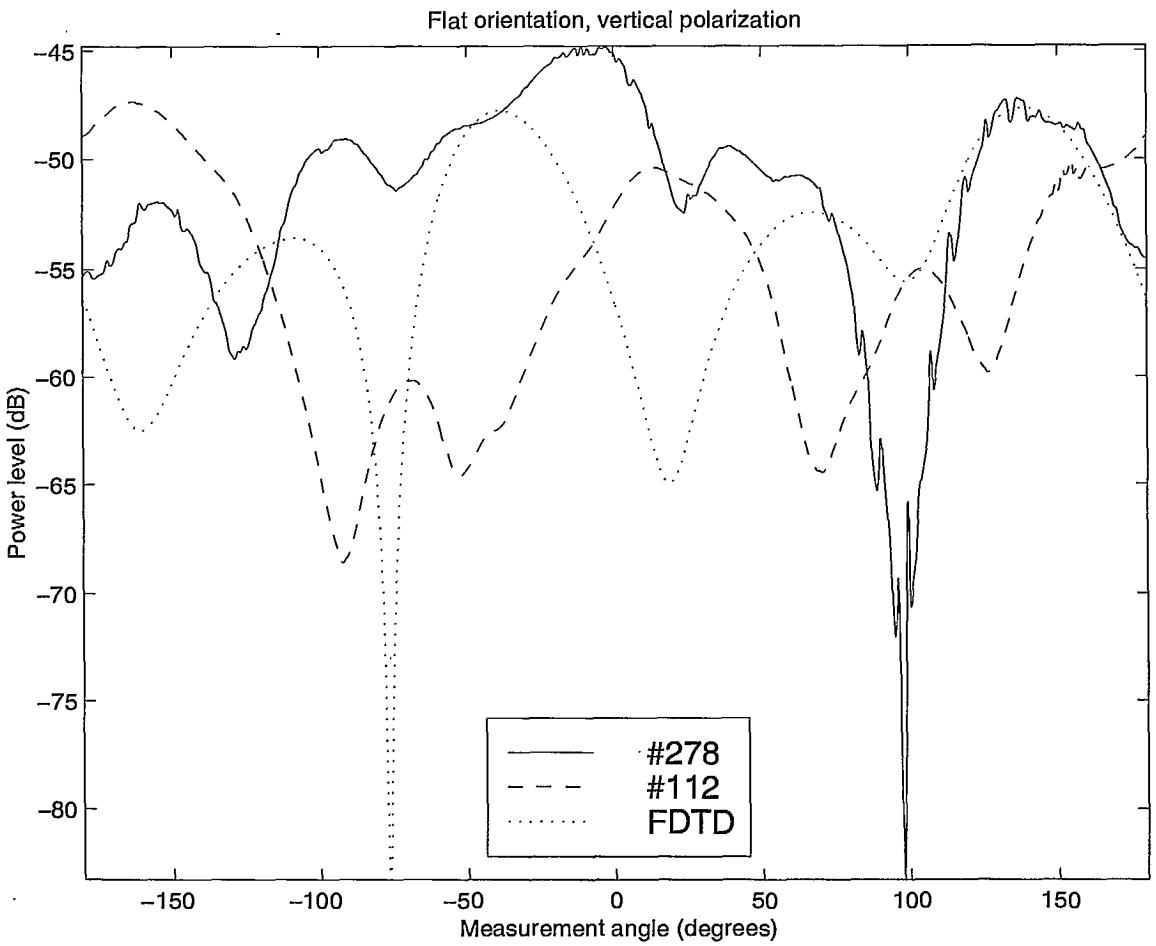

Figure 5.20: Comparison between the magnitudes of the FDTD predicted data, the 1997 measured data and the 1998 measured data in the vertical polarization for the flat orientation of the first test.

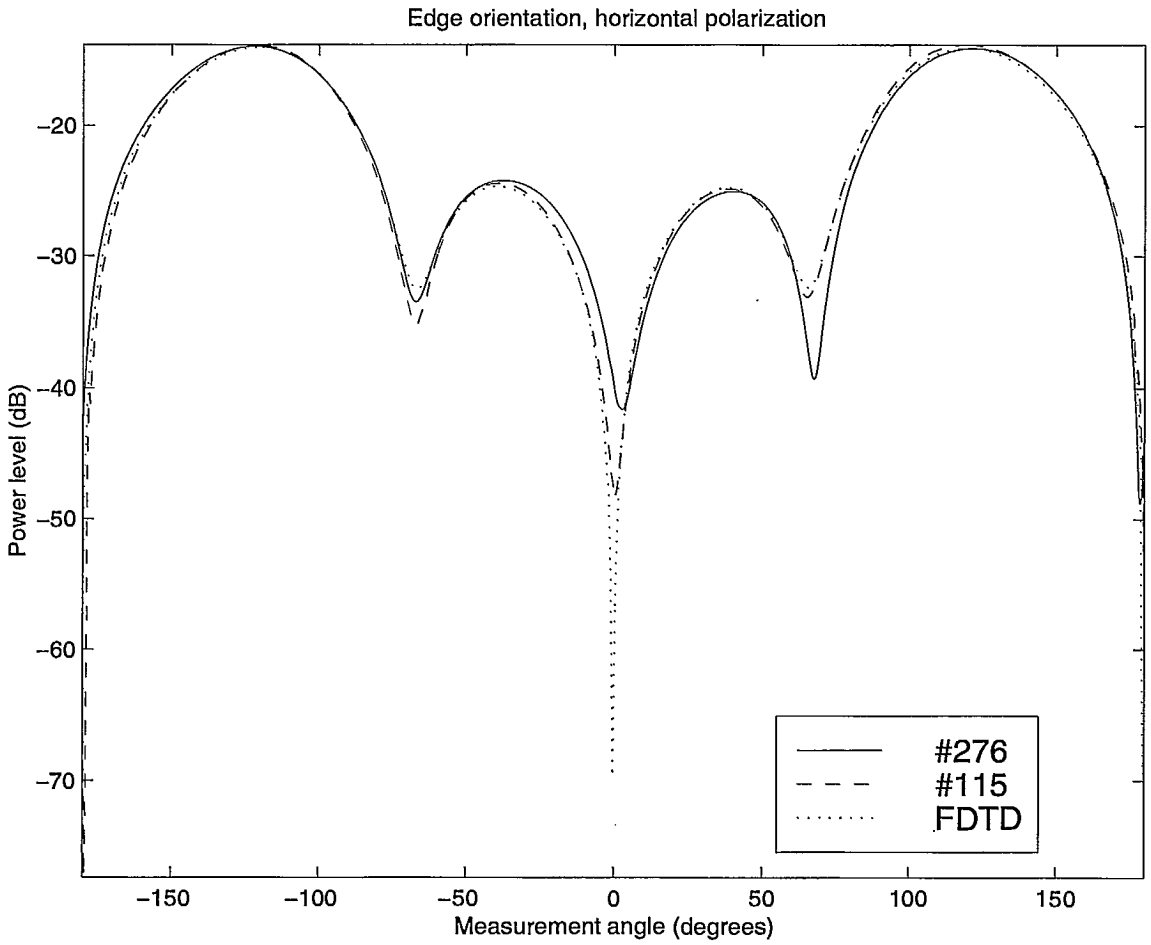

Figure 5.21: Comparison between the magnitudes of the FDTD predicted data, the 1997 measured data and the 1998 measured data in the horizontal polarization for the edge orientation of the first test.

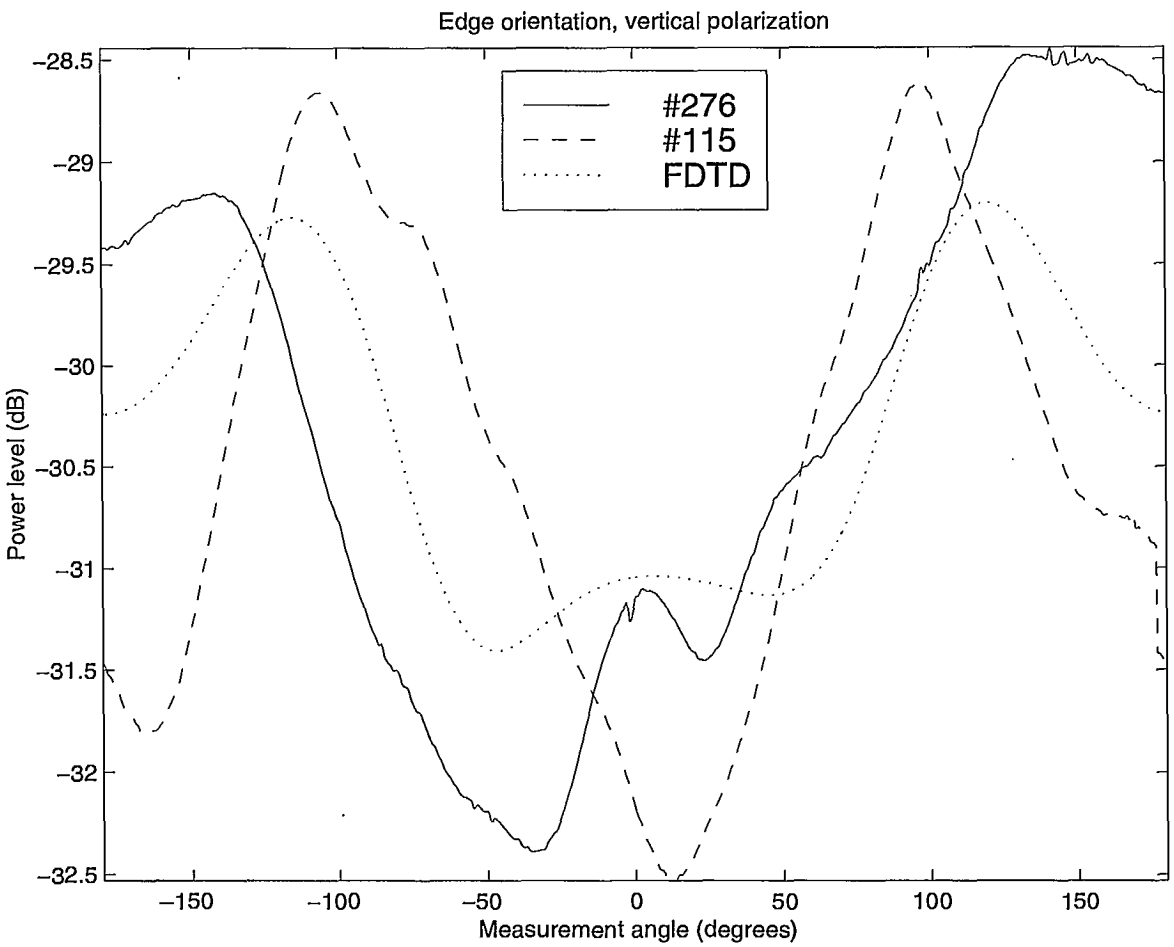

Figure 5.22: Comparison between the magnitudes of the FDTD predicted data, the 1997 measured data and the 1998 measured data in the vertical polarization for the edge orientation of the first test.

5.2.3 Discussion

Table 5.2 present the pertinent numerical values obtained from the comparison process. The offset angle values for #118, #112 and #115 shows clearly a difference in the alignment of the transmitter between the 1997 and the 1998 test. Figure 5.17 shows that for the vertical orientation, the 1998 measured data (#272) is much more in agreement with the FDTD predicted data than does the 1997 measured data (#118), even after allowing for an adjustment angle. Thus, the very shape of the horizontal polarization curve for the 1997 measured data of the vertical orientation seems to be less accurate.

On the other hand, Figures 5.19 and 5.21 show that the 1997 measured results (#112 and #115) are in better agreement with the FDTD predicted results than do the corresponding 1998 measured results (#278 and #276) for both the flat and the edge orientations, specially in the region of about $+80^o$ and $+70^o$ for the flat and the edge orientations, respectively. Consequently, the 1998 measured data (#276) shows a strong break in the symmetry of the radiation pattern whereas the corresponding 1997 measured data (#115) did not. According to Figure 5.7, the presence of the two small holes cannot account for much of the 5 dB asymmetry. Since the corresponding curve for the 1997 measured data does not show a strong break in symmetry, we surmise that the break might be due to one or many of the aforementioned changes made to the chamber or changes made to the transmitter (e.g. straightness of the monopole antenna wire[1]) in the intervening year between the two sets of measurement. The fact that the monopole antenna illuminated strongly the azimuth table for both orientations for which it was found that the 1998 measured data was not in better agreement than the 1997 measured data in spite of a better mechanical alignment suggests that the cause for the degradation owes to the change of styrofoam tower (the new tower presented a larger surface area of the metallic azimuth

[1]Note: In order to prevent damaging the monopole wire antenna whenever the transmitter is not in use, the transmitter is kept in a custom made protective metallic case with sponge molding cradling the box but leaving self-supporting the wire antenna. It might be possible that through months of remaining in the horizontal position, the wire acquired a droop. But more importantly, there have been a few instances of the wire having been lightly struck by accident in the course of handling the transmitter.

Table 5.2: Summary of the pertinent numerical values obtained from the process of comparing the FDTD predicted data and the 1997 measured data against the 1998 measured data for the first test.

Cases	Offset	Scaling factor (dB)		Total error ($dB/°$)	
	(°)	Horizontal	Vertical	Horizontal	Vertical
#118	-8.2	0.0033	0.9947	-1.6726	-0.4818
Vert2	-6.0	18.5046	20.3683	-8.5695	+2.4496
#112	-2.6	0.1748	7.4033	+4.9404	-3.7848
Flat2	+1.8	18.8884	5.8496	+5.2356	-7.6314
#115	-3.6	-0.2540	-0.2463	+4.4246	+4.7240
Edge2	-0.4	18.2705	18.7937	+3.2220	-0.9943
Vert: vertical orientation *Flat*: flat orientation *Edge*: edge orientation *2*: transmitter with holes; monopole being 40 cells long					

table exposed to radiation). Furthermore, Figure 5.20 shows a very different cross-polarization response of the chamber between the 1997 measured data (#112) and the 1998 measured data (#278).

Chapter 6

Conclusion

This report presented the test setup and the measurement results for the far fields radiated in the principal planes by a battery-operated portable transmitter when the transmitter was alone or in the presence of a phantom head. The agreement between the measured data and the data predicted by FDTD simulations for the first and second tests was good for both the co-polarization and the cross-polarization, albeit the comparison was carried out only on a relative basis by means of using a scaling factor between the measured and the predicted results.

Surprisingly, the far-field radiation pattern for the transmitter alone presents some strong lobes at some oblique angle toward the ground with respect to the transmitter being vertical. We also observed that the far-field radiation pattern is affected significantly by the presence of the phantom head, tending to fill nulls of the pattern, to increase the amount of cross-polarization and to create some shadowing by absorbing a part of the energy as the wave propagates through the head.

There remains to ascertain the cause for the strong symmetry break observed in the measured data for the edge orientation of the first test. The analysis presented in this report also revealed a few surprises:

- the portion of the metallic surface of the azimuth table left electromagnetically exposed by the presence of the styrofoam tower produces enough reflections to degrade noticeably the results whenever the transmitter radiates strongly in the

direction of that surface;

- the presence of a small hole in the metallic cover of the transmitter or the presence of a small bend in the monopole antenna can have a noticeable effect on the cross-polarization;
- modifying the placement of some absorbing material far away from the tower can affect the deep cross-polarization null by as much as 6 dB;
- the strength of the electrical noise was observed to vary with the orientation of the transmitter.

However, despite the relative success reported herein, it is felt that this DFL chamber is not the most appropriate environment to carry out the measurement of the far field radiation for a system with a broad radiation pattern at the relatively low frequency of 850 MHz because:

- the absorbing material currently used in this chamber is not designed to be effective at 850 MHz;
- the overhead crane and metallic monorail can act as unintended scatterers;
- the large electromagnetic window leaves the chamber susceptible to outside interference;
- the two corner lights in the approximate shape of corner reflectors can act as strong re-radiators;
- the heavy rail lying on the floor on one side of the chamber can act as an unintended scatterer and should have been removed as a precaution toward eliminating any unintended scattering;
- the azimuth-over-elevation-over-azimuth positioner has its bearing at the base of the lower azimuth axis worn out which situation causes an alignment error if no external corrective action is taken;
- an inordinate amount of time was required to properly position the receive horn because the setup lacked the flexibility to adjust independently the various

parameters of the horn (yaw, roll, pitch and location of the horn in the aperture of the pyramidal extension). Just recently, however, this difficulty has been mitigated by mounting the receive horn on a special bracket that allows to adjust pitch and roll independently of any other parameter.

References

[1] J.E. Roy, W.R. Lauber and J.M. Bertrand, Measurements of the Electromagnetic Far-Fields Produced by a Portable Transmitter (Principal Planes), CRC report CRC-RP-02-98, February 1998, pp. 116.

[2] R.M.T. Milne, Description And Calibration of the CRC R.F. Test Facility, CRC Technical Memorandum, Serial No. DFL-102, 1 May 1975.

[3] J.M. Bertrand and W.R. Lauber, CRC Model Transmitter, Technical Memorandum VPRB-05-97, CRC, Ottawa, May 1997.

[4] User's manual for XFDTD, version 4.03 for X-window, by Remcom Inc., June 1997, State College, PA.

[5] R.E. Collin, Foundations for Microwave Engineering, McGraw-Hill, 1966, pp. 389.

[6] C.W. Trueman and S.J. Kubina, A Research Study on Electromagnetic Fields Produced by Portable Transceivers, EMC Laboratory, Department of Electrical and Computer Engineering, University of Concordia, Final report #TN-EMC-98-01, March 31, 1998, pp. 161.

[7] C.W. Trueman, EMC Laboratory, Department of Electrical and Computer Engineering, University of Concordia, private communication, October 1998.

Appendix A

Drawings

This appendix presents the drawings for the transmitter, the phantom head and the styrofoam jig. Drawings FFPPM.1 to FFPPM.5 pertain to the first test whereas PHM01 to PHM17 pertain to the second and third tests. Drawings PHM18 and PHM19 pertain to all three tests.

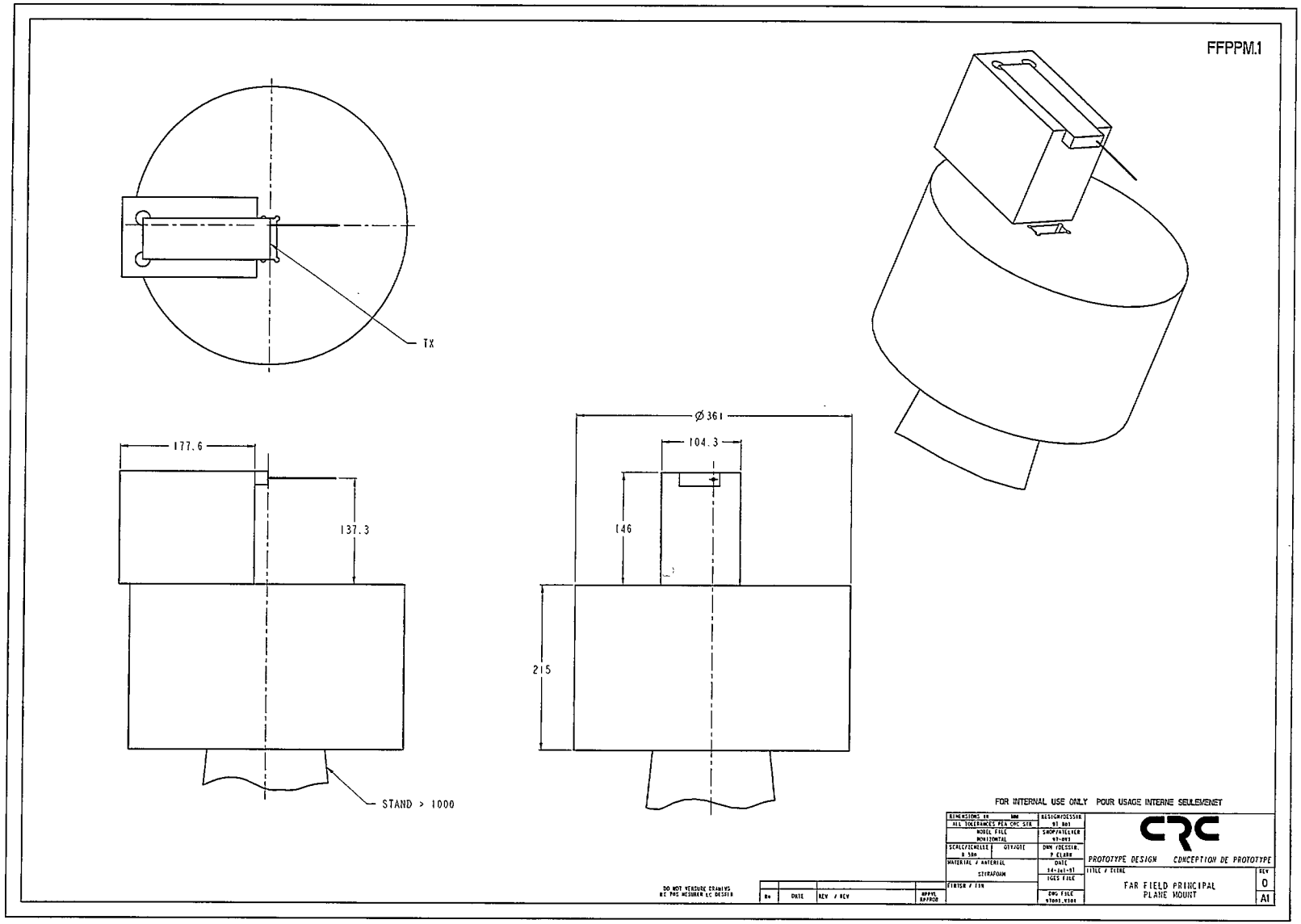
FFPPM.1
TX
177.6
137.3
STAND > 1000
Ø 361
104.3
146
215
FOR INTERNAL USE ONLY POUR USAGE INTERNE SEULEMENT
PROTOTYPE DESIGN CONCEPTION DE PROTOTYPE
FAR FIELD PRINCIPAL PLANE MOUNT
DO NOT MEASURE DRAWING NE PAS MESURER LE DESSIN

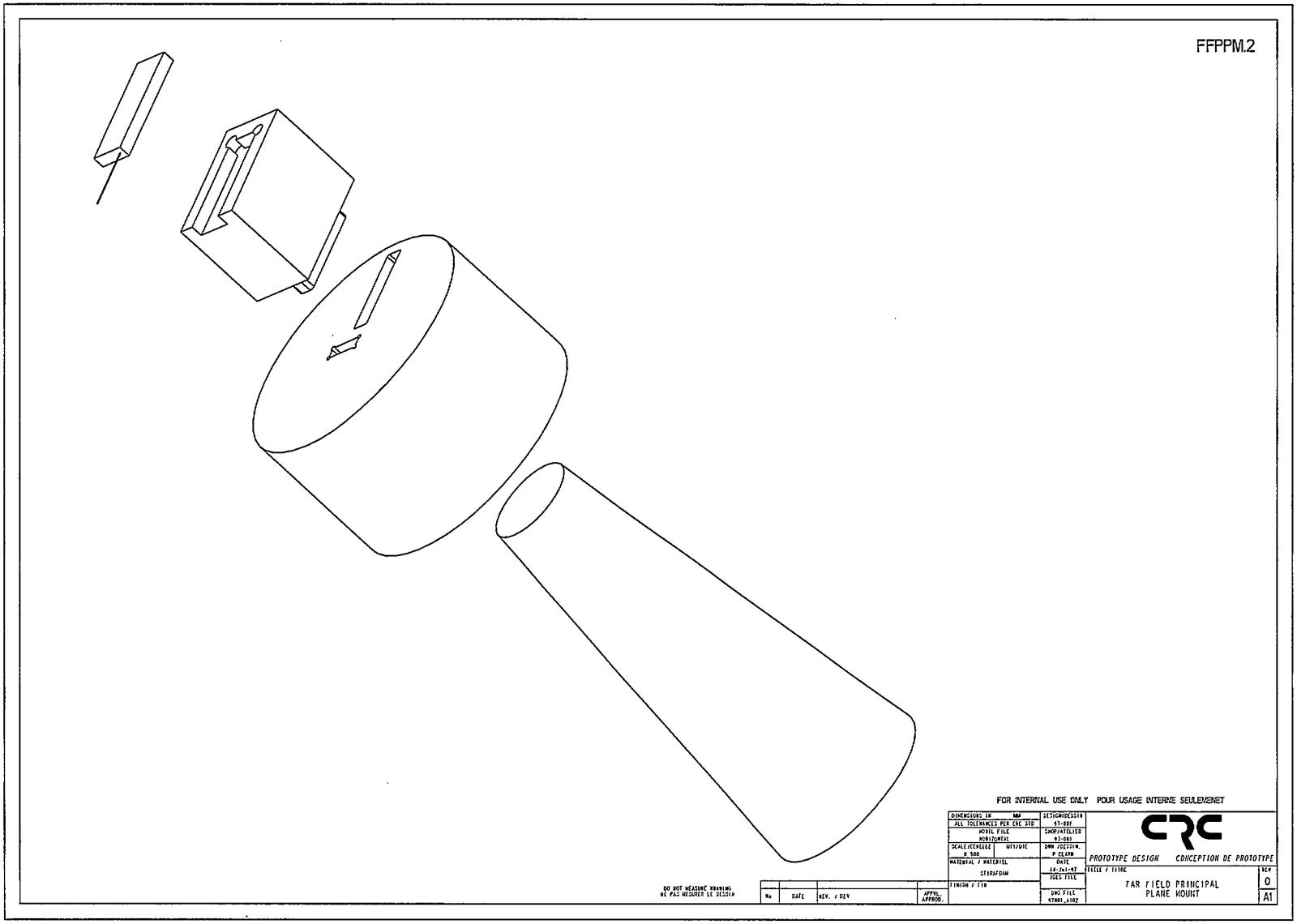
FFPPM.2
FOR INTERNAL USE ONLY POUR USAGE INTERNE SEULEMENET
DIMENSIONS IN MM
ALL TOLERANCES PER CNC STD
MODEL FILE
HORIZONTAL
SCALE/ECHELLE
0.500
QTY/DIE
MATERIAL / MATERIEL
STIRAFOAM
FINISH / FIN
DESIGN/DESSIN
97-001
SHOP/ATELIER
97-001
DWN /DESSIN.
P CLAWN
DATE
IGES FILE
DWG FILE
97001_A102
CRC
PROTOTYPE DESIGN CONCEPTION DE PROTOTYPE
TITLE / TITRE
FAR FIELD PRINCIPAL
PLANE MOUNT
REV
0
A1
DO NOT MEASURE DRAWING
NE PAS MESURER LE DESSIN
No
DATE
REV. / DEV
APPVL.
APPROB.

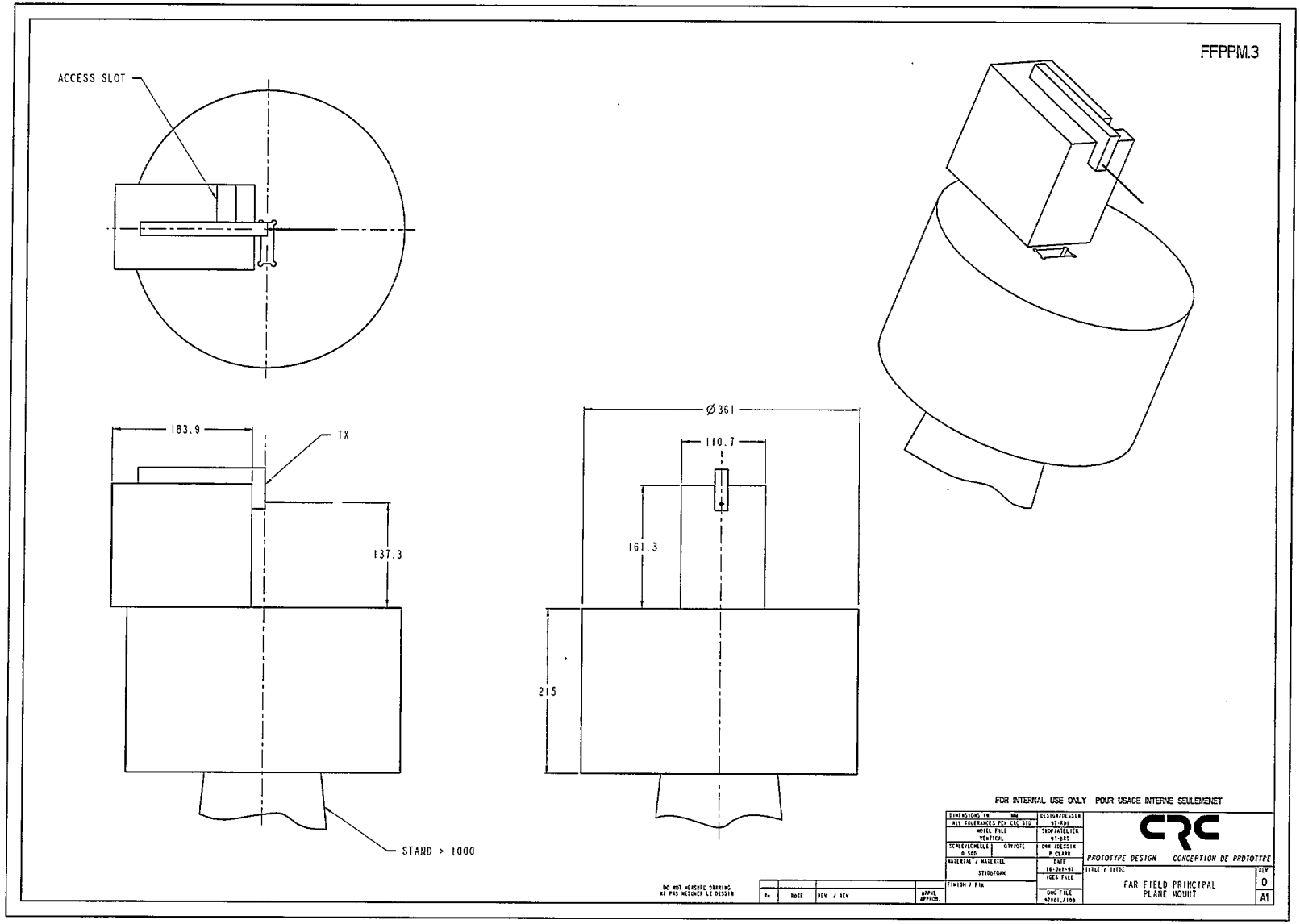
FFPPM.3
ACCESS SLOT
183.9
TX
137.3
STAND > 1000
Ø361
110.7
161.3
215
FOR INTERNAL USE ONLY POUR USAGE INTERNE SEULEMENT
PROTOTYPE DESIGN CONCEPTION DE PROTOTYPE
FAR FIELD PRINCIPAL PLANE MOUNT
DO NOT MEASURE DRAWING NE PAS MESURER LE DESSIN

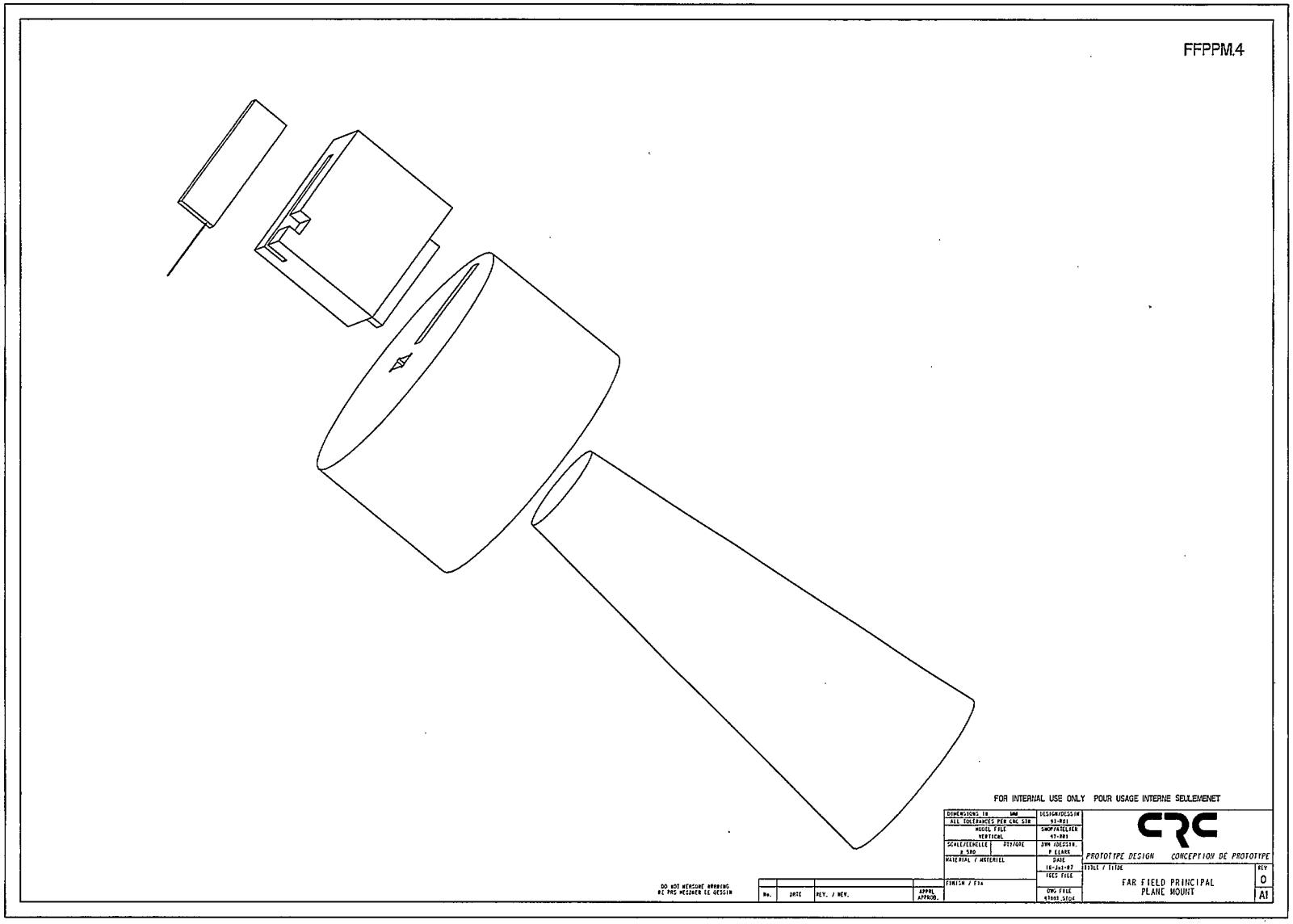
FFPPM.4
FOR INTERNAL USE ONLY POUR USAGE INTERNE SEULEMENET
DIMENSIONS IN MM
ALL TOLERANCES PER CRC STR
MODEL FILE
VERTICAL
SCALE/ECHELLE
DTY/QTE
MATERIAL / MATERIEL
FINISH / FIN
DESIGN/DESSIN
SHOP/ATELIER
DWN /DESSIN.
DATE
IGES FILE
DWG FILE
CRC
PROTOTYPE DESIGN
CONCEPTION DE PROTOTYPE
TITLE / TITRE
FAR FIELD PRINCIPAL
PLANE MOUNT
REV
0
A1
DO NOT MEASURE DRAWING
NE PAS MESURER LE DESSIN
No.
DATE
REV. / MEV.
APPRL
APPROB.

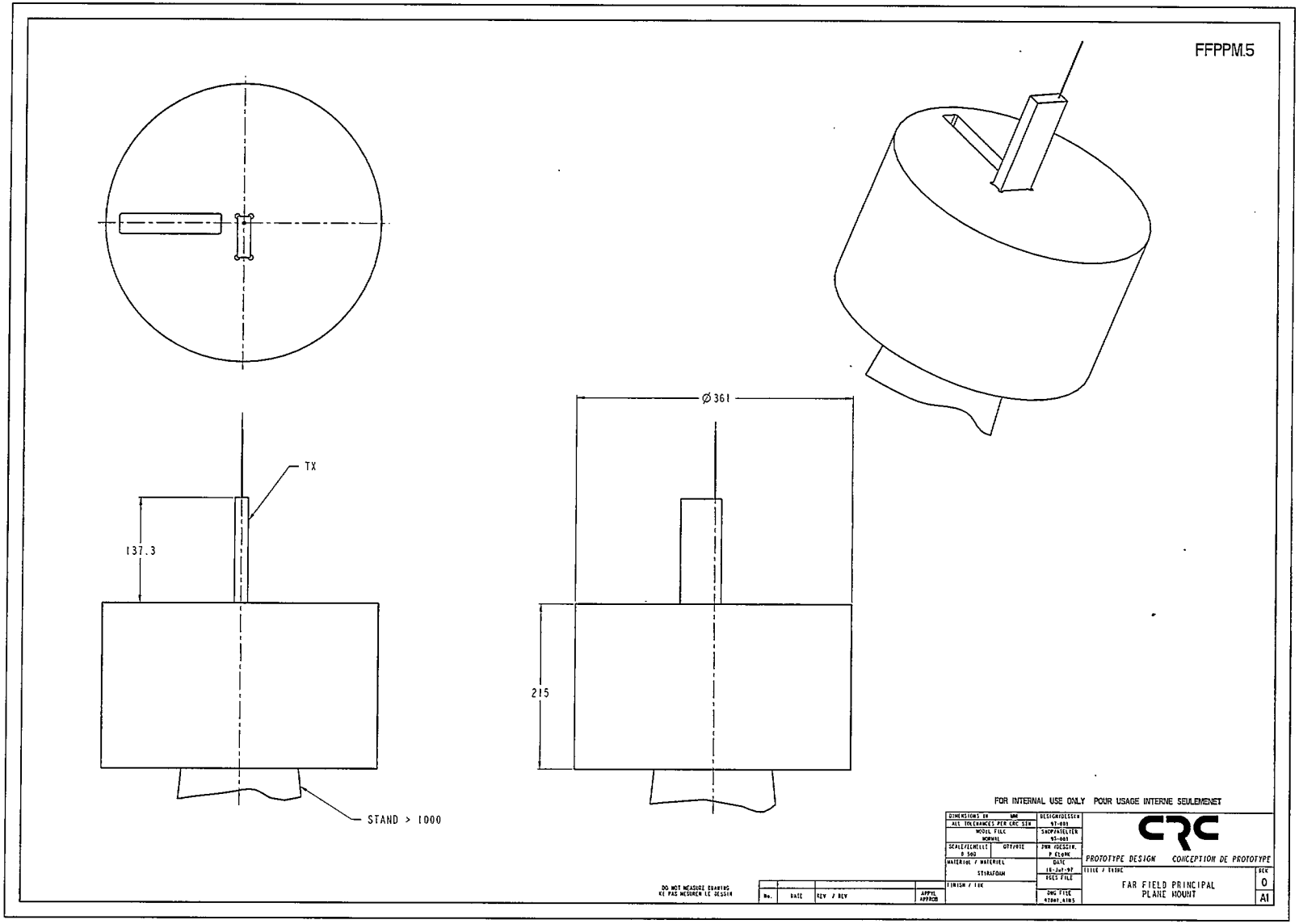
FFPPM.5
Ø361
TX
137.3
215
STAND > 1000
FOR INTERNAL USE ONLY POUR USAGE INTERNE SEULEMENT
PROTOTYPE DESIGN CONCEPTION DE PROTOTYPE
FAR FIELD PRINCIPAL PLANE MOUNT
DO NOT MEASURE DRAWING NE PAS MESURER LE DESSIN

PHM01

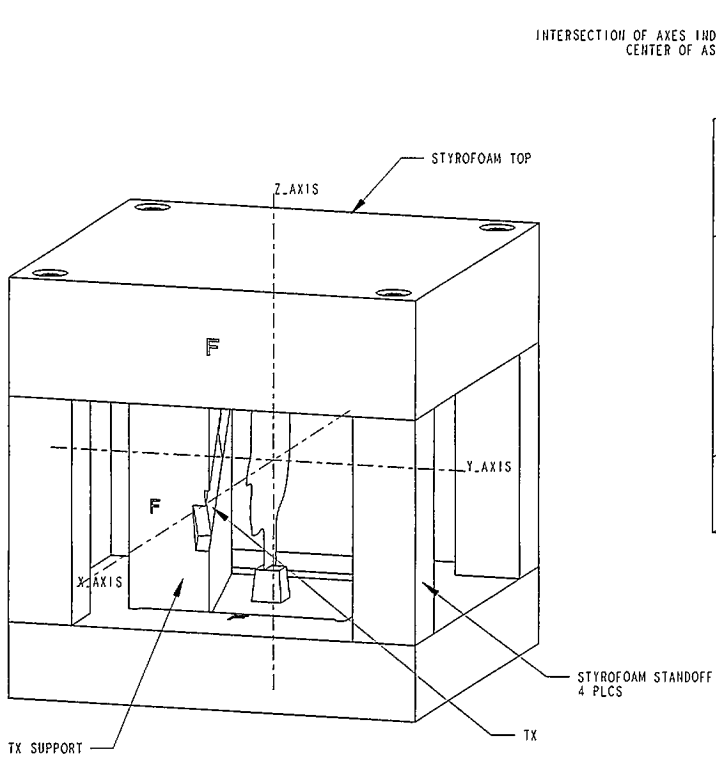

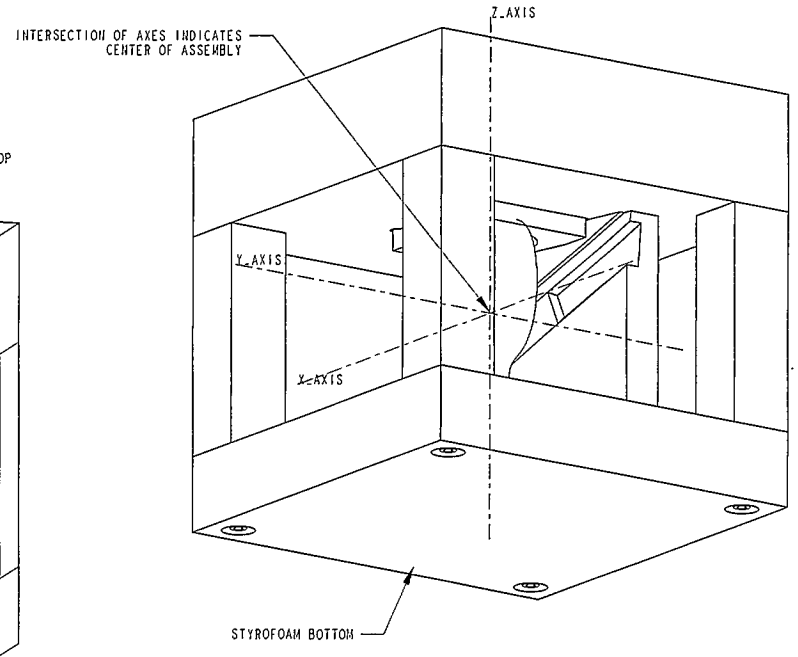

FOR INTERNAL USE ONLY POUR USAGE INTERNE SEULEMENT

DIMENSIONS IN MM	DESIGN/DESSIN
ALL TOLERANCES PER CRC STD	98-020
MODEL FILE CONCEPT2	SHOP/ATELIER
SCALE/ECHELLE 1:5 / QTY/QTE 1	DWN./DESSIN. A. GIROUX
MATERIAL / MATERIEL	DATE 14-Jul-98
FINISH / FIN.	IGES FILE
	DWG FILE 98020-01A3

CRC

PROTOTYPE DESIGN CONCEPTION DE PROTOTYPE

TITLE / TITRE: MOUNT FOR EM FIELD MEASUREMENTS WITH TX AND PHANTOM HEAD

REV.: A3

DO NOT MEASURE DRAWING
NE PAS MESURER LE DESSIN

No.	DATE	REV. / REV.	APPVL. APPROB.

PHM02

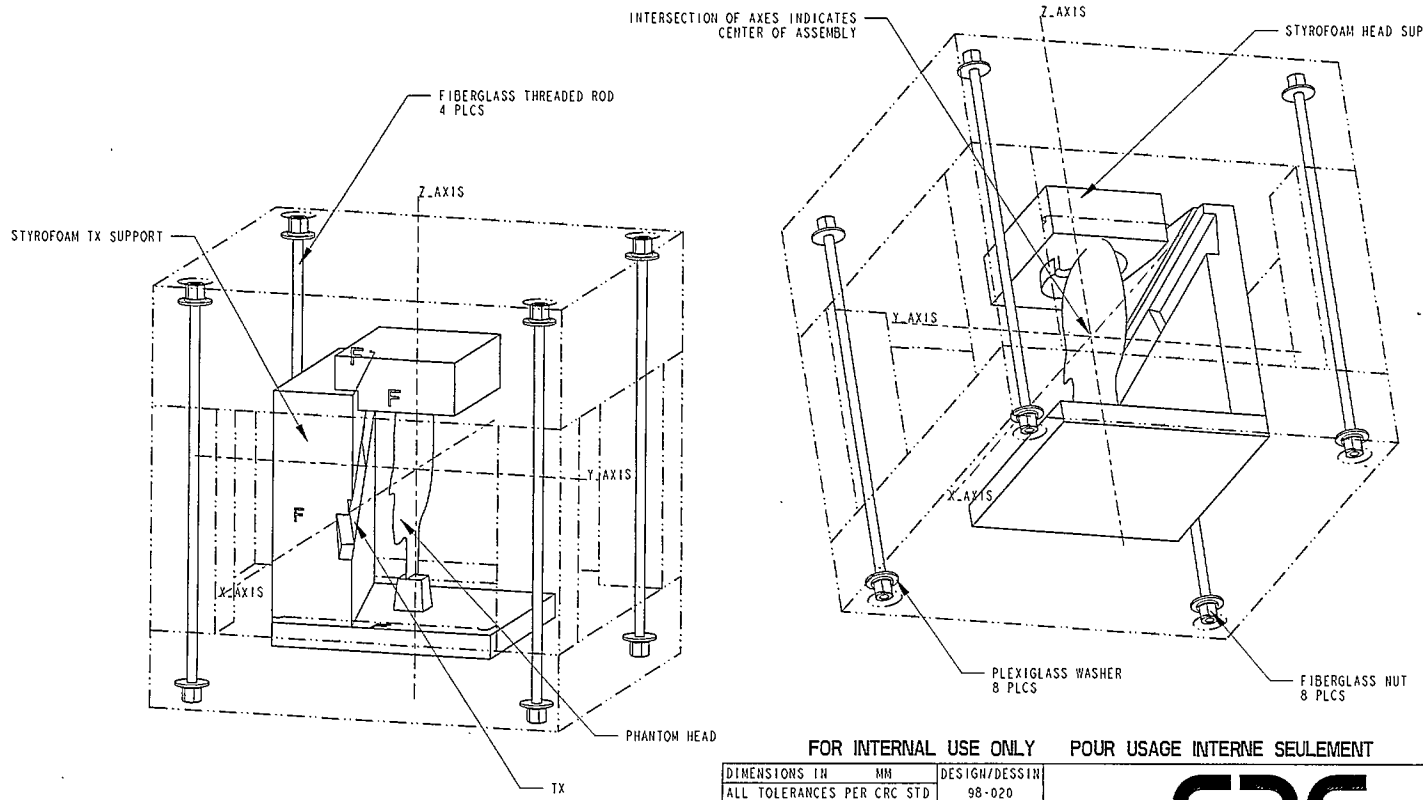

FOR INTERNAL USE ONLY POUR USAGE INTERNE SEULEMENT

DIMENSIONS IN MM	DESIGN/DESSIN
ALL TOLERANCES PER CRC STD	98-020
MODEL FILE CONCEPT2	SHOP/ATELIER
SCALE/ECHELLE 1:5 / QTY/QTE 1	DWN /DESSIN. A. GIROUX
MATERIAL / MATERIEL	DATE 14-Jul-98
	IGES FILE
FINISH / FIN.	DWG FILE 98020-01A3

CRC

PROTOTYPE DESIGN CONCEPTION DE PROTOTYPE

TITLE / TITRE: MOUNT FOR EM FIELD MEASUREMENTS WITH TX AND PHANTOM HEAD

REV.: A3

DO NOT MEASURE DRAWING
NE PAS MESURER LE DESSIN

No.	DATE	REV. / REV.	APPVL. APPROB.

PHM03

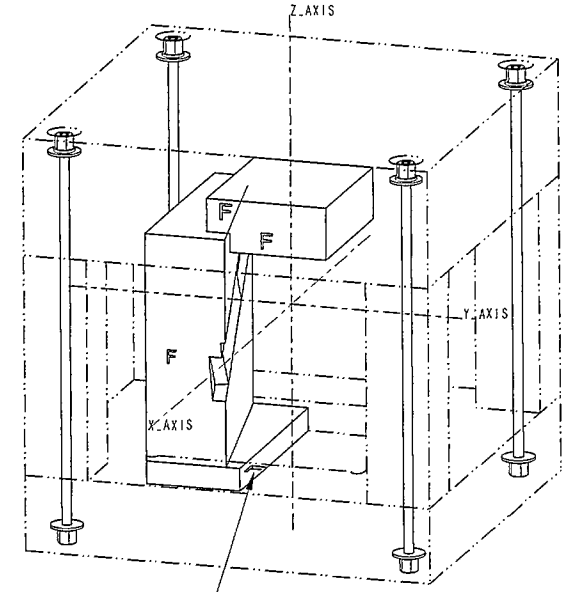

STYROFOAM TX SUPPORT SPACER
USE ONLY WHEN PHANTOM HEAD IS REMOVED

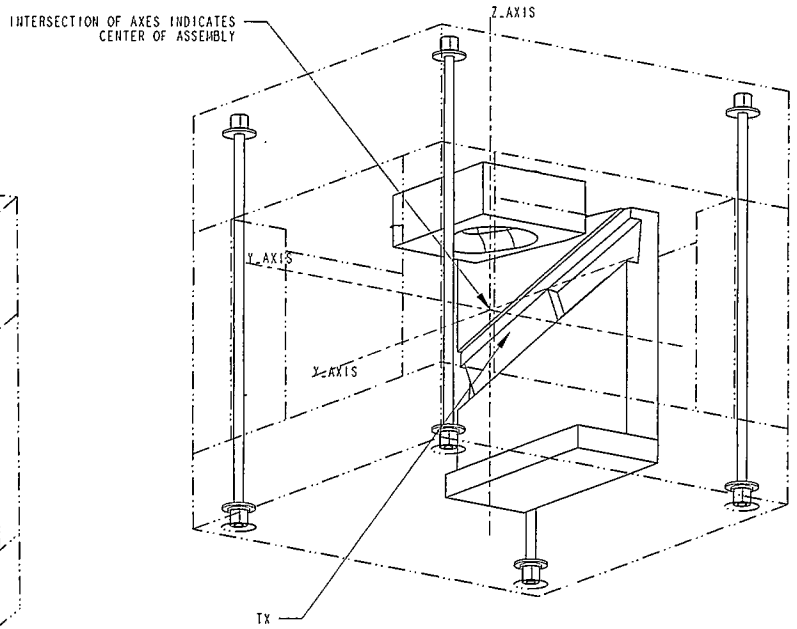

FOR INTERNAL USE ONLY POUR USAGE INTERNE SEULEMENT

DIMENSIONS IN MM		DESIGN/DESSIN
ALL TOLERANCES PER CRC STD		98-020
MODEL FILE CONCEPT2		SHOP/ATELIER
SCALE/ECHELLE 27:80	QTY/QTE 1	DWN./DESSIN. A. GIROUX
MATERIAL / MATERIEL		DATE 16-Jul-98
		IGES FILE
FINISH / FIN.		DWG FILE 98020-01A3

CRC

PROTOTYPE DESIGN CONCEPTION DE PROTOTYPE

TITLE / TITRE

MOUNT FOR EM FIELD MEASUREMENTS
WITH TX AND TX SUPPORT SPACER

REV. A3

DO NOT MEASURE DRAWING
NE PAS MESURER LE DESSIN

No.	DATE	REV. / REV.	APPVL. APPROB.

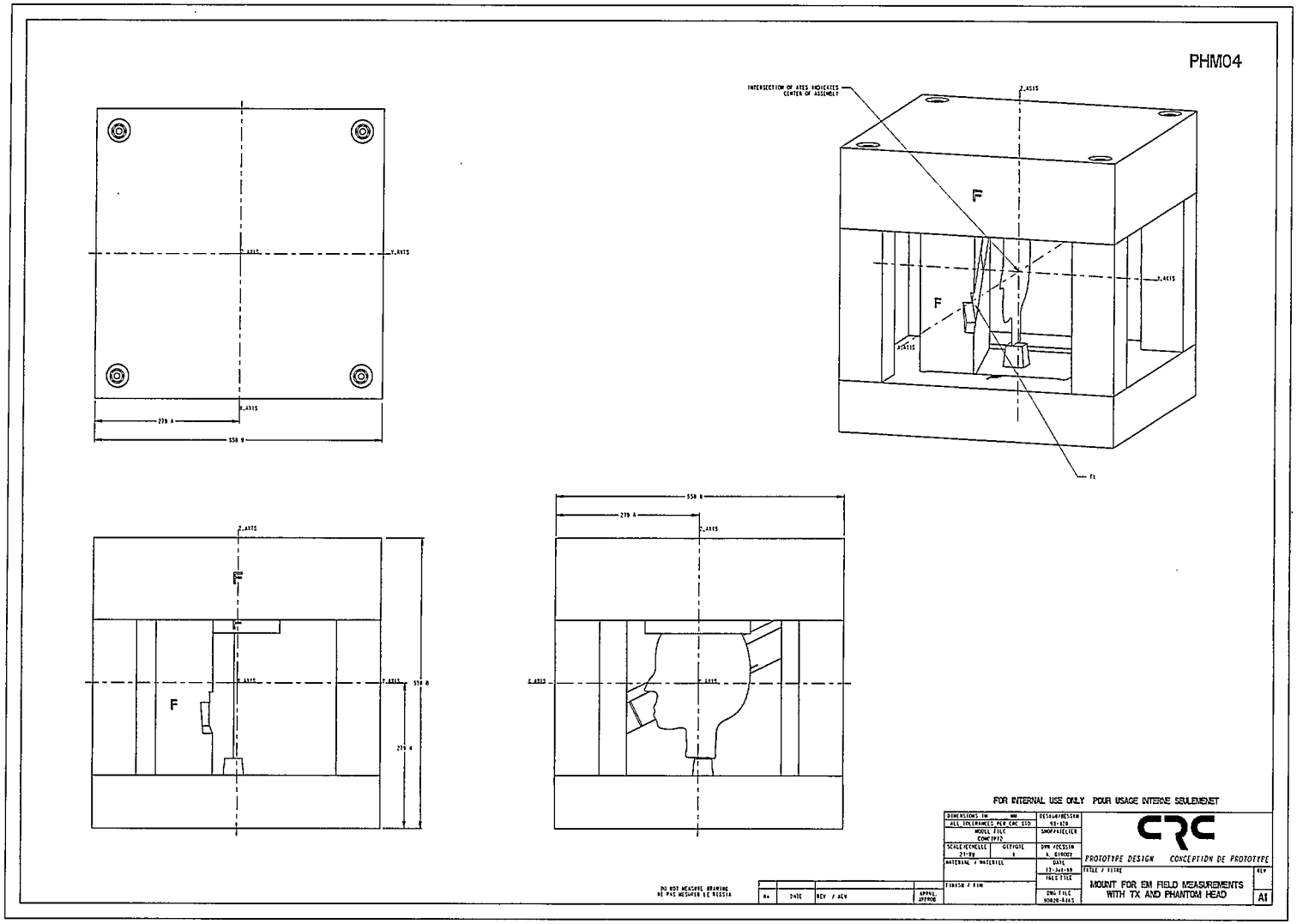
PHM04
INTERSECTION OF AXES INDICATES CENTER OF ASSEMBLY
Z_AXIS
Y_AXIS
X_AXIS
F
TX
279 A
558 B
FOR INTERNAL USE ONLY POUR USAGE INTERNE SEULEMENET
DIMENSIONS IN MM
ALL TOLERANCES PER CRC STD
MODEL FILE CONCIPIT2
SCALE/ECHELLE 21-BB
GEOPOTE 1
MATERIAL / MATERIEL
FINISH / FIN
DESIGN/DESSIN 99-420
SHOP/ATELIER
DWN /DESSIN A. GIROUX
DATE 12-Jul-99
IGES FILE
DWG FILE 00020-R165
CRC
PROTOTYPE DESIGN CONCEPTION DE PROTOTYPE
TITLE / TITRE
MOUNT FOR EM FIELD MEASUREMENTS WITH TX AND PHANTOM HEAD
REV
A1
DO NOT MEASURE DRAWING NE PAS MESURER LE DESSIN
No
DATE
REV / AEN
APPVL. APPROB

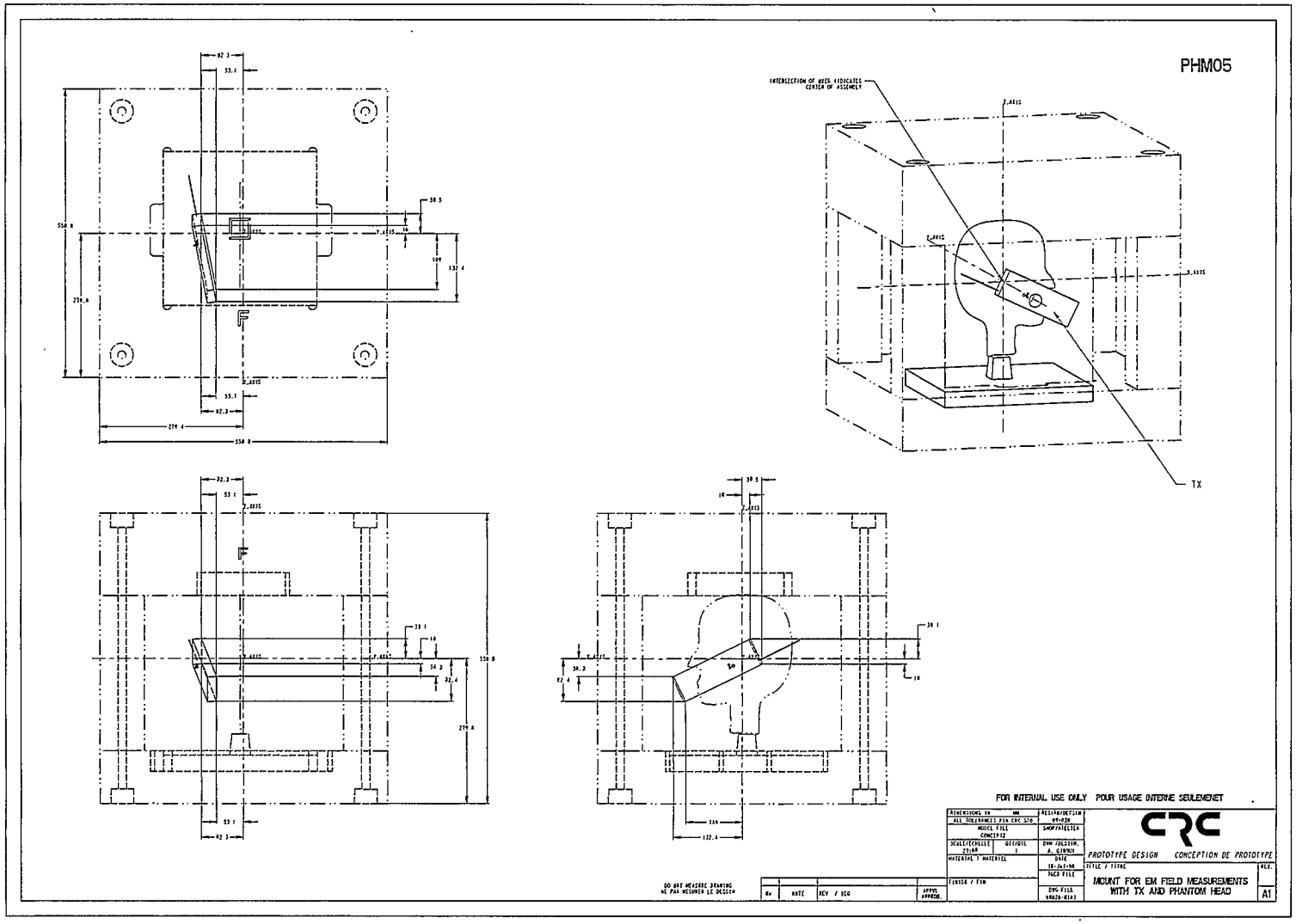
PHM05
TX
FOR INTERNAL USE ONLY POUR USAGE INTERNE SEULEMENET
CRC
PROTOTYPE DESIGN CONCEPTION DE PROTOTYPE
MOUNT FOR EM FIELD MEASUREMENTS
WITH TX AND PHANTOM HEAD
A1

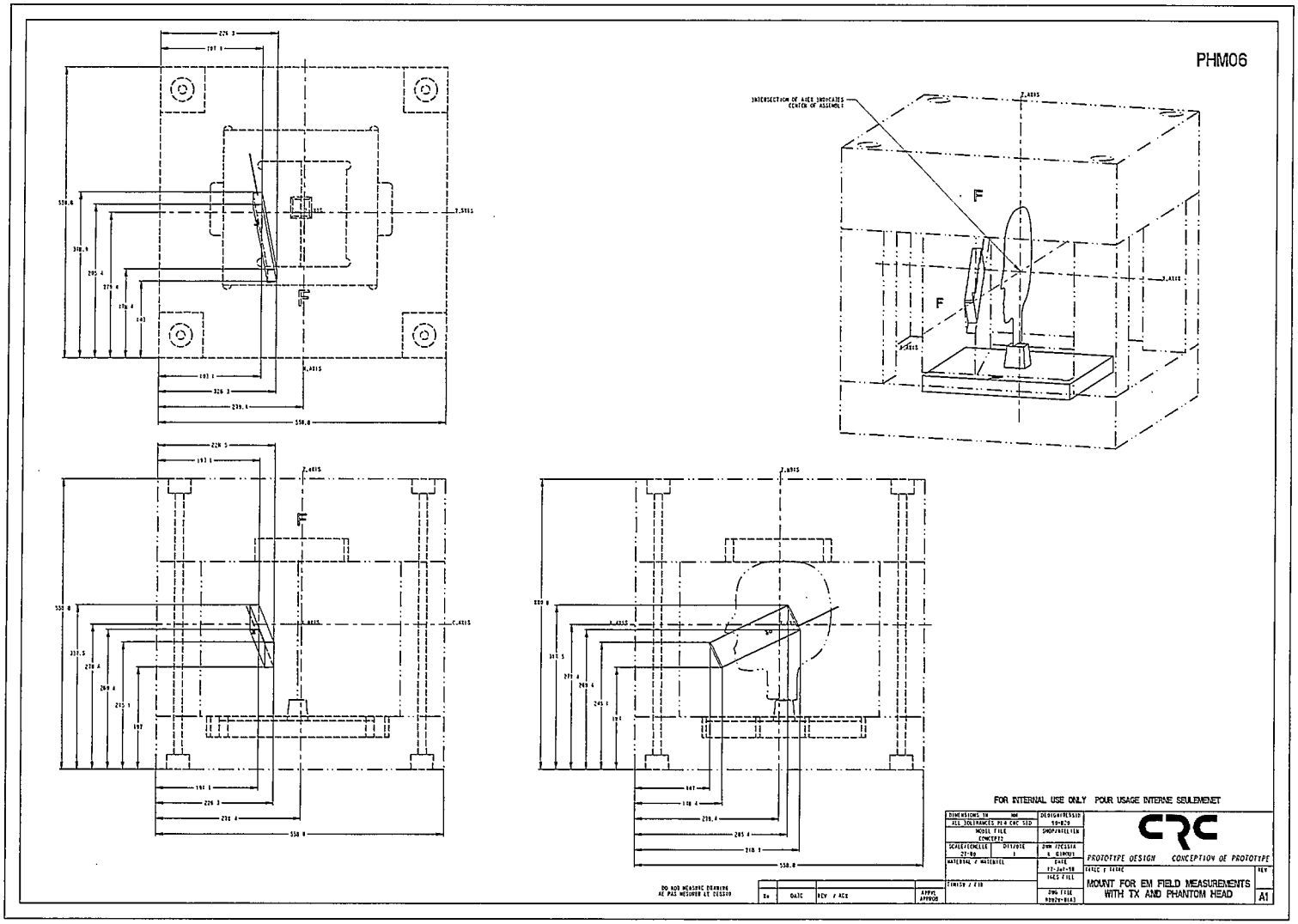
PHM06
INTERSECTION OF AXES INDICATES CENTER OF ASSEMBLY
F
F
F
FOR INTERNAL USE ONLY POUR USAGE INTERNE SEULEMENET
DIMENSIONS IN MM
ALL TOLERANCES PER CRC STD
MODEL FILE
CONCEPTS
SCALE/ECHELLE 27-90
DIT/DOE 1
MATERIAL / MATERIEL
DEVIGNIPRESSID 90-020
SHOP/ATELIER
DWN /DESSIN G. GIMOUX
DATE 17-Jul-98
IGES FILE
DWG FILE
CRC
PROTOTYPE DESIGN CONCEPTION OF PROTOTYPE
TITLE / TITRE
MOUNT FOR EM FIELD MEASUREMENTS WITH TX AND PHANTOM HEAD
REV
A1
DO NOT MEASURE DRAWING AE PAS MESURER LE DESSIN
No
DATE
REV / ACE
APPVL APPROB

PHM07

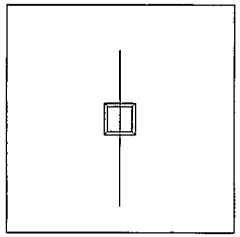

NOTE: THE CENTER OF THE PHANTOM HEAD (THE ORIGIN OF THE X,Y,Z AXES AND THE CENTER OF THE ASSEMBLY) IS DEFINED AS THE MIDPOINT THROUGH THE HEAD OF A LINE PASSING THROUGH THE AUDITORY CANALS REFERENCED TO THE BOTTOM LEFT CORNER OF THE BASEPLATE (-141.5, 154.6, 218.5)

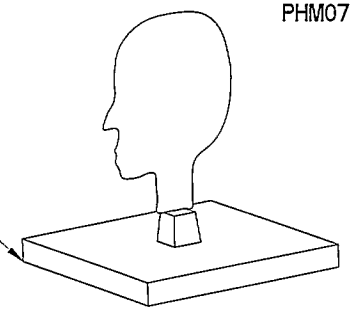

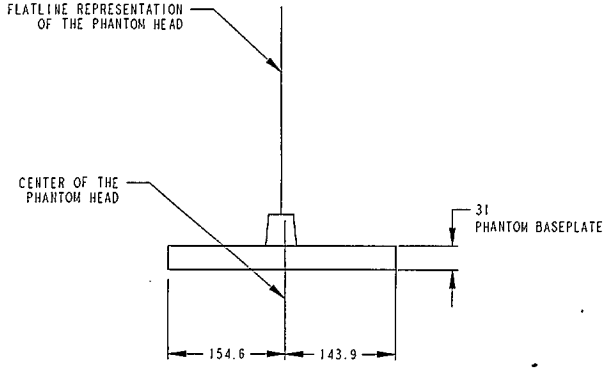

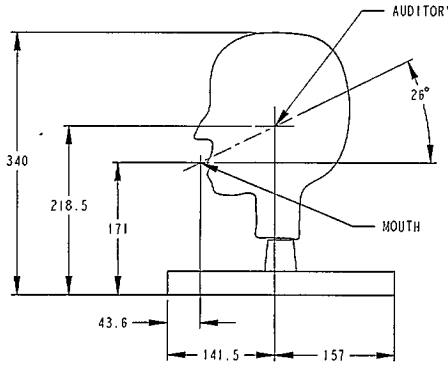

FOR INTERNAL USE ONLY POUR USAGE INTERNE SEULEMENT

DIMENSIONS IN MM			DESIGN/DESSIN
ALL TOLERANCES PER CRC STD			98-020
MODEL FILE			SHOP/ATELIER
PHANTOM_HEAD			
SCALE/ECHELLE	QTY/QTE		DWN./DESSIN.
1:5	1		
MATERIAL / MATERIEL			DATE
			15-Jul-98
			IGES FILE
FINISH / FIN.			
			DWG FILE
			98020-02A3

CRC

PROTOTYPE DESIGN CONCEPTION DE PROTOTYPE

TITLE / TITRE: PHANTOM HEAD

REV. 1

A3

DO NOT MEASURE DRAWING
NE PAS MESURER LE DESSIN

No.	DATE	REV. / REV.	APPVL. APPROB.

PHM08

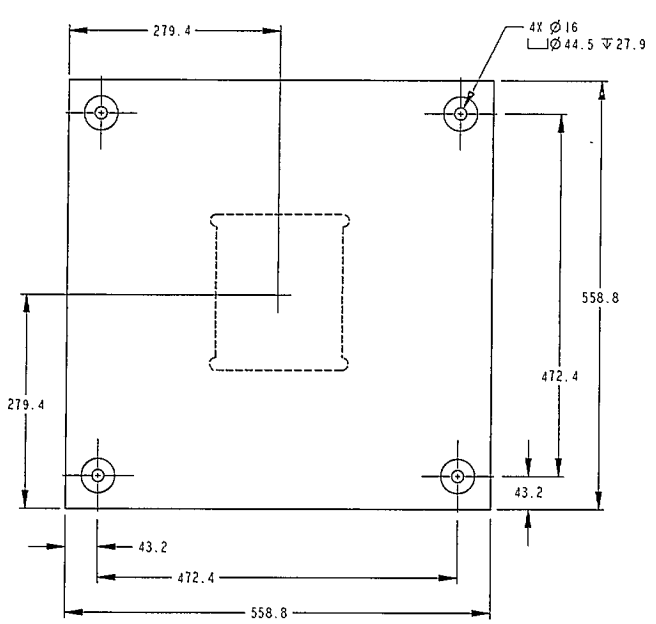

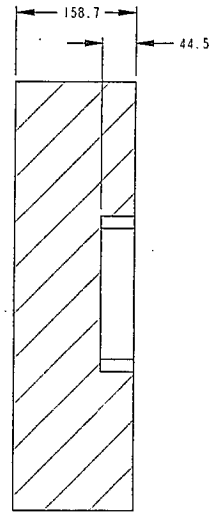

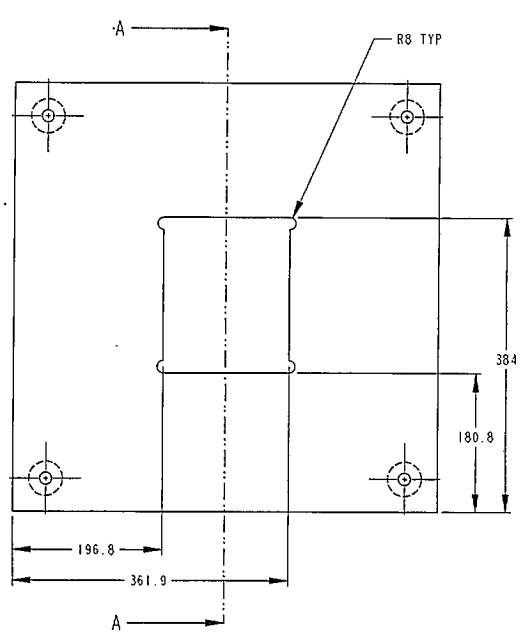

FOR INTERNAL USE ONLY POUR USAGE INTERNE SEULEMENT

DIMENSIONS IN MM		DESIGN/DESSIN	CRC
ALL TOLERANCES PER CRC STD		98-020	
MODEL FILE STYROFOAM_TOP		SHOP/ATELIER	
SCALE/ECHELLE 1:5	QTY/QTE 1	DWN./DESSIN. A. GIROUX	PROTOTYPE DESIGN CONCEPTION DE PROTOTYPE
MATERIAL / MATERIEL STYROFOAM		DATE 15-Jul-98	TITLE / TITRE: STYROFOAM TOP
		IGES FILE	REV.
FINISH / FIN. NATURAL		DWG FILE 98020-02A3	A3

DO NOT MEASURE DRAWING
NE PAS MESURER LE DESSIN

No.	DATE	REV. / REV.	APPVL. APPROB.

PHM09

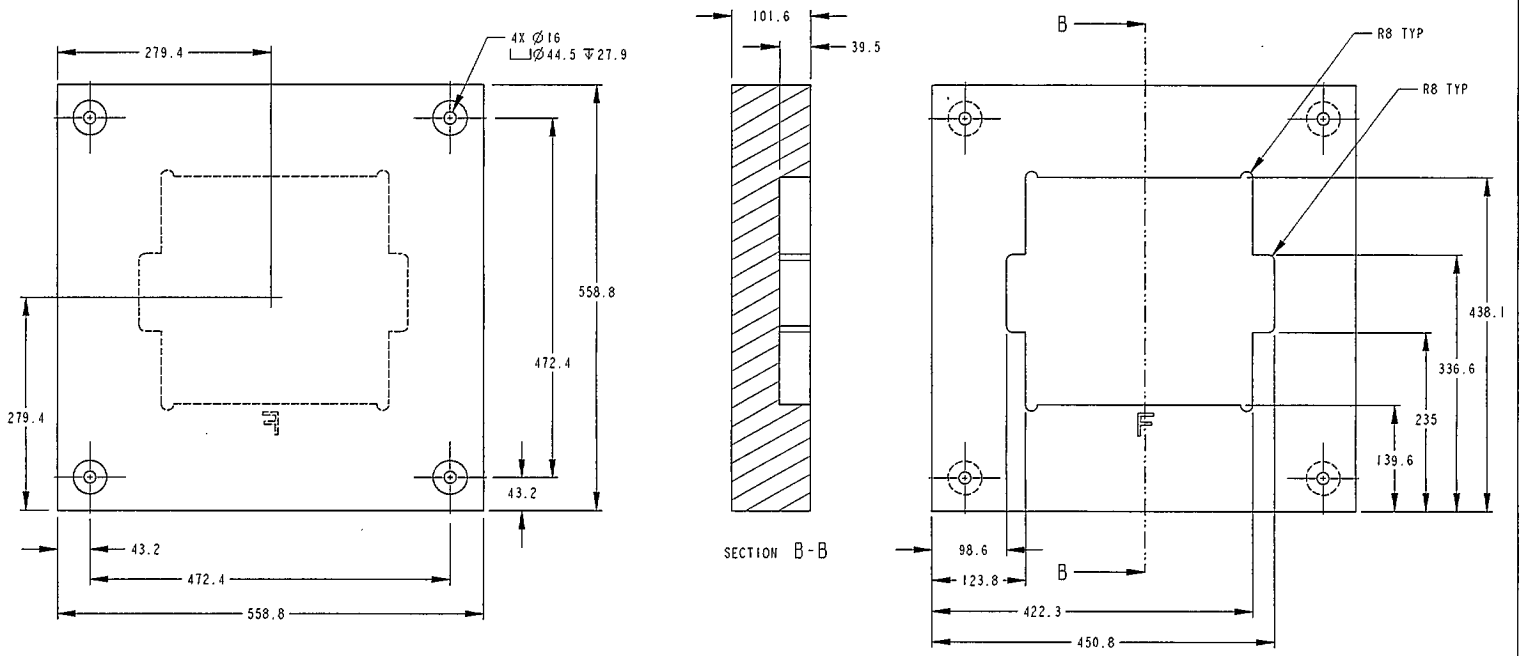

FOR INTERNAL USE ONLY POUR USAGE INTERNE SEULEMENT

DIMENSIONS IN MM		DESIGN/DESSIN
ALL TOLERANCES PER CRC STD		98-020
MODEL FILE		SHOP/ATELIER
TX		
SCALE/ECHELLE	QTY/QTE	DWN./DESSIN.
1:5	1	A. GIROUX
MATERIAL / MATERIEL		DATE
STYROFOAM		15-Jul-98
		IGES FILE
FINISH / FIN.		
NATURAL		DWG FILE
		98020-02A3

CRC

PROTOTYPE DESIGN CONCEPTION DE PROTOTYPE

TITLE / TITRE: STYROFOAM BOTTOM

REV.: A3

DO NOT MEASURE DRAWING
NE PAS MESURER LE DESSIN

No.	DATE	REV. / REV.	APPVL. APPROB.

PHM10

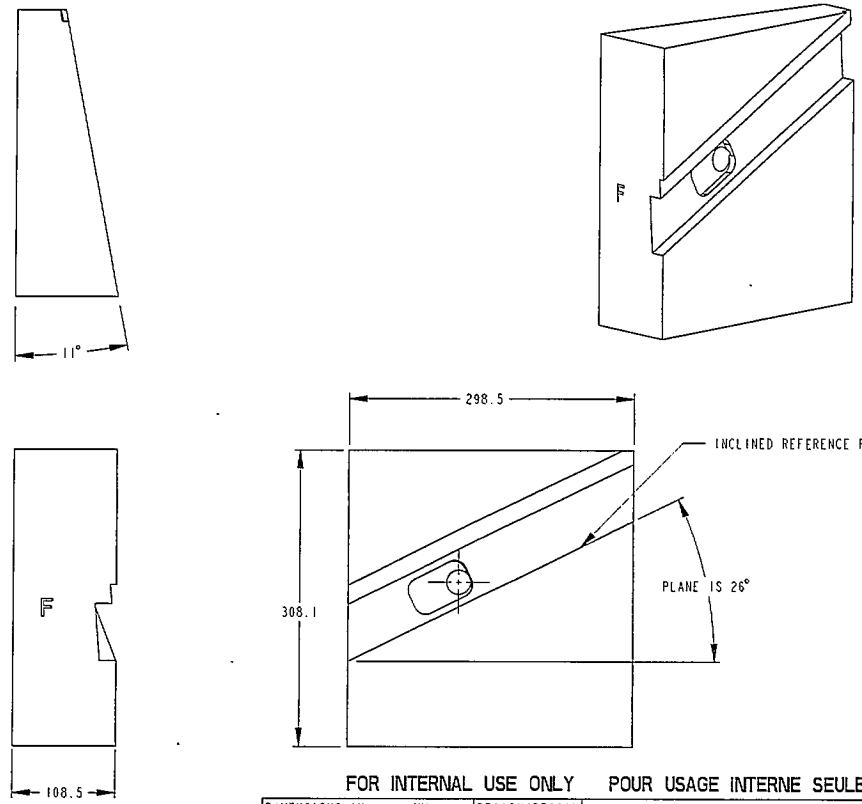

FOR INTERNAL USE ONLY POUR USAGE INTERNE SEULEMENT

DIMENSIONS IN MM		DESIGN/DESSIN	CRC
ALL TOLERANCES PER CRC STD		98-020	
MODEL FILE STYROFOAM_TX_SUPPORT		SHOP/ATELIER	PROTOTYPE DESIGN CONCEPTION DE PROTOTYPE
SCALE/ECHELLE 1:4	QTY/QTE 1	DWN /DESSIN. A. GIROUX	
MATERIAL / MATERIEL STYROFOAM		DATE 15-Jul-98	TITLE / TITRE: STYROFOAM TX SUPPORT
		IGES FILE	REV: A3
FINISH / FIN. NATURAL		DWG FILE 98020-02A3	

DO NOT MEASURE DRAWING
NE PAS MESURER LE DESSIN

No.	DATE	REV. / REV.	APPVL. APPROB.

PHM11

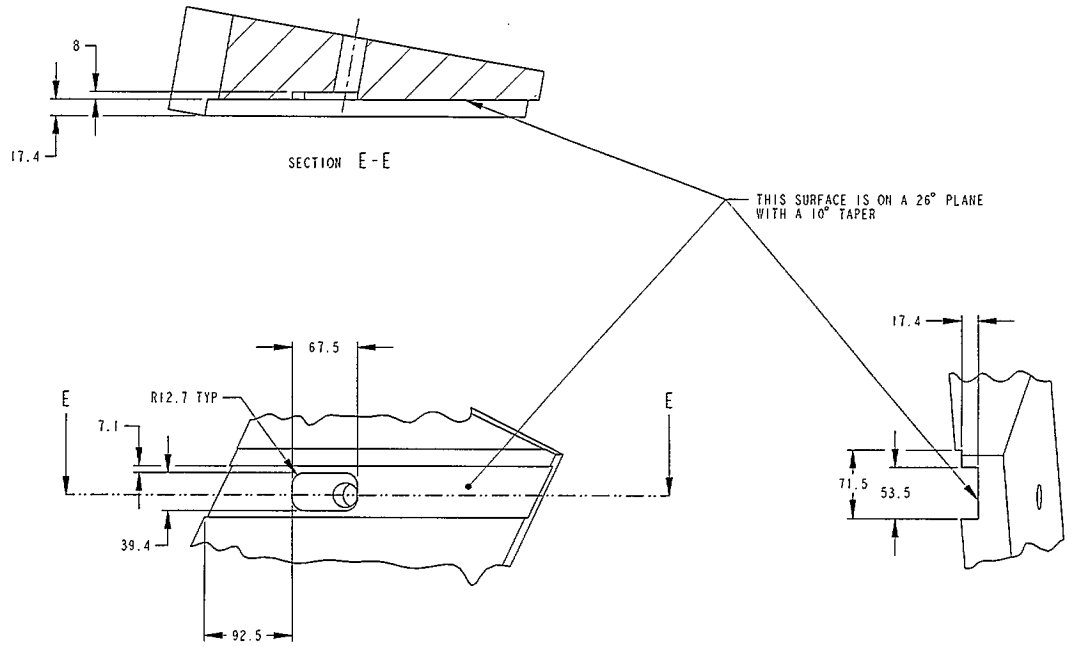

FOR INTERNAL USE ONLY POUR USAGE INTERNE SEULEMENT

DIMENSIONS IN MM ALL TOLERANCES PER CRC STD	DESIGN/DESSIN 98-020
MODEL FILE STYROFOAM_TX_SUPPORT	SHOP/ATELIER
SCALE/ECHELLE 1:4 QTY/QTE	DWN./DESSIN. A. GIROUX
MATERIAL / MATERIEL STYROFOAM	DATE 15-Jul-98
FINISH / FIN. NATURAL	IGES FILE
	DWG FILE 98020-02A3

CRC

PROTOTYPE DESIGN CONCEPTION DE PROTOTYPE

TITLE / TITRE

STYROFOAM TX SUPPORT
AUXILIARY VIEWS

REV. A3

DO NOT MEASURE DRAWING
NE PAS MESURER LE DESSIN

No.	DATE	REV. / REV.	APPVL. APPROB.

PHM12

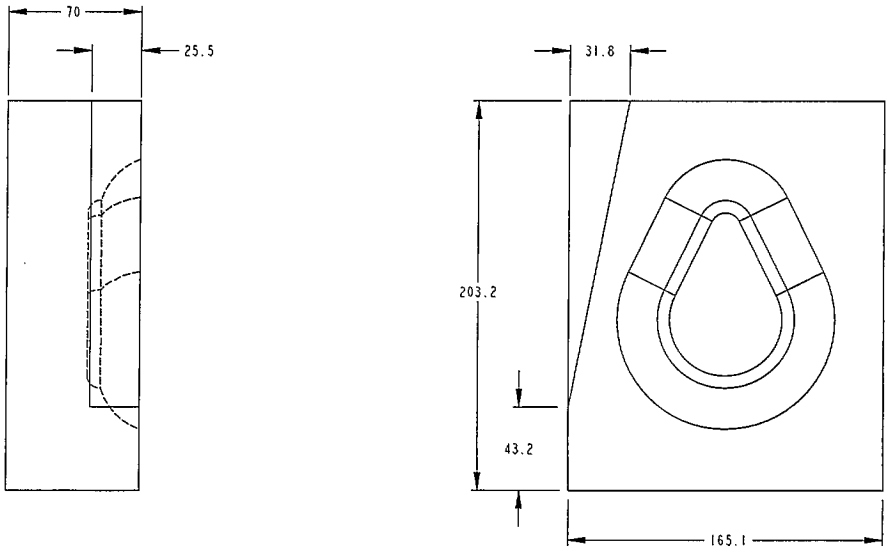

FOR INTERNAL USE ONLY POUR USAGE INTERNE SEULEMENT

DIMENSIONS IN MM		DESIGN/DESSIN	CRC
ALL TOLERANCES PER CRC STD		98-020	
MODEL FILE STYROFOAM_HEAD_SUPPORT		SHOP/ATELIER	PROTOTYPE DESIGN CONCEPTION DE PROTOTYPE
SCALE/ECHELLE 1:2	QTY/QTE 1	DWN./DESSIN. A. GIROUX	
MATERIAL / MATERIEL STYROFOAM		DATE 15-Jul-98	TITLE / TITRE: STYROFOAM HEAD SUPPORT
		IGES FILE	REV: A3
FINISH / FIN. NATURAL		DWG FILE 98020-02A3	

DO NOT MEASURE DRAWING
NE PAS MESURER LE DESSIN

No.	DATE	REV. / REV.	APPVL. APPROB.

PHM13

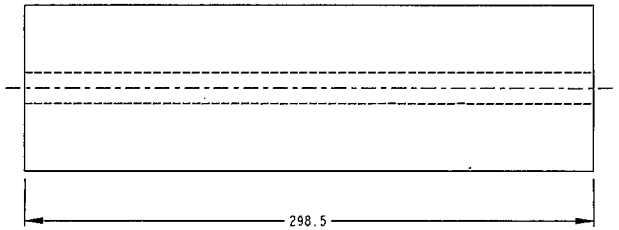

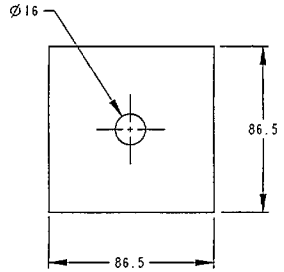

FOR INTERNAL USE ONLY POUR USAGE INTERNE SEULEMENT

DIMENSIONS IN MM	DESIGN/DESSIN
ALL TOLERANCES PER CRC STD	98-020
MODEL FILE STYROFOAM_STANDOFF	SHOP/ATELIER
SCALE/ECHELLE 1:2 / QTY/QTE 4	DWN./DESSIN. A. GIROUX
MATERIAL / MATERIEL STYROFOAM	DATE 15-Jul-98
	IGES FILE
FINISH / FIN. NATURAL	DWG FILE 98020-02A3

CRC

PROTOTYPE DESIGN CONCEPTION DE PROTOTYPE

TITLE / TITRE: STYROFOAM STANDOFF

REV.: A3

DO NOT MEASURE DRAWING
NE PAS MESURER LE DESSIN

No.	DATE	REV. / REV.	APPVL. APPROB.

PHM14

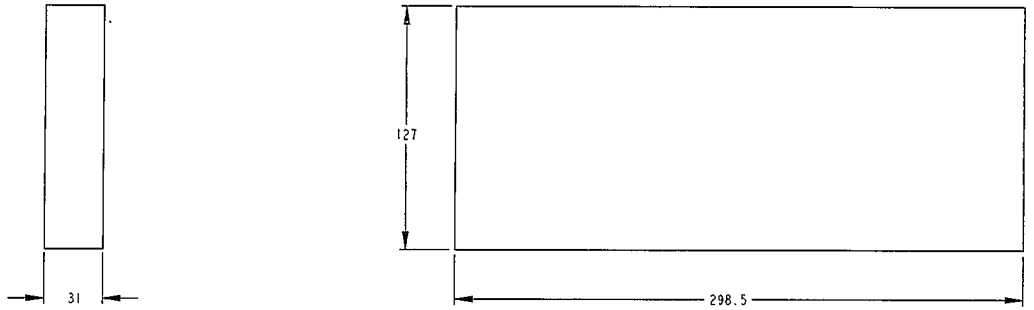

FOR INTERNAL USE ONLY POUR USAGE INTERNE SEULEMENT

DIMENSIONS IN MM		DESIGN/DESSIN	CRC
ALL TOLERANCES PER CRC STD		98-020	
MODEL FILE		SHOP/ATELIER	
STYROFOAM_TX_SUPPORT_SPACER			
SCALE/ECHELLE	QTY/QTE	DWN./DESSIN.	PROTOTYPE DESIGN CONCEPTION DE PROTOTYPE
1:2	1	A. GIROUX	
MATERIAL / MATERIEL		DATE	TITLE / TITRE REV.
STYROFOAM		15-Jul-98	
		IGES FILE	STYROFOAM TX SUPPORT SPACER
FINISH / FIN.			
NATURAL		DWG FILE	A3
		98020-02A3	

DO NOT MEASURE DRAWING
NE PAS MESURER LE DESSIN

No.	DATE	REV. / REV.	APPVL. APPROB.

PHM15

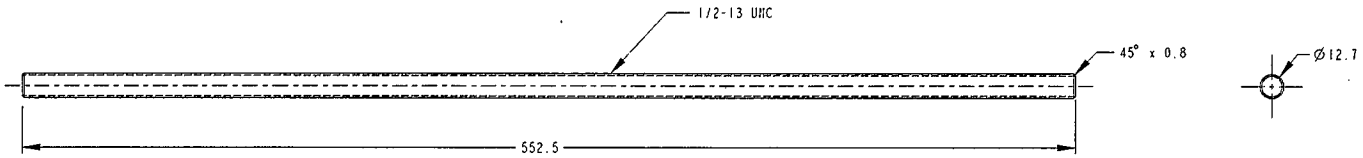

FOR INTERNAL USE ONLY POUR USAGE INTERNE SEULEMENT

DIMENSIONS IN MM		DESIGN/DESSIN	
ALL TOLERANCES PER CRC STD		98-020	
MODEL FILE		SHOP/ATELIER	
FIBREBOLT_STUD			
SCALE/ECHELLE	QTY/QTE	DWN./DESSIN.	
1:2	4	A. GIROUX	
MATERIAL / MATERIEL		DATE	
FIBERGLASS AND VINYL ESTER RESIN		15-Jul-98	
		IGES FILE	
FINISH / FIN.			
NATURAL		DWG FILE	
		98020-02A3	

CRC

PROTOTYPE DESIGN CONCEPTION DE PROTOTYPE

TITLE / TITRE

FIBERGLASS THREADED ROD

REV. A3

DO NOT MEASURE DRAWING
NE PAS MESURER LE DESSIN

No.	DATE	REV. / REV.	APPVL. APPROB.

PHM16

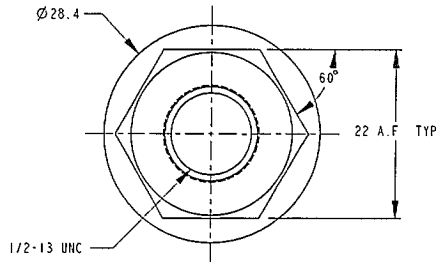

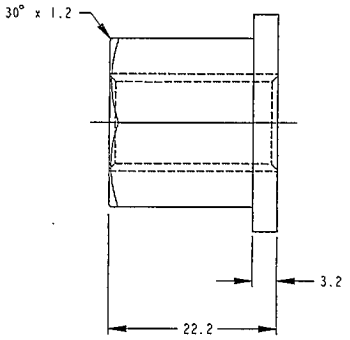

FOR INTERNAL USE ONLY POUR USAGE INTERNE SEULEMENT

DIMENSIONS IN MM		DESIGN/DESSIN	CRC
ALL TOLERANCES PER CRC STD		98-020	
MODEL FILE		SHOP/ATELIER	
FIBREBOLT_NUT			
SCALE/ECHELLE	QTY/QTE	DWN./DESSIN.	PROTOTYPE DESIGN CONCEPTION DE PROTOTYPE
2:1	8	A. GIROUX	
MATERIAL / MATERIEL		DATE	TITLE / TITRE: FIBERGLASS NUT
FIBERGLASS AND VINYL ESTER RESIN		15-Jul-98	REV.
		IGES FILE	
FINISH / FIN.		DWG FILE	A3
NATURAL		98020-02A3	

DO NOT MEASURE DRAWING
NE PAS MESURER LE DESSIN

No.	DATE	REV. / REV.	APPVL. APPROB.

PHM17

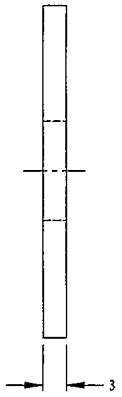

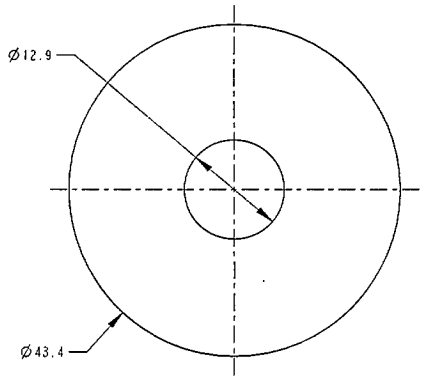

FOR INTERNAL USE ONLY POUR USAGE INTERNE SEULEMENT

DIMENSIONS IN MM		DESIGN/DESSIN	CRC
ALL TOLERANCES PER CRC STD		98-020	
MODEL FILE PLEXIGLASS_WASHER		SHOP/ATELIER	PROTOTYPE DESIGN CONCEPTION DE PROTOTYPE
SCALE/ECHELLE 2:1	QTY/QTE 8	DWN./DESSIN. A. GIROUX	
MATERIAL / MATERIEL WHITE ACRYLIC SHEET "PLEXIGLASS MC"		DATE 15-Jul-98	TITLE / TITRE: PLEXIGLASS WASHER
		IGES FILE	REV. A3
FINISH / FIN. NATURAL		DWG FILE 98020-02A3	

DO NOT MEASURE DRAWING
NE PAS MESURER LE DESSIN

No.	DATE	REV. / REV.	APPVL. APPROB.

PHM18

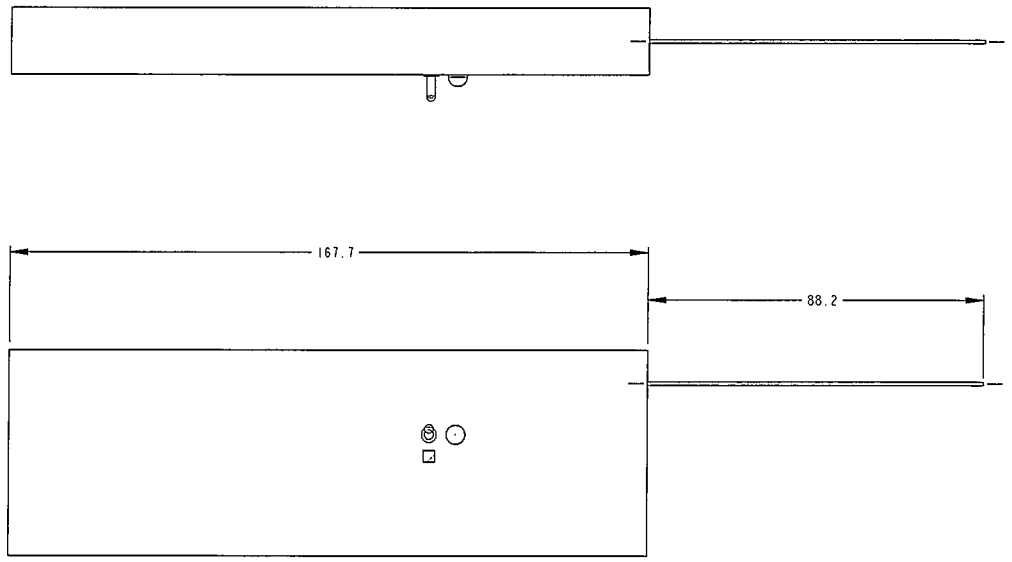

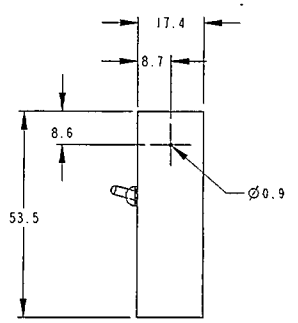

FOR INTERNAL USE ONLY POUR USAGE INTERNE SEULEMENT

DIMENSIONS IN MM		DESIGN/DESSIN	CRC
ALL TOLERANCES PER CRC STD		98-020	
MODEL FILE		SHOP/ATELIER	
TX			
SCALE/ECHELLE	QTY/QTE	DWN./DESSIN.	PROTOTYPE DESIGN CONCEPTION DE PROTOTYPE
1:1	1	A. GIROUX	
MATERIAL / MATERIEL		DATE	TITLE / TITRE: TX
6061-T6 ALUMINUM		15-Jul-98	REV.: A3
		IGES FILE	
FINISH / FIN.		DWG FILE	
NATURAL		98020-02A3	

DO NOT MEASURE DRAWING
NE PAS MESURER LE DESSIN

No.	DATE	REV. / REV.	APPVL. APPROB.

PHM19

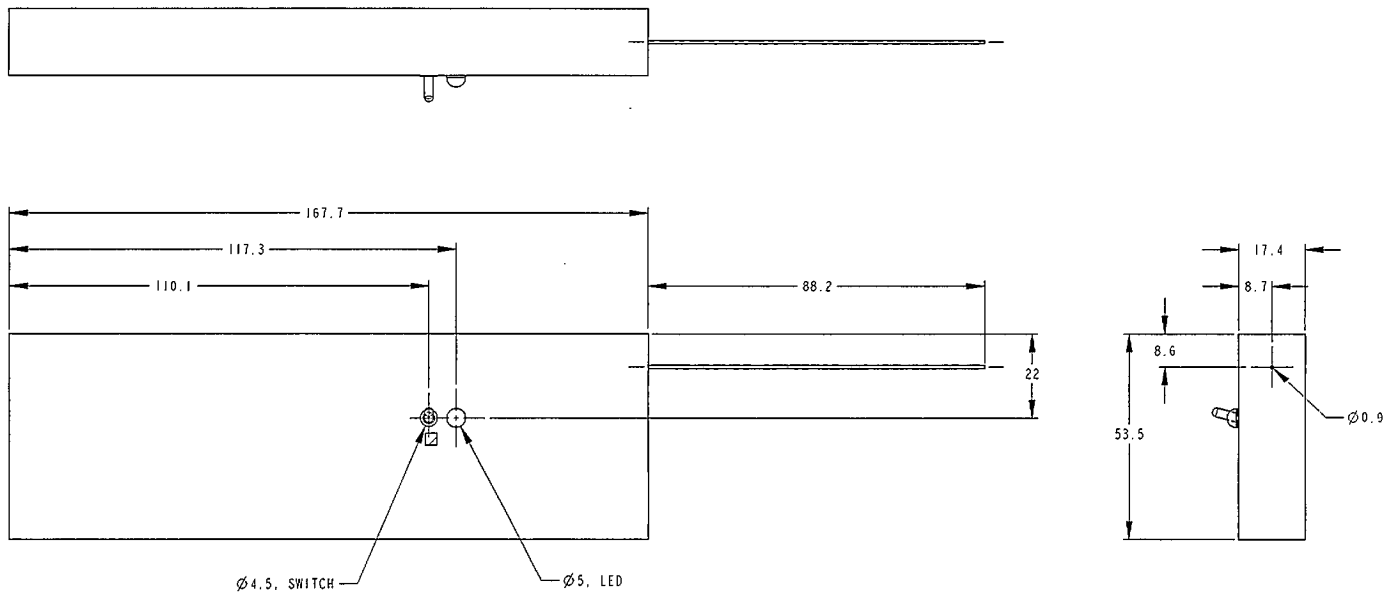

FOR INTERNAL USE ONLY POUR USAGE INTERNE SEULEMENT

DIMENSIONS IN MM ALL TOLERANCES PER CRC STD				DESIGN/DESSIN 98-020	CRC PROTOTYPE DESIGN CONCEPTION DE PROTOTYPE
MODEL FILE TX				SHOP/ATELIER	
SCALE/ECHELLE 1:1	QTY/QTE 1			DWN./DESSIN. A. GIROUX	
MATERIAL / MATERIEL 6061-T6 ALUMINUM				DATE 21-Oct-98	TITLE / TITRE TX
				IGES FILE	REV. A3
FINISH / FIN. NATURAL				DWG FILE 98020-02A3	
No.	DATE	REV. / REV.	APPVL. APPROB.		

DO NOT MEASURE DRAWING
NE PAS MESURER LE DESSIN

Appendix B

Coordinate Transformation

This appendix presents the mathematical steps for transforming between the E_ϑ and E_φ components of the spherical coordinate system used in a FDTD simulation, and the E_θ and E_ϕ components of the spherical coordinate system used in a measurement during the second test (see Figure 2.11). Figure B.1 presents the pictoral description of the situation.

The general coordinate transformation of a point P from a XYZ coordinate system to a UVW coordinate system which is static but otherwise arbitrarily rotated and arbitrarily translated with respect to the XYZ coordinate system is known as the static Galilean transformation. The transformation of a point P from the XYZ coordinate system to the UVW coordinate system is given as:

$$\begin{pmatrix} \hat{u}\cdot\hat{x} & \hat{u}\cdot\hat{y} & \hat{u}\cdot\hat{z} \\ \hat{v}\cdot\hat{x} & \hat{v}\cdot\hat{y} & \hat{v}\cdot\hat{z} \\ \hat{w}\cdot\hat{x} & \hat{w}\cdot\hat{y} & \hat{w}\cdot\hat{z} \end{pmatrix} \begin{pmatrix} P_x - Q_x \\ P_y - Q_y \\ P_z - Q_z \end{pmatrix} = \begin{pmatrix} P_u \\ P_v \\ P_w \end{pmatrix}$$

where here we had the following:

$$\begin{cases} \vec{u} = \vec{P}_5 - \vec{P}_6 = 23.5\hat{x} + 0\hat{y} + 48.1\hat{z} \\ \vec{v} = \vec{P}_2 - \vec{P}_6 = -2.7\hat{x} + 17.2\hat{y} + 1.3\hat{z} \\ \vec{w} = \vec{P}_8 - \vec{P}_6 = -148.4\hat{x} + -29.1\hat{y} + 72.4\hat{z} \end{cases}$$

with $\vec{P}_n$ referring to the coordinates given in Figure 2.11 for point n of the transmitter. The units are mm. The transformation of a vector proceeds simply from the

transformation of the two end points of the vector. In the particular case that the vector is a purely radial vector in the XYZ coordinate system, one end of the vector occupies the point at the origin O (see Figure B.1). The transformation of the tip end point P gives:

$$\begin{pmatrix} \hat{u}\cdot\hat{x} & \hat{u}\cdot\hat{y} & \hat{u}\cdot\hat{z} \\ \hat{v}\cdot\hat{x} & \hat{v}\cdot\hat{y} & \hat{v}\cdot\hat{z} \\ \hat{w}\cdot\hat{x} & \hat{w}\cdot\hat{y} & \hat{w}\cdot\hat{z} \end{pmatrix} \begin{pmatrix} P_x - Q_x \\ P_y - Q_y \\ P_z - Q_z \end{pmatrix} = \begin{pmatrix} P_u \\ P_v \\ P_w \end{pmatrix}$$

The transformation of the origin end point O gives:

$$\begin{pmatrix} \hat{u}\cdot\hat{x} & \hat{u}\cdot\hat{y} & \hat{u}\cdot\hat{z} \\ \hat{v}\cdot\hat{x} & \hat{v}\cdot\hat{y} & \hat{v}\cdot\hat{z} \\ \hat{w}\cdot\hat{x} & \hat{w}\cdot\hat{y} & \hat{w}\cdot\hat{z} \end{pmatrix} \begin{pmatrix} O_x - Q_x = -Q_x \\ O_y - Q_y = -Q_y \\ O_z - Q_z = -Q_z \end{pmatrix} = \begin{pmatrix} O_u \\ O_v \\ O_w \end{pmatrix}$$

since $O_x = O_y = O_z = 0$. Since the vector $\vec{P}$ is identified as the difference between the point P and the point O, the expression for the vector $\vec{P}$ in terms of the UVW coordinates is obtained simply by expressing each point in terms of the UVW coordinates before taking the difference. There results:

$$\begin{pmatrix} \hat{u}\cdot\hat{x} & \hat{u}\cdot\hat{y} & \hat{u}\cdot\hat{z} \\ \hat{v}\cdot\hat{x} & \hat{v}\cdot\hat{y} & \hat{v}\cdot\hat{z} \\ \hat{w}\cdot\hat{x} & \hat{w}\cdot\hat{y} & \hat{w}\cdot\hat{z} \end{pmatrix} \begin{pmatrix} (P_x - Q_x) - (-Q_x) = P_x \\ (P_y - Q_y) - (-Q_y) = P_y \\ (P_z - Q_z) - (-Q_z) = P_z \end{pmatrix} = \begin{pmatrix} P_u - O_u \\ P_v - O_v \\ P_w - O_w \end{pmatrix}$$

Since the left hand side of the last expression corresponds to projecting the vector $\vec{P}$ expressed in the XYZ coordinates onto each axis of the UVW coordinate system, the transformation of a radial vector in one coordinate system to another radial vector in another coordinate system consists simply of projecting the vector expressed in one coordinate system onto each axis of the other coordinate system, as expected.

Similarly, the transformation of the point P from the UVW coordinate system to the XYZ coordinate system is given as:

$$\begin{pmatrix} \hat{x}\cdot\hat{u} & \hat{x}\cdot\hat{v} & \hat{x}\cdot\hat{w} \\ \hat{y}\cdot\hat{u} & \hat{y}\cdot\hat{v} & \hat{y}\cdot\hat{w} \\ \hat{z}\cdot\hat{u} & \hat{z}\cdot\hat{v} & \hat{z}\cdot\hat{w} \end{pmatrix} \begin{pmatrix} P_u - O_u \\ P_v - O_v \\ P_w - O_w \end{pmatrix} = \begin{pmatrix} P_x \\ P_y \\ P_z \end{pmatrix}$$

Thus, as part of the two above transformations, we must identify $\vec{Q}$ in the XYZ coordinate system and $\vec{O}$ in the UVW coordinate system. With respect to the former, we observe that the FDTD simulation performed by the XFDTD403 software uses as part of its near-to-far zone transformation the centre of the computational space as the origin of a spherical coordinate system which corresponding Cartesian coordinate system is the UVW coordinate system in Figure B.1. Since the transmitter was centred in the computational space of the FDTD simulation, the centre of the transmitter coincided with the origin of the UVW coordinate system, $\vec{Q}$. From the knowledge of the coordinates for the points 1,2,5 and 6 given in Figure 2.11, the coordinates for the centre point of the bottom surface of the transmitter with respect to the forward bottom left corner of the styrofoam jig were computed as the intersection of the diagonal lines between these four corners. Similarly, the coordinates for the centre point of the top surface of the transmitter were computed from the knowledge of the coordinates for the points 3,4,7 and 8 given in Figure 2.11. The straight line joining the centre of these two end surfaces formed the centre line for the transmitter. From the knowledge of the overall length of the transmitter (including the monopole antenna) the centre of the transmitter was computed as the point lying at half the overall length (starting from the bottom surface of the transmitter) on the centre line. From the knowledge of the coordinates of the centre of the styrofoam jig with respect to the forward bottom left corner of the styrofoam jig, the coordinates of the centre point of the transmitter were computed as $\vec{Q} = (+8.81\hat{x} - 83.94\hat{y} - 3.75\hat{z})$ in terms of the XYZ coordinates. The units are mm.

To determine $\vec{O}$ in the UVW coordinate system, we applied the coordinate transformation from the XYZ to the UVW coordinates with $P = 0$. We thus obtained $\vec{O} = (-0.4980\hat{u} + 84.3360\hat{v} - 5.1517\hat{w})$. The units are again mm.

In order to compare the measured and the predicted data for the second test, the far field must be computed by the XFDTD403 software at the angles ϑ and φ corresponding to the angles θ and ϕ of the desired direction of observation. Then, the far field components computed by XFDTD403 in the spherical coordinate system of the transmitter must be converted to the corresponding far field components that would be measured in the spherical coordinate system of the chamber where the receive horn would be placed at location P and oriented with its aperture facing the

origin O. The step by step procedure is as follows.

- For a given observation direction expressed in terms of θ and ϕ, compute P_x, P_y and P_z from the knowledge of the transformation from spherical to Cartesian coordinates. For the Head-up-Nose-forward orientation, $\theta = 90^o$ while ϕ varies from 0° to 360°. For the Left-ear-up-Nose-forward orientation, $\phi = 0^o$ while θ varies from 0° to 360° with the understanding that for $\theta > 180^o$, the corresponding cut is that for $\phi = 180^o$ instead of $\phi = 0^o$. For the Left-ear-forward-Nose-down orientation, $\phi = 90^o$ while θ varies from 0° to 360° with the understanding that for $\theta > 180^o$, the corresponding cut is that for $\phi = 270^o$ instead of $\phi = 90^o$. Since $\vec{P}$ is purely radial, there obtains:

$$
\begin{aligned}
P_x &= P_{XYZ}\sin(\theta)\cos(\phi) \\
P_y &= P_{XYZ}\sin(\theta)\sin(\phi) \\
P_z &= P_{XYZ}\cos(\theta) \\
P_{XYZ} &= \sqrt{P_x^2 + P_y^2 + P_z^2}
\end{aligned}
$$

  The distance P_{XYZ} was taken herein as 3.350 m as if the phase centre of the receive horn laid directly in the aperture of the receive horn. This assumption was made because the ridges of the receive horn vary exponentially-like, causing its phase wavefront to be much more curved that that for a corresponding flat wall horn with the same dimensions, as if the phase wavefront originated from a source point located in the aperture of the horn rather than at the apex of the horn.

- Compute P_u, P_v and P_w from the knowledge of the transformation from the XYZ to the UVW coordinates.

- Compute the corresponding spherical coordinates in the UVW coordinate system from the knowledge of the transformation from Cartesian to spherical coordinates. There obtains:

$$
\begin{aligned}
\vartheta &= \text{Arccos}\left(\frac{P_w}{P_{UVW}}\right) \\
\varphi &= \text{Arctan}\left(\frac{P_v}{P_u}\right) \\
P_{UVW} &= \sqrt{P_u^2 + P_v^2 + P_w^2}
\end{aligned}
$$

- From the knowledge of the angles ϑ and φ, compute the field components E_ϑ and E_φ by the XFDTD403 software. Note that the field parameters computed by XFDTD403 are phasors, i.e. complex harmonic parameters. Note also that the magnitude of these phasors is given by XFDTD403 in dBi.

- Convert the magnitude values of the field phasors obtained by XFDTD403 from the decibel scale to the linear scale.

- Compute the corresponding Cartesian components E_u, E_v and E_w from the knowledge of the transformation from spherical to Cartesian coordinates assuming that the radial component of the far zone field is zero in the UVW coordinate system. There obtains:

$$\begin{aligned} E_u &= E_\vartheta \cos(\vartheta)\cos(\varphi) - E_\varphi \sin(\varphi) \\ E_v &= E_\vartheta \cos(\vartheta)\sin(\varphi) + E_\varphi \cos(\varphi) \\ E_w &= -E_\vartheta \sin(\vartheta) \end{aligned}$$

  Note that these expressions must be computed in complex arithmetic because the field variables are phasors.

- Compute in complex arithmetic the corresponding E_x, E_y and E_z from the knowledge of the transformation from the UVW to the XYZ coordinates, which operation corresponds also to projecting the field vector expressed in terms of the UVW coordinates onto each axis of the XYZ coordinate system. There obtains:

$$\begin{pmatrix} \hat{x}\cdot\hat{u} & \hat{x}\cdot\hat{v} & \hat{x}\cdot\hat{w} \\ \hat{y}\cdot\hat{u} & \hat{y}\cdot\hat{v} & \hat{y}\cdot\hat{w} \\ \hat{z}\cdot\hat{u} & \hat{z}\cdot\hat{v} & \hat{z}\cdot\hat{w} \end{pmatrix} \begin{pmatrix} E_u \\ E_v \\ E_w \end{pmatrix} = \begin{pmatrix} E_x \\ E_y \\ E_z \end{pmatrix}$$

- Compute in complex arithmetic the corresponding spherical coordinates components E_θ and E_ϕ from the knowledge of the transformation from Cartesian to spherical coordinates. There obtains:

$$\begin{aligned} E_\theta &= E_x \cos(\theta)\cos(\phi) + E_y \cos(\theta)\sin(\phi) - E_z \sin(\theta) \\ E_\phi &= -E_x \sin(\phi) + E_y \cos(\phi) \\ E_r &= E_x \sin(\theta)\cos(\phi) + E_y \sin(\theta)\sin(\phi) + E_z \cos(\theta) \end{aligned}$$

It should be noted that although the radial component of the far zone field is zero in the UVW coordinate system, the radial component of the far zone field is not necessarily zero in the XYZ coordinate system.

- Obtain the corresponding horizontal and vertical polarizations as $\vec{E}_{HOR} = \vec{E}_{\phi}$ and $\vec{E}_{VER} = -\vec{E}_{\theta}$ for the Head-up-Nose-forward orientation, and $\vec{E}_{HOR} = \vec{E}_{\theta}$ and $\vec{E}_{VER} = \vec{E}_{\phi}$ for the Left-ear-up-Nose-forward and the Left-ear-forward-Nose-down orientations, respectively. Note that since the phase of the measured data was not considered herein, a sign reversal is irrelevant.

- Convert the magnitude values of the field phasors E_{HOR} and E_{VER} from the linear scale to the decibel scale.

The above scheme needed to be repeated for every observation direction corresponding to the measurement angle varying from -180° to $+180^{o}$. Thus, a FORTRAN77 program was written to compute the ϑ and φ values from the knowledge of the θ and ϕ values corresponding to the three principal planes of the phantom head, and to compute E_{HOR} and E_{VER} from the knowldege of E_{ϑ} and E_{φ} obtained from the XFDTD403 software. The source code for the program appears in Appendix C.

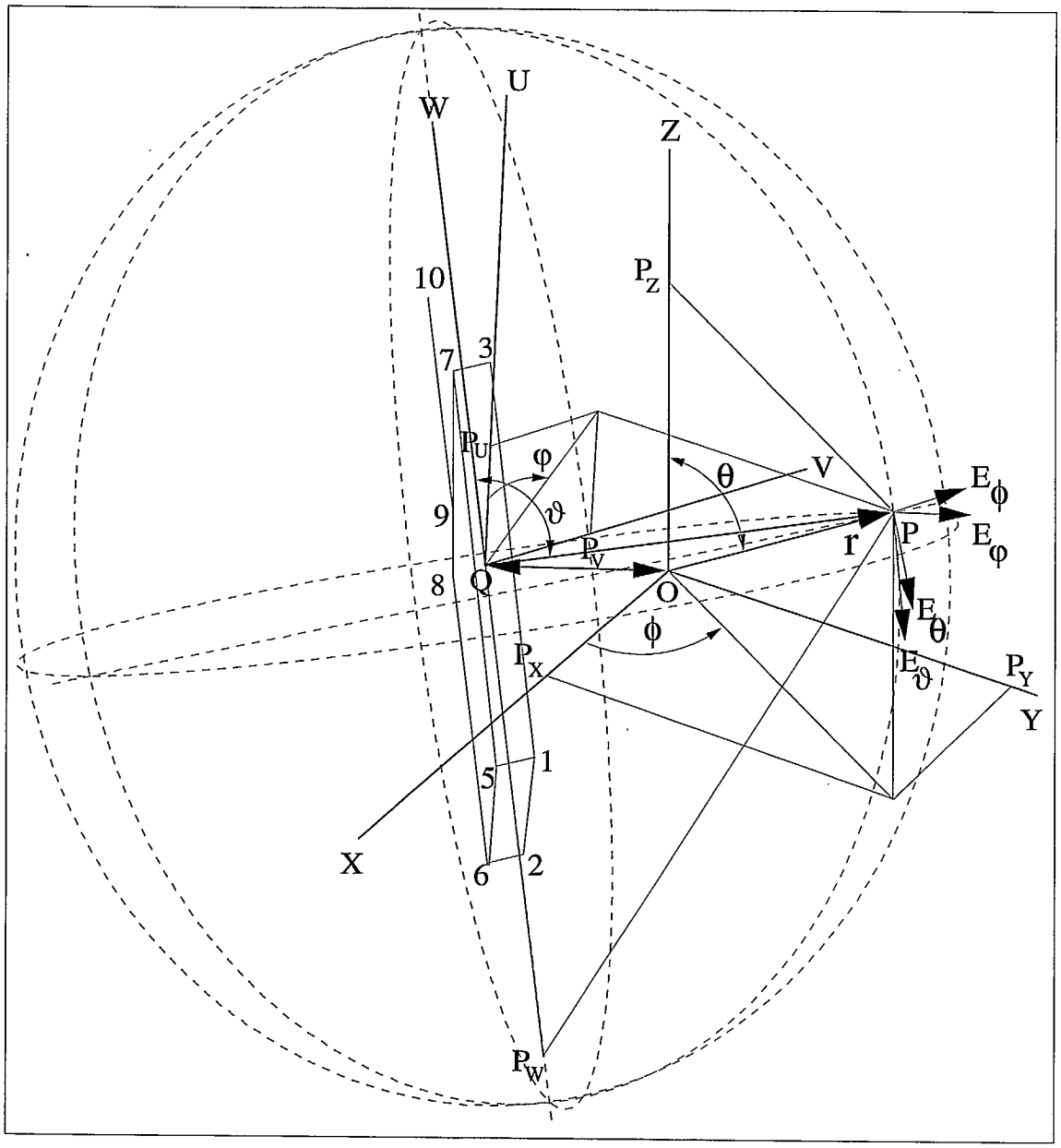

Figure B.1: Coordinate transformation between the spherical coordinates for the phantom head (XYZ) as per Figure 2.11 and those for the transmitter (UVW) in the second test.

Appendix C

FORTRAN source code

This appendix presents the source code for six programs written in FORTRAN77.

The first program was used to perform the comparison between the predicted and the measured data for the first test. The predicted values for the first test were obtained from a FDTD simulation (see section 5.1.2). The measured data $(M_{dB}^{H,V})_i$ were compared with the predicted data $(P_{dB}^{H,V})_i$, where the subindex i indentifies every data point of the sequence of data points that span the measurement range of -180° to $+180^o$, and the superindex H or V identifies the polarization type. The comparison was based on applying a scaling factor to the predicted data in order to account for the difference between the radiated power level during the simulation and the radiated power level during the measurement. Each scaling factor was itself a linear average of many scaling factors, i.e. $C_{dB}^{H,V} = \frac{1}{N}\sum_{i=1}^{N}(c_{dB}^{H,V})_i$, one factor for every data point of the sequence of $N = 360$ data points. Each factor was obtained as the absolute difference value on a dB scale between the measured and the predicted results, i.e. $(c_{dB}^{H,V})_i = |(M_{dB}^{H,V})_i - (P_{dB}^{H,V})_i|$. A variable offset angle was also added to the azimuth angle of the predicted data. The value of this offset was so selected as to minimize $\sum_i^N (c_{dB}^{H,V})_i$.

The second program was used to interpolate the data for increasing the resolution of the minimization process as part of the comparison process. In order to allow to search for the minimum value with a resolution finer than the 1° resolution used to acquire the measured data and to compute the predicted data, each sequence of data

was parabolically interpolated so as to produce a resolution of 0.2^o. However, for the few angular values in the immediate vicinity of the very deep nulls present at 0° and $\pm 180^o$ of the predicted data for the horizontal polarization of the vertical and the edge orientations, the parabolic interpolation failed to produce adequate results due to the extremely large gradient values existing at these points of the curves. For these few cases, the far field was computed (rather than interpolated) every 0.2^o over a few degrees about the troublesome angular values.

The third program pertains to the coordinate transformation presented in Appendix C.3.

The fourth program pertains to the mapping from the measurement angle to the appropriate spherical coordinate angle as per Tables 2.1 and 2.2.

The fifth program pertains to the power correction for obtaining absolute power levels from the relative power levels acquired by the network analyzer.

The sixth program computes the distance at which the total electric field is 1 V/m and 3 V/m in order to plot the corresponding contours.

NOTE: in spite of the visual appearance, all continuation lines starting with the symbol "&" should begin in the sixth column and all comments starting with the "C" letter should begin in the first column. Furthemore, the Latex word processor used to produce this document did not preserve consistently the "tab" indentation of the lines that was originally present in the FORTRAN source code.

C.1 Comparison program

```
C ***********************************************************************
C Last revised: 11 December 1998
C This program parses through files of experimental and predicted results
C to compute the error between these results and write output files for
C MATLAB to display the result of the comparison graphically.
C This program searches for the best value of ANGLE_OFFSET that provides
C the best match between the shapes of the predicted and measured plots.
C The coordinate system is that where the monopole aligns with the
C +z axis and the top of the case sticks out along the +x axis, or the
C +z axis is through the top of the phantom head and the +y axis is
C through the left ear canal of the phantom head.
C ***********************************************************************
C This revised version expects the predicted data to be in dB.
C The maximum number of data points per curve is 3601.
C NS is the integer number of points per degree.
C The program need not have the input data ordered in angular value.
C All mathematical operations are performed with the data on the linear
C scale.
C ***********************************************************************

PROGRAM COMPARE

PARAMETER(IMAX=3601)
C Don't forget to change also PARAMETER in the subroutine SCALE.

CHARACTER*50 INFILE_H,INFILE_V
CHARACTER*50 INFILE_P,INFILE_M
CHARACTER*50 OUFILEP_H,OUFILEP_V
CHARACTER*50 OUFILEM_H,OUFILEM_V
CHARACTER*50 OUFILEANG
```

```
INTEGER NS,ISTART,ISTOP,MFLAG,POINTER(IMAX)
INTEGER FLAG,FLAG1,FLAG2,FLAG3,FLAGPOL,FLAGREPEAT
INTEGER ORIENTATION,NNN

REAL*8 A(IMAX),B(IMAX),ALR,BLR,AN
REAL*8 A1(IMAX),B1(IMAX)
REAL*8 FACAVGA,FACAVGB,DELFACA,DELFACB
REAL*8 POWCORA1,POWCORB1,POWCORA,POWCORB
REAL*8 ERROR,ERRORMIN

REAL*8 ANG(IMAX),ANGLEORIG(IMAX)
REAL*8 ANGLE_OFFSET,ANGLE_OFFSET_BEST

  WRITE(6,*) 'INTEGER MULTIPLICATION FACTOR NS (<11) = ?'
READ(5,*) NS
  WRITE(6,*) 'ORIENTATION (>0=2; <0=5/6; 1=Vert, 2=Flat, 3=Edge,
     &4=HuNf, 5=LuNf, 6=LfNd) = ?'
READ(5,*) ORIENTATION
IF (ORIENTATION .LT. 0) THEN
  WRITE(6,*) 'INFILE_P (prediction) = ?'
READ(5,*) INFILE_P
ELSE
  WRITE(6,*) 'INFILE_H (prediction) = ?'
READ(5,*) INFILE_H
  WRITE(6,*) 'INFILE_V (prediction) = ?'
READ(5,*) INFILE_V
END IF
  WRITE(6,*) 'INFILE_M (measurement) = ?'
READ(5,*) INFILE_M
  WRITE(6,*) 'OUFILEP_H (prediction) = ?'
READ(5,*) OUFILEP_H
  WRITE(6,*) 'OUFILEP_V (prediction) = ?'
```

```
READ(5,*) OUFILEP_V
  WRITE(6,*) 'OUFILEM_H (measurement) = ?'
READ(5,*) OUFILEM_H
  WRITE(6,*) 'OUFILEM_V (measurement) = ?'
READ(5,*) OUFILEM_V
  WRITE(6,*) 'OUFILEANG = ?'
READ(5,*) OUFILEANG
  WRITE(6,*) 'ANGLE_OFFSET_BEST to be obtained from the horizontal
     &polarization (1=YES, 2=NO) ?'
READ(5,*) FLAGPOL
  WRITE(6,*) 'Are stop angles included in the experimental data
     &file (1=YES, 2=NO) ?'
        READ(5,*) FLAG2

OPEN (UNIT=10,FILE=INFILE_M,STATUS='OLD')
IF (ORIENTATION .LT. 0) THEN
OPEN (UNIT=11,FILE=INFILE_P,STATUS='OLD')
ELSE
OPEN (UNIT=11,FILE=INFILE_H,STATUS='OLD')
OPEN (UNIT=12,FILE=INFILE_V,STATUS='OLD')
END IF


DO 100 I=1,360*NS+1
IF (ORIENTATION .LT. 0) THEN
C Angle mapping is just identity.
C Measurement: -180 to +180 <------ measurement: -180 to +180.
C Single input file with measured data file format (5 or 6 columns).
C The results are assumed to be in decibels.
IF (FLAG2 .EQ. 1) THEN
C       The measurement data files include the stop angles
C in the second column.
READ (11,*) ANG(I),TEMP,A(I),TEMP,B(I),TEMP
```

```
ELSE
READ (11,*) ANG(I),     A(I),TEMP,B(I),TEMP
END IF
ELSE
C Double input files with simulated data file format (2 columns).
C The results are assumed to be in decibels.
READ (11,*) AN,ALR
READ (12,*) AN,BLR
GO TO (101,102,102,104,105,105) ORIENTATION
C IP stands for Iprediction and IM stands for Imeasurement.
C AN pertains to the angle for the predicted curve.
C ANG pertains to the angle for the measured curve.
101 CONTINUE
C VERTICAL orientation or theta=90 degrees cut:
C Measurement: - 90 to +180 <------ phi:   0 to 270 of simulation curve
IF (AN .LE. 270.0D0) THEN
C If IP=1,       AN=0.0,  ANG= -90.0,IM= 90*NS+1=90*NS+(       1)
C                                                        -->IM=90*NS+IP
C If IP=270*NS+1,AN=270.0,ANG=+180.0,IM=360*NS+1=90*NS+(270*NS+1)
C                                                        -->IM=90*NS+IP
ANG(90*NS+I)=AN-90.0D0
  A(90*NS+I)=ALR
  B(90*NS+I)=BLR
END IF
IF (AN .GE. 270.0D0) THEN
C Measurement: -180 to - 90 <------ phi: 270 to 360 of simulation curve
C If IP=270*NS+1,AN=270.0,ANG=-180.0,IM=      1=(270*NS+1)-270*NS
C                                                    -->IM=IP-270*NS
C If IP=360*NS+1,AN=360.0,ANG= -90.0,IM=90*NS+1=(360*NS+1)-270*NS
C                                                  -->IM=IP-270*NS
ANG(I-270*NS)=AN-450.0D0
  A(I-270*NS)=ALR
  B(I-270*NS)=BLR
```

```
END IF
GO TO 109
102 CONTINUE
C FLAT orientation (phi=0) or Edge orientation (phi=90):
IF (AN .LE. 180.0D0) THEN
C Measurement: 0 to -180 <------ theta:    0 to 180 of simulation curve
C If IP=1,       AN=  0.0,ANG=   0.0,IM=180*NS+1=180*NS+2-(       1)
C                                                    -->IM=180*NS+2-IP
C If IP=180*NS+1,AN=180.0,ANG=-180.0,IM=       1=180*NS+2-(180*NS+1)
C                                                    -->IM=180*NS+2-IP
ANG(180*NS+2-I)=-AN
  A(180*NS+2-I)=ALR
  B(180*NS+2-I)=BLR
END IF
IF (AN .GE. 180.0D0) THEN
C Measurement: +180 to 0 <------ theta:  180 to 360 of simulation curve
C If IP=180*NS+1,AN=180.0,ANG=+180.0,IM=360*NS+1=540*NS+2-(180*NS+1)
C                                                    -->IM=540*NS+2-IP
C If IP=360*NS+1,AN=360.0,ANG=   0.0,IM=180*NS+1=540*NS+2-(360*NS+1)
C                                                    -->IM=540*NS+2-IP
ANG(540*NS+2-I)=360.0D0-AN
  A(540*NS+2-I)=ALR
  B(540*NS+2-I)=BLR
END IF
GO TO 109
104 CONTINUE
C Head-up-Nose-forward orientation;
IF (AN .LE. 180.0D0) THEN
C Measurement: 0 to +180 <------ theta:    0 to 180 of simulation curve
C If IP=1,       AN=  0.0,ANG=  0.0, IM=180*NS+1=180*NS+(       1)
C                                                      -->IM=180*NS+IP
C If IP=180*NS+1,AN=180.0,ANG=+180.0,IM=360*NS+1=180*NS+(180*NS+1)
C                                                      -->IM=180*NS+IP
```

```
ANG(180*NS+I)=AN
  A(180*NS+I)=ALR
  B(180*NS+I)=BLR
END IF
IF (AN .GE. 180.0D0) THEN
C Measurement: -180 to 0 <------ theta:  180 to 360 of simulation curve
C If IP=180*NS+1,AN=180.0,ANG=-180.0,IM=       1=(180*NS+1)-180*NS
C                                                      -->IM=IP-180*NS
C If IP=360*NS+1,AN=360.0,ANG=   0.0,IM=180*NS+1=(360*NS+1)-180*NS
C                                                      -->IM=IP-180*NS
ANG(I-180*NS)=AN-360.0D0
  A(I-180*NS)=ALR
  B(I-180*NS)=BLR
END IF
GO TO 109
105 CONTINUE
C Left-ear-up-Nose-forward or Left-ear-forward-Nose-down orientation;
IF (AN .LE. 270.0D0) THEN
C Measurement: -90 to  +90 <------ theta:   0 to 180 of simulation curve
C If IP=1,       AN=0.0,  ANG=-90.0,IM= 90*NS+1=90*NS+(       1)
C                                                      -->IM=90*NS+IP
C If IP=180*NS+1,AN=180.0,ANG=+90.0,IM=270*NS+1=90*NS+(180*NS+1)
C                                                      -->IM=90*NS+IP
C Measurement: +90 to +180 <------ theta: 180 to 270 of simulation curve
C If IP=180*NS+1,AN=180.0,ANG= +90.0,IM=270*NS+1=90*NS+(180*NS+1)
C                                                      -->IM=90*NS+IP
C If IP=270*NS+1,AN=270.0,ANG=+180.0,IM=360*NS+1=90*NS+(270*NS+1)
C                                                      -->IM=90*NS+IP
ANG(90*NS+I)=AN-90.0D0
  A(90*NS+I)=ALR
  B(90*NS+I)=BLR
END IF
IF (AN .GE. 270.0D0) THEN
```

```
C Measurement: -180 to -90 <------ theta: 270 to 360 of simulation curve
C If IP=270*NS+1,AN=270.0,ANG=-180.0,IM=      1=(270*NS+1)-270*NS
C                                                        -->IM=IP-270*NS
C If IP=360*NS+1,AN=360.0,ANG= -90.0,IM=90*NS+1=(360*NS+1)-270*NS
C                                                        -->IM=IP-270*NS
ANG(I-270*NS)=AN-450.0D0
  A(I-270*NS)=ALR
  B(I-270*NS)=BLR
END IF
GO TO 109
109 CONTINUE
END IF
100 CONTINUE

DO 110 I=1,360*NS+1
         IF (FLAG2 .EQ. 1) THEN
C       The measurement data files include the stop angles
C in the second column.
C The results are assumed to be in decibels.
                READ (10,*) ANGLEORIG(I),TEMP,A1(I),TEMP,B1(I),TEMP
         ELSE
                READ (10,*) ANGLEORIG(I),     A1(I),TEMP,B1(I),TEMP
         END IF
110 CONTINUE

C It is very important that the linear power correction with respect to
C the battery drain be performed on the decibel scale.
POWCORA1=A1(1)-A1(360*NS+1)
POWCORB1=B1(1)-B1(360*NS+1)
POWCORA=A(1)-A(360*NS+1)
POWCORB=B(1)-B(360*NS+1)
IF (POWCORA1 .LT. 0.0) WRITE(6,*) '### POWCORA1(dB)=',POWCORA1,' < 0'
IF (POWCORB1 .LT. 0.0) WRITE(6,*) '### POWCORB1(dB)=',POWCORB1,' < 0'
```

```
IF (POWCORA  .LT. 0.0) WRITE(6,*) '### POWCORA (dB)=',POWCORA ,' < 0'
IF (POWCORB  .LT. 0.0) WRITE(6,*) '### POWCORB (dB)=',POWCORB ,' < 0'
  WRITE (6,*) 'Do you want battery drain power correction (1=YES, 2=NO)?'
READ(5,*) FLAG1
IF (FLAG1 .EQ. 1) THEN
C The power scaling is performed with the slope computed from the +180
C and -180 degrees data least affected by electrical noise.
GO TO (1111,1112,1111,1111,1112,1111) ABS(ORIENTATION)
1111 CONTINUE
C Battery drain power correction is performed according to the vertical
C polarization.
DO 1101 I=1,360*NS+1
A1(I)=A1(I)+POWCORB1*(DFLOAT(I-1)/360.0D0)
B1(I)=B1(I)+POWCORB1*(DFLOAT(I-1)/360.0D0)
 A(I)= A(I)+POWCORB *(DFLOAT(I-1)/360.0D0)
 B(I)= B(I)+POWCORB *(DFLOAT(I-1)/360.0D0)
1101 CONTINUE
GO TO 1119
1112 CONTINUE
C Battery drain power correction is performed according to the horizontal
C polarization.
DO 1102 I=1,360*NS+1
A1(I)=A1(I)+POWCORA1*(DFLOAT(I-1)/360.0D0)
B1(I)=B1(I)+POWCORA1*(DFLOAT(I-1)/360.0D0)
 A(I)= A(I)+POWCORA *(DFLOAT(I-1)/360.0D0)
 B(I)= B(I)+POWCORA *(DFLOAT(I-1)/360.0D0)
1102 CONTINUE
GO TO 1119
1119 CONTINUE
END IF

C It is very important that the search for the angle offset that produces
C the minimum error be performed on the linear scale.
```

```
DO 200 I=1,360*NS+1
C The results are assumed to be in decibels.
 A(I)=10.0D0**( A(I)/20.0D0)
   B(I)=10.0D0**( B(I)/20.0D0)
A1(I)=10.0D0**(A1(I)/20.0D0)
B1(I)=10.0D0**(B1(I)/20.0D0)
200 CONTINUE

  WRITE (6,*) 'Do you want the average of the horizontal and the vertical
     & polarization average factors (1=YES, 2=NO)?'
READ  (5,*) FLAG

  WRITE (6,*) 'Do you want to bypass the minimization process
     &(1=YES, 2=NO)?'
READ  (5,*) FLAG3
IF (FLAG3 .EQ. 2) THEN
ERRORMIN=1.0D+35
DO 888 I=1,360*NS+1
ANGLE_OFFSET=-180.0D0+(DFLOAT(I-1)/DFLOAT(NS))
CALL SCALE(ERROR,ANGLE_OFFSET,ANGLEORIG,ANG,
     &A,B,A1,B1,FLAG,FLAGPOL,NS)
C WRITE (6,*) 'ERROR for ANGLE_OFFSET =',
C    &ANGLE_OFFSET,' is =',ERROR
IF (ERROR .LT. ERRORMIN) THEN
ANGLE_OFFSET_BEST=ANGLE_OFFSET
ERRORMIN=ERROR
END IF
888 CONTINUE
  WRITE (6,*) ''
  WRITE (6,*) 'Computed ANGLE_OFFSET_BEST = ',
     &ANGLE_OFFSET_BEST
  WRITE (6,*) ''
END IF
```

```
9999 CONTINUE
  WRITE (6,*) 'ANGLE_OFFSET_BEST = ?'
READ (5,*) ANGLE_OFFSET_BEST

CALL FACAVG(FACAVGA,FACAVGB,ANGLE_OFFSET_BEST,ANGLEORIG,
     &ANG,A,B,A1,B1,NS,MFLAG,POINTER,FLAG)

  WRITE (6,*) ''
WRITE (6,*) 'Horizontal polarization average factor (dB) =',
     &20.0D0*DLOG10(FACAVGA)
WRITE (6,*) 'Vertical polarization average factor (dB) =',
     &20.0D0*DLOG10(FACAVGB)
  WRITE (6,*) ''

C From hereon, I need to distinguish between the two sets of angles.
C I is the index for the original angle values from -180 to +180.
C J is the index for the mapped angle values from -180 to +180.
IF (MFLAG) 121,122,123
121 CONTINUE
C MFLAG = -1 and no index value corresponds to -180 degrees.
         WRITE (6,*) 'NOTE: -180 degrees was not assigned.'
ISTART=2
ISTOP=360*NS+1
NNN=360*NS
GO TO 129
122 CONTINUE
C MFLAG = 0 and there is a one-to-one mapping between
C angle value and index value. This should be used
C only if ANGLE_OFFSET=0.
ISTART=1
ISTOP=360*NS+1
NNN=360*NS+1
```

```
GO TO 129
123 CONTINUE
C MFLAG = +1 and no index value corresponds to +180 degrees.
        WRITE (6,*) 'NOTE: +180 degrees was not assigned.'
ISTART=1
ISTOP=360*NS
NNN=360*NS
GO TO 129
129 CONTINUE

OPEN (UNIT=20,FILE=OUFILEANG,STATUS='UNKNOWN')
C The following 2 files are the measurement data files.
OPEN (UNIT=21,FILE=OUFILEM_H,STATUS='UNKNOWN')
OPEN (UNIT=22,FILE=OUFILEM_V,STATUS='UNKNOWN')
C The following 2 files are the prediction data files.
OPEN (UNIT=31,FILE=OUFILEP_H,STATUS='UNKNOWN')
OPEN (UNIT=32,FILE=OUFILEP_V,STATUS='UNKNOWN')

DO 150 I=ISTART,ISTOP
J=POINTER(I)
C It is the predicted data that is shifted in amplitude in the
C process of correlating the measured and the predicted data.
C However, if the angle offset is zero, a same predicted curve
C cannot be used to compare with different measured curves from
C the repetition of the same experiment.
DELFACA=A(J)/FACAVGA
DELFACB=B(J)/FACAVGB
WRITE (20,2000) ANGLEORIG(I)
  WRITE (21,2000) 20.0D0*DLOG10(A1(I))
  WRITE (22,2000) 20.0D0*DLOG10(B1(I))
  WRITE (31,2000) 20.0D0*DLOG10(DELFACA)
  WRITE (32,2000) 20.0D0*DLOG10(DELFACB)
150 CONTINUE
```

```
CALL SCALE(ERROR,ANGLE_OFFSET_BEST,ANGLEORIG,ANG,A,B,A1,B1,
     &FLAG,1,NS)
WRITE (6,*) ' '
C ERROR is an absolute value.
WRITE (6,*) 'Total error for horizontal polarization is = ',
     &20.0D0*DLOG10((ERROR/DFLOAT(NNN))*360.0D0),' dB'
CALL SCALE(ERROR,ANGLE_OFFSET_BEST,ANGLEORIG,ANG,A,B,A1,B1,
     &FLAG,0,NS)
C ERROR is an absolute value.
  WRITE (6,*) 'Total error for vertical polarization is = ',
     &20.0D0*DLOG10((ERROR/DFLOAT(NNN))*360.0D0),' dB'

2000 FORMAT (X,E15.7)

CLOSE(20)
CLOSE(21)
CLOSE(22)
CLOSE(31)
CLOSE(32)

WRITE (6,*) ''
WRITE (6,*) 'Do you want to try another offset angle value (1=YES, 2=NO) ?'
READ (5,*) FLAGREPEAT
IF (FLAGREPEAT .EQ. 2) STOP
GO TO 9999

END


C ---------------------------------------------------------------
SUBROUTINE SCALE(ERROR,ANGLE_OFFSET,ANGLEORIG,ANG,A,B,A1,B1,
     &FLAG,FLAGPOL,NS)
```

```
PARAMETER(IMAX=3601)

REAL*8 ERROR,FACAVGA,FACAVGB
REAL*8 A(IMAX),B(IMAX),A1(IMAX),B1(IMAX)
REAL*8 DELSUMA,DELSUMB,DELFACA,DELFACB

REAL*8 ANGLE_OFFSET,ANGLEORIG(IMAX),ANG(IMAX)

INTEGER NS,ISTART,ISTOP,MFLAG,POINTER(IMAX)
INTEGER FLAG,FLAGPOL

CALL FACAVG(FACAVGA,FACAVGB,ANGLE_OFFSET,ANGLEORIG,
     &ANG,A,B,A1,B1,NS,MFLAG,POINTER,FLAG)

IF (MFLAG) 121,122,123
121 CONTINUE
C MFLAG = -1 and no index value corresponds to -180 degrees.
ISTART=2
ISTOP=360*NS+1
GO TO 129
122 CONTINUE
C MFLAG = 0 and there is a one-to-one mapping between
C angle value and index value. This should be used
C only if ANGLE_OFFSET=0.
ISTART=1
ISTOP=360*NS+1
GO TO 129
123 CONTINUE
C MFLAG = +1 and no index value corresponds to +180 degrees.
ISTART=1
ISTOP=360*NS
GO TO 129
```

```
129 CONTINUE

DELSUMA=0.0D0
DELSUMB=0.0D0
DO 150 I=ISTART,ISTOP
J=POINTER(I)
C It is the predicted data that is shifted in amplitude in the
C process of correlating the measured and the predicted data.
C However, if the angle offset is zero, a same predicted curve
C cannot be used to compare with different measured curves from
C the repetition of the same experiment.
DELFACA=A(J)/FACAVGA
DELFACB=B(J)/FACAVGB
C I use the absolute value rather than the signed value.
DELFACA=DABS(A1(I)-DELFACA)
DELFACB=DABS(B1(I)-DELFACB)
DELSUMA=DELSUMA+DELFACA
DELSUMB=DELSUMB+DELFACB
150 CONTINUE
IF (FLAGPOL .EQ. 1) THEN
C The horizontal polarization is used to obtain ANGLE_OFFSET_BEST.
ERROR=DELSUMA
ELSE
C The vertical polarization is used to obtain ANGLE_OFFSET_BEST.
ERROR=DELSUMB
END IF
C WRITE (6,*) 'ANGLE_OFFSET= ',ANGLE_OFFSET,'      DELSUMA= ',
C    & DELSUMA,' DELSUMB= ',DELSUMB


RETURN
END
C ---------------------------------------------------------------------
```

```
SUBROUTINE FACAVG(FACAVGA,FACAVGB,ANGLE_OFFSET,ANGLEORIG,
     &ANG,A,B,A1,B1,NS,MFLAG,POINTER,FLAG)

PARAMETER(IMAX=3601)

REAL*8 FACA(IMAX),FACB(IMAX),A(IMAX),B(IMAX),A1(IMAX),B1(IMAX)
REAL*8 FACSUMA,FACSUMB,FACAVGA,FACAVGB

REAL*8 ANG(IMAX),ANGLE(IMAX),ANGLEORIG(IMAX),ANGLE_OFFSET,EPS

INTEGER NS,ISTART,ISTOP,JSTART,JSTOP,MFLAG,POINTER(IMAX)
INTEGER MAPFLAG,NNN,FLAG


C Note that a positive value of offset angle makes the predicted
C curve shift rightward, i.e. toward +180 degrees, except for the
C section of the curve that folds back onto the -180 to +180 range.

EPS=0.1D0/DFLOAT(NS)
C The parameter EPS is necessary to avoid the truncation error to
C cause the test on ANGLE(I) to fail which would result in missing
C the mapping of -180 or +180 degree.

MFLAG=0
DO 120 I=1,360*NS+1
C It is the predicted data that is shifted in angle in the process
C of correlating the measured and the predicted data.
C With zero degree offset, the two different angles -180 and +180
C degrees are assigned two different index values, I=1 and I=360*NS+1,
C respectively, and thus, two different measurement values.
C If the conversion algorithm merely mapped the new angular range
C onto the span of -180 to +180 degrees by simply adding or
```

```
C subtracting 360 degrees whenever the new angular value exceeded
C the -180 to +180 degree range, then for, say, a +10 degree offset,
C both new angular values -170 and +190 degrees would correspond to the
C same -170 degrees. But since two possibly different index values
C could not be assigned to -170 degrees, one of the two measurement
C values and its corresponding index value would need to be dropped.
C If the offset is positive, -180 degree gets dropped. If the offset
C is negative, +180 degree gets dropped.

ANGLE(I)=ANG(I)+ANGLE_OFFSET
C The parameter EPS is necessary to avoid the truncation error to
C cause the following test to fail which would result in missing
C the mapping of -180 degree.
IF (ANGLE(I) .LT. -180.0D0-EPS) THEN
C No index value corresponds to +180 degrees.
C The value ANGLE(360*NS+1) overwrites the value ANGLE(1).
ANGLE(I)=ANGLE(I)+360.0D0
IF (MFLAG .EQ. -1) THEN
WRITE (6,*) 'ERROR: Mapping is too broad'
ELSE
MFLAG=+1
END IF
END IF
C The parameter EPS is necessary to avoid the truncation error to
C cause the following test to fail which would result in missing
C the mapping of +180 degree.
IF (ANGLE(I) .GT. +180.0D0+EPS) THEN
C No index value corresponds to -180 degrees.
C The value ANGLE(360*NS+1) overwrites the value ANGLE(1).
ANGLE(I)=ANGLE(I)-360.0D0
IF (MFLAG .EQ. +1) THEN
WRITE (6,*) 'ERROR: Mapping is too broad'
ELSE
```

```
MFLAG=-1
END IF
END IF
120 CONTINUE

C From hereon, I need to distinguish between the two sets of angles.
C I is the index for the original angle values from -180 to +180.
C J is the index for the mapped angle values from -180 to +180.
IF (MFLAG) 121,122,123
121 CONTINUE
C MFLAG = -1 and no index value corresponds to -180 degrees.
ISTART=2
ISTOP=360*NS+1
C The value ANGLE(360*NS+1) overwrote the value ANGLE(1).
JSTART=2
JSTOP=360*NS+1
NNN=360*NS
GO TO 129
122 CONTINUE
C MFLAG = 0 and there is a one-to-one mapping between
C angle value and index value. This should be used
C only if ANGLE_OFFSET=0.
ISTART=1
ISTOP=360*NS+1
JSTART=1
JSTOP=360*NS+1
NNN=360*NS+1
GO TO 129
123 CONTINUE
C MFLAG = +1 and no index value corresponds to +180 degrees.
ISTART=1
ISTOP=360*NS
C The value ANGLE(360*NS+1) overwrote the value ANGLE(1).
```

```
JSTART=2
JSTOP=360*NS+1
NNN=360*NS
GO TO 129
129 CONTINUE

DO 131 I=ISTART,ISTOP
MAPFLAG=0
DO 130 J=JSTART,JSTOP
C I chose to drop the index value I=360*NS+1 unless ANGLE_OFFSET=0.
                        IF (DABS(ANGLE(J)-ANGLEORIG(I)) .LE. EPS) THEN
IF (MAPFLAG .EQ. 1) THEN
WRITE (6,*) 'Error: overmapping'
ELSE
FACA(J)=A(J)/A1(I)
FACB(J)=B(J)/B1(I)
POINTER(I)=J
MAPFLAG=1
END IF
END IF
130 CONTINUE
                IF (MAPFLAG .EQ. 0) THEN
          WRITE (6,*) 'No mapping found for angle',
     &ANGLEORIG(I)
                END IF
131 CONTINUE

FACSUMA=0.0D0
FACSUMB=0.0D0
DO 140 J=JSTART,JSTOP
C I use the signed value rather than the absolute value.
FACSUMA=FACSUMA+FACA(J)
FACSUMB=FACSUMB+FACB(J)
```

```
140 CONTINUE
FACAVGA=FACSUMA/DFLOAT(NNN)
FACAVGB=FACSUMB/DFLOAT(NNN)

IF (FLAG .EQ. 1) THEN
FACAVGA=0.5D0*(FACAVGA+FACAVGB)
FACAVGB=FACAVGA
END IF

RETURN
END
```

C.2 Parabolic interpolation program

```
C ***************************************************************************
C Last revised: 17 December 1998
C This program performs a parabolic interpolation with the parabola axis
C parallel to the vertical axis.
C This program is tailored to work with the output format of XFDTD.
C NS is the number of points per degree.
C ***************************************************************************

PROGRAM INTERPOLATE_DATA

PARAMETER(IMAX=3601)

C CHARACTER*50 INFILE_H,INFILE_V,INFILE_P
C CHARACTER*50 OUFILE_H,OUFILE_V,OUFILE_P
CHARACTER*50 INFILE_P,OUFILE_P,OUFILE_THETA,OUFILE_PHI
INTEGER ORIENTATION

REAL*4 ANGLE(IMAX),A(IMAX),B(IMAX),TEMP
REAL*4 X1,YA1,YB1,X2,YA2,YB2,X3,YA3,YB3,X,YA,YB
REAL*4 INTERPOLATE

  WRITE(6,*) 'INTEGER MULTIPLICATION FACTOR NS (<11) = ?'
READ(5,*) NS
C WRITE(6,*) 'ORIENTATION (>0=2; <0=5/6) = ?'
  WRITE(6,*) 'ORIENTATION (>0=5; <0=5/6) = ?'
READ(5,*) ORIENTATION
C IF (ORIENTATION .LT. 0) THEN
  WRITE(6,*) 'INFILE_P = ?'
READ(5,*) INFILE_P
C ELSE
```

```
C WRITE(6,*) 'INFILE_H = ?'
C READ(5,*) INFILE_H
C WRITE(6,*) 'INFILE_V = ?'
C READ(5,*) INFILE_V
C END IF

  IF (ORIENTATION .LT. 0) THEN
  WRITE(6,*) 'OUFILE_P = ?'
READ(5,*) OUFILE_P
  ELSE
  WRITE(6,*) 'OUFILE_THETA = ?'
  READ(5,*) OUFILE_THETA
  WRITE(6,*) 'OUFILE_PHI = ?'
  READ(5,*) OUFILE_PHI
  END IF

C IF (ORIENTATION .LT. 0) THEN
OPEN (UNIT=11,FILE=INFILE_P,STATUS='OLD')
C ELSE
C OPEN (UNIT=11,FILE=INFILE_H,STATUS='OLD')
C OPEN (UNIT=12,FILE=INFILE_V  ,STATUS='OLD')
C END IF
  IF (ORIENTATION .LT. 0) THEN
OPEN (UNIT=21,FILE=OUFILE_P,STATUS='UNKNOWN')
  ELSE
  OPEN (UNIT=21,FILE=OUFILE_PHI  ,STATUS='UNKNOWN')
  OPEN (UNIT=22,FILE=OUFILE_THETA,STATUS='UNKNOWN')
  END IF


IF (ORIENTATION .LT. 0) THEN
WRITE(6,*) 'Are stop angles included in the input data file
     &(1=YES, 2=NO)?'
```

```
READ(5,*) FLAG2
END IF
DO 100 I=1,361
IF (ORIENTATION .LT. 0) THEN
IF (FLAG2 .EQ. 1) THEN
READ(11,*) ANGLE(I),TEMP,A(I),TEMP,B(I),TEMP
ELSE
READ(11,*) ANGLE(I),     A(I),TEMP,B(I),TEMP
END IF
ELSE
C READ(11,*) ANGLE(I), A(I)
C READ(12,*) ANGLE(I), B(I)
READ(11,*) ANGLE(I),A(I),B(I),TEMP,TEMP
END IF
100 CONTINUE

TEMP=0.0
X1=ANGLE(1)
YA1=A(1)
YB1=B(1)
X2=ANGLE(2)
YA2=A(2)
YB2=B(2)
X3=ANGLE(3)
YA3=A(3)
YB3=B(3)
DO 250 J=1,NS
X=X1+(FLOAT(J-1)/FLOAT(NS))
YA=INTERPOLATE(X1,YA1,X2,YA2,X3,YA3,X)
YB=INTERPOLATE(X1,YB1,X2,YB2,X3,YB3,X)
IF (ORIENTATION .LT. 0) THEN
IF (FLAG2 .EQ. 1) THEN
WRITE (21,1000) X,TEMP,YA,TEMP,YB,TEMP
```

```
ELSE
WRITE (21,1100) X,     YA,TEMP,YB,TEMP
END IF
ELSE
WRITE (21,2000) X, YA
WRITE (22,2000) X, YB
END IF
250 CONTINUE
DO 300 I=2,360
X1=ANGLE(1)+FLOAT(I-2)
YA1=A(I-1)
YB1=B(I-1)
X2=ANGLE(1)+FLOAT(I-1)
YA2=A(I)
YB2=B(I)
X3=ANGLE(1)+FLOAT(I)
YA3=A(I+1)
YB3=B(I+1)
DO 350 J=1,NS
X=X2+(FLOAT(J-1)/FLOAT(NS))
YA=INTERPOLATE(X1,YA1,X2,YA2,X3,YA3,X)
YB=INTERPOLATE(X1,YB1,X2,YB2,X3,YB3,X)
IF (ORIENTATION .LT. 0) THEN
IF (FLAG2 .EQ. 1) THEN
WRITE (21,1000) X,TEMP,YA,TEMP,YB,TEMP
ELSE
WRITE (21,1100) X,     YA,TEMP,YB,TEMP
END IF
ELSE
WRITE (21,2000) X, YA
WRITE (22,2000) X, YB
END IF
350 CONTINUE
```

```
300 CONTINUE
IF (ORIENTATION .LT. 0) THEN
IF (FLAG2 .EQ. 1) THEN
WRITE (21,1000) ANGLE(361),TEMP,A(361),TEMP,B(361),TEMP
ELSE
WRITE (21,1100) ANGLE(361),     A(361),TEMP,B(361),TEMP
END IF
ELSE
WRITE (21,2000) ANGLE(361),A(361)
WRITE (22,2000) ANGLE(361),B(361)
END IF


1000 FORMAT (F7.1,2X,F3.1,2X,E15.7,2X,F3.1,2X,E15.7,2X,F3.1)
1100 FORMAT (F7.1,2X,        E15.7,2X,F3.1,2X,E15.7,2X,F3.1)
2000 FORMAT (F7.1,2X,E15.7)

STOP
END

C ---------------------------------------------------------------------
FUNCTION INTERPOLATE(X1,Y1,X2,Y2,X3,Y3,X)
REAL*4 X1,Y1,X2,Y2,X3,Y3,X,INTERPOLATE

INTERPOLATE=Y1*((X-X2)*(X-X3))/((X1-X2)*(X1-X3))+
     &              Y2*((X-X1)*(X-X3))/((X2-X1)*(X2-X3))+
     &              Y3*((X-X1)*(X-X2))/((X3-X1)*(X3-X2))

RETURN
END
```

C.3 Coordinate transformation program

```
C ***************************************************************
C Last revised: 27 July 1999
C This program performs a coordinate transformation based on the
C static Galilean transformation.
C This program is tailored to work with the output format of XFDTD.
C 3 passes are required:
C 1) to generate the angles for XFDTD then abort;
C 2) to generate OUFILE in linear scale for the
C field to be interpolated with INTERPOLATE3,
C ignoring for now the results in OUFILEHOR
C and OUFILEVER;
C 3) to transform coordinates so that OUFILEHOR and
C OUFILEVER will be input to COMPARE13_LINEAR.
C ***************************************************************

PROGRAM COORDINATE_TRANSFORMATION

PARAMETER(NNMAX=3601, EPS=1.0D-2)

REAL*8 DARCTAND,DELANG,ANGLE(NNMAX)
REAL*8 OU,OV,OW,QX,QY,QZ
REAL*8 PXYZ,PX,PY,PZ,THA,PHI,VARTHA,VARPHI
REAL*8 PUVW,PU,PV,PW
REAL*8 WIDTH,WIDTHX,WIDTHY,WIDTHZ
REAL*8 THICK,THICKX,THICKY,THICKZ
REAL*8 HEIGHT,HEIGHTX,HEIGHTY,HEIGHTZ
REAL*8 T(3,3)
REAL*8 VTHA(NNMAX),VPHI(NNMAX),TTHA(NNMAX),PPHI(NNMAX)
REAL*4 TEMP
```

```
INTEGER ORIENTATION

CHARACTER*50 OUFILE,FILENAME,OUFILEHOR,OUFILEVER,FILEDAT,OUFIELD,INFIELD
REAL*8 EMAGVARTHA;EMAGVARPHI,EPHSVARTHA,EPHSVARPHI
REAL*8 EPS,EUVW,EXYZ,RVARTHA,IVARTHA,RVARPHI,IVARPHI
REAL*8 EPHIMOD,ETHAMOD,PHIM,THAM
COMPLEX*16 DCMPLX,CDABS,CDSQRT
COMPLEX*16 EU,EV,EW,EVARTHA,EVARPHI
COMPLEX*16 EX,EY,EZ,ETHA,EPHI,ER

C The units are mm.
PXYZ=3350.0
WIDTHX=23.5
WIDTHY=0.0
WIDTHZ=48.1
THICKX=-2.7
THICKY=17.2
THICKZ=1.3
HEIGHTX=-148.4
HEIGHTY=-29.1
HEIGHTZ=72.4
QX=8.81
QY=-83.94
QZ=-3.75

WIDTH =DSQRT(( WIDTHX**2)+( WIDTHY**2)+( WIDTHZ**2))
THICK =DSQRT(( THICKX**2)+( THICKY**2)+( THICKZ**2))
HEIGHT=DSQRT((HEIGHTX**2)+(HEIGHTY**2)+(HEIGHTZ**2))

T(1,1)= WIDTHX/WIDTH
T(2,1)= WIDTHY/WIDTH
T(3,1)= WIDTHZ/WIDTH
T(1,2)= THICKX/THICK
```

```
T(2,2)= THICKY/THICK
T(3,2)= THICKZ/THICK
T(1,3)=HEIGHTX/HEIGHT
T(2,3)=HEIGHTY/HEIGHT
T(3,3)=HEIGHTZ/HEIGHT

OU=(-QX)*T(1,1)+(-QY)*T(2,1)+(-QZ)*T(3,1)
OV=(-QX)*T(1,2)+(-QY)*T(2,2)+(-QZ)*T(3,2)
OW=(-QX)*T(1,3)+(-QY)*T(2,3)+(-QZ)*T(3,3)

C The name of OUFILE for pass #2 and pass #3 should be different from
C that for pass #1 or else the list of angles from which the
C interpolated data was made will be lost.
        WRITE (6,*) 'OUFILE for angles = ?'
        READ  (5,*) OUFILE
        OPEN (UNIT=10,FILE=OUFILE,STATUS='UNKNOWN')

C The increment value is 1.0 degree for pass #1 and pass #2 but
C 0.2 degree for pass #3.
  WRITE (6,*) 'Angular value of increment = ?'
  READ  (5,*) DELANG
NN=IIDINT(360.0D0/DELANG)
IF (NN .GT. NNMAX) THEN
WRITE (6,*) 'NN too large'
STOP
END IF

WRITE (6,*) 'Desired cut (1=HuNf, 2=LuNf, 3=LfNd) = ?'
READ  (5,*) ORIENTATION

        GO TO (10,20,30), ORIENTATION
10      CONTINUE
                THAM=90.0D0
```

```
        GO TO 99
20      CONTINUE
                PHIM=0.0D0
        GO TO 99
30      CONTINUE
                PHIM=90.0D0
        GO TO 99
99      CONTINUE

C The sequence of the PHI angle is NOT reversed so that when using the
C UNIX "ls -ltr" command, the list of xfdtd output files appears
C almost in the correct sequence, requiring only small displacements
C of the cursor for editing the list in order to create the file
C sequence that will be given the name indicated by FILENAME.
C The loop runs all the way up to NN+1 instead of NN in order to avoid
C some extra house-keeping later on when we will want to process the
C variables corresponding to the angular value of 360 degrees.
WRITE (10,*) NN+1
        DO 100 I=1,NN+1
                IF (ORIENTATION .EQ. 1) THEN
                        PHI=DFLOAT(I-1)*DELANG
                        ANGLE(I)=PHI
                        THA=THAM
                ELSE
                        THA=DFLOAT(I-1)*DELANG
C For interpolation in a subsequent process, ANGLE(I) needs to be a
C continuous stream (from 0 to 360 degrees for a 1 degree increment)
C even though the angle theta is not defined beyond 180 degrees in the
C spherical coordinate system.
                        ANGLE(I)=THA
                        IF (THA .GT. 180.0D0) THEN
                                THA=360.0D0-THA
                                PHI=DMOD(PHIM+180.0D0,360.0)
```

```
                    ELSE
                            PHI=DMOD(PHIM        ,360.0)
                    END IF
                END IF
                TTHA(I)=THA
                PPHI(I)=PHI

PX=PXYZ*DSIND(THA)*DCOSD(PHI)
PY=PXYZ*DSIND(THA)*DSIND(PHI)
PZ=PXYZ*DCOSD(THA)

PU=(PX-QX)*T(1,1)+(PY-QY)*T(2,1)+(PZ-QZ)*T(3,1)
PV=(PX-QX)*T(1,2)+(PY-QY)*T(2,2)+(PZ-QZ)*T(3,2)
PW=(PX-QX)*T(1,3)+(PY-QY)*T(2,3)+(PZ-QZ)*T(3,3)
PUVW=DSQRT((PU**2)+(PV**2)+(PW**2))

VTHA(I)=DACOSD(PW/PUVW)
VPHI(I)=DARCTAND(PV,PU)
WRITE(10,1000) 0,VPHI(I),VPHI(I),1.0,VTHA(I)
100 CONTINUE
1000 FORMAT (X,I2,2X,2(E15.6,X),2X,F3.1,2X,E15.6)
CLOSE(10)

WRITE (6,*) '*****ABORT NOW IF ONLY THE LIST OF ANGLES WAS WANTED*****'
C End of pass #1.

WRITE (6,*) 'FILENAME for list of files = ?'
READ  (5,*) FILENAME
OPEN (UNIT=11,FILE=FILENAME,STATUS='UNKNOWN')
READ (11,*) NFILES
IF (NFILES .NE. NN) THEN
WRITE (6,*) '(NN= ',NN,') .NE. (NFILES =',NFILES,')'
WRITE (6,*) 'Was the field interpolated (1=YES, 2=NO)?'
```

```
READ (5,*) INTERPOLFLAG
IF (INTERPOLFLAG .EQ. 2) THEN
WRITE (6,*) 'ERROR: (NN= ',NN,') .NE. (NFILES =',NFILES,')'
STOP
END IF
ELSE
INTERPOLFLAG=2
END IF

IF (INTERPOLFLAG .EQ. 2) THEN
C Pass #2. NN corresponds to the number of angular values from 0 to 359
C degrees for a 1 degree increment. Since there is no need to duplicate
C the computation of the far field with XFDTD for the value of 360
C degrees, the loop runs only up to NN.
WRITE (6,*) 'OUFIELD for the field (in linear scale)= ?'
READ  (5,*) OUFIELD
OPEN (UNIT=20,FILE=OUFIELD,STATUS='UNKNOWN')
DO 200 I=1,NN
READ (11,*) FILEDAT
OPEN (UNIT=30, FILE=FILEDAT, STATUS='old')
C       Skip the first line of each data file.
READ (30,*)
READ (30,*) TEMP,EMAGVARPHI,EMAGVARTHA,EPHSVARPHI,EPHSVARTHA
CLOSE(30)
3000 FORMAT (X,5(E15.6,X))
C The XFDTD403 software from the steady-state far-zone transformation
C gives the field values in dB. These values must be converted from dB
C to linear before coordinate transformation be performed.
EMAGVARTHA=10.0D0**(EMAGVARTHA/20.0D0)
EMAGVARPHI=10.0D0**(EMAGVARPHI/20.0D0)
WRITE (20,3000) ANGLE(I),EMAGVARPHI,EPHSVARPHI,EMAGVARTHA,EPHSVARTHA
200 CONTINUE
CLOSE(11)
```

```
CLOSE(20)
ELSE
C Pass #3. If the FDTD program was run to obtain the last angular value
C as 359 degrees rather than 360 degrees with a 1 degree increment,
C don't forget to duplicate the first line and add it as the last line
C before interpolating the data with 0.2 degree increment. Then, this
C program is run again but with 0.2 degree increment thus making NN now
C correspond to the number of angular values from 0 to 360.0 degrees
C in 0.2 degree increment.
WRITE (6,*) 'INFIELD for the field (in linear scale)= ?'
READ  (5,*) INFIELD
OPEN (UNIT=40,FILE=INFIELD,STATUS='OLD')
WRITE (6,*) 'OUFILE for horizontal polarization = ?'
READ  (5,*) OUFILEHOR
OPEN (UNIT=12,FILE=OUFILEHOR,STATUS='UNKNOWN')
WRITE (6,*) 'OUFILE for vertical polarization = ?'
READ  (5,*) OUFILEVER
OPEN (UNIT=13,FILE=OUFILEVER,STATUS='UNKNOWN')
DO 201 I=1,NN+1
VARTHA=VTHA(I)
VARPHI=VPHI(I)
THA=TTHA(I)
PHI=PPHI(I)
C The interpolated data is in the linear scale.
READ (40,*) ANGLE(I),EMAGVARPHI,EPHSVARPHI,EMAGVARTHA,EPHSVARTHA
RVARTHA=EMAGVARTHA*DCOSD(EPHSVARTHA)
IVARTHA=EMAGVARTHA*DSIND(EPHSVARTHA)
EVARTHA=DCMPLX(RVARTHA,IVARTHA)
RVARPHI=EMAGVARPHI*DCOSD(EPHSVARPHI)
IVARPHI=EMAGVARPHI*DSIND(EPHSVARPHI)
EVARPHI=DCMPLX(RVARPHI,IVARPHI)

EU= EVARTHA*DCOSD(VARTHA)*DCOSD(VARPHI)-EVARPHI*DSIND(VARPHI)
```

```
EV= EVARTHA*DCOSD(VARTHA)*DSIND(VARPHI)+EVARPHI*DCOSD(VARPHI)
EW=-EVARTHA*DSIND(VARTHA)
EUVW=CDABS(CDSQRT((EU**2)+(EV**2)+(EW**2)))

EX=EU*T(1,1)+EV*T(1,2)+EW*T(1,3)
EY=EU*T(2,1)+EV*T(2,2)+EW*T(2,3)
EZ=EU*T(3,1)+EV*T(3,2)+EW*T(3,3)
EXYZ=CDABS(CDSQRT((EX**2)+(EY**2)+(EZ**2)))

IF (DABS(EUVW-EXYZ) .GT. EPS*EXYZ) THEN
WRITE (6,*) 'Error: EXYZ - EUVW = ',EXYZ-EUVW
END IF

ETHA= EX*DCOSD(THA)*DCOSD(PHI)+EY*DCOSD(THA)*DSIND(PHI)-EZ*DSIND(THA)
EPHI=-EX            *DSIND(PHI)+EY*           DCOSD(PHI)
ER  = EX*DSIND(THA)*DCOSD(PHI)+EY*DSIND(THA)*DSIND(PHI)+EZ*DCOSD(THA)
EPHIMOD=CDABS(EPHI)
ETHAMOD=CDABS(ETHA)

GO TO (11,21,21), ORIENTATION
11 CONTINUE
C Horizontal direction is the phi unit vector.
WRITE (12,2000) ANGLE(I),20.0D0*DLOG10(EPHIMOD)
C Vertical direction is the -tha unit vector.
WRITE (13,2000) ANGLE(I),20.0D0*DLOG10(ETHAMOD)
GO TO 98
21 CONTINUE
C Horizontal direction is the tha unit vector.
WRITE (12,2000) ANGLE(I),20.0D0*DLOG10(ETHAMOD)
C Vertical direction is the phi unit vector.
WRITE (13,2000) ANGLE(I),20.0D0*DLOG10(EPHIMOD)
GO TO 98
98 CONTINUE
```

```
201 CONTINUE
CLOSE(12)
CLOSE(13)
CLOSE(40)
END IF

2000 FORMAT (X,E15.7,3X,E15.7)
STOP
END


FUNCTION DARCTAND(A,B)
REAL*8 DARCTAND,A,B
IF ((A .EQ. 0.0D0) .AND. (B .EQ. 0.0D0)) THEN
DARCTAND=0.0D0
ELSE
DARCTAND=DATAN2D(A,B)
END IF
RETURN
END
```

C.4 Mapping from the measurement angle to the appropriate spherical coordinate angle

```
C ***********************************************************************
C Last revised: 18 December 1998
C The coordinate system is that where the monopole aligns with the
C +z axis and the top of the case sticks out along the +x axis, or the
C       +z axis is through the top of the phantom head and the +y axis is
C       through the left ear canal of the phantom head.
C ***********************************************************************
C This revised version expects the predicted data to be in dB.
C NS is the integer number of points per degree.
C The program need not have the input data ordered in angular value.
C ***********************************************************************

PROGRAM MEASUREMENT2SPHERICAL

PARAMETER(IMAX=361,NS=1)

CHARACTER*50 INFILE,OUFILE

INTEGER NS,ORIENTATION

REAL*4 A (IMAX),HRMAG(IMAX),HRPHS(IMAX),VRMAG(IMAX),VRPHS(IMAX)
REAL*4 AN(IMAX),HMAG (IMAX),HPHS (IMAX),VMAG (IMAX),VPHS (IMAX)
REAL*4 ANG,     HORMAG,     HORPHS,     VERMAG,     VERPHS
REAL*4 POWCORA,POWCORB,TMP

  WRITE(6,*) 'ORIENTATION (1=Vert, 2=Flat, 3=Edge,
     & 4=HuNf, 5=LuNf, 6=LfNd) = ?'
READ(5,*) ORIENTATION
WRITE(6,*) 'INFILE (measurement) = ?'
```

```
READ(5,*) INFILE
  WRITE(6,*) 'OUFILE (measurement) = ?'
READ(5,*) OUFILE

OPEN (UNIT=10,FILE=INFILE,STATUS='OLD')
        WRITE(6,*) 'Are stop angles included in the experimental data
     &file (1=YES, 2=NO) ?'
        READ(5,*) FLAG2

DO 10 I=1,360*NS+1
                IF (FLAG2 .EQ. 1) THEN
C The measurement data files include the stop angles in the second column.
READ (10,*) A(I),TMP,HRMAG(I),HRPHS(I),VRMAG(I),VRPHS(I)
ELSE
READ (10,*) A(I),    HRMAG(I),HRPHS(I),VRMAG(I),VRPHS(I)
END IF
10 CONTINUE

C It is very important that the linear power correction with respect to
C the battery drain be performed on the decibel scale.
POWCORA=HRMAG(1)-HRMAG(360*NS+1)
POWCORB=VRMAG(1)-VRMAG(360*NS+1)
IF (POWCORA  .LT. 0.0) WRITE(6,*) '### POWCORA (dB)=',POWCORA ,' < 0'
IF (POWCORB  .LT. 0.0) WRITE(6,*) '### POWCORB (dB)=',POWCORB ,' < 0'
WRITE (6,*) 'Do you want battery drain power correction (1=YES, 2=NO)?'
READ(5,*) FLAG1
IF (FLAG1 .EQ. 1) THEN
C       The power scaling is performed with the slope computed from the +180
C       and -180 degrees data least affected by electrical noise.
GO TO (1111,1112,1111,1111,1112,1111) ABS(ORIENTATION)
1111                    CONTINUE
C Battery drain power correction is performed according to the vertical
C polarization.
```

```
DO 1101 I=1,360*NS+1
HRMAG(I)=HRMAG(I)+POWCORB*(DFLOAT(I-1)/360.0D0)
VRMAG(I)=VRMAG(I)+POWCORB*(DFLOAT(I-1)/360.0D0)
1101                    CONTINUE
GO TO 1119
1112                    CONTINUE
C Battery drain power correction is performed according to the horizontal
C polarization.
DO 1102 I=1,360*NS+1
HRMAG(I)=HRMAG(I)+POWCORA*(DFLOAT(I-1)/360.0D0)
VRMAG(I)=VRMAG(I)+POWCORA*(DFLOAT(I-1)/360.0D0)
1102                    CONTINUE
GO TO 1119
1119            CONTINUE
END IF

DO 100 I=1,360*NS+1
HORMAG=HRMAG(I)
HORPHS=HRPHS(I)
VERMAG=VRMAG(I)
VERPHS=VRPHS(I)
ANG=A(I)
GO TO (101,102,102,104,105,105) ORIENTATION
C AN pertains to the angle for the predicted curve.
C ANG pertains to the angle for the measured curve.
101 CONTINUE
C VERTICAL orientation or theta=90 degrees cut:
IF (ANG .LE. -90.0) THEN
C Measurement: -180 to  -90 ------> phi: 270 to 360 of theta=90 cut
C If IM=  1,  ANG =-180.0,    AN=270.0, IP=271= 1+270*NS thus IP=IM+270*NS
C If IM= 91,  ANG = -90.0,    AN=360.0, IP=361=91+270*NS thus IP=IM+270*NS
  AN(I+270*NS)=ANG+450.0
HMAG(I+270*NS)=HORMAG
```

```
HPHS(I+270*NS)=HORPHS
VMAG(I+270*NS)=VERMAG
VPHS(I+270*NS)=VERPHS
END IF
IF (ANG .GE. -90.0) THEN
C Measurement:  -90 to   +180 ------> phi:   0 to 270 of theta=90 cut
C If IM= 91,   ANG = -90.0,    AN=  0.0, IP=  1= 91-90*NS thus IP=IM-90*NS
C If IM=361,   ANG=+180.0,     AN=270.0, IP=271=361-90*NS thus IP=IM-90*NS
  AN(I-90*NS)=ANG+90.0
HMAG(I-90*NS)=HORMAG
HPHS(I-90*NS)=HORPHS
VMAG(I-90*NS)=VERMAG
VPHS(I-90*NS)=VERPHS
END IF
GO TO 109
102 CONTINUE
C FLAT orientation (phi=180 degrees cut) or
C EDGE orientation (phi=270 degrees cut):
IF (ANG .LE. 0.0) THEN
C Measurement: -180 to 0 ------> theta: +180 to 0    of phi=0 or 90 cut
C If IM=1,   ANG=-180.0, AN=180.0, IP=181=180*NS+2-1   thus IP=180*NS+2-IM
C If IM=181, ANG=   0.0, AN=  0.0, IP=  1=180*NS+2-181 thus IP=180*NS+2-IM
  AN(180*NS+2-I)=-ANG
HMAG(180*NS+2-I)=HORMAG
HPHS(180*NS+2-I)=HORPHS
VMAG(180*NS+2-I)=VERMAG
VPHS(180*NS+2-I)=VERPHS
END IF
IF (ANG .GE. 0.0) THEN
C Measurement: 0 to +180 ------> theta:    0 to +180 of phi=180 or 270 cut
C If IM=181, ANG=   0.0, AN=360.0, IP=361=540*NS+2-181 thus IP=540*NS+2-IM
C If IM=361, ANG=+180.0, AN=180.0, IP=181=540*NS+2-361 thus IP=540*NS+2-IM
  AN(540*NS+2-I)=360.0-ANG
```

```
HMAG(540*NS+2-I)=HORMAG
HPHS(540*NS+2-I)=HORPHS
VMAG(540*NS+2-I)=VERMAG
VPHS(540*NS+2-I)=VERPHS
END IF
GO TO 109
104 CONTINUE
C Head-up-Nose-forward orientation;
IF (ANG .LE. 0.0) THEN
C Measurement: -180 to 0 ------> phi: +180 to +360
C If IM=  1, ANG=-180.0, AN=180.0, IP=181=  1+180*NS thus IP=IM+180*NS
C If IM=181, ANG=   0.0, AN=360.0, IP=361=181+180*NS thus IP=IM+180*NS
  AN(I+180*NS)=ANG+360.0
HMAG(I+180*NS)=HORMAG
HPHS(I+180*NS)=HORPHS
VMAG(I+180*NS)=VERMAG
VPHS(I+180*NS)=VERPHS
END IF
IF (ANG .GE. 0.0) THEN
C Measurement: 0 to +180 ------> phi:    0 to +180
C If IM=181, ANG=   0.0, AN=  0.0, IP=  1=181-180*NS thus IP=IM-180*NS
C If IM=361, ANG=+180.0, AN=180.0, IP=181=361-180*NS thus IP=IM-180*NS
  AN(I-180*NS)=ANG
HMAG(I-180*NS)=HORMAG
HPHS(I-180*NS)=HORPHS
VMAG(I-180*NS)=VERMAG
VPHS(I-180*NS)=VERPHS
END IF
GO TO 109
105 CONTINUE
C Left-ear-up-Nose-forward or Left-ear-forward-Nose-down orientation;
IF (ANG .LE. -90.0) THEN
C Measurement: -180 to -90 ------> theta:  90 to   0 of phi=180 or 270 cut
```

```
C If IM=1,  ANG =-180.0,  AN=270.0, IP=271=270*NS+ 1 thus IP=270*NS+IM
C If IM=91, ANG = -90.0,  AN=360.0, IP=361=270*NS+91 thus IP=270*NS+IM
  AN(270*NS+I)=ANG+450.0
HMAG(270*NS+I)=HORMAG
HPHS(270*NS+I)=HORPHS
VMAG(270*NS+I)=VERMAG
VPHS(270*NS+I)=VERPHS
END IF
IF (ANG .GE. -90.0) THEN
C Measurement: -90 to  +90 ------> theta:   0 to 180 of phi=0 or 90 cut
C If IM=91,  ANG= -90.0,   AN=  0.0, IP=  1= 91-90*NS thus IP=IM-90*NS
C If IM=271, ANG= +90.0,   AN=180.0, IP=181=271-90*NS thus IP=IM-90*NS
C Measurement: +90 to +180 ------> theta: 180 to  90 of phi=180 or 270 cut
C If IM=271, ANG= +90.0,   AN=180.0, IP=181=271-90*NS thus IP=IM-90*NS
C If IM=361, ANG=+180.0,   AN=270.0, IP=271=361-90*NS thus IP=IM-90*NS
  AN(I-90*NS)=ANG+90.0
HMAG(I-90*NS)=HORMAG
HPHS(I-90*NS)=HORPHS
VMAG(I-90*NS)=VERMAG
VPHS(I-90*NS)=VERPHS
END IF
GO TO 109
109 CONTINUE
100 CONTINUE

OPEN (UNIT=21,FILE=OUFILE,STATUS='UNKNOWN')

DO 300 I=1,360*NS+1
WRITE (21,1000) AN(I),0.0,HMAG(I),HPHS(I),VMAG(I),VPHS(I)
300 CONTINUE
1000    FORMAT (X,F7.1,2X,F3.1,2X,2(2X,E15.7,2X,F7.2))

END
```

C.5 Power correction of the acquired data with respect to the power transfer function of the network analyzer

```
C ***********************************************************************
C Last revised: 18 December 1998
C This program performs a parabolic interpolation between measured
C points of the power curve for the network analyzer.
C ***********************************************************************

PROGRAM POWER_CORRECTION

PARAMETER(IMAX=1801,NA=12,NB=12)

CHARACTER*50 INFILE,OUFILE

REAL*4 ANGLE(IMAX),A(IMAX),B(IMAX),TEMP
REAL*4 Y,PRELA(NA),PABSA(NA),PRELB(NB),PABSB(NB)

INTEGER FLAG2,APOINTER(IMAX),BPOINTER(IMAX)

C Horizontal polarization
DATA PABSA/-5.,-10.,-15.,-20.,-25.,-30.,-35.,-40.,-45.,-50.,-55.,-60./
DATA PRELA/-8.48,-13.07,-18.07,-23.02,-28.03,-33.05,-38.01,-42.98,
     &-47.84,-52.55,-56.57,-59.48/
C Vertical polarization
DATA PABSB/-5.,-10.,-15.,-20.,-25.,-30.,-35.,-40.,-45.,-50.,-55.,-60./
DATA PRELB/-9.06,-13.66,-18.64,-23.60,-28.60,-33.63,-38.59,-43.56,
     &-48.42,-53.13,-57.14,-60.05/

  WRITE(6,*) 'INFILE = ?'
READ(5,*) INFILE
  WRITE(6,*) 'OUFILE = ?'
```

```
READ(5,*) OUFILE

OPEN (UNIT=11,FILE=INFILE,STATUS='OLD')
OPEN (UNIT=21,FILE=OUFILE,STATUS='UNKNOWN')

        WRITE(6,*) 'Are stop angles included in the input data file
     &(1=YES, 2=NO)?'
        READ(5,*) FLAG2
        WRITE(6,*) 'NNN = ?'
        READ(5,*) NNN

DO 100 I=1,NNN
IF (FLAG2 .EQ. 1) THEN
READ(11,*) ANGLE(I),TEMP,A(I),TEMP,B(I),TEMP
ELSE
READ(11,*) ANGLE(I),     A(I),TEMP,B(I),TEMP
END IF
DELMIN=1.0E+9
DO 200 J=1,NA
DEL=ABS(A(I)-PRELA(J))
IF (DEL .LT. DELMIN) THEN
DELMIN=DEL
JDELMIN=J
END IF
200 CONTINUE
APOINTER(I)=JDELMIN
DELMIN=1.0E+9
DO 300 J=1,NB
DEL=ABS(B(I)-PRELB(J))
IF (DEL .LT. DELMIN) THEN
DELMIN=DEL
JDELMIN=J
END IF
```

```
300 CONTINUE
BPOINTER(I)=JDELMIN
100 CONTINUE

DO 500 I=1,NNN
CALL CORRECT(A(I),Y,APOINTER(I),NA,PRELA,PABSA)
A(I)=Y
CALL CORRECT(B(I),Y,BPOINTER(I),NB,PRELB,PABSB)
B(I)=Y
WRITE (21,1000) ANGLE(I),0.0,A(I),0.0,B(I),0.0
500 CONTINUE

1000    FORMAT (X,F7.1,2X,F3.1,2X,2(2X,E15.7,2X,F3.1))


CLOSE(21)
STOP
END

C ------------------------------------------------------------
SUBROUTINE CORRECT(X,Y,POINTER,N,PREL,PABS)

REAL*4 X1,Y1,X2,Y2,X3,Y3,X,Y
REAL*4 PREL(N),PABS(N)

INTEGER POINTER

IF ((POINTER .EQ. 1) .OR. (POINTER .EQ. N)) THEN
IF (POINTER .EQ. 1) THEN
X1=PREL(1)
Y1=PABS(1)
X2=PREL(2)
Y2=PABS(2)
```

```
X3=PREL(3)
Y3=PABS(3)
END IF
IF (POINTER .EQ. N) THEN
X1=PREL(N-2)
Y1=PABS(N-2)
X2=PREL(N-1)
Y2=PABS(N-1)
X3=PREL(N)
Y3=PABS(N)
END IF
ELSE
J=POINTER
X1=PREL(J-1)
Y1=PABS(J-1)
X2=PREL(J)
Y2=PABS(J)
X3=PREL(J+1)
Y3=PABS(J+1)
END IF
Y=Y1*((X-X2)*(X-X3))/((X1-X2)*(X1-X3))+
     &    Y2*((X-X1)*(X-X3))/((X2-X1)*(X2-X3))+
     &    Y3*((X-X1)*(X-X2))/((X3-X1)*(X3-X2))
RETURN
END
```

C.6 Total electric field contour level

```
C ***********************************************************************
C Last revised: 24 December 1998
C ***********************************************************************
C This version expects the data to be in dB.
C NS is the integer number of points per degree.
C ***********************************************************************

PROGRAM ISOLINE

PARAMETER(IMAX=361,NS=1)

CHARACTER*50 INFILE,OUFILE

INTEGER NS,ORIENTATION

REAL*8 A (IMAX),HRMAG(IMAX),HRPHS(IMAX),VRMAG(IMAX),VRPHS(IMAX)
REAL*8 POWCORA,POWCORB,TMP
REAL*8 R,R1(IMAX),R2(IMAX),LOSS,ETA,AEFF,P2E,EDES1,EDES2
REAL*8 HOR,EHREAL,EHIMAG,VER,EVREAL,EVIMAG,ETOT

R=3.350D0
ETA=376.728778D0
C ETA is the intrinsic impedance of free space.
AEFF=0.080D0
C AEFF is the effective aperture of the receive horn.
P2E=(2.0D0*ETA/AEFF)*1.0D-3
C P2E is a conversion factor from power (in W) to EM field power density
C (in W/m^2). The factor 1.0D-3 takes into account the fact that dBm
C refers to mW.
LOSS=1.04D0
```

```
C LOSS includes 0.90 dB for insertion loss of the cable and 0.14 dB for
C impedance mismatch loss of the receive horn.
C Two field level contours are desired: 1V/m and 3V/m.
EDES1=1.0D0
EDES2=3.0D0

  WRITE(6,*) 'ORIENTATION (1=Vert, 2=Flat, 3=Edge,
     & 4=HuNf, 5=LuNf, 6=LfNd) = ?'
READ(5,*) ORIENTATION
  WRITE(6,*) 'INFILE (measurement) = ?'
READ(5,*) INFILE
  WRITE(6,*) 'OUFILE (measurement) = ?'
READ(5,*) OUFILE

OPEN (UNIT=10,FILE=INFILE,STATUS='OLD')
        WRITE(6,*) 'Are stop angles included in the experimental data
     &file (1=YES, 2=NO) ?'
        READ(5,*) FLAG2

DO 10 I=1,360*NS+1
                IF (FLAG2 .EQ. 1) THEN
C The measurement data files include the stop angles in the second column.
READ (10,*) A(I),TMP,HRMAG(I),HRPHS(I),VRMAG(I),VRPHS(I)
ELSE
READ (10,*) A(I),    HRMAG(I),HRPHS(I),VRMAG(I),VRPHS(I)
END IF
10 CONTINUE

C It is very important that the linear power correction with respect to
C the battery drain be performed on the decibel scale.
POWCORA=HRMAG(1)-HRMAG(360*NS+1)
POWCORB=VRMAG(1)-VRMAG(360*NS+1)
IF (POWCORA  .LT. 0.0) WRITE(6,*) '### POWCORA (dB)=',POWCORA ,' < 0'
```

```
IF (POWCORB  .LT. 0.0) WRITE(6,*) '### POWCORB (dB)=',POWCORB ,' < 0'
WRITE (6,*) 'Do you want battery drain power correction (1=YES, 2=NO)?'
READ(5,*) FLAG1
IF (FLAG1 .EQ. 1) THEN
C The power scaling is performed with the slope computed from the +180
C and -180 degrees data least affected by electrical noise.
GO TO (1111,1112,1111,1111,1112,1111) ABS(ORIENTATION)
1111                    CONTINUE
C Battery drain power correction is performed according to the vertical
C polarization.
DO 1101 I=1,360*NS+1
HRMAG(I)=HRMAG(I)+POWCORB*(DFLOAT(I-1)/360.0D0)
VRMAG(I)=VRMAG(I)+POWCORB*(DFLOAT(I-1)/360.0D0)
1101                    CONTINUE
GO TO 1119
1112                    CONTINUE
C Battery drain power correction is performed according to the horizontal
C polarization.
DO 1102 I=1,360*NS+1
HRMAG(I)=HRMAG(I)+POWCORA*(DFLOAT(I-1)/360.0D0)
VRMAG(I)=VRMAG(I)+POWCORA*(DFLOAT(I-1)/360.0D0)
1102                    CONTINUE
GO TO 1119
1119            CONTINUE
END IF

DO 200 I=1,360*NS+1
HOR=DSQRT(P2E*(10.0D0**((HRMAG(I)-LOSS)/10.0D0)))
EHREAL=HOR*(DCOSD(HRPHS(I)))
EHIMAG=HOR*(DSIND(HRPHS(I)))
VER=DSQRT(P2E*(10.0D0**((VRMAG(I)-LOSS)/10.0D0)))
EVREAL=VER*(DCOSD(VRPHS(I)))
EVIMAG=VER*(DSIND(VRPHS(I)))
```

```
ETOT=DSQRT(((EHREAL+EVREAL)**2)+((EHIMAG+EVIMAG)**2))
R1(I)=(ETOT/EDES1)*R
R2(I)=(ETOT/EDES2)*R
200 CONTINUE

OPEN (UNIT=21,FILE=OUFILE,STATUS='UNKNOWN')

DO 300 I=1,360*NS+1
WRITE (21,1000) A(I),R1(I),R2(I)
300 CONTINUE

1000    FORMAT (X,F7.1,2X,2(2X,E15.7,2X,E15.7))

END
```

Appendix D

Gain Measurement of the Receive Horn

The gain for the receive horn (quad-ridged horn from Condor Systems, Model As 48450, Part #637542-001) was measured by the two antenna method in the summer of 1997. This method consists in determining the unknown gain of an antenna by measuring the power transfered between this antenna and another antenna, then computing the unknown gain from the knowledge of the gain for the second antenna while taking into account the propagation loss between the two antennas, the loss through the cables and the reflection loss from the antennas. It was assumed herein that the two antennas were perfectly linearly polarized and perfectly aligned at their respective boresight, and that the characteristic impedance of all cables and measuring equipment was 50 Ω. Only the vertical polarization channel of the quad-ridged horn was measured since neither the horn with known gain (Scientific Atlanta standard gain horn, Model 12-0.75, 0.75-1.12 GHz) nor the quad-ridged horn could readily be rotated by 90° for measuring the horizontal polarization channel of the quad-ridged horn. However, it is safe to assume that the two channels of the quad-ridged horn have the same gain since this horn is symmetrical with respect to both the vertical and the horizontal planes. Figure D.1 depicts the diagram of the equipment setup.

The equations for the system are as follows:

$$\frac{P_R}{P_T} = \left(\frac{\lambda}{4\pi R}\right)^2 G_R G_T \Longrightarrow \chi = 10\ log_{10}\left[\frac{P_R}{P_T}\right] \tag{D.1}$$

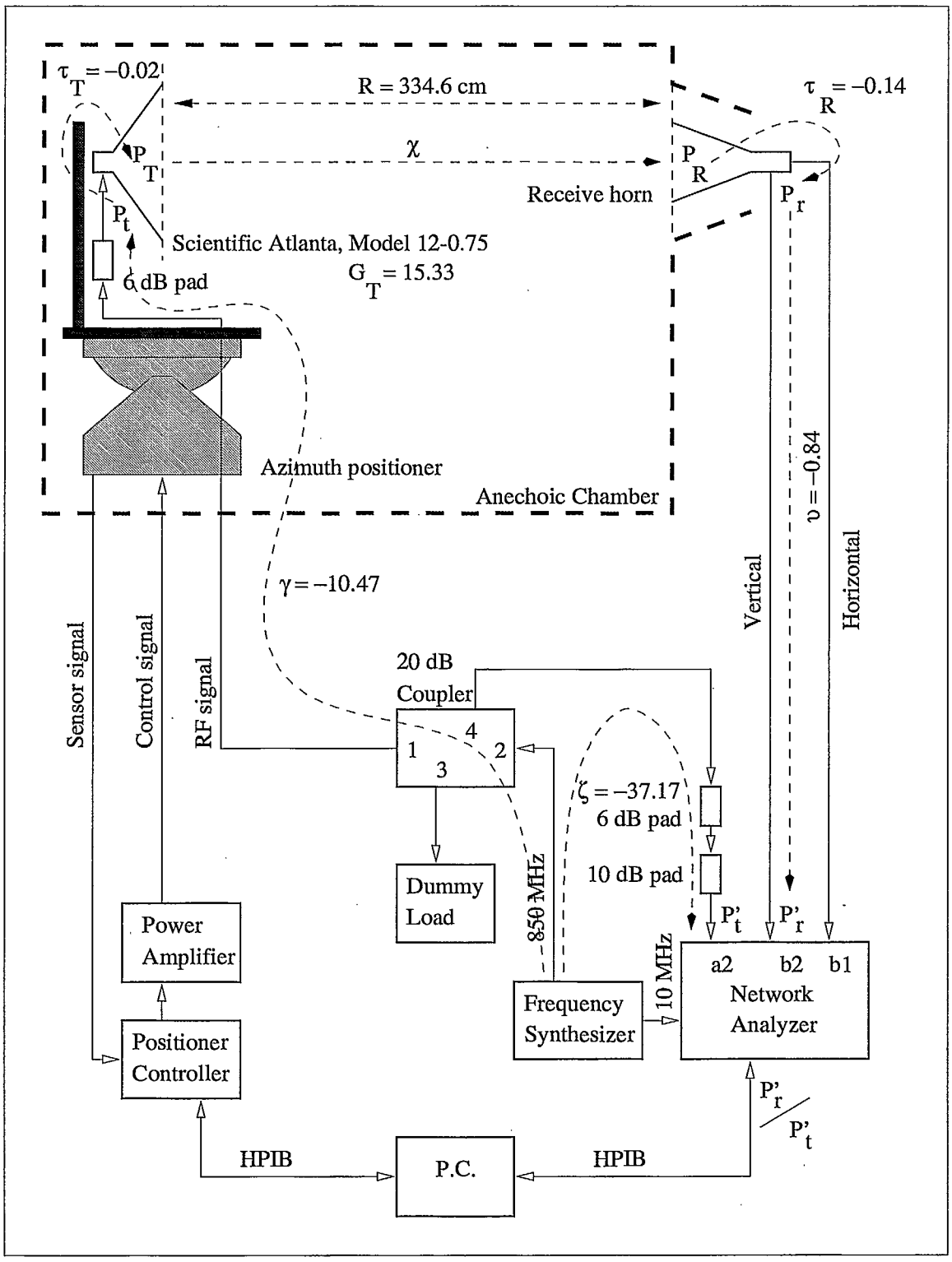

Figure D.1: The schematic diagram of the equipment setup for measuring the gain of the receive horn.

$$10\ log_{10}\left[\frac{P_R'}{P_T'}\right] = (\gamma + \tau_T + \chi + \tau_R + \nu) - (\zeta) \tag{D.2}$$

where P is the power level, $\lambda = 0.353\ m$ is the wavelength corresponding to 850 MHz in free space, $\tau = 1 - |\Gamma|^2$ with Γ being the reflection coefficient of the receive or transmit antenna as identified by the subscript, and γ, ν and ζ are as shown on the diagram of Figure D.1.

The measured quantities were as follows:

$$\text{R} = 334.6\ \text{cm} \Longrightarrow 10\ log_{10}\left[\left(\frac{\lambda}{4\pi R}\right)^2\right] = -41.53\ \text{dB}$$

$$10\ log_{10}\left[\frac{P_R'}{P_T'}\right] = 8.55\ \text{dB}$$

$$20\ log_{10}\left[|\Gamma_T|\right] = -22.80\ \text{dB} \Longrightarrow \tau_T = 10\ log_{10}\left[1 - |\Gamma_T|^2\right] = -0.02\ \text{dB}$$

$$\gamma = -10.47\ \text{dB}$$

$$\nu = -0.84\ \text{dB}$$

$$\zeta = -37.17\ \text{dB}$$

The measurement of the quantities γ and Γ_T required the use of a long coaxial cable that was included as part of the calibration setup of the network analyzer. This long coaxial cable was required to reach the transmit horn mounted on the positioner from the position of the network analyzer located outside the anechoic chamber.

The quantities obtained from manufacturers' data were as follows:

$$20\ log_{10}\left[|\Gamma_R|\right] \approx 15.0\ \text{dB} \Longrightarrow \tau_R = 10\ log_{10}\left[1 - |\Gamma_R|^2\right] = -0.14\ \text{dB}$$

$$10\ log_{10}\left[G_T\right] = 15.33\ \text{dB}$$

Therefore, the directivity (or lossless gain) of the quad-ridged horn became:

$$10\ log_{10}\left[G_R\right] = 9.05\ \text{dB}$$

and the corresponding maximum effective aperture area became:

$$A = \frac{\lambda^2}{4\pi} G_R = 0.080 \ m^2$$

This value is to be compared with the physical aperture area of 0.192 m^2.

LKC
TK5102.5 .C673e #99-001
c.2
Measurements of the
electromagnetic far-fields
produced by a portable
transmitter (principal
planes) : part II

DATE DUE
DATE DE RETOUR